Effects of ionic concentration dynamics on neuronal activity

Dissertation

zur Erlangung des akademischen Grades

Doctor rerum naturalium
(Dr. rer. nat.)

eingereicht an der
Lebenswissenschaftlichen Fakultät
der Humboldt-Universität zu Berlin

von

Susana Andrea Contreras Ceballos
M.Sc.

Präsident der Humboldt-Universität zu Berlin:
Prof. Dr. Peter Frensch

Dekan der Lebenswissenschaftlichen Fakultät:
Prof. Dr. Christian Ulrichs

Gutachter/innen:

1. Prof. Dr. Susanne Schreiber
2. Prof. Dr. Benjamin Lindner
3. Prof. PhD Nicolas Brunel

Tag der mündlichen Prüfung: 16. April 2021

Abstract

Neurons are essential in the information transfer mechanisms of the central nervous system. Their activity underlies both basic signal processing, and higher cognitive processes. Neurons are embedded in the extracellular space, which contains multiple particles, including ions which are vital to their functioning. Ionic concentrations are not static, intense neuronal activity alters the intracellular and extracellular ionic concentrations which in turn affect neuronal functioning. In this thesis, I study the interplay between neuronal activity and ionic concentration dynamics. I focus specifically on the extracellular potassium and intracellular sodium concentrations. Using dynamical systems theory, I illustrate how moderate changes in these ionic concentrations can qualitatively change neuronal activity, potentially altering signal processing. I then model a conductance-based spiking neural network. The model predicts that a moderate change in the concentrations surrounding a microcircuit of neurons could modify the power spectral density of the population activity. Altogether, this work highlights the need to consider ionic concentration dynamics to understand neuronal activity on long time scales and provides technical insights on how to model and analyze the interplay between them.

Zusammenfassung

Neuronen sind bei der Informationsübertragung des zentralen Nervensystems von entscheidender Bedeutung. Ihre Aktivität liegt der Signalverarbeitung und höheren kognitiven Prozessen zugrunde. Neuronen sind in den extrazellulären Raum eingebettet, der mehrere Teilchen, darunter auch Ionen, enthält. Ionenkonzentrationen sind nicht statisch. Intensive neuronale Aktivität kann intrazelluläre und extrazelluläre Ionenkonzentrationen verändern. In dieser Arbeit untersuche ich das Wechselspiel zwischen neuronaler Aktivität und der Dynamik der Ionenkonzentrationen. Dabei konzentriere ich mich hauptsächlich auf extrazelluläre Kalium- und intrazelluläre Natriumkonzentrationen. Mit Hilfe der Theorie dynamischer Systeme zeige ich, wie moderate Änderungen dieser Ionenkonzentrationen die neuronale Aktivität qualitativ verändern können, wodurch sich möglicherweise die Signalverarbeitung verändert. Dann modelliere ich ein leitfähigkeitsbasiertes neuronales Netzwerk mit Spikes. Das Modell sagt voraus, dass eine moderate Änderung der Konzentrationen, die einen Mikroschaltkreis von Neuronen umgeben, die Leistungsspektraldichte der Populationsaktivität verändern könnte. Insgesamt unterstreicht diese Arbeit die Bedeutung der Dynamik der Ionenkonzentrationen für das Verständnis neuronaler Aktivität auf langen Zeitskalen und liefert technische Erkenntnisse darüber, wie das Zusammenspiel zwischen ihnen modelliert und analysiert werden kann.

Contents

Part I

Literature review

1 Introduction

1.1 Context

Sometimes cravings for such thing as a sunny day, a cold lake, or a warm soup are very intense and take up all our thoughts. Such cravings can be very intense, but fortunately they do not occur all the time. We don't crave a warm soup when the environmental temperature is 35°C, and we don't wish to swim in a cold lake when it's freezing cold outside. Cravings are all relative to our current situation. I, particularly, find joy in a long night's sleep after being deprived from it, or enjoy listening to a good piece of music while cooking. However, it irritates me tremendously when I get woken up by the exact same piece. The way in which we perceive the environment surrounding us does not solely depend on the particular stimuli that elicit our perceptions. Rather, a big part of our perception depends on our brain state.

Many factors can alter brain state, extrinsic and intrinsic. Extrinsic factors like environmental changes or ingesting drugs like coffee or alcohol can trigger changes in our brain activity. Or, intrinsically generated neurotransmitters like dopamine or serotonin might activate previously inactive regions of the brain. Besides neurotransmitters, many other molecules and proteins are released and stored in a coordinated fashion such that neuronal activity supports the current brain state.

Among those molecules are ions. These are crucial molecules, whose concentrations allow and affect neuronal activity. I am particularly intrigued by the effect that ionic concentrations can have on the brain state. Ionic concentrations can change as a function of previous activity (Singer and Lux, 1975), as well as throughout behavioral states (Amzica et al., 2002; Ding et al., 2016). Yet, it is not clear whether such changes enhance brain state or whether they are just a by-product of a change in the brain activity.

In this work, I start by investigating the effect that ionic concentrations have on single neuron dynamics, as well as the effect such single neuronal dynamics have on ionic concentrations. I show how prolonged spiking activity, by altering ionic concentrations, reduces transmembrane gradients and changes voltage dynamics. Individual neurons, thus, may respond very differently to the same input stimuli depending on their recent patterns of activity or the current brain-state. In addition, I illustrate how the response of neurons can be predicted based on the ionic concentrations and input stimuli. Based on these predictions, I demonstrate how the dynamics of a neuronal microcircuit undergoing ionic concentration changes are distorted.

Before going into the details of how this subject is targeted in this thesis, it is useful to revisit some concepts about brain function.

1.1.1 Information transfer in the brain

The brain is one of the most complex organs. It integrates information about the environment surrounding the animal, and coordinates reactions by controlling the activity of other organs and muscle fibers. Information from the brain to the organs and muscle fibers can be delivered through chemical or electrical signals. Electrical signals are efficiently propagated through specialized cells in the central nervous system called neurons.

Neurons are able to propagate electrical pulses rapidly over large distances. Such electric pulses are known as action potentials or spikes. Neurons can react to incoming input by generating action potentials that can in turn stimulate other cells. The incoming signals are received by dendrites, then integrated in the somata. If the soma produces an action potential in response to the incoming signals, it is propagated by the axon, which targets another neuron, muscle or gland.

1.1.2 Action potential generation

In our contemporary view of brain computation, the action potential is an essential component of information transmission. This inspired a thorough study of action potential generation in this thesis.

An action potential, or spike, is a fast transient depolarization of the membrane electrical potential. Such a depolarization occurs when small electrical incoming signals from the dendrites are amplified by transmembrane ion channels in the soma (more precisely the axon initial segment). Incoming depolarizing pulses can alter the conformation of transmembrane ion channels, by increasing or decreasing their permeability to an ion (or multiple ions). Given the electrochemical ionic gradients across the neuronal membrane, such permeability changes result in transmembrane ionic fluxes.

Ionic fluxes can depolarize or hyperpolarize the neuronal membrane. Ions are electrically charged particles, and therefore, ionic fluxes result in electrical currents. For instance, when ions have a positive electric charge and the net ionic flux goes from the intracellular space to the extracellular space, the ionic current hyperpolarizes the neuronal membrane. When the direction of the flux or the electric charge of the ion is inverted, the current depolarizes the neuronal membrane potential. The coordinated sequence of depolarizing and hyperpolarizing currents gives rise to action potentials.

The possible repertoire of transmembrane ionic channels is very large across neurons, even within different locations in a single neuron. The diverse ionic fluxes resulting from the ample repertoire of transmembrane ionic channels can yield different spike generation and termination mechanisms. Given that the spike generation mechanism can vary, the same stimulus can produce an action potential in one neuron, while none in other neurons. These distinct response properties of neurons form the basis of the concept of "excitability class", which will be revisited later in the thesis. Different response properties among

neurons from different brain regions, yield different ways to transform incoming stimuli into outputs *i.e* a diverse decoding scheme across the brain.

In order to understand decoding schemes in individual neurons, one approach is to predict what type of stimulus makes a neuron spike. A useful tool to predict spike generation is mathematical modelling, which will be used throughout this thesis.

1.1.3 Modelling spike generation

1.1.3.1 The Hodgkin-Huxley model

The pioneers in using models to understand neuronal membrane potential dynamics were Hodgkin and Huxley (1952). They proposed that the membrane potential fluctuations measured in the squid giant axon could be mimicked with a mathematical model. The model was inspired by the resemblance of the neuronal membrane to an electrical circuit. Transmembrane ionic channels resemble resistors, through which electric currents can flow. Ionic channels impose a resistance that is proportional to the permeability of the channel to the specific ions flowing through it. While the lipid bilayer that constitutes the neuronal membrane is effectively a capacitor, which stores electrical energy by preserving the ionic gradient from the intracellular space to the extracellular space.

Hodgkin and Huxley (1952) showed that the dynamics of currents flowing through the neuronal membrane can be described by the following differential equation,

$$I_{in} = C_m \frac{dV_m}{dt} + \sum I_i. \tag{1.1}$$

The first term on the right-hand side, is the current that flows through the lipid bilayer. The second term is the sum of the ionic currents flowing through the transmembrane channels:

$$I_i = g_i(V - E_i). \tag{1.2}$$

The net ionic current flowing through a transmembrane channel can be expressed as the product of the ionic conductance of the transmembrane channel (g_i) and the difference between the membrane potential (V) and the Nernst equilibrium potential for each ion i (E_i).

Hodgkin and Huxley considered three currents, which they had measured from patch clamp experiments; One voltage-gated transient sodium (Na^+), one voltage-gated persistent potassium (K^+), and a passive (Ohmic) leak current (a mixture of chloride Cl^- and potassium K^+). Thus in their model, the total current flowing through the neuronal membrane is the sum of the sodium, potassium, leak, and the capacitive current,

$$I_{in} = C_m \frac{dV}{dt} + g_K(V - E_K) + g_{Na}(V - E_{Na}) + g_l(V - E_l). \tag{1.3}$$

Transmembrane ionic channels have gates, which switch between open and closed states. When the gates are in an open state they allow the flux of ions to which they are permeable. Such transitions are stochastic but when considering large populations of

ion channels, it is possible to estimate the average proportion of open ion channels (p). Thus, the expected value for the conductance of a specific ion channel is the product of the proportion of ion channels, and the maximal conductance of the channel ($\bar{g_i}$),

$$g_i = \bar{g_i} p. \tag{1.4}$$

The probability of being in an open state (p) may be sensitive to the membrane potential, to intracellular agents (like Ca^{2+}), or to extracellular neuromodulatory agents like NMDA[1], GABA[2] or AMPA[3]. In this thesis only the membrane potential sensitivity of the channels will be modelled ($p(V)$). However, later in this review chapter the sensitivity to extracellular agents will be discussed.

Hodgkin and Huxley explored the conductance dependence of channels on membrane potential by measuring transmembrane currents at different membrane potentials. They used a technique developed by Cole and Moore (1960) termed the "voltage clamp", where the current needed to hold the membrane potential fixed is measured. Such current must equal the transmembrane currents (equation 1.3). Therefore, the time course of transmembrane currents can be derived (notice that the first term in the right hand side of equation 1.3 is zero).

In order to quantify the sodium (Na^+) current independently from the potassium (K^+) current, Hodgkin and Huxley assumed that immediately after the voltage is depolarized the transmembrane current is mostly resulting from the flux through the voltage-gated transient sodium (Na^+) channel. To quantify the potassium (K^+) current, Hodgkin and Huxley replaced the extracellular sodium (Na^+) with choline, and compared the currents measured with no extracellular sodium (Na^+) to the ones measured with normal extracellular sodium (Na^+). This was done in order to calculate the ratio of potassium vs sodium currents (with the baseline assumption that the potassium K^+ current is independent from the extracellular sodium Na^+).

After observing the resulting potassium (K^+) and sodium (Na^+) currents, Hodgkin and Huxley proposed a mathematical expression to describe the time evolution of transmembrane channel conductance as a function of the membrane voltage. The parameters of the expressions were fitted to the data.

For the voltage-dependent persistent potassium (K^+) channel, the probability of being in an open state (p) could be described with the fourth power of a dynamic dimensionless variable n that acquires values between 0 and 1. Thus,

$$g_K = \bar{g_K} n^4, \tag{1.5}$$

$$\tau_n(V)\frac{dn}{dt} = n_\infty(v) - n, \tag{1.6}$$

[1] NMDA stands for N-Methyl-d-aspartate. NMDA is an excitatory neurotransmitter (Purves, 2004).

[2] GABA stands for gamma-Aminobutyric acid. GABA is an inhibitory neurotransmitter in the mature brain (Purves, 2004).

[3] AMPA stands for α-amino-3-hydroxy-5-methyl-4-isoxazolepropionic acid, an excitatory neurotransmitter (Purves, 2004).

where $\tau_n(V)$ and $n_\infty(v)$ are determined from experimental data. For the voltage-dependent transient sodium (Na^+) channel, the probability of being in an open state (p) could be described with two dynamic dimensionless variables m, and h.

$$g_{Na} = g\bar{}_{Na} m^3 h. \tag{1.7}$$

The evolution in time of m and h can be expressed in the same way as n (equation 1.6).

$$\tau_m(V)\frac{dm}{dt} = m_\infty(v) - m, \tag{1.8}$$

$$\tau_h(V)\frac{dh}{dt} = m_\infty(h) - h, \tag{1.9}$$

Thus, the expression for the total current flowing through the membrane can be expressed as,

$$I_{in} = C_m\frac{dV}{dt} + g\bar{}_K n^4(V - E_K) + g\bar{}_{Na} m^3 h(V - E_{Na}) + g_l(V - E_l). \tag{1.10}$$

For a deeper and more graphical explanation of voltage dependent gating dynamics the reader can refer to Izhikevich (2007).

1.1.3.2 Analysing action potential generation in conductance based models

Action potentials come about from the coordinated sequence of depolarizing and hyperpolarizing currents, as explained above. In the Hodgkin-Huxley model, it is the interplay between sodium and potassium currents that generate spikes. Depolarized membrane potentials rapidly increase the conductance of the transient sodium channel (g_{Na}), and with a short lag the conductance of the persistent potassium channel (g_K). The Nernst potential for sodium (E_{Na}) is much more depolarized than the resting membrane potential of neurons, so an increase in the sodium conductance results in a depolarizing current. An increase in the potassium conductance on the other hand, results on a net hyperpolarizing current, because the Nernst potential for potassium (E_K) is more hyperpolarized than the resting membrane potential (see equation 1.3).

The sequential increase and decrease in the conductances of sodium and potassium channels, can produce different membrane potential dynamics. They can lead to a small perturbation of the membrane potential much lower than an action potential, to a single action potential, or to a cyclic depolarization and hyperpolarization of the membrane potential (regular firing).

In Figure 1.1, the solutions for the Hodgkin-Huxley equations are shown for different initial conditions. Notice that some solutions display a small perturbation of the membrane potential, and some a single action potential. However, for this set of parameters all solutions converge to the same **stable equilibrium** or resting state. When the input current (I_{in}) is increased (see Figure 1.2), the same initial conditions always lead to a cyclic depolarization of the membrane potential (regular spiking).

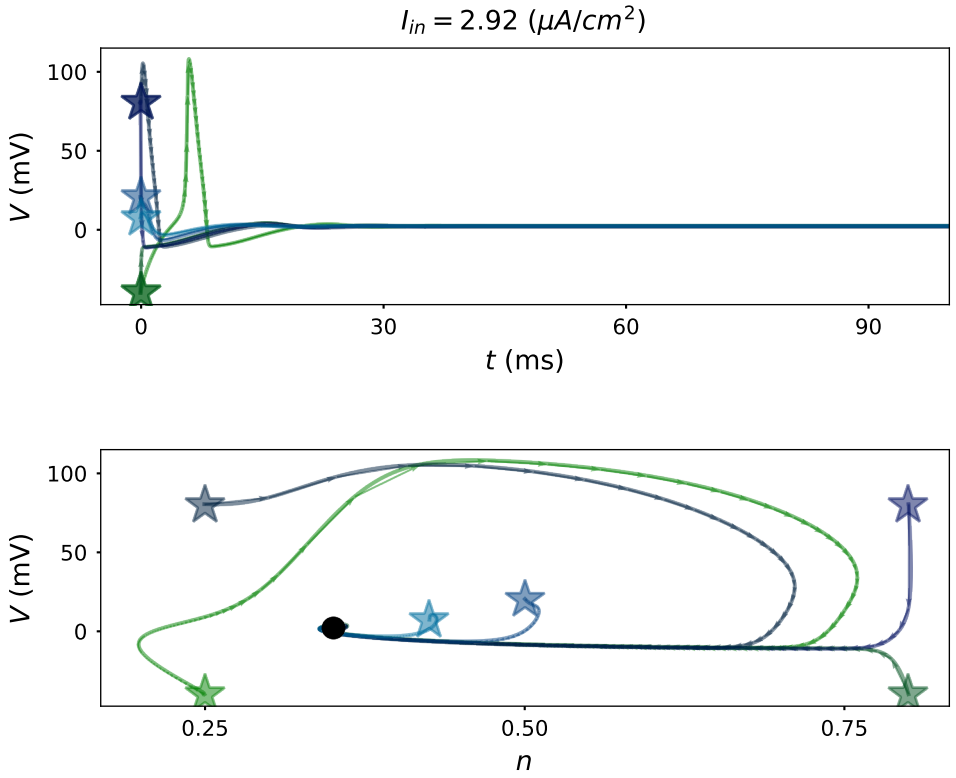

FIGURE 1.1: Solution of the Hodgkin-Huxley equations, given a constant input current $I_{in} = 2.92\ \mu A/cm^2$ and different initial conditions (denoted with a star). **Top panel** shows the membrane potential trace in time. **Bottom panel** shows the same trajectories shown in the top panel, but projected to the 2D plane (membrane potential, and potassium channel activation variable in equations 1.7 and 1.6). The black dot represents the stable equilibrium of the system. Here it is possible to observe that even though initial conditions differed in the trajectories portrayed, they all converge to the stable node.

From Figures. 1.1 and 1.2, it is possible to observe that the input current (I_{in}) can change the response of the dynamical system from quiescence to regular spiking. In other words, the input current (I_{in}) has the potential to change the **attractors** [4] of the system. In Figure 1.1, all trajectories are attracted to a single point in the state space, or a **stable focus** [5], which corresponds to the resting membrane potential. In Figure 1.2, all trajectories are attracted to a **limit cycle**[6], the neuron-model generates regular spiking.

1.1.3.3 Spike generating bifurcations

In dynamical systems theory, a qualitative modification of the system dynamics caused by a small change in the parameters is called a **bifurcation**. For the example shown here

[4] An attractor is the state to which the system converges, regardless of the initial conditions. When there is more than one attractor, the system converges to the attractor whose basin of attraction is closer to the initial conditions.

[5] A stable focus is a point in state space that attracts trajectories. Trajectories rotate when approaching a stable focus.

[6] A limit cycle is a closed orbit that repeats itself in time. If a trajectory converges to a limit cycle, then the limit cycle is stable (limit cycle attractor).

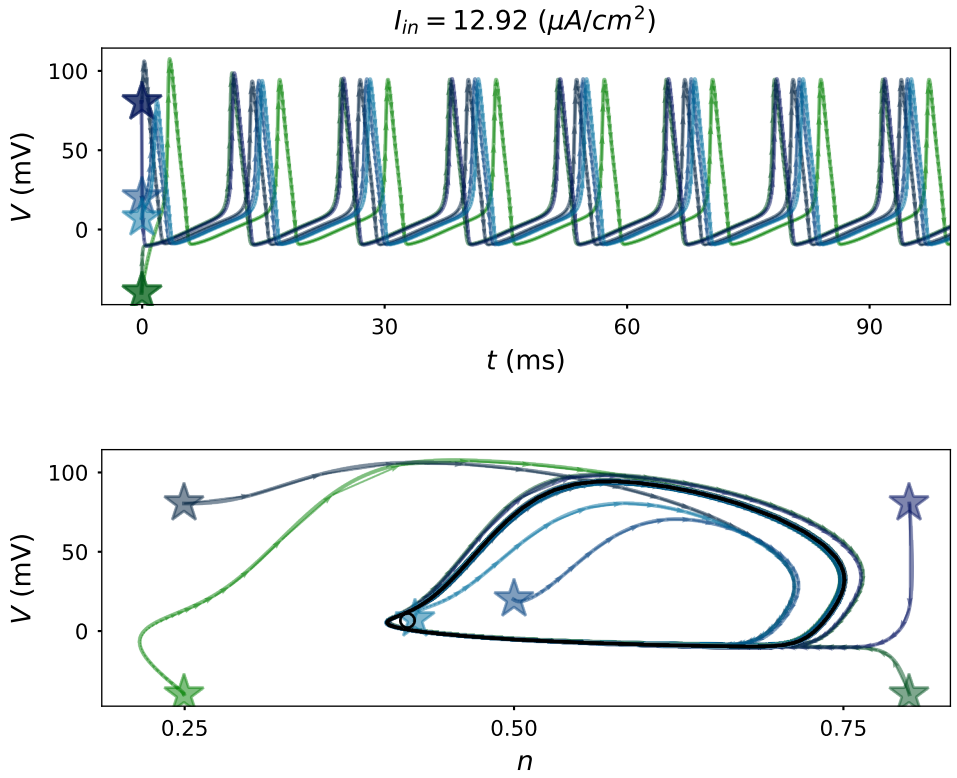

FIGURE 1.2: Solution of the Hodgkin-Huxley equations, given a constant input current $I_{in} = 12.92\ \mu A/cm^2$ and different initial conditions (denoted with a star). **Top panel** shows the membrane potential trace in time. **Bottom panel** shows the trajectories projected to the 2D (membrane potential, and potassium channel activation variable) plane. Open circle denotes an unstable fixed point of the system, and the orbit in black a stable limit cycle.

(Figures.1.1 and 1.2) the bifurcation parameter is the input current (I_{in}), which changes the stability of the stable node from stable to unstable, while a stable limit cycle appears. The Hodgkin-Huxley model, and other conductance based models that where inspired by this model, all contain a bifurcation of that sort which makes those models excitable (Izhikevich, 2007). There are different types of bifurcations that allow dynamical systems to transition from quiescence to spiking. It is these different, but finite, bifurcation types that form the mathematical basis for different functional excitability classes.

The bifurcation type reveals information regarding stimuli features that generate spikes for each neuron-model, which is why studying models from this perspective is very useful for understanding stimuli encoding. Furthermore, even though it is very hard to measure every transmembrane current in a real neuron, it is feasible to predict the bifurcation type from the experimentally-measurable excitability properties.

There are four main types of bifurcations that induce the change from quiescence to regular firing in conductance based models; The **subcritical Hopf**, the **supercritical Hopf**, **saddle-node** (or saddle homoclinic orbit, HOM), and the **saddle-node on invariant circle (SNIC)** bifurcations. Here, a brief description of the first three bifurcations will be provided. For a more detailed description of the dynamics of all those bifurcations the reader can refer to Izhikevich (2007).

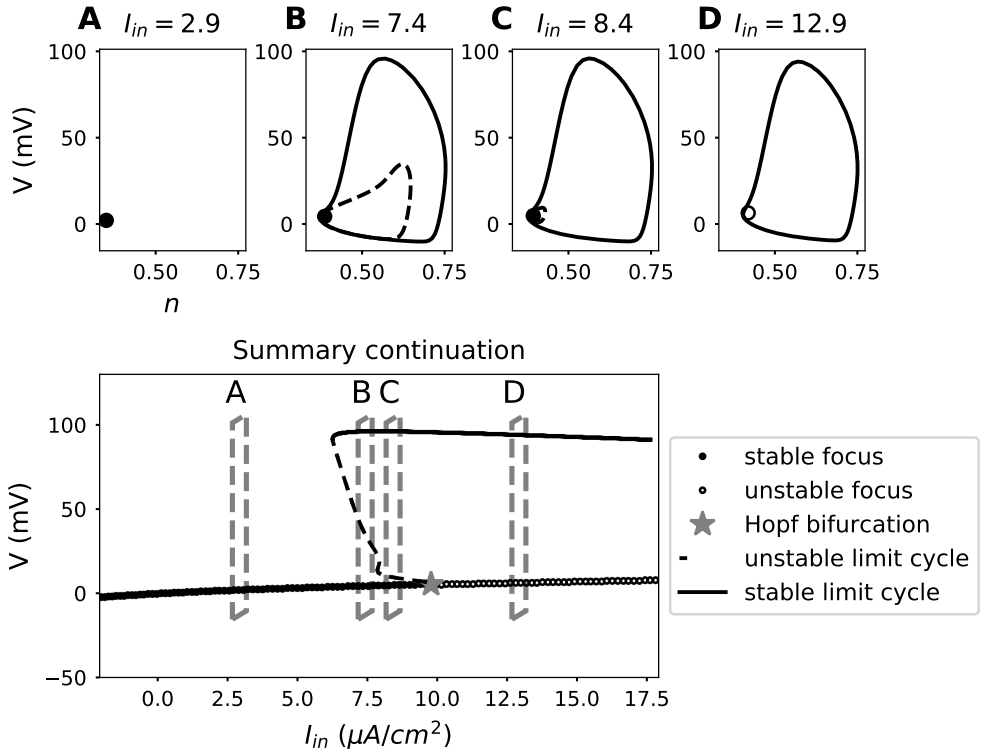

FIGURE 1.3: Subcritical Hopf bifurcation.**Top panel**: Phase planes (stable states projected into the membrane potential - potassium channel activation variable 2D plane) of the system for different input currents. **Bottom panel**: Dependence of the attractors of the dynamical system on the input current I_{in}. For low input currents I_{in}, the system has a stable focus (black dot in **A**). For input currents just before the bifurcation, a stable (black orbit) and an unstable limit cycle (dashed orbit) emerge, the system has two stable attractors (**B** and **C**). At the Hopf bifurcation, marked by a grey star, the unstable limit cycle collides with the stable focus and makes it lose stability, and an unstable node (empty dot) emerges. For higher input currents, the only attractor of the system is the limit cycle (**D**).

The **subcritical Hopf** bifurcation, is the one that generates action potentials in the Hodgkin-Huxley model. In the subcritical Hopf bifurcation, a stable focus becomes unstable when an unstable limit cycle collides with it (see Figure 1.3). Notice that before the stable focus looses its stability, it coexists with a stable limit cycle. Thus, for a range of input currents, the dynamical system has two attractors and is bistable. For trajectories in the attraction domain of the stable limit cycle, depicted in Figure 1.4**A**, the neuron model displays regular spiking. For trajectories in the attraction domain of the stable focus, depicted in Figure 1.4**B**, oscillations occur around the resting membrane potential until they reach it. The neuron model can move from the basin of attraction of the stable focus to the one of the limit cycle due to perturbations.

When a model displays the subcritical Hopf spike generating bifurcation, damped oscillations of the membrane potential are observed (notice the spirals in Figure 1.4**B** and 1.11). Thus, when incoming stimulus has a similar frequency to the one of the

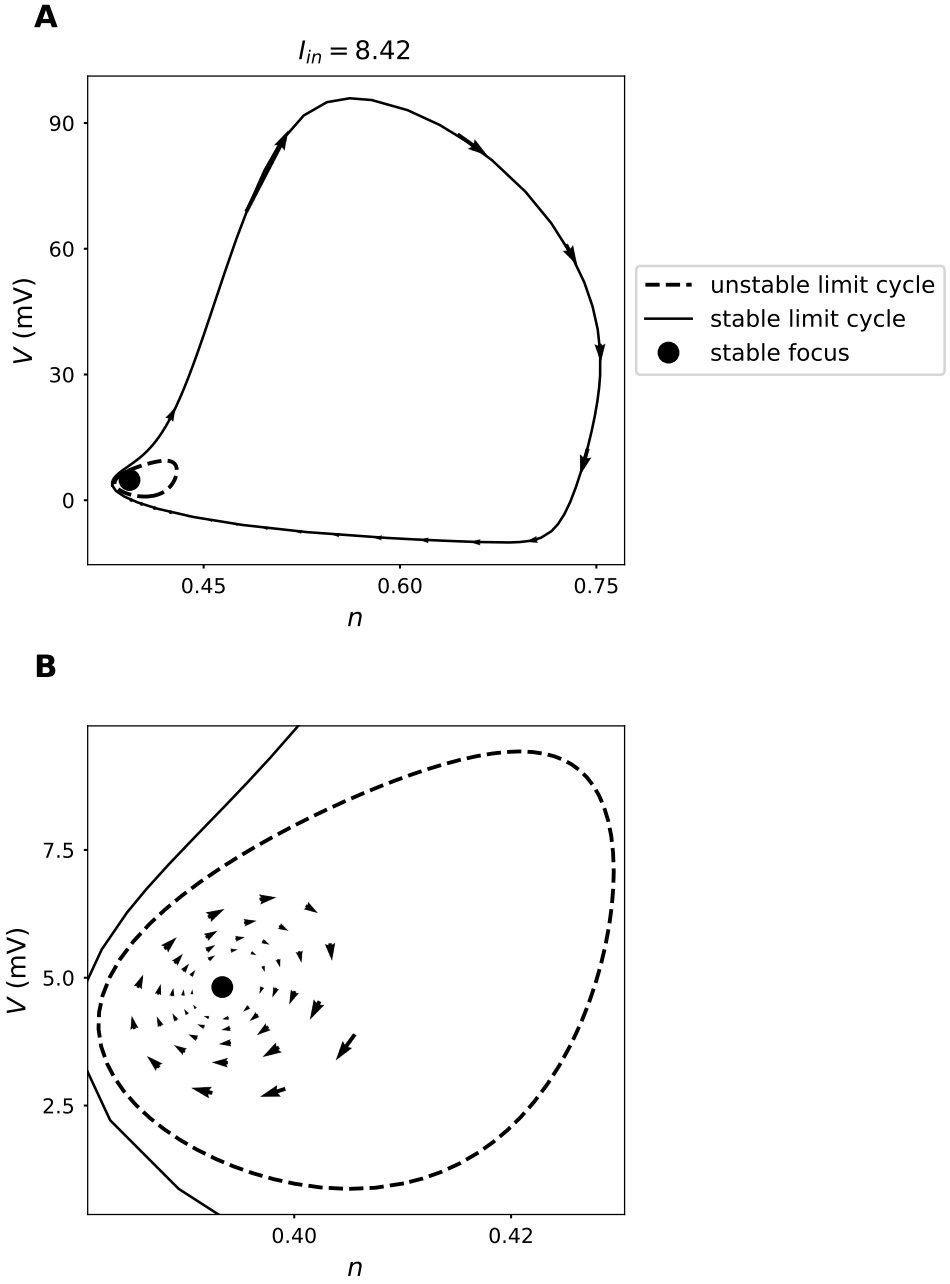

FIGURE 1.4: Phase plane in the bistable region of the Hodgkin-Huxley model. **A**: Phase plane denoting the attractors of the Hodgkin-Huxley model for input current $I_{in} = 8.42\ \mu A/cm^2$. A stable limit cycle (black line) coexists with a stable node (black dot). The separatrix between both attractors is the unstable limit cycle (dashed line). The arrows denote the direction and speed of trajectories. **B**: Zoom into the phase plane in (**A**). Trajectories lying in the basin of attraction of the stable focus, approach it spiraling into it.

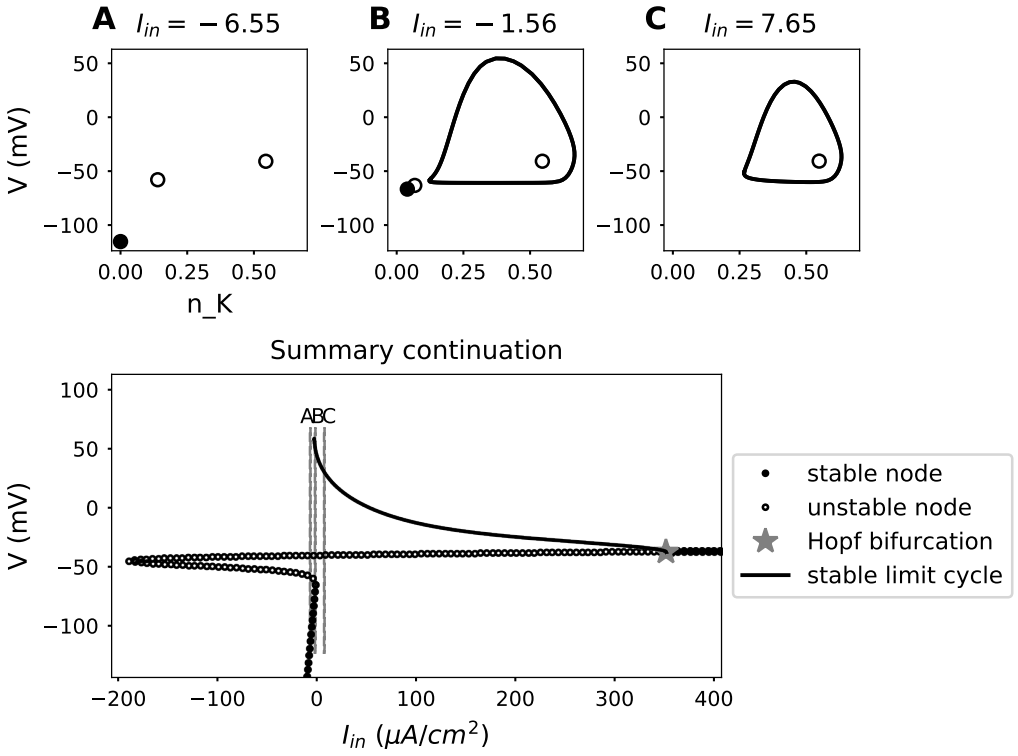

FIGURE 1.5: Saddle-node bifurcation. **Top panel**: Phase planes (stable states projected into the membrane potential - potassium channel activation variable 2D plane) of the system for different input currents. **Bottom panel**: Dependence of the attractors of the dynamical system on the input current I_{in}. For low input currents I_{in}, the system has a stable node, and two unstable nodes (**A**). For input currents just before the bifurcation, a limit cycle emerges, the system has two stable attractors (**B**). At the saddle-node bifurcation, one unstable node (saddle) collides with the stable node and makes it lose stability. For higher input currents, the only attractor of the system is the limit cycle (**C**).

membrane potential oscillations it is more likely to elicit spikes. This phenomenon is known as **resonance**. Izhikevich (2007) provide a deeper understanding of the link between the dynamics close to the bifurcation and the encoding properties of neurons exhibiting the subcritical Hopf bifurcation.

In the **saddle-node or saddle homoclinic orbit (HOM)** bifurcation, the **stable node**[7] loses stability when it collides with a **saddle point**[8]. Before the stable node collides with the saddle, a limit cycle attractor emerges. Thus, for a range of input currents the system is bistable (see Figure 1.5 and 1.12). What is unusual about the saddle-node bifurcation is that close to the saddle, the trajectories slow down. This bifurcation will be studied further along chapters 2, 3 and 4.

[7] A stable node is a point in state space to which the system converges. Trajectories don't rotate when approaching the stable node, as happens with the stable focus.

[8] A saddle point is an unstable node, with at least one stable and one unstable manifold. Most saddle points of conductance based neuron models have one unstable manifold, and all other manifolds are stable. This similarity between conductance-based neuron models can be explained by the Jacobian matrix structure.

The **saddle-node on invariant circle (SNIC)** is similar to the saddle-node bifurcation. The stable node also loses stability when colliding with a saddle node. The main difference between the SNIC and the HOM bifurcations is that in the SNIC , the stable limit cycle emerges only when the stable node loses its stability. At limit cycle onset, the stable orbit is born at the saddle node. The orbit diverges from the saddle node through its unstable manifold, and returns to it through its stable manifold.

The mentioned bifurcations are said to be codimension one. This means that by varying only one parameter, the bifurcation can be induced; in the previous examples, that parameter was the input current. There are also codimension two bifurcations, that occur when varying two parameters. In chapters 2 and 3, the occurrence of a codimension two bifurcation due to variations of the input current and a ionic (extracellular potassium) concentration, is analyzed. The codimension two bifurcation makes the neuron model transition from the SNIC spike generation to the HOM spike generation mechanism. Given the potential of ionic concentrations to change the spike generating mechanism of neurons, it is relevant to understand how they are distributed and regulated in the brain.

1.2 Ionic concentrations in the brain

Electrical signaling in the brain relies on ionic concentration differences between the intracellular and the extracellular space. Such differences generate electrochemical gradients that create the electrical potential for neuronal transmembrane currents. Ionic concentrations are dynamical variables, their dynamics are the consequence of ionic fluxes across the cellular membranes. Some ionic fluxes come about from homeostatic processes, like the active transport of sodium and potassium through the Na-K-ATPase pump. Other fluxes are the consequence of neuronal signaling, like the sodium and potassium currents that generate spikes (See Figure 1.6).

Here, I review some relevant concepts to understand ionic dynamics. First I introduce the reader to the ionic composition of the brain (Section 1.2.1). Then I mention the biophysical mechanisms that regulate ionic composition in the brain (Section 1.2.2), followed by how ionic concentrations vary in time (Section 1.2.3), and finally I mention studies proving the relevance of ionic dynamics in neuronal coding (Section 1.2.4).

1.2.1 Ionic distribution in the brain

Electrical activity in neurons results from ionic fluxes across their membranes. Given that ions, by definition, are not electrically neutral, those fluxes result in currents. The most studied currents are the ones resulting from sodium Na^+, potassium K^+, calcium Ca^{2+}, and chloride Cl^- fluxes. The driving force for the movement of these ions through the cell membrane, is the electrochemical gradient caused by the different concentrations of these ions inside and outside the cell (See Table.1.1).

The electrochemical gradient is driven by two forces, the concentration gradients of the ions and the electrical gradient caused by them. By diffusion, ions flow to the spaces with the lowest concentration. For instance, if ion_i has a higher concentration inside

Ionic concentrations in the CNS			
	Neuron	**Astrocyte**	**Extracellular space**
$[Na]^+$	5-15 mM	55 mM	145 mM
$[K]^+$	125-150 mM	80 mM	3-12 mM
$[Cl]^-$	6.6 mM	6-40 mM	110 mM
$[Ca]^{2+}$	0.1 μM		1.0-3 mM

TABLE 1.1: Average ionic concentrations in the CNS Ding et al. (2016); Somjen (2004); Izhikevich (2007).

the cell, it will tend to flow through the cell membrane towards the extracellular space. However, given that ion_i is charged, exiting the cell will produce a net charge change inside the cell, which tends to attract the ion back towards the cell membrane. Thus, positive and negative charges accumulate close to the cell membrane building up the membrane potential. The equilibrium potential can be approximated with the Nernst equation (Izhikevich, 2007).

$$E_{ion_i} = \frac{RT}{zF} \ln \frac{[ion_i]_{out}}{[ion_i]_{in}}, \tag{1.11}$$

where $[ion_i]_{out}$ denotes the extracellular concentration of ion_i, and $[ion_i]_{in}$ denotes the intracellular concentration of ion_i. R is the universal gas constant ($8.315 \frac{mJ}{KMol}$), T is the temperature in degrees Kelvin, F is the Faraday's constant ($96.480 \ \frac{coulomb}{Mol}$), and z is the valence, or charge of the ion.

It is not surprising that ionic concentrations in the brain are tightly regulated, because without the electrochemical gradients, electrical signaling would be compromised (among many other cellular processes).

1.2.2 Ionic homeosthasis

Ionic concentrations are tightly regulated and there are multiple mechanisms for doing so. One particularly important mechanism is the sodium potassium pump, an active transport mechanism located in every cell type, with different isoforms being expressed on different cell types. Another ionic regulation mechanism is performed by glial cells, which regulate the extracellular ionic concentrations. In the next subsections these mechanisms are described.

1.2.2.1 Na,K-ATPase: The sodium potassium pump

Na,K-ATPase is an abundant enzyme in the plasma membrane of cells which maintains its sodium and potassium ion gradients. It also drives the sodium-dependent transport of calcium (through an antiporter that uses the energy stored in the sodiium electrochemical gradient to transport calcium ions to the extracellular space) as well as the uptake of neurotransmitters (Moseley et al., 2002). Every cycle of its action pumps 3 sodium ions out of the cell and pumps 2 potassium ions into the cell while it hydrolyzes one ATP. This net extrusion of positive ions makes the pump electrogenic. The electrogeneity of

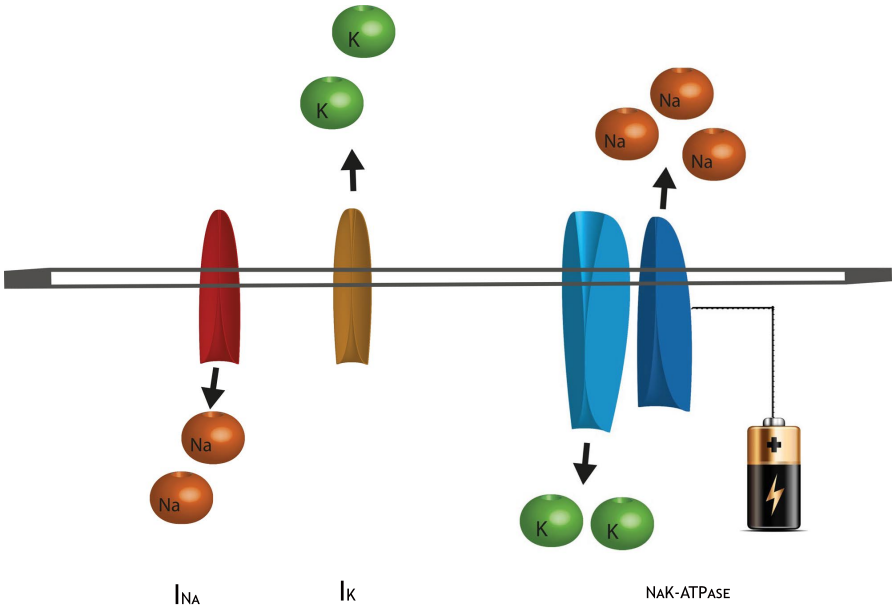

FIGURE 1.6: Schematic representation of the Na,K-ATPase. Every cycle the Na,K-ATPase pumps 3 sodium Na^+ ions out of the cell and pumps 2 potassium K^+ ions into the cell while it hydrolyzes one ATP. The pump restores the ionic homeosthasis in neurons, that other spike generating currents perturb. Here two example currents are shown, a fast sodium I_{Na} current, and a delayed rectifier I_K current. While the $[Na+]$ and $[K_o+]$ currents make use of the electrochemical forces to depolarize and hyperpolarize the membrane, the pump restores the electrochemical potential.

Na,K-ATPases makes them modulate activity through their direct effect on the resting membrane potential (see Figure 1.6, for schematic representation).

There are various Na,K-ATPases. They all result from the association of 2 isoforms, α and β. The α subunit contains the binding sites for sodium (Na^+), potassium (K^+), and ATP. Different α isoforms, have different affinities to Na^+, K^+, and ATP, which determine their operating regimes. The β subunit is needed for normal activity of the Na,K-ATPase while different β isoforms determine the catalytic properties of the Na,K-ATPases.

Na,K-ATPase α isoform is expressed differentialy in every tissue. In the rat intestine for example, $\alpha 1$ is expressed while the retina and in the brain tissues the expressed forms are $\alpha 1$,$\alpha 2$, and $\alpha 3$. Every isoform is equipped to operate in different physiological regimes. Presumably they are all equipped to maintain the homeostatic needs of the tissue in which they are expressed.

Studies have shown that in some tissues, different α isoforms are expressed depending on developmental stages. In heart developmental studies, the replacement of $\alpha 3$ by the $\alpha 2$ isoform coincides with a switch in the excitability of myocardiocytes. This suggests that the specific properties of the Na,K-ATPases are crucial in determining the electrical properties of the heart (Blanco, 2005).

In the brain, as in the heart, α isoforms are differentially expressed along development. Studies of isoform expression in the brain have also shown that neuronal cells from

newborn mice express mainly $\alpha 2$, whereas adult animals express mainly $\alpha 3$ (Moseley et al., 2002). The main difference between both isoforms is that $\alpha 2$ has a much higher sensitivity to extracellular potassium and membrane potential than $\alpha 3$ isoform (Clausen et al., 2017). The differential expression of $\alpha 2$ and $\alpha 3$ might be linked with the critical developmental shift in the regulation of potassium and chloride, where due to the different ionic concentrations, gabaergic synapses transition from depolarizing to hyperpolarizing (Blaesse et al., 2009).

$\alpha 3$ has a relatively low affinity for intracellular sodium compared to $\alpha 2$, or $\alpha 1$ which means that the current will activate only at higher sodium concentrations. Isoform $\alpha 3\beta 1$ has a Na activation at 27.9 mM and $\alpha 3\beta 2$ has a Na^+ activation at 17.1 mM, while isoform $\alpha 2\beta 1$ has a Na^+ activation at 12.4 mM and $\alpha 2\beta 2$ has an activation at 8.8 mM, $\alpha 1\beta 1$ on the other hand has a Na^+ activation at 16.4 mM. (Blanco, 2005). Regarding ATP affinity, $\alpha 3$ displays a very similar affinity to that of $\alpha 2$. This means that both isoforms would be similarly depleted when ATP is scarce which occurs due to some types of physiological stress. However, $\alpha 3$ has a much higher affinity to ATP than $\alpha 1$, which means that under physiological stress $\alpha 1$ would shut down earlier than $\alpha 3$.

Azarias et al. (2012) studied the relative contribution of $\alpha 3$ and $\alpha 1$ isoforms during neuronal activity in a primary culture of hippocampal neurons from rats. Their experimental observations suggest that even though both isoforms contribute to the basal maintenance of intracellular sodium, $\alpha 3$ isoform plays a unique role in restablishing intracellular sodium concentrations following suprathreshold synaptic activity. Consistent with the low affinity of this isoform for intracellular sodium, compared to the other isoforms, $\alpha 3$ would be mainly active when intracellular sodium accumulates due to spiking activity, beyond 17-28 mM (Crambert et al., 2000) (other authors report 25-50 mM (Clausen et al., 2017; Zahler et al., 1997)).

1.2.2.2 Glial cells

Glial cells regulate the extracellular space of neurons, from neurotransmitter concentrations to extracellular potassium. Excess extracellular potassium ions are temporarily stored in glial cells, possibly due to the high permeability of the glial cell membrane to potassium ions.

Functionally coupled glial cells transfer potassium ions from regions of elevated concentrations to regions with lower concentrations. When a glial cell has a net influx of potassium, its membrane potential depolarizes. This electrical signal propagates along the glial network and when it reaches other glial cells with lower intracellular potassium concentration, the potassium follows the electrical gradient and is extruded from the network. These mechanisms have been reviewed in detail by Kofuji and Newman (2004).

1.2.3 Ionic dynamics in the brain

Extracellular and intracellular ionic concentrations are not static, and their fluctuations alter neuronal function. With the recent advances on fluorescent calcium imaging,

it has been possible to unravel intracellular calcium dynamics (Grienberger and Konnerth, 2012). Intracellular calcium $[Ca]^{2+}$ accumulation in the presynaptic terminals triggers neurotransmitter release (Neher and Sakaba, 2008), and postsynaptically it enables activity-dependent synaptic plasticity (Zucker, 1999).

These exciting discoveries have put calcium $[Ca]^{2+}$ in the research spotlight. However, not surprisingly other ionic species are also changing in parallel with (and/or as a consequence of) neuronal spiking. Intracellular sodium has been shown to accumulate as a consequence of somatic spiking (Gulledge et al., 2013).

Also, recently Ding et al. (2016) showed that the mean extracellular potassium concentration $[K_o]^+$ changes together with brain states (among other ionic species), from awake to sleep. And more strikingly, perfusing the brain with certain concentrations has been found to induce either awake or sleep states. On shorter time scales, it has been observed that the extracellular potassium concentration $[K_o]^+$ oscillates locked to the, slow wave sleep characteristic, local field potential oscillation (Amzica et al., 2002).

Furthermore, observations in different species and brain areas, have confirmed that the extracellular potassium concentration $[K_o]^+$ increases as a consequence of stimulus induced neuronal spiking (Lux and Neher, 1973; Hounsgaard and Nicholson, 1983; Skinner and Molnar, 1983).

1.2.3.1 Ionic dynamics as a consequence of neuronal activity

Extracellular potassium accumulation as a consequence of neuronal activity. Several studies have related stimulus induced neuronal activity, with extracellular potassium accumulation (Lux and Neher, 1973; Hounsgaard and Nicholson, 1983; Skinner and Molnar, 1983).

Skinner and Molnar (1983), showed that after stimulating awake cats with cutaneous shock, a field potential was evoked in their frontal cortex. The authors observed an increase in the extracellular potassium concentration with a rapid onset that paralleled the field potential, however, the duration of the increased extracellular potassium concentration after stimulation lasted longer (duration on the order of minutes) than the field potential. It is worth mentioning, that the results from this study have been challenged, because of the sensitivity of the electrodes the authors used (potassium-ion specific microelectrodes) to neurotransmitters and neuromodulators that can be secreted when cutaneous shock evokes cortical activity (Fröhlich et al., 2008).

In their work, Lux and Neher (1973) showed that evoking potentials with direct cortical stimulation in the sensory area of the posterior sigmoid gyrus, or mid-suprasylvian gyrus of an anesthetized cat's cortex, increased the extracellular potassium concentration $[K_o]^+$ by 6-15 mM from the 2.5-4 mM baseline. The increase in extracellular potassium concentration after stimulation, depended on the intensity and the frequency of the stimulus. The rate at which the concentration returned to baseline, also depended on the features of the stimuli. Short burst stimuli had a faster $[K_o]^+$ recovery than long cortical train like stimulation, with a range between 1 and 5 seconds.

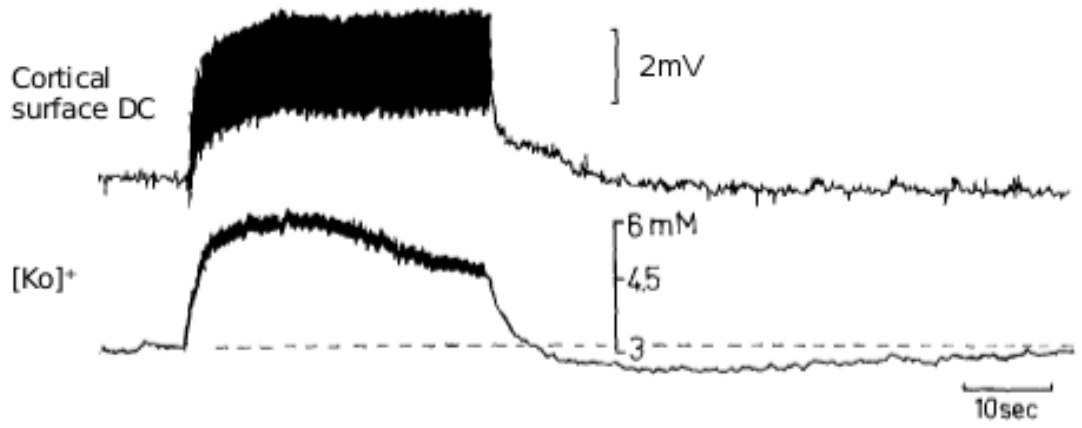

FIGURE 1.7: Extracellular potassium accumulation 500 μ below the cortex co-occurs with cortical surface potential shift measured with a DC electrode. The cortical response was measured during long lasting intense cortical stimulation at a frequency of 10/sec in cat posterior sigmoid gyrus. Adapted from Lux and Neher (1973).

One of the most surprising results of their work (Lux and Neher, 1973), is that the cortical DC potential displayed striking similarities with the extracellular potassium concentration during long lasting intense stimulation (See Figure 1.7). The cortical DC potential reflects the activity of an ensemble of neurons, and the fact that the extracellular potassium concentration resembles it, could mean that this concentration is an indicator of the mean activity of the ensemble.

The authors state, that the main differences between the $[K_o]^+$, and the cortical DC signal, was that the slope right after stimulus onset was steeper for the cortical DC signal. Another noteworthy feature of their observations is that after recovery from stimulation, the extracellular potassium concentration decreased to 0.2-0.7 mM below the baseline concentration before stimulation. And the baseline concentration before stimulation would only be reached after 20-90 seconds after stimuli termination (refer to Figure 1.7).

Extracellular potassium accumulation differs in the viccinity of somata and dendrites. Hounsgaard and Nicholson (1983), measured neuronal activity dependent potassium accumulation in the extracellular space in Guinea pig cerebellum, in-vitro. Ion selective micro-electrodes in the vicinity of Purkinje cell bodies and dendritic branches were combined with intracellular recordings to understand the potassium accumulation dynamics relative to the spiking frequency and source. Spontaneous fast sodium (Na^+) dependent spikes, as well as slow Ca^{2+} dependent spikes were identified. Sodium (Na^+) dependent spikes originated at the soma, while Ca^{2+} dependent spikes originated at the dendrites. Extracellular potassium accumulation differed in soma and in the dendritic branches, and its magnitude depended on the type of spike that was being fired. Next to the soma, extracellular potassium accumulation was faster and larger, than next to the dendritic branches (soma, 1-1.5 mM vs. dendrites 0.5-1 mM). In both locations, extracellular potassium accumulated more when a Ca^{2+} spike was fired, than when a Na^+ spike was fired.

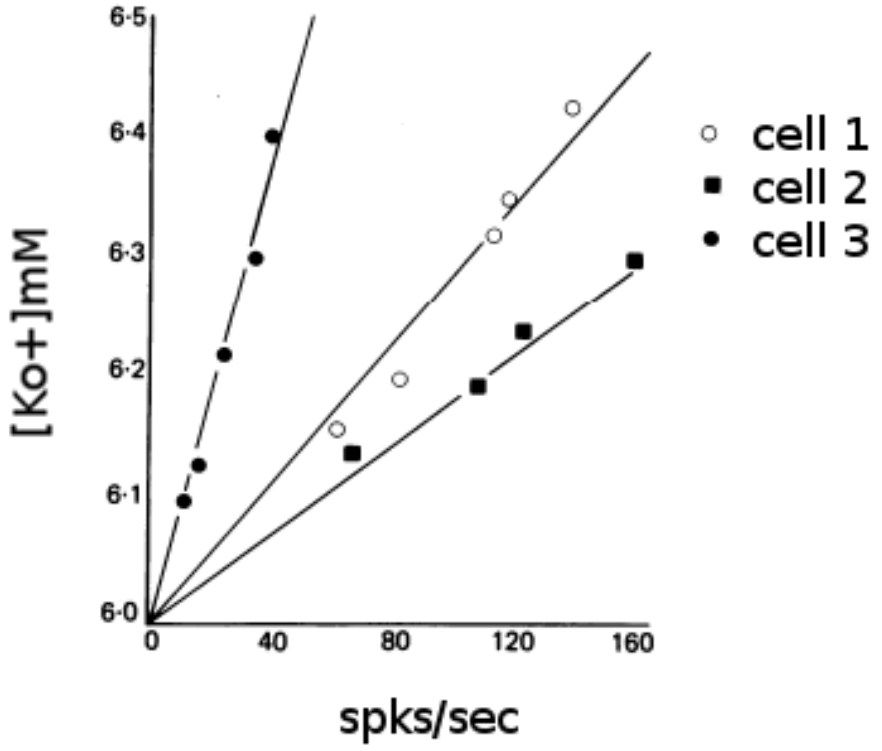

FIGURE 1.8: Extracellular potassium accumulation in the vicinity of Guinea-pig Purkinje cells, depends on their firing frequency. Adapted from Hounsgaard and Nicholson (1983)

Consequently, evoked neuronal activity in purkinje cells resulted in extracellular potassium accumulation (Hounsgaard and Nicholson, 1983). Similar to what was found by Lux and Neher (1973), the stronger current injection elicited higher spiking frequencies, as well as larger increases in the extracellular potassium concentration (refer to Figure 1.8). When high intensity stimuli was used, Ca^{2+} spikes were evoked, which led to even higher accumulation than high frequency Na^{+} spiking.

Intracellular sodium accumulation as a consequence of neuronal activity. Gulledge et al. (2013), demonstrated that intracellular (somatic) sodium accumulates as a consequence of stimuli induced neuronal firing of mouse neocortical layer 5 and hyppocampal CA1 pyramidal neurons. The intracellular sodium concentration returned to baseline only after several seconds. The authors proposed that intracellular sodium accumulation enhances the Na-K-ATPase activity, and demonstrated that its activity produces a slow afterhyperpolarization (AHP) current with a similar time scale to the intracellular sodium concentration recovery.

1.2.4 Consequences of ionic dynamics in neuronal coding

The collection of experiments mentioned in the previous section provide strong evidence supporting the hypothesis of ionic concentrations being dynamic. Furthermore, those experiments suggest that ionic concentrations depend on neuronal activity. But how is

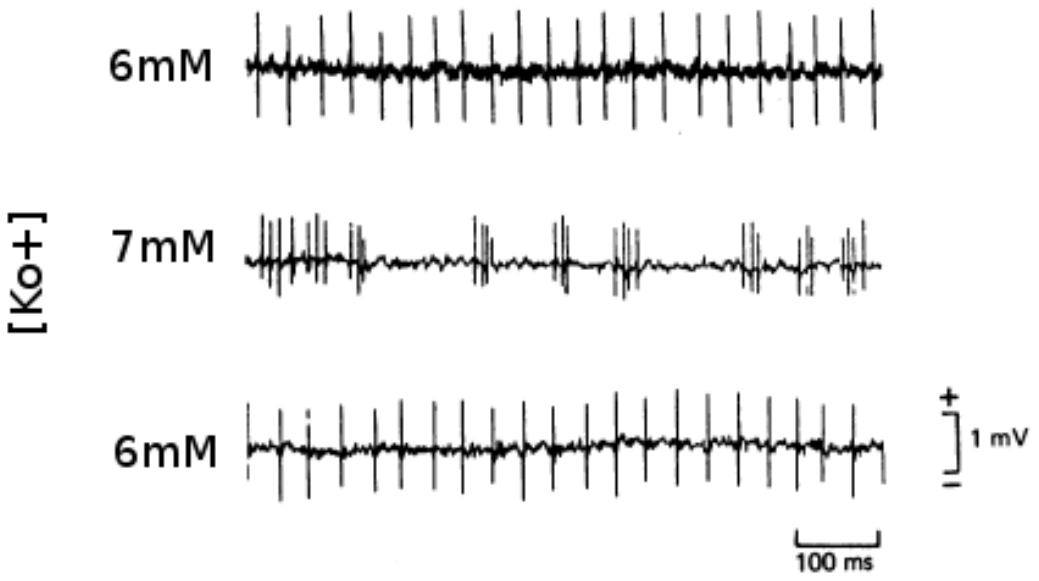

FIGURE 1.9: Extracellular potassium accumulation in Guinea-pig purkinje cells leads to different firing patterns. Extracellular recordings in the vicinity of purkinje cells are shown, for different extracellular potassium concentrations $[K_o]^+$. Adapted from Hounsgaard and Nicholson (1983)

the neuronal activity shaped by the ionic concentrations? In this section evidence of altered neuronal activity as a consequence of changes in ionic concentrations is provided.

1.2.4.1 Extracellular potassium

Irregular firing on the single cell level. In their work, Hounsgaard and Nicholson (1983), characterized the effect of increasing the extracellular potassium concentration $[K^+]_o$ by 1 mM in the intracellular response of Purkinje cells of guinea pig (refer to Figure 1.9). When Purkinje cells were exposed to $[K_+]_o = 6$ mM, regular firing was elicited. When the concentration was increased to $[K^+]_o = 7$ mM, more irregular, bursting-like firing was elicited.

This observation poses a very intriguing question, namely whether neurons can be categorized as intrinsically bursters or regular spikers, or whether a neuron can change its "identity" when exposed to different extracellular concentrations. In this work, but particularly in chapter 2 evidence supporting the second hypothesis will be provided.

Altering frequency content of the microcircuit activity. Other authors have attempted to understand the effect of increasing the extracellular potassium concentration on the microcircuit (LeBeau et al., 2002; Bellot-Saez et al., 2018). In their study, LeBeau et al. (2002), observed that the CA1, or CA3 microcircuit activity generated fast oscillations as a consequence of receiving a pressure ejection of a solution with extremely high extracellular potassium $[K_+]_o$ concentration (1M). After increasing the extracellular potassium concentration, the power spectral density of the slices local field potential changed. The authors report an increase in the gamma (30–80 Hz), beta (12–30 Hz)

and ultrafast (>80 Hz) frequencies with respect to the baseline condition. It is worth mentioning that the values of extracellular potassium concentration used for the study are largely above physiological conditions, the average extracellular potassium concentration measured in the cortex is around 3 mM (Lux and Neher, 1973; Amzica et al., 2002). Thus, a perturbation 1000 times bigger, cannot reflect a physiological process. It illustrates however, that different concentrations might elicit different microcircuit responses.

Other studies observed similar effects by using less extreme perturbations. In their study, Bellot-Saez et al. (2018), observed that perturbing slices from somatosensory cortical areas of mice, with a solution containing 30 mM extracellular potassium concentration, tend to increase the power on different frequency bands of the extracellular field potential. They found significant increases in the power of Beta and gamma frequency bands. However, from their data it seems that in other frequency bands, like delta (1-4Hz) and alpha (8-12), there was a trend towards increased power after extracellular potassium concentration increase, although it was not significantly different from baseline.

1.2.4.2 Intracellular sodium

Spike frequency adaptation Gulledge et al. (2013), demonstrated that the Na-K-ATPase pump activity is enhanced when intracellular potassium concentration is increased. The Na-K-ATPase pump current, produces a slow afterhyperpolarization (AHP) of the membrane potential which shifts the neuron farther from spiking (current) threshold. As a consequence of this dynamic hyperpolarization, spiking probability is decreased resulting in spike frequency adaptation.

1.3 Models of ionic dynamics

In this section a theoretical framework for modelling ionic dynamics is provided. An overview of the most relevant computational models that contain ionic concentration dynamics relative to neuronal activity is shown. As mentioned previously, ionic concentrations can alter neuronal activity, and neuronal activity can alter ionic concentrations. This makes it complicated to define causality experimentally.

Computational modelling is a useful technique to unravel causality, given that in a model it is easy to separate the activity dependent ionic accumulation from the effect it has on it. Different modelling approaches have focused on the former, on the latter or on both.

The early generation of models focused on explaining single neuron dynamics, while the latter focused on microcircuit dynamics.

1.3.0.1 Single cell models

Effect of potassium concentration on neuronal activity. One of the early studies was performed by Aihara and Matsumoto (1983), who focused on understanding how the extracellular potassium concentration $[K_+]_o$ altered the dynamics of the Hodgkin and Huxley (1952) model. Aihara and Matsumoto (1983) found that the Hodking-Huxley model becomes bistable for high extracellular potassium concentrations. The bistability that the authors report consists of a stable node and a limit cycle for very hyperpolarized input currents, and a stable focus and a stable limit cycle surrounding it for depolarized input currents (saddle homoclinic orbit and subcritical hopf spike generation respectively, see section 1.1.3.3). This was a novel finding, whose significance is still not fully understood. One of the reasons why this is the case is that the extracellular potassium concentration at which Aihara and Matsumoto report the bistability is $[K^+]_o = 60$ mM, which exceeds physiological and pathological concentrations.

Later, Hahn and Durand (2001), reported the same type of bistability, for the Hodgkin and Huxley (1952) model, and for the Pinsky and Rinzel (1994) model. For the Hodking-Huxley model, they reported that the bistability occured for extracellular concentration values closer to physiological ranges than Aihara and Matsumoto (1983), however, for a very narrow range 15 mM $< [K^+]_o <$ 15.5 mM. For the Pinsky and Rinzel (1994) model, Hahn and Durand found the bistability for an even narrower range -11.589 mV $< E_K <$ -11.576 mV, which is also far from physiological considering that the Nernst potential E_K, in neurons, is usually close to the resting membrane potential, which is usually more hyperpolarized $V_m << 10$ mV. The main contribution from Hahn and Durand (2001), however, was not the exact values at which the bistable region was found but the finding that the phase response curve[9] of neurons can be altered by extracellular potassium, where even a singularity can be induced by $[K^+]_o$ when the bistable region is reached. Another important contribution of their work is that the bistable region not only depends on the extracellular potassium concentration, but that the region can be broadened or shrunken by altering the input current or the leak current (Hahn and Durand, 2001).

The difference between the resulting concentrations $[K_+]_o$ that induce the bistability in both studies, Hahn and Durand (2001) and Aihara and Matsumoto (1983), is due to the different parameters used. Both assume different temperatures and activation curves for the sodium current. In Aihara and Matsumoto (1983) the temperature was taken as 18°C, and in Hahn and Durand (2001) 6.3°C. The difference between activation curves in both models comes from the fact that Aihara and Matsumoto (1983), used parameters from the activation curves calculated for different extracellular calcium $[Ca]^{2+}$ and magnesium $[Mg]^{2+}$ extracellular concentrations (Frankenhaeuser and Hodgkin, 1957). The discrepancy between both results highlights the potential effect of temperature, as well as the extracellular concentration of multiple ions *in-vivo* and *in-vitro* on neuronal activity.

[9]The phase response curve is a measure of the amount of delay or advance of the next spike given an incoming perturbation on a certain phase of the previous spike. It is only defined for regularly spiking neurons.

Effect of potassium concentration on calcium dynamics. Fröhlich and Bazhenov (2006), proposed a two compartment conductance-based model, and analyzed its multidimensional dynamics for different extracellular potassium concentrations $[K^+]_o$. The two compartment model represents the dendritic and axo-somatic compartments of a pyramidal neuron. The authors included 6 dendritic currents, transient and persistent sodium currents ($I_{Na,D}$, $I_{Nap,D}$) slow voltage dependent potassium current (I_{Km}), calcium-dependent noninactivating potassium current (I_{KCa}), high threshold calcium current I_{Ca} and hyperpolarization-activated depolarizing current (I_h). The somatic compartment also included transient and persistent sodium currents ($I_{Na,S}$, $I_{Nap,S}$), and a delayed rectifier potassium current (I_{Kv}).

In this mathematical model, low extracellular potassium (5.5 mM) leads to stable tonic spiking. Higher extracellular potassium (5.75-6.4 mM) generates a bistability between calcium dependent bursting and tonic spiking. Increasing extracellular potassium even further ($[K^+]_o$ >6.4 mM) only allows bursting to be stable. The intraburst and interburst periods are constant in the absence of noise. Burst duration depends on the time scale of calcium accumulation, and the timing in between bursts depends on the reestablishment of the intracellular calcium concentration.

The authors report that when the model is exposed to $[K^+]_o$ from 5.75 to 6.4 mM, it becomes bistable. The bistability reported by Fröhlich and Bazhenov, is due to the emergence of two stable limit cycles (see Figure 1.10). The first limit cycle has a small period, and every cycle has a similar voltage trajectory as a spike (minimum voltage around -55 mV and maximal voltage around -17 mV), Figure 1.10 bottom panel. The second limit cycle has a longer period than the first, and every cycle has a similar voltage trajectory as a burst, with multiple spikes (generated from oscillations around a stable focus) and a silent period; see Figure 1.10 top panel.

Notice that the bistability reported by Fröhlich and Bazhenov is very different than the one observed by Hahn and Durand (2001); Aihara and Matsumoto (1983). Thus, the voltage traces produced by both dynamical systems differ as well. On the bistability reported by Hahn and Durand (2001); Aihara and Matsumoto (1983), long silent periods could occur (trajectories lying on the basin of attraction of the stable node, or resting state), and bursts of spikes can occur as well (trajectories lying on the basin of attraction of the limit cycle). However, variability in the spike count per burst is expected. On the bistability reported by Fröhlich and Bazhenov (2006), the bursts of spikes are expected to have a similar spike count, and very rare long silent periods can be expected.

Effect of neuronal activity on ionic concentration dynamics. The previous studies focused on the effect of extracellular potassium concentration on neuronal spiking. However, they ignored the non-stationarity of extracellular potassium when the neurons spike. In their study Hübel and Dahlem (2014) focused on the latter effect. They added sodium $[Na^+]$, potassium $[K^+]$, and chloride $[Cl^-]$ concentration dynamics, and a Na-K-ATPase pump to the Hodgkin and Huxley (1952) model. In this study, a very complete analysis of the slow ionic dynamics is provided, and with it the authors suggest that there must be a specific regulatory mechanism for the extracellular potassium concentration

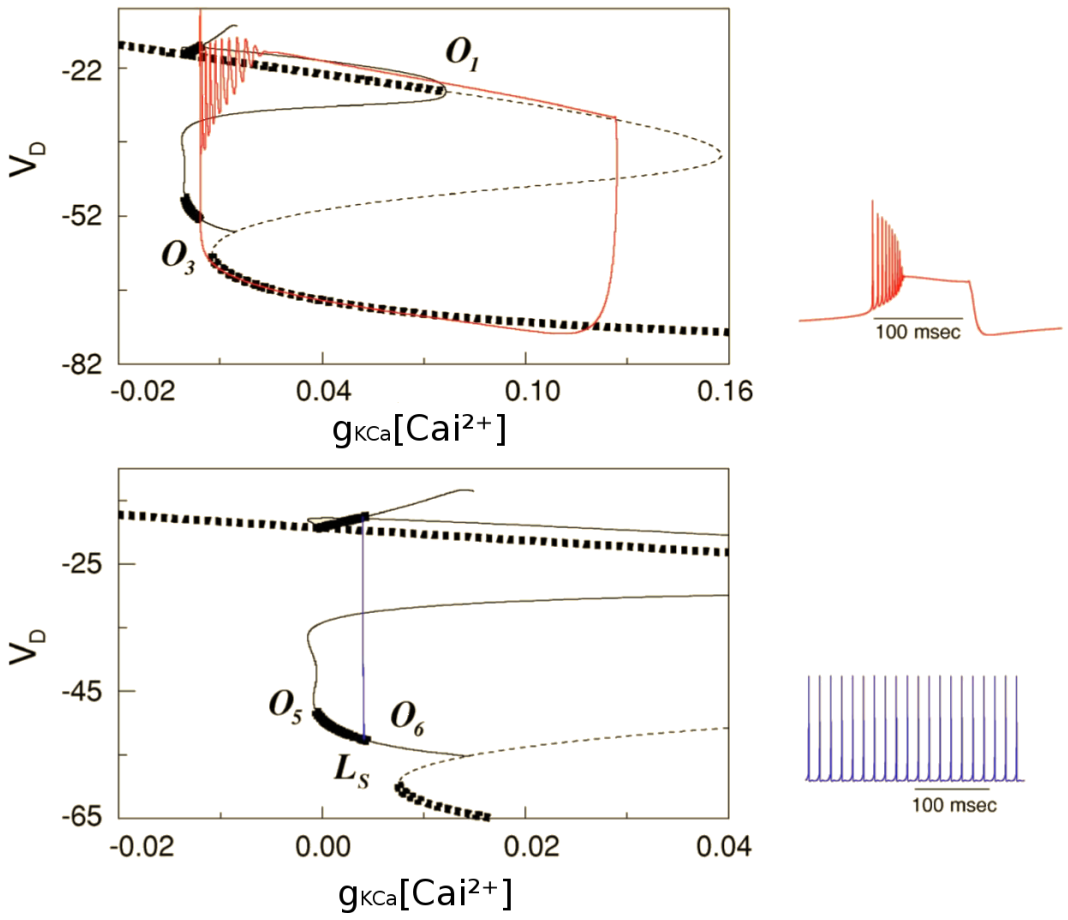

FIGURE 1.10: Illustration of bistability in a projection of the dynamical system studied by Fröhlich and Bazhenov (2006). Stable fixed points are portrayed in the thick dashed line, unstable fixed points portrayed in the thin dashed line, a stable limit cycle is represented with thick solid line, and an unstable limit cycle is represented with a thin solid line. The bifurcation parameter shown here is the g_{KCa}. When the parameter is not fixed, its dynamics are very slow and depend on $[Ca_i^{2+}]$. Notice that the slow limit cycle that emerges from the $[Ca_i^{2+}]$ dynamics is shown in red, and the fast limit cycle emerges from the fixed, very low, g_{KCa} in the range where the limit cycle is stable (thick lines). It is worth pointing out that $[Ca_i^{2+}]$ can not reach negative values in reality, thus, the results of this work should be interpreted qualitatively but not quantitatively. Adapted from Fröhlich and Bazhenov (2006).

besides the pump, given that the model always ends up with concentration depletion otherwise.

1.3.0.2 Network and mean field models

The extracellular potassium concentration affects multiple neurons simultaneously, and collective neuronal activity might have a strong contribution to extracellular potassium accumulation.

Effect of potassium concentration on calcium dynamics and potassium accumulation as a function of spiking. Bazhenov et al. (2004), studied a network

model of pyramidal neurons with almost identical dynamics as Fröhlich and Bazhenov (2006). They simulated a small population of 100 excitatory and 25 inhibitory neurons, connected through GABA-A, NMDA, and AMPA synaptic currents (with a similar structure as Bazhenov et al. (2002)). Furthermore, they included the extracellular potassium concentration dynamics as a consequence of neuronal activity, lateral diffusion, and glial buffering. When a strong DC stimulus was injected to a sub-population of 20 neurons, extracellular potassium accumulated locally. The neurons in contact with the high extracellular potassium concentration displayed calcium dependent bursting, as in Bazhenov et al. (2004); the ones far from it displayed bursting induced by the synaptic input from the first sub-population. The authors tested blocking different extracellular potassium homeostatic mechanisms, and noticed that collective bursting lasts longer. Specifically, they propose that the pump and the glial extracellular potassium buffering play a major role in maintaining the network away from what they propose is a pathological oscillation. Similar results were reported in a different study (where Bazhenov was a coauthor as well) Krishnan et al. (2015) with a focus on the role of the Na-K-ATPase pump.

The model proposed by Bazhenov and colleagues is one of the few models joining both the effect of ionic concentrations on neuronal activity and the effect of neuronal activity on ionic concentrations. It has as well a very complete repertoire of homeostatic mechanisms. However, with completeness comes the complication of the vast amount of state variables, and the number of parameters that should be guessed. It would be interesting to understand how their results hold with more heterogeneous populations, as well as for a broader range of parameter assumptions. However, exploring broad ranges of parameters is generally unfeasible due to the time needed to simulate such big networks.

Effect of potassium concentration on calcium dynamics. Rasmussen et al. (2017), used a faster approach to understand a microcircuit of pyramidal neurons exposed to different extracellular potassium concentrations. They modified a mean field model proposed by Tatsuki et al. (2016), which resembles the dynamics of the mean field of Bazhenov et al. (2002). The model is built with a single pyramidal neuron that feeds back to itself directly and indirectly through synaptic conductances (AMPA, NMDA, and GABA-A). They change the ionic concentrations as parameters, except for calcium which accumulates in the extracellular space as a function of the calcium currents. In this model the authors fix the ionic concentrations to resemble the ones measured by Ding et al. (2016) during waking states, and initial sleep phases in mice. The goal of the authors was to understand if the effect of fixing the ionic concentrations measured by Ding et al. (2016), would have a similar effect on the mean field dynamics as the one it had on the mice cortex. They found that the ionic concentration change was not enough, and that other parameters like g_{KCa} should also change in order to elicit similar effects.

Their results are not surprising, given that the spiking dynamics of their model is mostly driven by calcium oscillations. It would be interesting to understand if neurons in a different dynamical regime (no calcium dependent bursting) respond similarly to what the authors observed. As mentioned above, their study uses a practical technical

approach with a good compromise between simulation speed (allowing broad parameter searches), and the prediction of second order interactions, or diffusion effects as the one studied by Bazhenov et al. (2004).

1.3.0.3 Overview

Computational modelling is an appealing tool to understand the interplay between ionic concentrations and cortical dynamics. The main contribution of computational modelling to the understanding of such multidimensional systems comes from the possibility to analyse the effect of ionic concentrations on neuronal dynamics independent of the effect of neuronal dynamics on ionic concentrations.

Most of the studies mentioned here focused on the effect of ionic concentrations on neuronal dynamics, (Aihara and Matsumoto, 1983; Hahn and Durand, 2001; Fröhlich and Bazhenov, 2006; Rasmussen et al., 2017). The slow ionic concentration dynamics was mainly targeted by Hübel and Dahlem (2014).

The proposition of a feedback loop generated by the effect of ionic concentrations on neuronal dynamics and the effect of neuronal dynamics on ionic concentrations, can be attributed to Bazhenov et al. (2004); Krishnan et al. (2015). This approach allows the understanding of the interplay between homeostatic mechanisms and neuronal dynamics. However, only one of the two mentioned effects (in 1.3.0.1) of extracellular potassium concentration on neuronal spiking has been explored with this two-fold approach. Mainly calcium driven excitability. It remains to be studied how other types of excitability, like the one shown in Aihara and Matsumoto (1983); Hahn and Durand (2001) challenges homeostatic mechanisms. Another point that has not been addressed is how different stimuli features could create different types of slow ionic dynamics, with a similar approach to the one used by Hübel and Dahlem (2014).

In this work I will study the effect of ionic concentration changes on neuronal dynamics and the effect of neuronal dynamics on ionic concentrations for a spiking model that does not rely on calcium oscillations.

1.3.1 Appendix

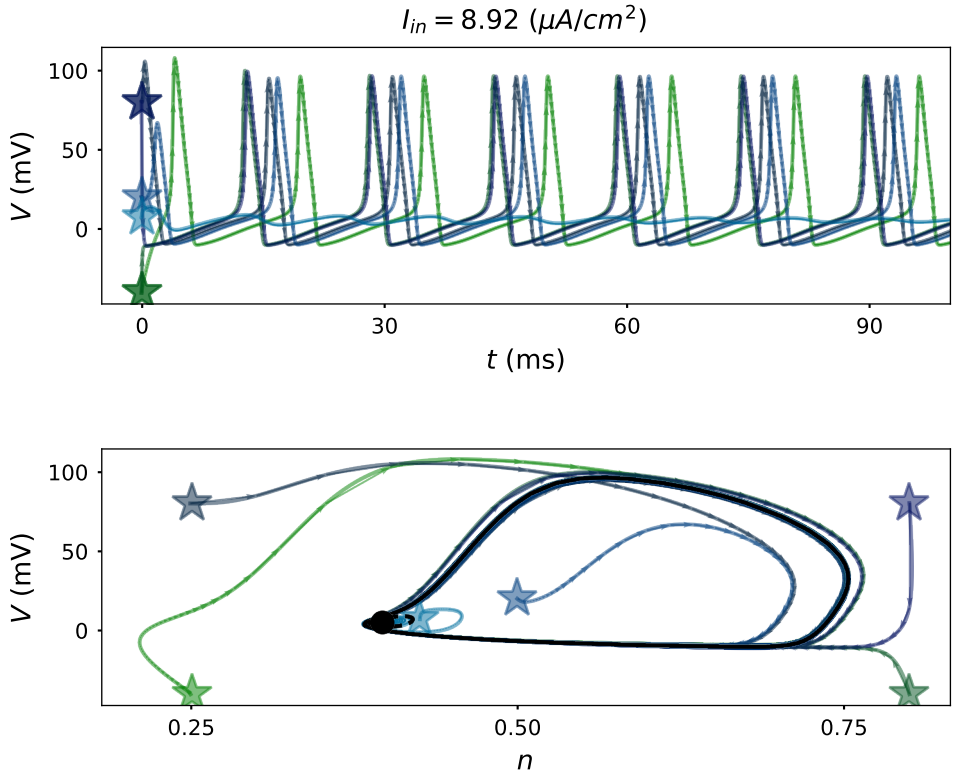

FIGURE 1.11: Bistability in the subcritical Hopf bifurcation. Initial conditions determine the attractor to which the dynamical system converges. Trajectories with initial conditions in the attraction domain of the stable focus approach it, spiraling around it (light blue trajectory). Trajectories with initial conditions in the attraction domain of the limit cycle converge to it.

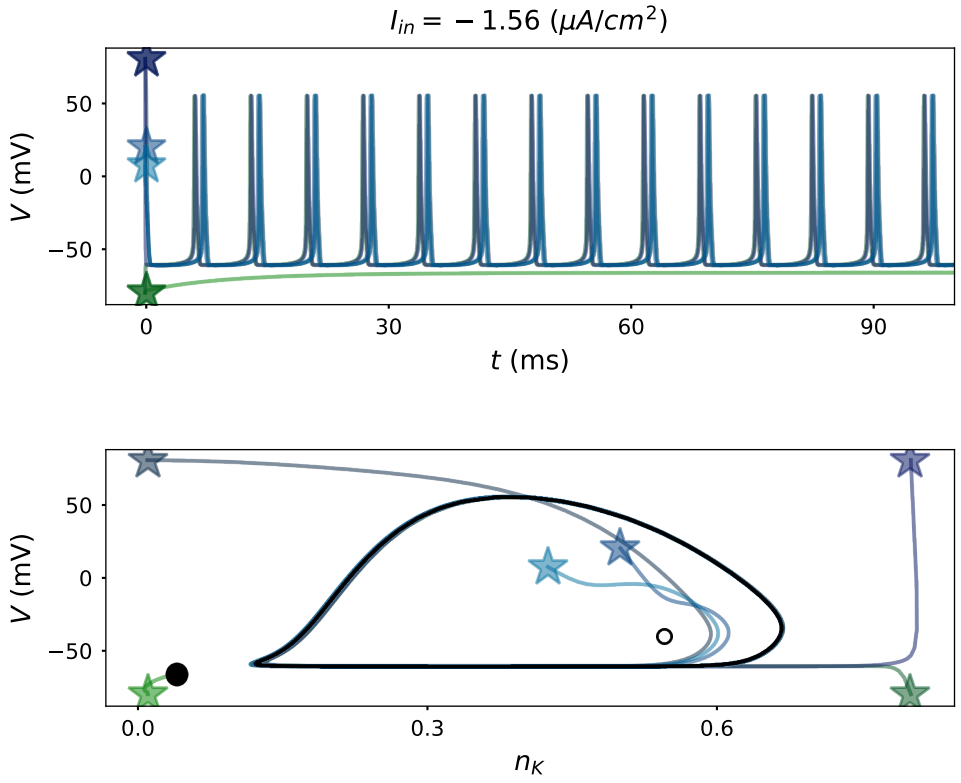

FIGURE 1.12: Bistability in the saddle-node bifurcation. Initial conditions determine the attractor to which the dynamical system converges. Trajectories with initial conditions in the attraction domain of the stable node converge to it. Trajectories with initial conditions in the attraction domain of the limit cycle converge to it.

Part II

Original research

2 | Non stationarity of neurons

The experimental data presented in this chapter is the result of a collaboration with the lab of Allan T. Gulledge, Molecular and Systems Biology, Geisel School of Medicine at Dartmouth College. Allan T. Gulledge designed the experimental protocol and performed the recordings. Susanne Schreiber, Allan T. Gulledge and Jan-Hendrik Schleimer contributed to the edition of this chapter.

2.1 Introduction

Ever since the introduction of Hodgkin-Huxley's famous neuron model for the squid giant axon, its governing equations have been a useful tool to understand the mechanisms of spike generation. The original model assumed fixed ionic concentrations inside and outside the cell, establishing constant driving forces for ionic flux otherwise modulated only by the channels' gating kinetics (Hodgkin and Huxley, 1952). In the brain, however, ionic concentrations are not constant, and the ionic composition of the extracellular space varies with behavioral states (Ding et al., 2016; Amzica and Steriade, 2000) and as a function of neuronal activity (Singer and Lux, 1975; Gulledge et al., 2013).

The concentrations of sodium [Na^+] and potassium [K^+] ions – the two ionic species essential for sodium action potentials – are known to vary in response to neuronal activity *in vitro* and *in vivo* at relatively slow timescales (on the order of seconds). Intracellular sodium concentration has been found to increase with activity in mammalian pyramidal neurons responding to physiologically relevant stimuli (on the order of 3-10 seconds) (Gulledge et al., 2013). In cat neocortex, the concentration of extracellular potassium can oscillate in correlation with local field potentials (LFPs) during slow wave ($\sim$1 Hz) sleep (Amzica and Steriade, 2000) or when presenting oscillating graded stimuli to the cat's retina on the order of seconds (Singer and Lux, 1975). Nevertheless, how stimulus-induced changes in ionic concentration gradients impact ongoing neuronal activity is currently not well understood.

In this study, we use a conductance-based model to predict and experimentally test how changes in transmembrane ionic concentration gradients that arise during periods of increased neuronal activity impact action-potential generation. We find that prolonged stimulation ($\sim$10 seconds) can generate ionic concentration changes substantial enough to modify action potential generation in neurons; intracellular sodium accumulation, in particular, alters action-potential amplitude on slow timescales matching

the ionic changes. This had been previously primarily attributed to the inactivation of sodium channels (Jung et al., 1997; Bromm and Frankenhaeuser, 1972; Frankenhaeuser and Vallbo, 1965).

Extracellular potassium accumulation, on the other hand, can qualitatively switch the spike-generating mechanism, thus changing fundamental properties of firing patterns, encoding and network behaviour. Mathematically, the transition corresponds to a so-called co-dimension-two bifurcation, at which the spike generating mechanism changes qualitatively from a regular saddle-node on invariant cycle (SNIC), when extracellular potassium concentrations are low, to a homoclinic orbit bifurcation (HOM), when extracellular potassium concentrations become high. The switch in the firing regime most notably results in a transition from regular spiking to a burst-like, intermittently interrupted firing mode in the HOM regime, caused by a so-called bistability of the dynamical system. In the HOM regime, the option of a fixed, resting-like voltage state and regular firing co-exists for the same input levels, resulting in stimulus- and noise-induced switches between both states.

Prolonged electrical activity can therefore have significant effects on spiking patterns and neuronal dynamics. We uncover these properties by analysis of conductance-based neuronal models that include ionic concentration dynamics. First, we dissect both potassium ion and sodium ion contributions to spike generation and, then, we test predictions in *in vitro* electrophysiological recordings.

2.2 Results

In order to analyze how neurons respond to prolonged stimulation, we examined the temporal evolution of activity-dependent changes in transmembrane ionic gradients and assessed their impact on ongoing neuronal activity. To this end, we implemented a single-neuron, conductance-based model including dynamic ion concentrations (detailed in Methods). Ionic gradients determine the equilibrium (Nernst) potentials that, in turn, influence the driving forces of spike-generating ionic currents. Ionic accumulation alters the Nernst potentials, thus, alters spike generating currents and, consequently, the spike generation. The mechanism that establishes and regulates concentration gradients ($[Na^+]$ and $[K^+]$) is the Na-K-ATPase pump. The Na-K-ATPase pump is an electrogenic active-transporter whose activity intensifies when $[Na^+]_i$ accumulates. Increased activity of the Na-K-ATPase pump, alters the membrane potential due to its electrogenicity.

2.2.1 Noise-free analysis

We analyzed the response of the model to a step input current - a typical protocol in patch-clamp experiments. Stimulating the model for almost 10 seconds (Figure 2.1A) led to an accumulation of intracellular sodium, $[Na^+]_i$, as well as an increase in extracellular potassium, $[K^+]_o$ (Figure 2.1B). The concentration changes resulted from the prolonged spiking activity and were indeed substantial enough to alter features of the generated action potentials during the duration of the stimulation protocol. Three major changes

that have often been reported in experiments were observed in the model: (a) the emergence of a slow after-hyperpolarization (AHP), (b) adaptation (i.e., a reduction) of spike frequency, and (c) reduction of spike amplitudes (Figure 2.1A).

a) The slow AHP became visible when the stimulus was set back to baseline and neuronal spiking stopped (Figure 2.1A). The slow AHP resulted from the hyperpolarising Na-K-ATPase pump current: Na-K-ATPase pump activity was enhanced with the action-potential-driven rise in intracellular sodium concentration, because $[Na^+]_i$ accumulation, increases the pump activity. When the stimulation ended, the neuron stopped firing and the membrane potential hyperpolarized with respect to the original resting membrane potential (due to the transient change in the Na-K-ATPase pump current). As ongoing Na-K-ATPase activity progressively lowered the intracellular sodium concentration back to baseline levels, the hyperpolarization slowly diminished (Figure 2.1A).

b) Spike frequency adaptation, evident in Figure 2.1A, also resulted from the activity-dependent increase in Na-K-ATPase current, which effectively reduced the net excitatory drive of the neuron. The model does not contain adaptation currents besides the Na-K-ATPase pump (*e.g.*, M-currents). Note that the pump current used in the model is only sensitive to Na^+, which idealizes the pump $\alpha 3$ isoform of the Na-K-ATPase. The pump $\alpha 3$ isoform is negligibly sensitive to K^+ and V, but highly sensitive to changes in intracellular sodium concentration over the ranges simulated in this study (Crambert et al., 2000; Clausen et al., 2017). The impact of the pump current on spike-frequency adaptation is, however, preserved in models of other pump isoforms.

c) In our model, reductions in spike amplitude are directly related to intracellular sodium accumulation, see Figure 2.1C. Activity-dependent reduction of action potential amplitude has previously been attributed primarily to Na^+-channel inactivation during prolonged stimulation (Jung et al., 1997; Colbert et al., 1997). Our simulations, however, demonstrate that the time course of amplitude reduction mirrors the drop in sodium reversal potential (see Figure 2.1A), which is related to the time course of sodium accumulation (see Figure 2.1B). The Na^+-channel inactivation is more than an order of magnitude faster than the timescale of spike-amplitude reduction; the slow spike amplitude decay is modulated by intracellular sodium. A dynamical system's perspective of this finding and an experimental confirmation are presented in the next sections.

2.2.2 Analysis in the presence of noise

The results so far reflect idealized model responses in the absence of noise. To include the stochasticity of synaptic inputs that is typical for many neurons in the central nervous system, we next added coloured noise with stationary statistics to the input current - a useful exercise that reveals an interesting property in the response that was masked in the noise-free case discussed above.

Stimulating the model again with a step current yet in the presence of an additional colored noise component (Figure 2.2, the details of the injected noise are described in the method section), the model neuron's response during the first second was comparable to

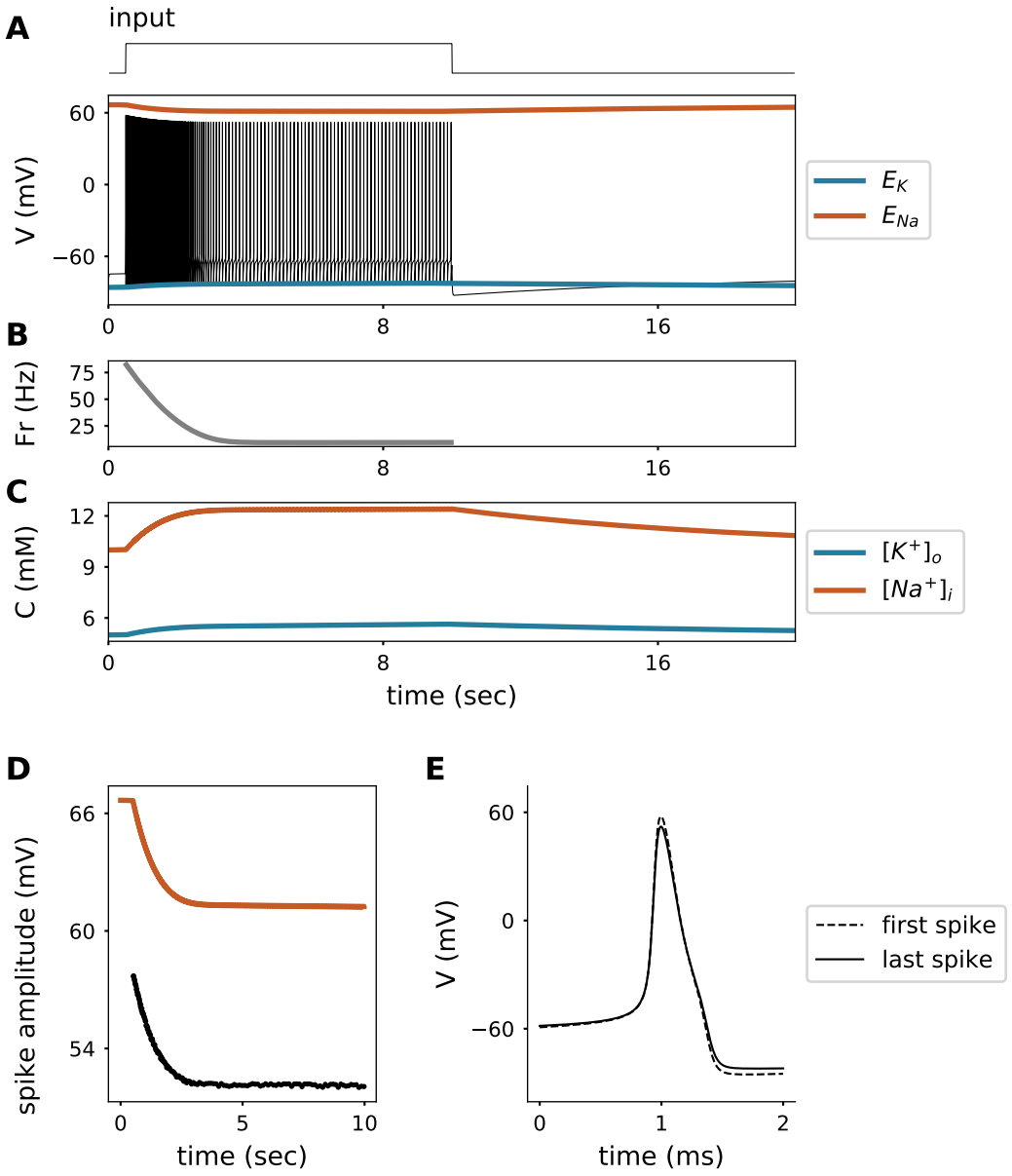

FIGURE 2.1: **Response of the model to a step current of $2\mu A/cm^2$ input as shown in the top.** **A**. Voltage trace with reversal potentials for sodium (Orange) and potassium (Blue).**B**. Firing rate of neuron model. **C**. Intracellular sodium (Orange) and extracellular potassium (Blue) dynamics. **D**. Spike amplitude and reversal potential for sodium (Orange) for the trace shown in **A**. **E**. First and last spike (peaks aligned).

the noise-free case presented before: $[Na^+]_i$ and $[K^+]_o$ accumulated (resulting in changes in the reversal potentials E_{Na} and E_K); spike frequency adaptation, and spike-amplitude reduction were observed (compare to Figure 2.1A). Surprisingly, after the first second of stimulation, the response exhibited a sudden transition from regular spiking to an intermittently-interrupted, burst-like firing mode. Note that the stimulus statistics are in a wide-sense stationary such that there was no qualitative change in the stimulus during the simulation duration. This means that the qualitative switch in the firing pattern must arise from a bifurcation in the neuron's dynamics. The switch in firing pattern occurred 1.2 seconds after stimulus onset, a time scale that largely exceeds the time scale associated with the dynamics of spike-generating conductances (which are about two orders of magnitude faster). Yet this time scale matches the time scale of changes in ionic concentrations, suggesting that the switch is causally related to the ion accumulation. Ion accumulation influences spike generation by changing ionic reversal potentials and engaging the electrogenic Na-K-ATPase.

2.2.3 Separating the fast and the slow dynamics

To disentangle the origin of the transition, in a next step, the fast spike-generating dynamics was separated from the slow ionic concentration dynamics using a slow-fast analysis. To this end, we systematically analyzed the fast system with fixed ionic concentrations (i.e., constant values of the slow concentration variables). The latter, however, were chosen from "snapshots" of the values that the concentrations had exhibited in the full system (where concentrations were varying). This approach allowed us to systematically determine how ionic changes shaped the ongoing properties of the fast sub-system. Time scale separation is valid because ionic concentration changes were much slower ($\sim$ seconds) than the spike generating currents ($\sim$ milliseconds) (see the methods section).

Analysis of the slow-fast system revealed that the qualitatively different spiking response was triggered by a switch in the dynamics of action-potential generation. Mathematically, the model started out in a setting where spiking is initiated via a saddle-node on invariant circle bifurcation (SNIC) (Ermentrout, 1996). This type of dynamics is characterized by the existence of a unique stable attractor for each input level, *i.e.* only one, well-defined state that the system converges to. For low inputs this is a fixed point, *i.e.* the resting state, while for high inputs it is a limit cyle attractor, *i.e.* the regular spiking state. In models with fixed intra- and extracellular ionic concentrations, this type of dynamics would persist as long as cellular properties remain constant, *i.e.* across the whole stimulation period. Alterations in the level of ionic concentrations (and hence their transmembrane gradients in terms of reversal potentials), however, can qualitatively switch the dynamics to a different spike-generating bifurcation. A switch in the spike generating bifurcation, can be perceived in some qualitative characteristic features of spike trains. Such a transition can, for example, be reflected in an increased or decreased number of attractors. Indeed, when monitoring the number of stable attractors of the corresponding fast system at each point in time, their number changes exactly at

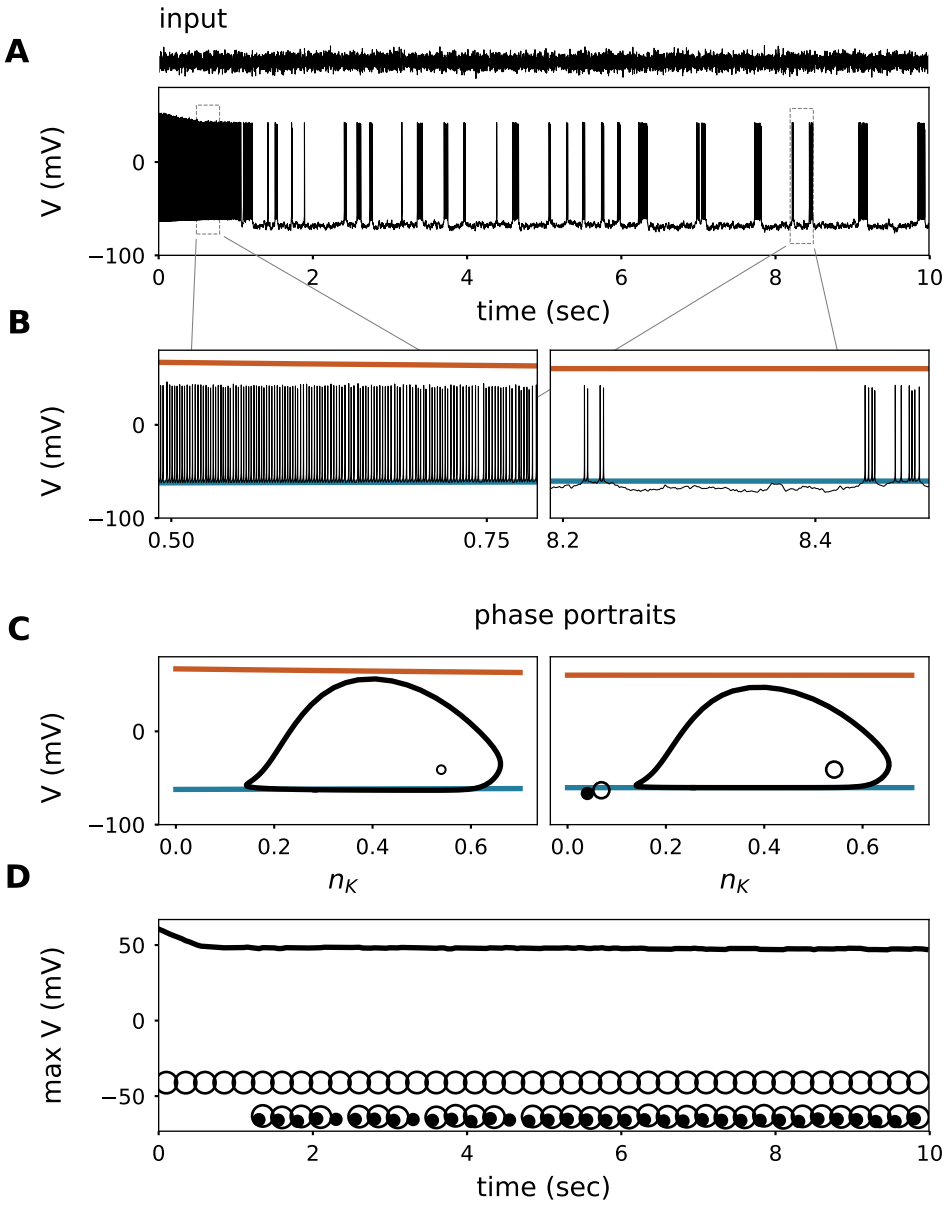

FIGURE 2.2: **Response of the model to a step current with colored noise filtered at 500Hz (mean input is $1\mu A/cm^2$ and standard deviation 1 $\mu A/cm^2$, shown above. The colored noise is built up with an stochastic white noise Gaussian process low-pass filtered at 500Hz.). A.**: Voltage trace (membrane potential) of the model responding to a noisy step current (Top of panel). **B.** Zoom of the voltage trace from panel A. at the beginning and towards the end of stimulation showing the evolution of the reversal potentials for sodium (orange) and potassium (blue), as in Figure 2.1. **C.**: Phase portraits of the steady state of the fast spike generating sub-system, when imposing the average reversal potentials of panel B. as parameters. Vertical axes show the voltage and the horizontal axes show the potassium current gating-variable (n_K) . Empty dots are the unstable nodes, filled dots the stable nodes, and the orbits are stable limit cycles. **D.** Evolution of the maximum voltage of the system attractors. Empty dots represent the unstable nodes, filled dots the stable nodes, and the black line denotes the maximum voltage of the stable limit cycles (action potential peak).

the ionic concentrations reached at 1.2 seconds. Here, an additional stable fixed point (i.e. a stable voltage) appears in parallel to the spiking mode for the same size of input current; the system becomes bistable. Which of the two attractors (regular spiking or a fixed voltage) the system converges to, depends on the initial conditions and/or noise in the system. In Figure 2.1, initial conditions are such that the neuron keeps up regular spiking because concentration changes are not substantial enough to reach the switch in spiking dynamics (the emergence of an additional fixpoint attractor). When ionic concentration changes are substantial enough the reach the swiching point, in the presence of noise (like in Figure 2.2), however, the system permanently receives perturbations and, therefore, when entering the bistable dynamics (at ∼1.2 sec) only temporarily settles onto one of the two attractors before being kicked into the other one. This dynamical state results in a long-lasting, stochastic back-and-forth between periods of spiking and silence (Figure 2.2). The transition from single attractor to bistability ∼1.2 seconds after stimulation onset is confirmed in the corresponding phase portraits of the fast system (Figure 2.2**C.**).

Bistable *vs.* uni-stable states lead to qualitatively very different responses. The natural question that follows is: what generates the bistability? Mathematically, the bistability is caused by the emergence of a separatrix attached to a saddle point, i.e. a trajectory in phase space that separates the so-called basins of attraction of the two attractors. Depending on which side of the separatrix the system is located at a given point in time, it will then converge towards the respective attractor (unless noise or an input fluctuation kick the system across the separatrix to the other side). Dynamics in this region are strongly affected by the reversal potential for potassium (see Figure 2.2 **C.**). Therefore, we next systematically explored the effects of extracellular potassium on the fast system.

2.2.4 Consequences of Extracellular potassium accumulation

2.2.4.1 Dynamical systems analysis

We analyzed the dynamics of the fast system (i.e., the neuron model with fixed ionic concentrations) for different values of extracellular potassium. Figure 2.3 shows the resulting two-parameter bifurcation diagram, which depicts the dynamical state as a function of extracellular potassium concentration and size of the applied input current (for details see the methods section). Four different dynamical regimes can be found: a silent subthreshold state, a regularly spiking state, a bistable state, and a silent state of depolarization block (when the model is depolarized so strongly that spiking cannot occur any more).

Let's look at the diagram in more detail, starting at lower extracellular potassium values (*i.e.*, the bottom of the diagram). Depending on the input strength, the system here either remains subthreshold or exhibits regular firing. The transition to spiking corresponds to a SNIC bifurcation (See FigureS 2.8). When elevating the levels of extracellular potassium (to ∼12 mM), the situation changes. Here, an additional (bistable) region appears between the subthreshold and the regular spiking areas. The transition is

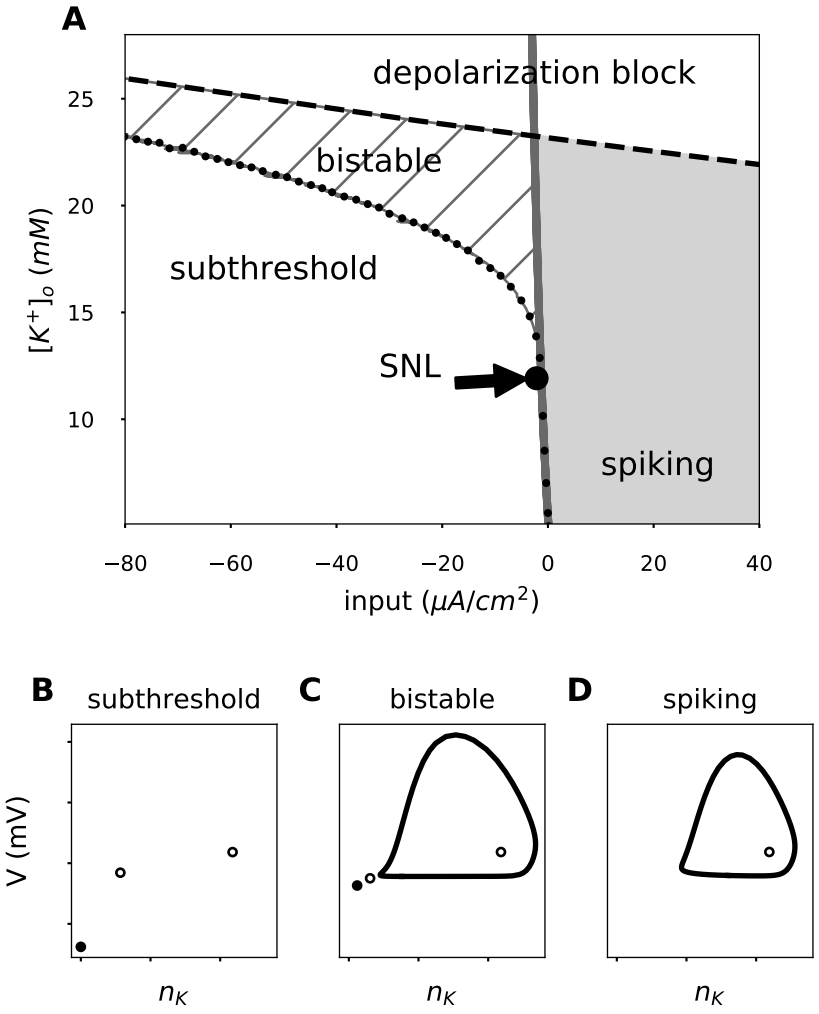

FIGURE 2.3: **Characteristic phase portraits in the extracellular potassium / applied current space.** Different combinations of extracellular potassium and input current yield different phase portraits of the fast spike generating sub-system. **A.**The background color represents the characteristic response of that area; Subthreshold or depolarization block : White; Bistable: Dashed; Spiking: Gray. The different regions are separated by the disappearance of the stable node (gray line) and the limit cycle onset (black dots). Examples of phase portraits in each region of the extracellular potassium - input current plane are portrayed; **B.** subthreshold, **C.** bistable, and **D.** spiking state.

marked by a codimension-two bifurcation called a saddle-node loop (SNL) (Hesse et al., 2017). The width of the bistable region increases for higher values of extracellular potassium concentration (dashed lines in Figure 2.3). The firing threshold corresponds to the left border of the bistable region. The transition to spiking now corresponds to a HOM bifurcation. In the bistable zone, in the presence of noise intermittently-interrupted firing can be observed. Moreover, at elevated extracellular potassium values, the depolarization block (as the name suggests, usually occurring at very large depolarization levels) can be observed at progressively lower input currents. At very high extracellular potassium values, it directly borders the bistable zone.

The full system (with variable concentrations and pump activity), as analyzed in

Figure 2.2, "lives" in the bottom part of the bifurcation diagram (Figure 2.3) at the onset of the stimulation, as here the values of extracellular potassium are moderate. Over time, extracellular potassium accumulates and the switching point to HOM dynamics is passed. Here, the bistable range is entered and the burst-like, intermittently interrupted firing mode can be observed in Figure 2.2 due to the presence of noise. The diagram shows that extracellular potassium is the bifurcating parameter that leads to the qualitative switches in spiking.

2.2.4.2 Experimental manipulation of extracellular potassium

To experimentally test whether elevated levels of extracellular potassium can induce HOM dynamics of action potential generation, a verification of the model-predicted intermittently-interrupted burst-like firing mode suggests itself. In vitro, activity-driven accumulation of extracellular potassium is difficult to reproduce due to the continuously perfused bathing solution that constrains extracellular ion concentrations. We, therefore, recorded current-induced activity in mouse cortical pyramidal neurons exposed to different fixed concentrations of extracellular potassium. Action potentials were induced by constant-current stimulation in baseline conditions (3 mM extracellular potassium), and after increasing the concentration of extracellular potassium to 10 or 12 mM (see methods section). Neurons were stimulated with somatic current injection sufficient to maintain the membrane potential close to spiking threshold (see first panel of Figure 2.4), which, in terms of dynamical system analysis, is close to limit cycle onset and, for HOM dynamics, also to the bistable region, see Figure 2.3.

Our experimental results support the model prediction portrayed in Figure 2.3, in which an increase in extracellular potassium concentration switches the spike generating mechanism. When extracelluar potassium is low (3 mM), the neuron shows very rhythmic (regular) action potential generation over time (see Figure 2.4 left panel). In contrast, when extracellular potassium is increased to 10 or 12 mM, action potential generation in the same neuron becomes irregular (see Figure 2.4 right panel). In 7 out of 8 neurons tested, we observed an increase in spiking irregularity when potassium levels were increased from 3 mM to 12 mM (see supplementary material Figure S.2.11 and S.2.12). In 3 out of 10 neurons tested, we observed an increase in spiking irregularity when potassium levels were increased from 3 mM to 10 mM (see supplementary material Figure 2.13), confirming a crucial prediction of the model. We hypothesize that not all neurons exhibited the same qualitative behavior because the distance to the switching point depends on other parameters as well (Hesse et al., 2017) and hence is likely to be variable across cells (Marder and Goaillard, 2006). It remains to be determined whether the activity of a single neuron generates the $[K^+]_o$ accumulation that induces the SNL bifurcation. Presumably such transitions would be more likely when there are multiple neurons activated simultaneously, which would generate a larger $[K^+]$ flux to the extracellular space.

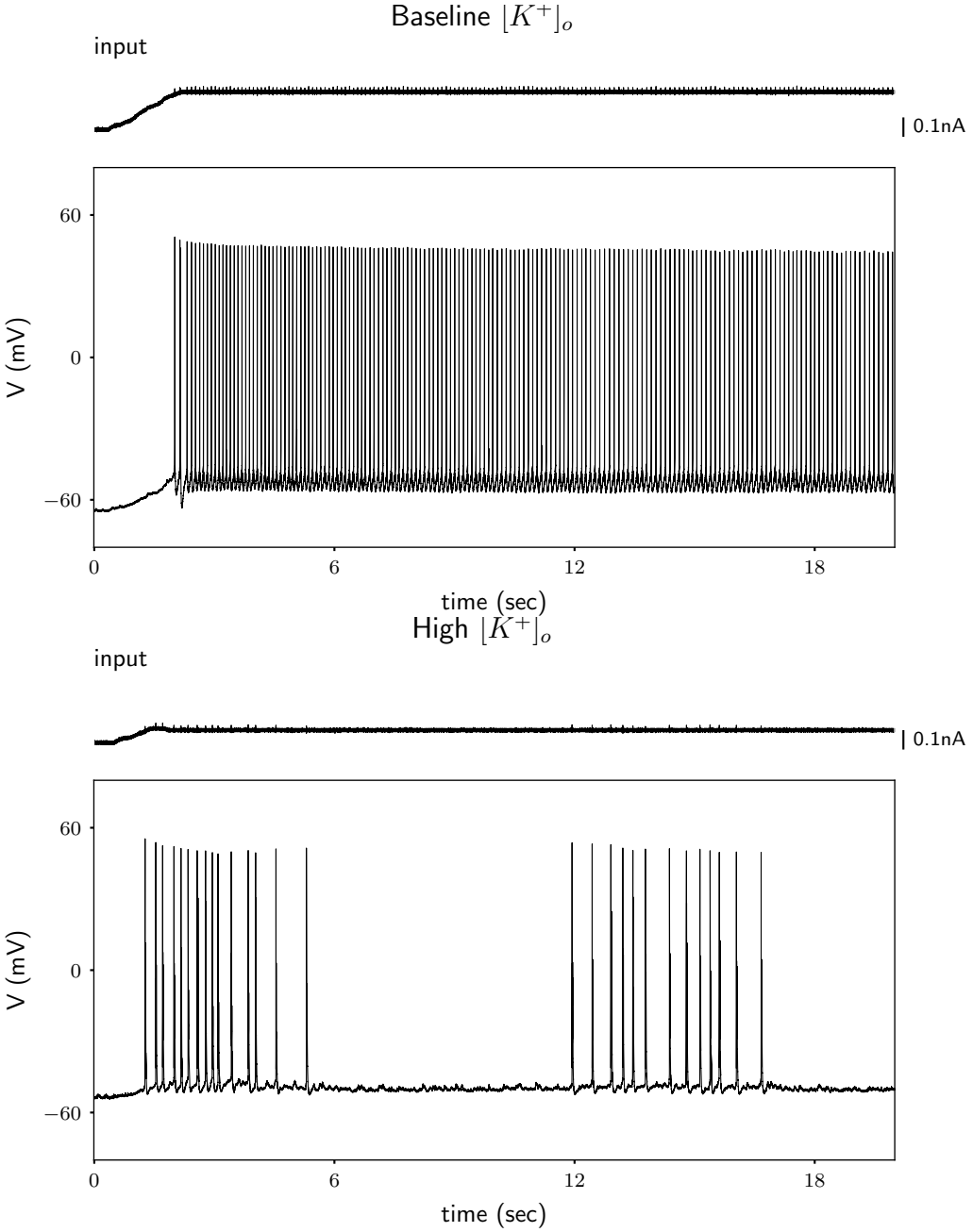

FIGURE 2.4: **Rodent cortical neurons exposed to high extracellular potassium show intermittently interrupted firing.** Example cell; Response of a neuron to a just suprathreshold stimulus in low (3 mM; Top) and high (10 mM; Bottom) extracellular potassium conditions. The suprathreshold current is taken as the current needed to elicit the first spike when injecting a ramp with a shallow slope.The small spikelets visible in the current trace are artifacts resulting from limited capacitive coupling of two channels at the digitizer (i.e., of the action potentials present in the voltage trace), and are not reflective of current injected into the neuron.

2.2.5 Consequences of intracellular sodium accumulation

The dynamical system analysis described above, provides a mechanistic explanation for the emergence of intermittently-interrupted firing. However, the only concentration we varied for the analysis was that of potassium ions. Yet long periods of spiking accumulate both extracellular potassium and intracellular sodium ions. In the following section, we therefore describe physiological features that are altered by sodium accumulation. The space of sodium concentrations is explored to determine whether the results from the dynamical system analysis performed to understand the consequences of extracellular potassium accumulation, hold up under conditions of parallel sodium accumulation.

Sodium accumulation shapes two main properties of spike generation: spike amplitude and spiking threshold, which are determinant features for information transmission and encoding, respectively.

2.2.5.1 Intracellular-sodium-dependent spike amplitude reduction

As outlined above, action potential amplitude is reduced as intracellular sodium accumulates during spiking (Figure 2.1 and Figure 2.2), reducing E_{Na} and hence the driving force. This effect is also reflected in the phase portraits (Figure 2.2**C.**). The height of the stable limit cycle is squeezed during stimulation, correlating with the E_{Na} reduction (Figure 2.1**A.**). We tested this model prediction in mouse cortical neurons *in vitro* during extended periods of current-induced spiking.

Extended activation of rodent cortical neurons leads to slow spike amplitude reduction (Figure 2.5 and Figure 2.9). Rodent cortical neurons are activated for 40 seconds using short (2 ms) depolarizing current pulses (3 nA) generated at 40 Hz. These neurons exhibit a slow and progressive reduction in spike amplitude that is best fit by double exponential decay with an average fast time constant (τ_{fast}) of 480 ms and an average slow time constant (τ_{slow}) of 17.7 s (n=50) (See Supplementary material Figure S. 2.10 and Table S.2.1 for details of the data distribution). The observed slow spike amplitude decay fits the prediction of the model, given that sodium accumulation occurs on the order of seconds, and the faster time scale coincides with the previously reported effects of sodium inactivation (Fleidervish et al., 1996).

More than one process leads to spike amplitude decay: a fast process (sodium channel inactivation) and a slow process (sodium accumulation). In order to disentangle the contribution of both processes, we used somatic current injection to drive rodent cortical neurons with periodic brief (100 to 1000 ms) hyperpolarizing currents (Figure 2.5) that are long enough to reset (deinactivate) sodium channels, but too short for the Na-K-ATPase to clear activity-dependent increases in intracellular sodium. We observed a progressive reduction in action potential amplitudes that was not rescued by even 1000 ms hyperpolarizations. Further, the slow time constant of spike amplitude decay was found to coincide with that measured in the previous protocol, $\tau_{slow} = 15.7s$ (Figure 2.10 and Tab. 2.1,2.2). These observations suggest that the slow component of amplitude

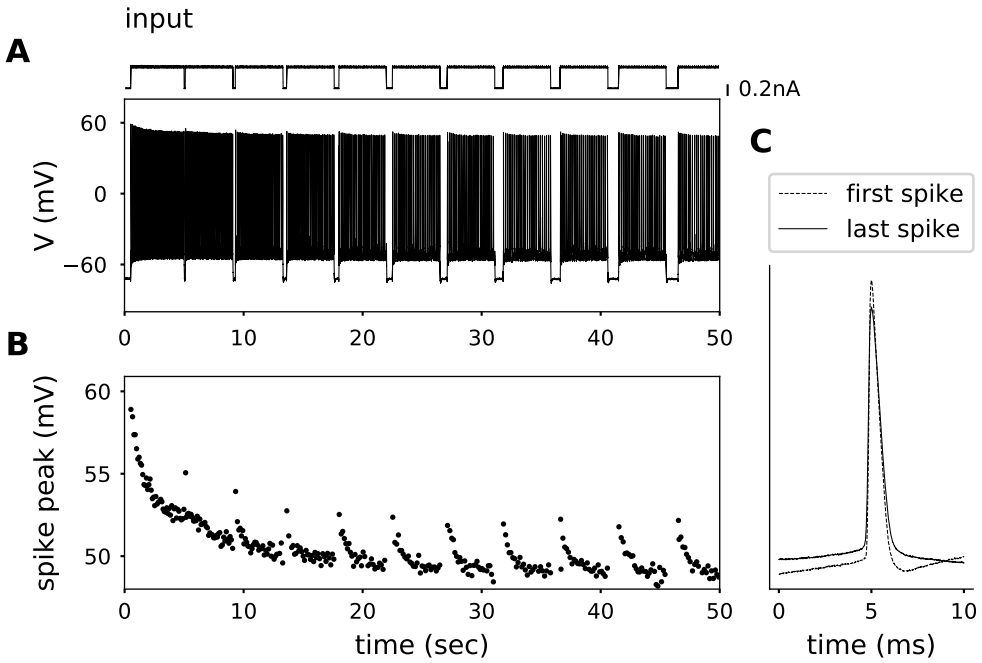

FIGURE 2.5: **Example trace: Evolution of spike peak in time. A** Membrane potential of a rodent cortical neuron, subjected to prolonged stimulation, and brief hyperpolarizing pulses with different duration. **B** Zoom into the membrane potential peak is shown. **C** First and last spike aligned at 5 ms for comparison.

decay cannot result from sodium channel inactivation, and instead is likely driven by intracellular sodium accumulation and the resulting decrease in E_{Na}.

2.2.5.2 Intracellular sodium accumulation shifts the spiking threshold in the model

Given that an accumulation of intracellular sodium ($[Na^+]_i$) is likely to affect spike generation, we next systematically evaluated the dynamical regimes identified in the bifurcation diagram for a fixed $[Na^+]_i$ concentration for different parameter values (Figure 2.6).

We find an identical bifurcation structure and splitting into different dynamical regimes for a wide range of $[Na^+]_i$ levels, with the exception of a shift towards higher input currents with larger $[Na^+]_i$ (Figure 2.6). In other words, as $[Na^+]_i$ accumulates, the spiking threshold is shifted to higher inputs. This shift can be attributed to the dependence of the Na-K pump on $[Na^+]_i$; accumulation of $[Na^+]_i$ thus strengthens the hyperpolarizing pump current, counteracting the input current and reducing the net excitatory drive. Consequently, also the bistable region is shifted along the current axis. Neither a significant change in the area of the bistable region, nor in the location of the transition point towards bistability (i.e., the SNL bifurcation) on the $[K^+]_o$ axis are observed.

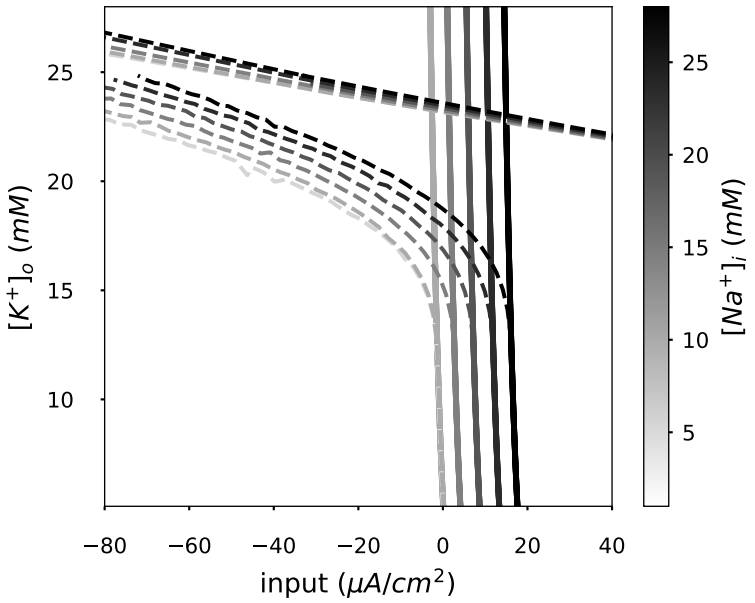

FIGURE 2.6: **Extracellular potassium and intracellular sodium dependent bistable area.** Same bifurcation diagram portrayed in Figure 2.3 for different intracellular sodium concentrations $[Na^+]_i$. $[Na^+]_i$ controls the input current required to transition from resting to spiking regimes. $[Na^+]_i$ accumulation shifts the bistable region to higher current values.

2.2.6 Consequences of simultaneous $[Na^+]_i$ and $[K^+]_o$ changes

The effect of ionic concentrations on neuronal voltage dynamcis unfold via changes in the respective reversal potentials, E_{Na} and E_K. Fixing the input current, we can summarize how the spiking regime depends on the concentrations ($[Na^+]_i$ and $[K^+]_o$) in a plot that depicts the spiking regime (reached in the steady-state of the fast subsystem) as a function of the two corresponding reversal potentials (Figure 2.7). The regime is determined via the phase plane of each system (Figure 2.3**B.,C.,D.**) and can be classified as bistable, regularly spiking, or stable-resting (i.e., either subthreshold or in depolarization block). To relate the reduced fast subsystem with the complete system including slow concentration dynamics, three example trajectories of the complete system at different initial conditions in the space of reversal potentials are shown on top of the steady states of the fast subsystem. Each trajectory represents the evolution of ionic concentrations during 10 seconds of stimulation with a fixed current in the presence of noise (as in Figure 2.2). The corresponding voltage traces are depicted for comparison (Figure 2.7**B.,C.,D.**). Traces that started at a higher firing rate (and, consequently, were accompanied by larger changes of ionic concentrations) moved farther than the ones that starting out at a lower rate.

Which spiking regime a model neuron enters during stimulation, can be read from the corresponding trajectory taken by the complete system. The trajectory depends on the initial ionic concentrations at stimulation onset. A neuron starting with a very low E_K yet high E_{Na} tends to move from regular spiking either to a resting state or to a lower firing rate within the regularly spiking regime (yellow trajectory in Figure 2.7,

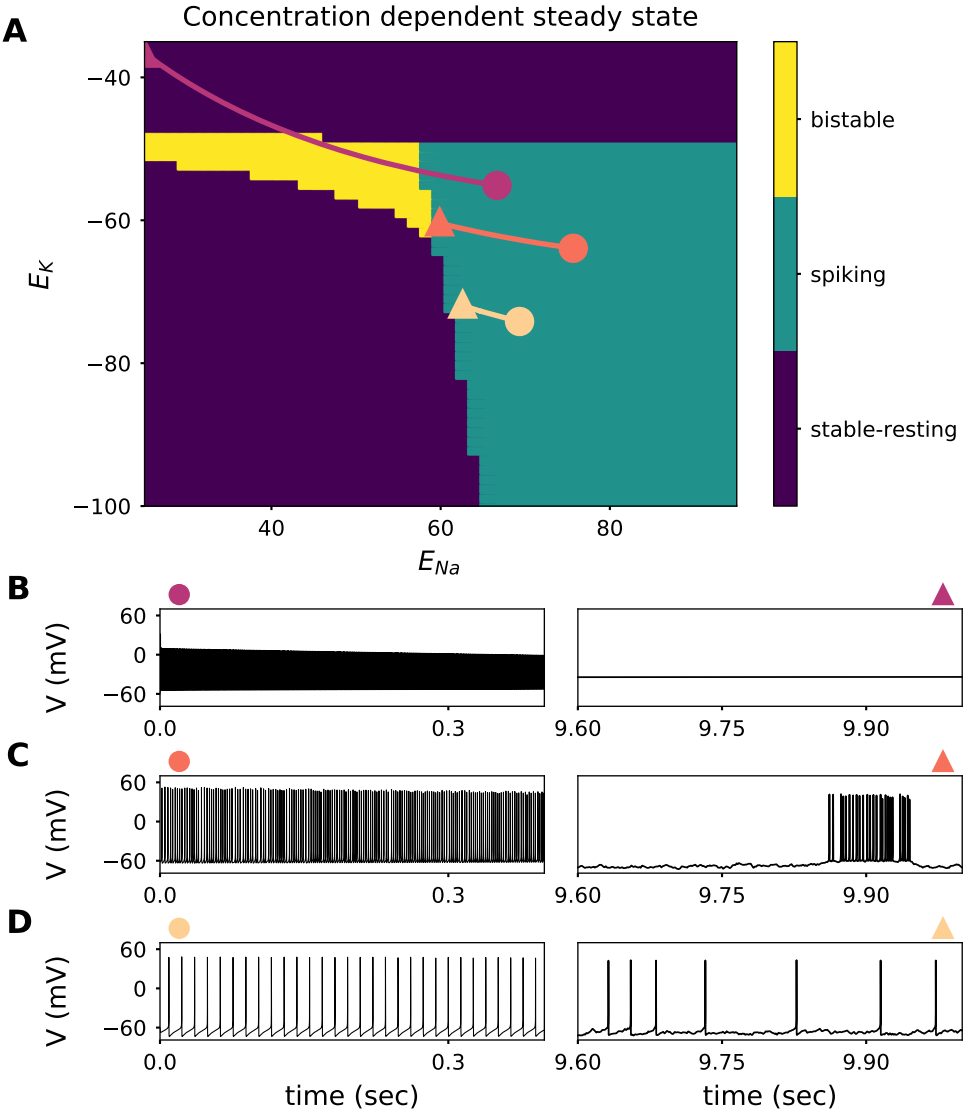

FIGURE 2.7: **Consequences of simultaneous $[Na^+]_i$ and $[K^+]_o$ changes A.**: Characteristic response of the reduced model (receiving a constant input current stimulus of $1\mu A/cm^2$) along the reversal potential plane. The characteristic response can be split in three categories; stable-resting state (lower left corner, subthreshold regime; upper part of the figure: depolarization block. Both represented in purple), spiking state (green), and bistable (yellow). Three example trajectories of the complete system (Including the slow concentration dynamics) simulated during 10 seconds (with an irregular input of mean of $1\mu A/cm^2$ and standard deviation of $1\mu A/cm^2$). The initial conditions represented by a circle, and the state of the system 10000 ms later with a triangle. **B.**: Membrane potential trace of the trajectory with initial conditions $E_K = -55.1mV$ and $E_{Na} = 66.7mV$ displayed in A. Left panel shows the first 400ms of simulation (marked with a circle), and the right panel shows the last 400ms out of the 10 seconds simulation (marked with a triangle). **C.**: Membrane potential trace of the trajectory with initial conditions $E_K = -63.9mV$ and $E_{Na} = 75.7mV$ displayed in A. **B.**: Membrane potential trace of the trajectory with initial conditions $E_K = -74.2mV$ and $E_{Na} = 69.3mV$ displayed in A.

similar to the example trace in Figure 2.7**D.**). Biophysically, spike-frequency adaptation results from the activity of the electrogenic pump, which generates a progressively larger hyperpolarizing current as levels of intracellular sodium increase. Trajectories initialized at low E_K do not reach the bistable region. They tend to a quiescent mode, remaining close to the border to regular firing. If the initial E_K is more elevated, however, a neuron that starts in the regularly spiking regime can reach the bistable region (orange trajectory in Figure 2.7, similar to the example trace in Figure 2.2). Very high initial extracellular potassium concentrations promote depolarization block, but, depending on initial conditions, the bistable regime may also be encountered as an intermediate state (magenta trajectory in Figure 2.7).

The three example trajectories displayed in Figure.2.7, illustrate that a neurons with identical ion channels and stimulation can generate extremely different responses depending on the extracellular environment. Recent spiking activity of neurons alters their response, even when stimulation is unchanged; the rate of change of ionic concentrations strongly depends on neuronal firing rate. Consequently, neurons receiving strong and prolonged stimulation are more likely to experience dynamical regime changes due to ionic accumulation than neurons with weaker stimulation.

2.3 Discussion

In this study, we show that activity-dependent changes in ionic gradients during prolonged neuronal activation can indeed qualitatively change the underlying neuronal dynamics. This fact is seen most pronouncedly in a change in spiking pattern from regular to an intermittently interrupted mode, which appears when extracellular potassium accumulates. Intracellular sodium accumulation, in contrast, mediates a long-lasting spike-frequency adaptation via engagement of the sodium potassium pump, and lowers spike amplitude by its effect on the reversal potential E_{Na}.

We claim that for highly active neurons, an assumption of stationarity of neuronal dynamics is not precise; neurons are intrinsically affected by their recent electrical activity, beyond any other changes that may arise from network feedback. Extended spiking activity results in modifications of the intracellular and extracellular concentrations of sodium and potassium, respectively, and triggers homeostatic mechanisms that regulate ionic gradients at time scales much slower than action potential genesis and bears consequences for neural computation.

Switching to the HOM firing regime: We demonstrate that neuron models that start out with SNIC dynamics (i.e., the classical type I dynamics that has been thought to underlie the firing of most cells with a smooth onset of firing at threshold) can flip to HOM dynamics only seconds after the onset of the spike-inducing stimulation. This transition most obviously manifests in the spiking pattern, which turns from a regular firing mode to an intermittently interrupted one. Our bifurcation analysis shows that an accumulation of extracellular potassium drives this change, instantiating a bistability of the membrane potential.

This finding is consistent with previous work in neuronal models with static ionic concentrations at different levels of extracellular potassium (Hahn and Durand, 2001; Aihara and Matsumoto, 1983). In the presence of a fluctuating input (be it noise or signal), the bistability renders neurons susceptible to switches between the two stable states, giving rise to an irregular, intermittently interrupted firing pattern of short firing phases and pauses of different durations. Long periods of silence, which can be prominent in this mode, can resemble the ones observed during deterministic bursting reported by (Krishnan et al., 2015; Hübel and Dahlem, 2014; Bazhenov et al., 2004; Barreto and Cressman, 2011; Fröhlich and Bazhenov, 2006). In contrast to these deterministic bursters, however, the burst-like firing we describe here is driven by the input fluctuations and the bistable state. Thus, neurons in an environment with high extracellular potassium concentration, promoting HOM dynamics, may be more sensitive to input variability.

The SNIC and the HOM regimes yield very different neuronal encoding properties. For instance, the relationship between the input current and the neuronal firing rate (i.e., the gain) depends on the dynamical regime. The gain function of a neuron in the SNIC regime is continuous, the firing rate of such neuron is a continuous function of the input current. In contrast, the gain function of a neuron in the HOM regime is discontinuous when irregular input is injected, meaning that the firing rate doesn't smoothly increase as a function of the input current but it transitions from no spikes to high frequency spiking abruptly. The phase response curve (PRC), which captures the temporal sensitivity to inputs, also differs between the two regimes. In the SNIC regime, neurons display symmetric PRCs. As PRC symmetry predicts the synchronization of the neurons in the network (Hesse et al., 2017; Fink et al., 2011; Y. Kuramoto, 1984), the switch in firing regime and the underlying bifurcation must also impact the propensity of the neuron to synchronize with other cells in its local network and beyond. Encoding capabilities (such as the profile of frequencies transmitted) are likely to be affected, as they also depend on the PRC characteristics.

Interestingly, intracellular sodium accumulation only quantitatively modulates the qualitative change in spiking regime, underlining the importance of potassium accumulation in this process. The effect of extracellular potassium on neuronal activity has been widely studied (LeBeau et al., 2002; Bellot-Saez et al., 2018; Hounsgaard and Nicholson, 1983). Experimental observations have found extracellular potassium dependent bursting (Hounsgaard and Nicholson, 1983) and its influence on other dynamical features (Aihara and Matsumoto, 1983; Hahn and Durand, 2001; Pinsky and Rinzel, 1994). While a bistability has been previously observed "in passing" (Hahn and Durand, 2001; Aihara and Matsumoto, 1983), we report a systematic effect and provide mechanistic explanations for the activity-driven changes.

Interpreting these results, we speculate that activity-dependent extracellular potassium accumulation can contribute to, or even induce, epileptiform activity (Bazhenov et al., 2004). Both the bursting nature of HOM dynamics (Traub and Wong, 1982; Dichter and Ayala, 1987), as well as their comparatively high susceptability to synchronization in inhibitory networks because of the HOM-characteristic PRC (Hesse et al.,

2017), favour synchronized, hyperexcitable states. *In vivo*, Singer and Lux observed that extracellular potassium accumulates in the visual cortex when a rapidly changing visual stimulus is presented to the cat's retina (Singer and Lux, 1975). Remarkably, similar visual stimuli elicit reflex seizures in 4–7% of human epilepsy patients (Panayiotopoulos, 2005). Reflex seizures could be promoted by extracellular potassium accumulation occurring throughout the visual cortical region that is activated by visual stimulation.

Indeed, the observed drastic consequences of potassium accumulation might occur more frequently *in vivo* than *in vitro*. *In vitro*, extracellular potassium concentrations are clamped. The tissue is perfused with a solution that has a fixed $[K^+]_o$ (consequently $[K^+]_o$) concentration, analogous to an infinite buffer. *In vivo*, however, extracellular potassium concentration undergoes stimulus-induced changes. In the cat visual cortex, for instance, extracellular potassium accumulates when a graded stimulus is presented to the cat's retina (Singer and Lux, 1975). Regarding the universality of the dynamical changes described here, we expect these to generalize beyond the specific model choice of this study. Specifically, the bistability of conductance based models arises from a slow-down of hyperpolarization, which pushes the limit cycle trajectory to approach the saddle node through a very attractive path (i.e., a strong manifold). This feature can be expected in any neuron model that starts out with SNIC dynamics and ubiquitously favours a switch to HOM dynamics (Hesse et al., 2017; Kirst et al., 2015). The exact reversal potential at which the bistability is induced could be shifted by other parameters. Thus,the exact switching point between the two dynamical regimes can vary between neurons, as their properties are diverse (Marder and Goaillard, 2006; Marder, 2011). Therefore, we expect that the exact location of the switching point (i.e., the potassium concentration at which the switch is to be expected) depends on cellular characteristics, both in neuron models as well as in experiments. Along these lines, milder extracellular potassium accumulations could suffice to induce the transition in cells with a lower critical value, singling out cells with a higher likelihood to switch their dynamics.

Attenuation of the spike amplitude: Next to the very prominent change in spiking regime, accumulation of ions are also reflected in the shape of action-potentials, namely their peak amplitude. Such an attenuation is a regular feature observed in electrophysiological recordings. It has, however, been previously attributed to an inactivation of sodium channels (Jung et al., 1997; Fleidervish et al., 1996). Our data, however, suggest that the activity-induced changes in reversal potentials contribute substantially to the attenuation, especially during long periods of activity, as they far outlast the effects inactivation. Our deinactivation experiments with hyperpolarizing current steps support this hypothesis and confirm that the larger and slower component of spike amplitude reduction persist even when sodium channel inactivation is largely diminished. Moreover, the timescales of E_{Na} and amplitudes attennuation are matched.

Concentration-change induced spike-frequency adaptation: Spike-frequency adaptation resulted from an activity-dependent increase in the hyperpolarizing sodium pump current (again mediated by sodium accumulation). This observation was previously reported for leech mechanoreceptor neurons (Arganda et al., 2007) as well as for

rodent cortical neurons (Gulledge et al., 2013). The later study (Gulledge et al., 2013) demonstrated not only that the pump current produces a slow afterhyperpolarization (AHP) as a consequence of neural activity, but that its time-course mirrors the time-course of intracellular sodium decay. Results from our model are consistent with this finding.

Interestingly, for both spike amplitude attenuation and spike frequency adaptation, ion-channel-mediated equivalent effects on short timescales are well known. The dynamics of concentrations seem to smoothly extend these effects in time.

Limitations: We note that our model does not consider extracellular uptake of potassium by glial cells. The latter maintain the ionic homeostasis of the extracellular environment and serve as extracellular potassium buffers (Kofuji and Newman, 2004). Experimental work Dallerac et al. (Dallérac et al., 2013) has shown that glial buffering of extracellular potassium saturates at high values when changes are relatively fast. Yet the presence of glial cells *in vivo* is likely to slow the timescale of potassium accumulation. The effects described here can be expected to arise most prominently in pathological conditions, be it glial dysfunction or energy-deprivation that impairs the pumps and thus facilitates accumulation of both extracellular potassium and intracellular sodium.

We also note that the experiments in this study were performed in the absence of synaptic blockers. This keeps the pharmacological cocktail "neater", but it also raises the possibility that changes in synaptic input may contribute to the irregularity displayed in the single-cell measurements. Specifically, two opposing effects may come into play: (i) Extracellular potassium accumulation shifts E_K to more depolarized potentials; this in turn may foster the passive inflow of chloride, moving also E_{Cl} to a more depolarized state. These effects reduce GABA-A and GABA-B efficacy and reduce synaptic inhibition, by shifting the inhibitory postsynaptic potential's equilibrium (Fertziger and Ranck, 1970). (ii) Also extracellular potassium dependent inhibition of glutamate transporters may contribute (Rimmele et al., 2017), decreasing excitatory synaptic transmission. Having said so, an increase in extracellular potassium also increases the firing rate of neurons in the whole network and it is not probable that the synaptic efficacy reduction could counterbalance the increase in the network input. Network interactions may have many nonlinear effects, and it is not trivial to draw conclusions on causality.

2.4 Methods

With the purpose of understanding the effect of different ionic concentrations on the neuron's response, we used two approaches: simulations of a single-neuron mathematical model with dynamic concentrations, and whole-cell recording of rodent cortical neurons while perfusing the medium to control the extracellular ionic concentrations.

2.4.1 Ethics statement

Physiological experiments were approved by the Institutional Animal Care and Use Committee of Dartmouth College.

2.4.2 Computational model

Our goal is to understand the effects of ionic concentration dynamics on the excitability of neurons. Two ingredients are needed: an excitable system (capable of generating spikes) for which we use the Traub-Miles formulation Traub and Miles (1991), and a description for the slow ionic concentration dynamics. For the excitable system we chose the Traub-Miles model because is one of the simplest mammalian models with type I dynamics (which display continuous and smooth FI curves). (See equations (2.1),(2.2),(2.3),(2.4)), and a description for the ionic concentration changes that occur due to ionic currents. The action potential dynamics at a membrane is governed by a current balance equation involving the following ionic currents,

$$C_{\mathrm{m}}\frac{dV}{dt} = I_{\mathrm{app}} - I_{\mathrm{Na}} - I_{\mathrm{K}} - I_{\mathrm{L}} - I_{\mathrm{pump}}. \tag{2.1}$$

In figure 2.2, and 2.7, a noisy current is also injected. The current is built up with an stochastic white noise Gaussian process low-pass filtered at 500Hz.

$$I_{\mathrm{Na}} = g_{\mathrm{Na}} m_{Na}^3 h_{Na}(V - E_{\mathrm{Na}}) \tag{2.2}$$

$$I_{\mathrm{K}} = g_{\mathrm{K}} n_K^4 (V - E_{\mathrm{K}}) \tag{2.3}$$

$$I_{\mathrm{L}} = g_L(V - E_{\mathrm{L}}) \tag{2.4}$$

$$E_{\mathrm{K}} = \frac{RT}{F}\ln(\frac{[\mathrm{K}^+]_o}{[\mathrm{K}^+]_i}) \tag{2.5}$$

$$E_{\mathrm{Na}} = \frac{RT}{F}\ln(\frac{[\mathrm{Na}^+]_o}{[\mathrm{Na}^+]_i}) \tag{2.6}$$

The leak potential (E_L) is described as an approximation of the Goldman–Hodgkin–Katz (GHK) equation for the membrane potential;

$$E_{\mathrm{L}} = \frac{RT}{F}\ln(\frac{P_{\mathrm{K}}[\mathrm{K}^+]_o + P_{\mathrm{Na}}[\mathrm{Na}^+]_o}{P_{\mathrm{K}}[\mathrm{K}^+]_i + P_{\mathrm{Na}}[\mathrm{Na}^+]_i}). \tag{2.7}$$

Given that we don't consider chloride dynamics, $I_L = I_{L_K} + I_{L_{Na}}$. Where $I_{L_K} = g_L P_K(V - E_K)$, and $I_{L_{Na}} = g_L P_{Na}(V - E_{Na})$.

$$I_{\mathrm{pump}} = \begin{cases} 0 & [\mathrm{Na}^+]_i \leq [\mathrm{Na}]_s \\ \frac{I_{\mathrm{maxp}}}{1+\exp(k_{\mathrm{Na}}([\mathrm{Na}^+]_i - [\mathrm{Na}]_s))} & [\mathrm{Na}^+]_i > [\mathrm{Na}]_s \end{cases} \tag{2.8}$$

The pump model in Eq. (2.8) constitutes a homeostatic mechanism that counteracts the movement of ions due to chemical gradients during neuronal spiking activity. Specifically, the sodium potassium pump (Na-K-ATPase) pumps 3 sodium ions out of the cell, while 2 potassium ions enter the cell every pump cycle. The pump is represented by sigmoidal function of the intracellular Na^+ concentration in Eq. (2.8) Hübel and Dahlem (2014); Zandt et al. (2011). I_{maxp} is the maximum pump rate which was chosen such that the neuron does not run into depolarization block for a broad range of stimulus

intensities. Here, the pump's dependence on potassium and on voltage is ignored. This feature is an analog of the $\alpha 3$ isoform of the Na-K-ATPase, which reacts very strongly to intracellular sodium changes, but is rather insensitive to potassium in the range we study ($[K^+]_o$ 4-20 mM) Crambert et al. (2000). k_{Na} is the sodium sensitivity of the pump to sodium, and $[\mathrm{Na}]_s$ is the target sodium concentration. Both values were set to 0.1/mM and 20 mM respectively, to match the range of highest pump $\alpha 3$ affinity to intracellular sodium Clausen et al. (2017).

Other modelling studies use pump models that resemble more closely the Na-K-ATPase $\alpha 2$ isoform Owen et al. (2013); Wei et al. (2014); Kager et al. (2000). The main difference between both isoforms is that $\alpha 2$ has a much higher sensitivity to extracellular potassium and membrane potential than $\alpha 3$ isoform Clausen et al. (2017). Developmental studies of isoform expression in the brain have shown that neuronal cells from newborn mice express mainly $\alpha 2$, whereas adult animals express mainly $\alpha 3$ Moseley et al. (2002). And given that our our physiological experiments were performed in neurons from adult mice, we found $\alpha 3$ isoform more appropriate.

The concentration dynamics is influenced by the transmembrane currents due to ion channels and the pump as follows.

$$\frac{d[\mathrm{Na}^+]_i}{dt} = \frac{\rho}{F}(-3I_{\mathrm{pump}} - I_{\mathrm{Na}} - I_{L_{Na}}) \tag{2.9}$$

$$\frac{d[\mathrm{K}^+]_i}{dt} = \frac{\rho}{F}(2I_{\mathrm{pump}} - I_{\mathrm{K}} - I_{L_K}) \tag{2.10}$$

$$\frac{d[\mathrm{K}^+]_o}{dt} = -\frac{d[\mathrm{K}^+]_i}{dt}\frac{\mathrm{Vol}_i}{\mathrm{Vol}_e} \tag{2.11}$$

Where ρ represents the surface to volume area, and here is set to 4000/cm Hübel and Dahlem (2014), $\frac{Vol_i}{Vol_e}$ is set to 0.2 (note that this is a very small value mainly because we are not including extracellular regulation mechanisms, thus we assume glial cells, blood vessels, myelin, and other structures are part of the extracellular volume. Previous experimental measurements yield a $\frac{Vol_i}{Vol_e}$ of approximately 0.4 Pilgrim et al. (1982), however we decreased it to compensate for the lack of other homeostatic mechanisms and allow reproducibility of experimental observations. Even though the extracellular sodium changes as well its effect on the neuronal dynamics can be elicited as well by the intracellular sodium change. For simplicity here only the intracellular sodium change is tracked.

All expressions and parameters used in the simulations can be found in Tables S. 2.3, S.2.4, and S.2.5. Simulations were performed in python and the code is available in *this repository.*

2.4.2.1 Time scale separation

Simulating the model dynamics with an ODE solver is very time consuming (This was done for voltage traces in Figures. 2.1, 2.2, and 2.7). Therefore, in order to characterize

the system's response to a broad set of initial conditions using shorter simulation times, we used time scale separation for the analysis. This technique is particularly useful for our set of equations because the system contains variables changing in very slow and very fast time scales.

Ionic concentration dynamics change with a time scale in the order of seconds, while spike generating currents are changing in the order of milliseconds. Thus, we can split the system into two subsystems. The fast subsystem (Equations 2.2,2.3,2.4,2.8 ,2.7,2.1) receives ionic concentrations ($[Na^+]_i, [K^+]_i, [K^+]_o,$) as fixed parameters. For each parameter combination the steady states are portrayed in phase portraits (See Figure 2.2 bottom panel). A parameter combination that yields a phase portrait containing only one stable node is characterized as resting state, one containing only a stable limit cycle is characterized as regular firing, and one with a stable node and a stable limit cycle is characterized as bistable (See Figure 2.7 **A.**).

2.4.2.2 Bifurcation analysis

The numerical bifurcation software AUTO (Doedel et al., 2008) was used to find the limit cycle onset (spike onset), the disappearance of the steady state, and the hopf bifurcation (depolarization block). The analysis was repeated for different ionic concentrations (See in Figures. 2.3 and 2.6). First a particular combination of ionic concentrations is chosen and the steady states of the dynamical system with the combination of parameters are calculated with a regular ODE, secondly the applied current is used as the continuation parameter. AUTO, detects the stable/unstable nodes and limit cycles, it also points where the stability of such objects changes (bifurcations). For this work the most relevant ones are; the points where the stable node transitions from being stable to unstable (saddle-node bifurcation), the point where a stable limit cycle orbit emerges (HOM), and the point where the stable limit cycle disappears (Hopf bifurcation). Such points can be continued along all the model parameters efficiently in AUTO. Figure 2.6 is constructed by continuing the 3 points mentioned above, in the extracellular potassium - applied current plane.

2.4.3 Experimental protocol

Physiological experiments were approved by the Institutional Animal Care and Use Committee of Dartmouth College. Female and male adult (3- to 4-month-old) C57BL/6J mice were bred in facilities accredited by the Association for Assessment and Accreditation of Laboratory Animal Care and maintained on a 12h-12h light-dark cycle with continuous free access to food and water.

On the day of experiments, mice were anesthetized with vaporized isoflurane and decapitated, with brains rapidly removed into an artificial cerebral spinal fluid (aCSF) composed of (in mM): 125 NaCl, 25 $NaHCO_3$, 3 KCl, 1.25 NaH_2PO_4, 0.5 $CaCl_2$, 6 $MgCl_2$ and 25 glucose (saturated with 95% O2-5% CO_2). Coronal brain slices (250 μm thick) of the frontal cortex were cut using a Leica VT 1200 slicer and stored in a holding chamber

filled with aCSF containing 2 mM $CaCl_2$ and 1 mM $MgCl_2$. Slices were maintained in the holding chamber for 45 minutes at 35° C, and then at room temperature ($\sim$ 25 °C) until use in experiments.

Slices were transferred to a recording chamber on a fixed-stage microscope (Olympus), and continuously perfused ($\sim$ 7 ml/min) with oxygenated aCSF heated to 35-36 °C. Layer 5 pyramidal neurons in the prelimbic cortex were visually targeted using a 60X water-immersion objective, and whole-cell recordings made with patch pipettes (5-7 MΩ) filled with a solution containing the following (in mM): 135 potassium gluconate, 2 NaCl, 2 $MgCl_2$, 10 HEPES, 3 Na_2ATP and 0.3 Na_2GTP, pH 7.2 with KOH. Data were acquired using a BVC-700 amplifier (Dagan Corporation) connected to a HEKA 8+8 digitizer or an ITC-18-USB digitizer driven by AxoGraph software (AxoGraph Scientific; RRID: SCR - 014284). Membrane potentials were sampled at 50 to 100 kHz and filtered at 5 or 10 kHz. Voltage measurements were corrected for a +12 mV liquid junction potential. Concentrations of KCl (3, 10, or 12 mM) and NaCl (125, 118, or 116 mM, respectively) were adjusted as indicated to test the impact of extracellular potassium concentration on action potential dynamics. In some experiments fast synaptic transmission was blocked with continuous bath-application of the AMPA receptor blocker DNQX (25 μM; Tocris), the NMDA receptor blocker D-AP5 (25 μM; Tocris), and the $GABA_A$ receptor blocker picrotoxin (50 μM; Tocris).

2.4.4 Data analysis

Data analysis was done in python.

Spiking irregularity Spiking irregularity is measured as

$$CV = \frac{\sigma}{\mu}, \tag{2.12}$$

where σ is the standard deviation of the interspike interval (ISI), and μ is the mean. In the experiment in which synaptic input was blocked we excluded cells that showed patterns different from regular type I neurons in the baseline condition to rule out pathological firing (CV>0.5).

Time scale of spike amplitude decay

The fast and the slow components of the spike amplitude decay were calculated by fitting the time dependent spike-voltage-peak to a double exponential function,

$$D_{fast} \exp[\tfrac{-t}{\tau_{fast}}] + D_{slow} \exp[\tfrac{-t}{\tau_{slow}}] + D_{ss}. \tag{2.13}$$

The distribution of the parameters that yield the best fit across all traces measured are shown in Figure 2.10, Table. 2.1 and Table. 2.2.

2.5 Appendix

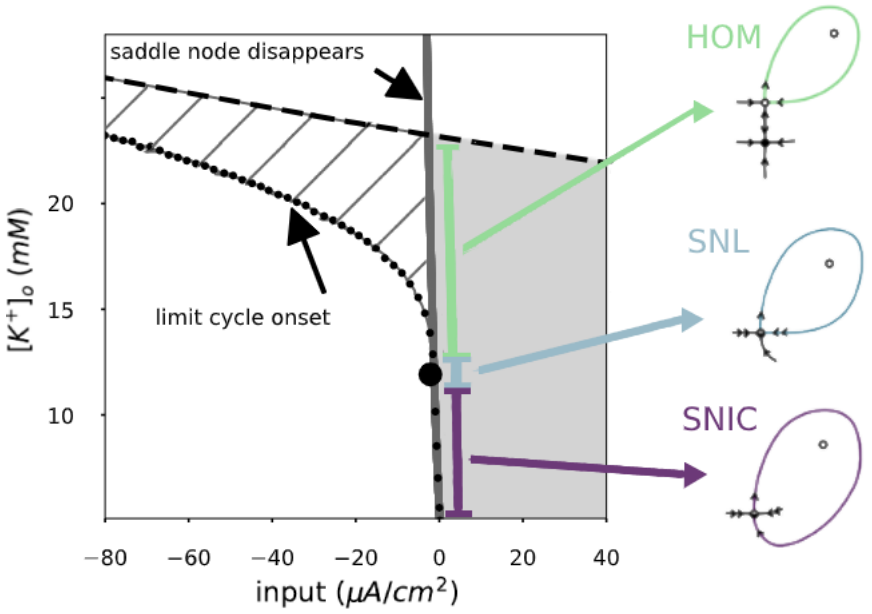

FIGURE 2.8: Transition from rest to spiking (limit cycle onset bifurcations) for different extracellular potassium concentrations. From bottom to top; SNIC (saddle-node on invariant circle): Purple, SNL (Saddle-node-loop): Blue; HOM (saddle homoclinic orbit): Green. In the SNIC regime the stable node collides with an unstable node, giving rise to a saddle node. The limit cycle orbit passes through the saddle node, the trajectory leaves the saddle node along the semi-stable manifold. After one period trajectory approaches the saddle node along the same semi-stable manifold. At the SNL point, trajectories leave the saddle node along the semi-stable manifold as in the SNIC case, but after one period those trajectories approach the saddle node along the strongly stable manifold. Notice that the SNL orbit is smaller than the SNIC orbit, and has a shorter period. In the HOM regime a stable node and a limit cycle coexist. External perturbations shift the state of the system from the stable node to the attraction domain of the limit cycle attractor.

	τ_{fast} (ms)	τ_{slow} (ms)	D_{fast} (mV)	D_{slow} (mV)	D_{ss} (mV)
count	48.000000	48.000000	48.000000	48.000000	4.800000e+01
mean	480.314157	17728.034470	5.906181	20.379248	2.352945e+01
std	676.504019	7919.924120	2.470383	6.366880	1.147889e+01
min	61.687083	4312.710113	0.000001	7.860144	6.323943e-07
25%	170.353968	12050.396908	4.334064	17.144954	1.672852e+01
50%	232.372743	16797.597216	5.823583	20.102315	2.359666e+01
75%	368.297499	21156.877421	7.097274	22.357364	3.093022e+01
max	3083.939293	45815.441228	14.308320	48.164289	5.970884e+01

TABLE 2.1: Summary of the distribution of the best fit of the parameters for each of the 50 traces. Depolarizing pulses applied at a 40Hz rate

	τ_{fast} (ms)	τ_{slow} (ms)	D_{fast} (mV)	D_{slow} (mV)	D_{ss} (mV)
count	73.000000	73.000000	73.000000	73.000000	73.000000
mean	935.652651	15707.653647	5.064957	7.737310	40.589393
std	599.644611	9936.369466	2.492782	4.081336	7.589756
min	125.198826	1485.350564	0.965347	0.000004	0.000024
25%	466.154928	10033.043848	3.045424	5.644995	36.885021
50%	745.856489	13876.630769	4.882892	7.078889	42.152299
75%	1319.313755	18294.743647	6.750978	8.840077	45.033475
max	2436.623039	52548.189654	11.642939	32.905853	52.764149

TABLE 2.2: Summary of the distribution of the best fit of the parameters for each of the 73 traces. Hyperpolarizing pulses.

Gating dynamics	
$\frac{dm_{Na}}{dt}$	$\alpha_m (1 - m_{Na}) - \beta_m m_{Na}$
$\frac{dh_{Na}}{dt}$	$\alpha_h (1 - h_{Na}) - \beta_h h_{Na}$
$\frac{dn_K}{dt}$	$\alpha_n (1 - n_K) - \beta_n n_K$

TABLE 2.3: Gating dynamics used for the Traub-Miles model.

Functions	
E_K	$\frac{RT}{F} \log\left(\frac{K_o}{K_i}\right)$
E_L	$\frac{RT}{F} \log\left(\frac{K_o P_K + Na_o P_{Na}}{K_i P_K + Na_i P_{Na}}\right)$
E_{Na}	$\frac{RT}{F} \log\left(\frac{Na_o}{Na_i}\right)$
α_h	$\frac{0.128 q_h e^{-\frac{\alpha_h V}{18} - \frac{v}{18mV}}}{ms}$
β_h	$\frac{4 q_h}{ms\left(e^{-\frac{\beta_h V}{5} - \frac{v}{5mV}} + 1\right)}$
α_m	$\frac{q_m\left(0.32\alpha_{mV} + \frac{0.32v}{mV}\right)}{ms\left(1 - e^{-\frac{\alpha_{mV}}{4} - \frac{v}{4mV}}\right)}$
β_m	$\frac{q_m\left(0.28\beta_{mV} + \frac{0.28v}{mV}\right)}{ms\left(e^{\frac{\beta_{mV}}{5} + \frac{v}{5mV}} - 1\right)}$
β_n	$\frac{0.5 q_n e^{-\frac{\beta_n V}{40} - \frac{v}{40mV}}}{ms}$

TABLE 2.4: Expressions used for the Traub-Miles model.

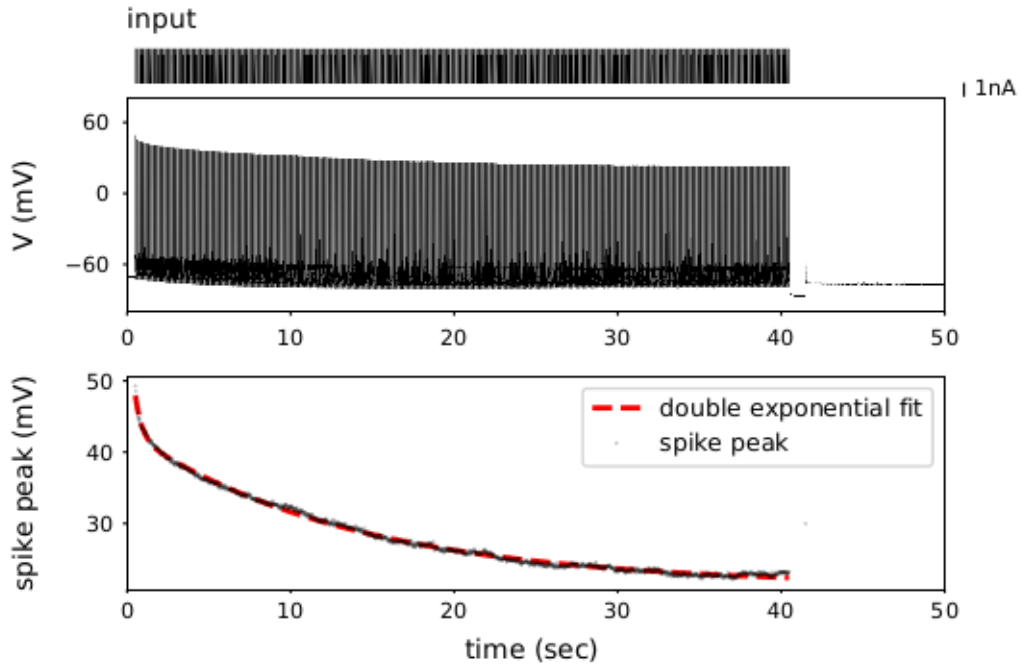

FIGURE 2.9: Spike amplitude slow decay. Depolarizing pulses applied at a 40Hz rate. Spike amplitude decay $\tau_{slow} = 13.6$ (seg), and $\tau_{fast} = 410$ (ms). Notice that the amplitude of the last spike doesn't recover its amplitude after the hyper-polarizing pulse.

Parameters excitable portion	
g_K	$\frac{200mS}{cm^2}$
g_L	$\frac{0.1mS}{cm^2}$
g_{Na}	$\frac{100mS}{cm^2}$
C	$\frac{1.0uF}{cm^2}$
α_{hV}	50
α_{mV}	54
α_{nV}	52
β_{hV}	27
β_{mV}	27
β_{nV}	57

TABLE 2.5: Parameters used for the Traub-Miles model.

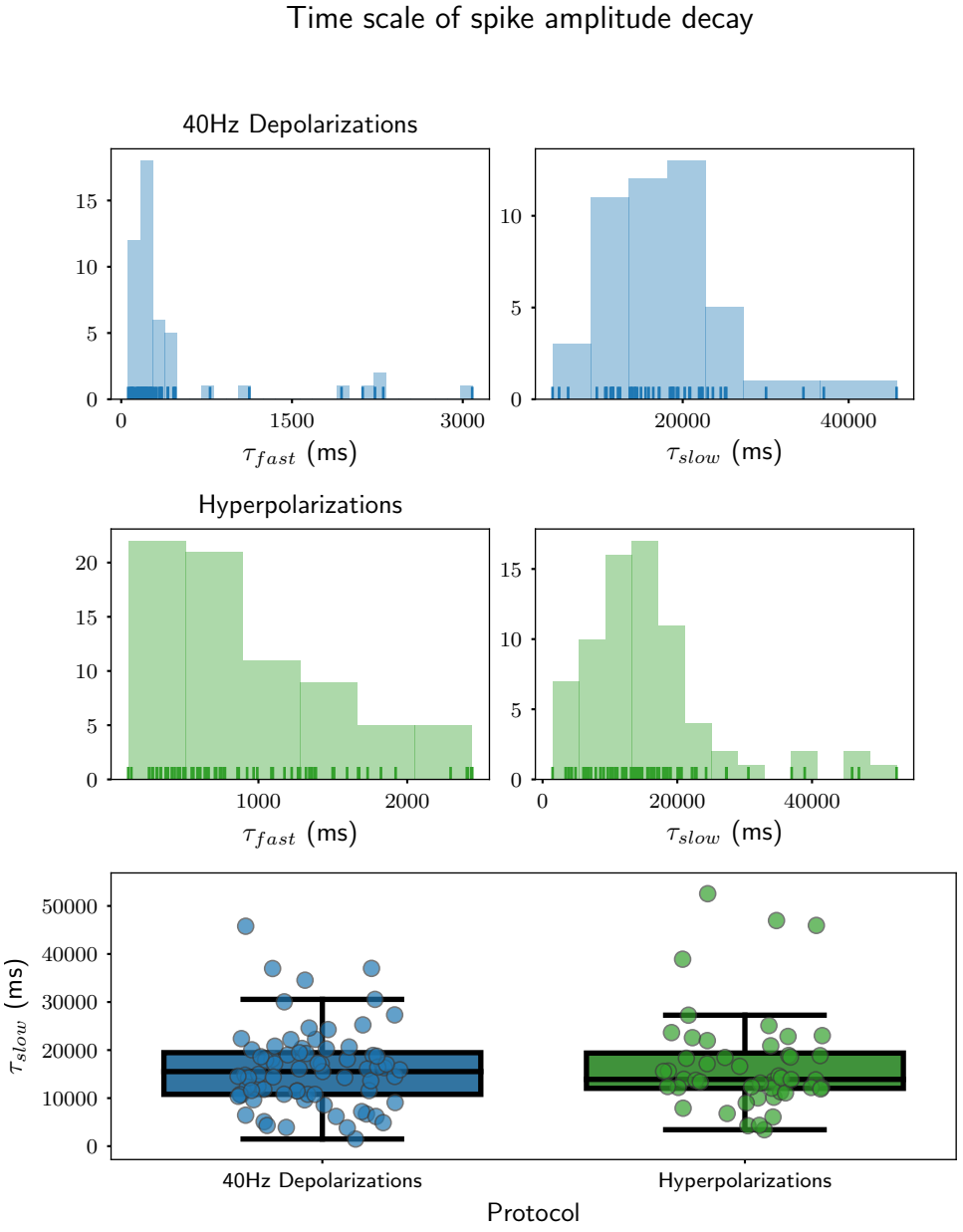

FIGURE 2.10: Distribution of time scales of the double exponential decay (equation 2.13) of the spike amplitude. Two protocols were used to measure the time scales of spike amplitude decay, an example of the "40 Hz Depolarizations" is shown in Figure 2.9, and an example of the "Hyperpolarization" is shown in Figure 2.5. Notice that the distribution of τ_{slow} is independent of the protocol used.

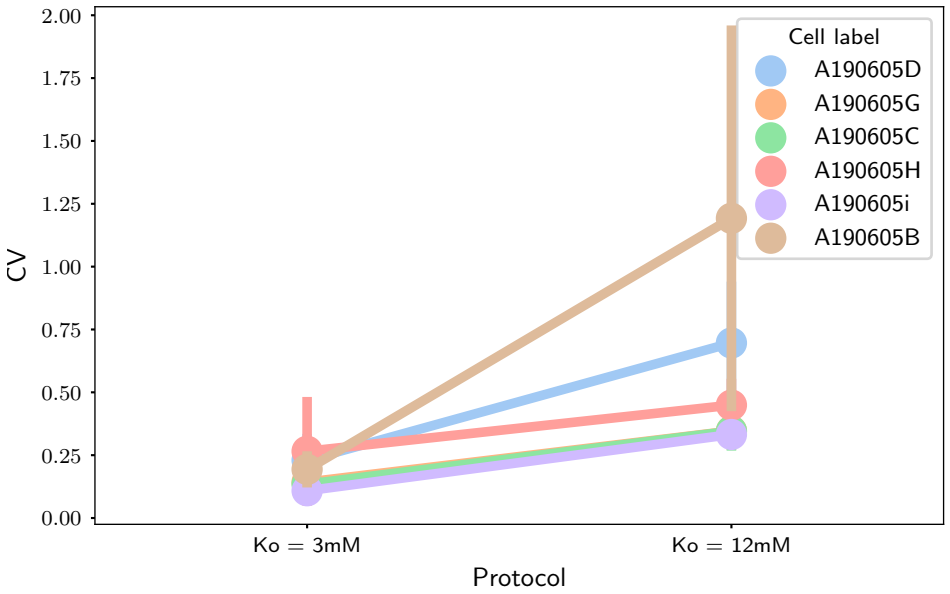

FIGURE 2.11: Spiking variability calculated as the coefficient of variation ($CV = \frac{\sigma}{\mu}$) for all cells sampled, when stimulating with white noise added to the baseline input. An increase from 3mM to 12mM in extracellular potassium increased the spiking variability of 5 out of 6 cells measured.

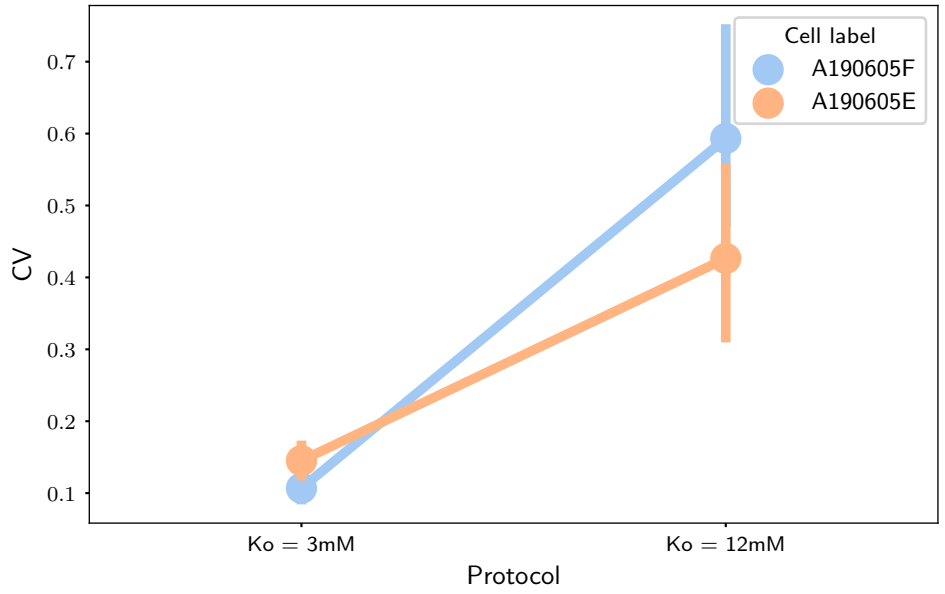

FIGURE 2.12: Spiking variability calculated as the coefficient of variation ($CV = \frac{\sigma}{\mu}$) for all cells sampled, when stimulating with baseline input. An increase from 3mM to 12mM in extracellular potassium increased the spiking variability of 2 out of 2 cells measured. The main source of stimuli irregularity was the network activity.

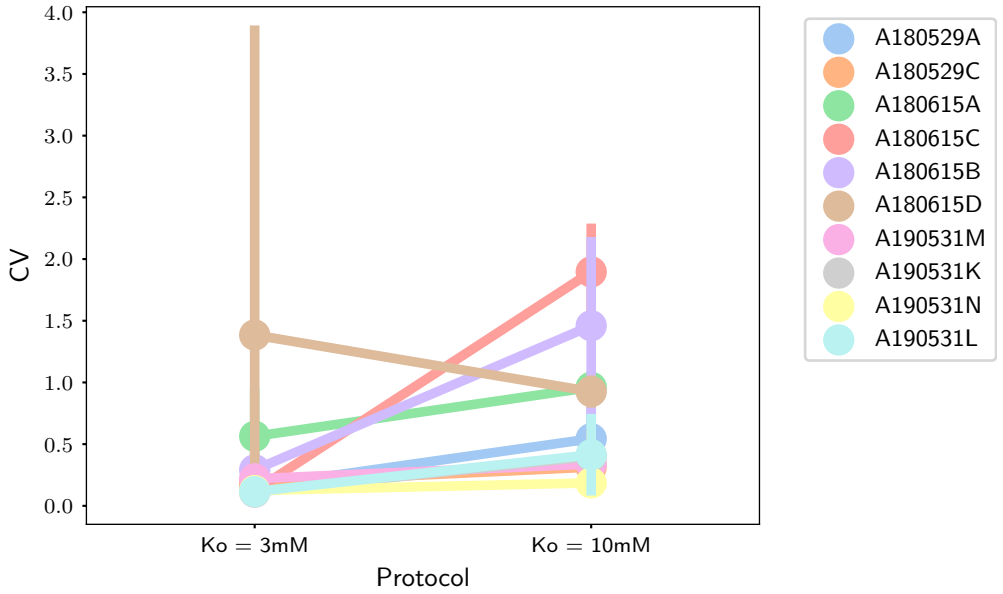

FIGURE 2.13: Spiking variability calculated as the coefficient of variation ($CV = \frac{\sigma}{\mu}$) for all cells sampled. An increase from 3mM to 10mM in extracellular potassium increased the spiking variability of 3 out of 10 cells measured. The main source of stimuli irregularity was the network activity.

Parameters ionic concentration dynamics	
ρ	$\frac{4000}{cm}$
F	$\frac{96484.6C}{mol}$
$\frac{Vol_i}{Vol_e}$	0.2
I_{max}	$\frac{40.0uA}{cm_2}$
$[Na^+]_o$	$140mM$
Na_s	$\frac{0.1}{mM}$
K_{Na}	$20mM$

TABLE 2.6: **Parameters used for the ionic concentration dynamics portion of the model.**

3 | Ionic dependency of single cell spiking statistics

In the first part of the thesis it was shown how extracellular potassium could potentially induce a co-dimension 2 bifurcation. The transition through the bifurcation changes the system from having a single stability to being bistable. The neuron model in the bistable regime, displays stochastic bursting, in contrast to the "all or nothing" firing observed in the region where the system has a single attractor.

The results from the previous chapter (chapter 2) also raised the question, is the effect of extracellular potassium on the single cell spiking enough to alter the whole circuit dynamics? In-vivo, neurons are not isolated, their activity depends on the activity of their neighboring neurons. Furthermore, extracellular environment changes can potentially alter the activity of several neurons simultaneously. Given that a single neuron exposed to an increase in extracellular potassium could undergo the bifurcation (discussed in chapter 2), other neurons in the local microcircuit could undergo the bifurcation as well. Then how are the network dynamics altered when multiple neurons go through the transition?

In order to address the previous questions, an analytical simplification for the single cell spiking statistics is needed. Typically inter-spike interval distributions are one important aspect of spiking statistics. Although they don't capture some aspects like temporal correlations in between spikes, inter-spike interval distributions are a good summary of the neuronal spiking statistics. Here I implement the technique proposed in our article (Schleimer et al., 2021) (for 2D neuron models), to derive the interspike interval distribution of the 4D model described in the previous chapter 2.

3.1 Introduction

In the brain, the extracellular environment varies across different physiological states and even across different brain areas. In cat neocortex for instance, the concentration of extracellular potassium can oscillate locked to the local field potentials (LFPs) during slow wave (∼1 Hz) sleep (Amzica and Steriade, 2000). These extracellular potassium changes could potentially alter the dynamical regime in which neurons operate. As proposed in the previous chapter (chapter 2), extracellular potassium accumulation can

induce a codimension two bifurcation that alters the response of neurons, and potentially their coding properties.

Mathematical modelling predicts that increases in the extracellular potassium concentration change the dynamical regime in which neurons are. More specifically the spike generating bifurcation switches from the saddle node on invariant cycle (SNIC) to the homoclinic spike generation (HOM). The switch in the spike generating bifurcation has enormous consequences for neuronal encoding of input stimulus (Ermentrout, 1996). The switch also induces a stochastic bursting response given irregular incoming inputs to single neurons (chapter 2).

When neurons generate spikes via the HOM, their phase response curve has a symmetry change with respect to the SNIC spike generation. This symmetry change not only alters neuronal encoding, but can alter network synchronicity (Hesse et al., 2017). Neuronal ensemble synchrony is thought to underlie high brain processes such as sensory processing (Purves, 2004) and learning (Huber et al., 2004; Clemens et al., 2007; Axmacher et al., 2006). Alterations in neuronal synchrony are also thought of having an important role in causing epileptic seizures (Warren et al., 2010).

Given the potential effect of homoclinic spiking on information encoding, and physiological and pathological transitions to synchronous states, it is important to understand under which conditions is homoclinic spiking occurring in the brain. Is homoclinic spiking feasible under physiological extracellular potassium concentrations? In order to answer this question, first we need to determine how exactly can homoclinic spiking be detected.

Detecting extracellular potassium-induced homoclinic spiking experimentally is not a straightforward task. Mild extracellular potassium accumulation makes neurons more excitable, even before eliciting homoclinic spiking. The dependence of neuronal excitability on extracellular potassium concentration creates a potential confounder when detecting homoclinic spiking, specifically with *in-vitro* patch clamp setups, where not only extracellular potassium must be controlled, but also the input current injected to the neuron. The input current is a parameter that can make the neuron transition from a subthreshold regime, to a regularly spiking regime. When irregular input is injected to the neuron, right before the transition to the regularly spiking regime, noise driven spiking could be observed. In the noise driven regime, spiking is very irregular and could be mistakenly placed as homoclinic spiking. Thus, irregularity alone is not enough to characterize homoclinic spiking and more fingerprints are needed to characterize *in-vitro* experimental setups.

Here, the possible dynamical regimes that result from different ranges of extracellular potassium concentrations are shown. Furthermore, the interspike interval (ISI) distributions that result from each of those dynamical regimes when injecting irregular input are characterized. The proposed analytical description of ISI distributions in each dynamical regime, could be compared to *in-vitro* experimental observations, and together with maximum likelihood algorithms it could provide more concise conclusions on whether neurons display homoclinic spiking during experiments or not.

In this section I describe how the analytical derivation for the ISI distribution depends on the dynamical system's features particular for each regime. First, I mention the dynamical system's features used to describe the spiking statistics. More specifically, I will use the stable states of the system, i.e the fixed point, and stable limit cycle. The stable states are the ones reached when a constant input is injected to the dynamical system for long enough time. If the system is in a stable state and receives a perturbation, it moves away from the stable state. However, if the perturbation is small, the system comes back to the same stable state. Using this reasoning, it is natural to assume that when small noise is injected to the neuron model, the trajectories would fluctuate around the steady states of the system. This assumption is the basis of the theory that will be used in this chapter to understand the effect of changing extracellular potassium on the neuronal spiking statistics.

3.2 Steady states of the system

Extracellular potassium and the applied current define the steady states of the dynamical system (proposed in chapter 2). Those steady states shape the response of the model when an irregular input is injected.

Here, I consider the fast subsystem of the model proposed in chapter 2, equations 2.1,2.2,2.3,2.4,2.8 ,2.7 (fixed ionic concentrations), receiving an irregular input I_{in}:

$$C_{\mathrm{m}}\frac{dV}{dt} = -I_{\mathrm{Na}} - I_{\mathrm{K}} - I_{\mathrm{L}} - I_{\mathrm{pump}} + I_{in}, \tag{3.1}$$

$$I_{in} = I_{app} + \sqrt{2}\sigma\eta(t). \tag{3.2}$$

Where I_{app} and σ are constants, and $\eta(t)$ is a Gaussian random number. The averaged autocorrelation function of $\eta(t)$ yields a delta function,

$$\langle \eta(t)\eta(t')\rangle = \delta(t-t'), \tag{3.3}$$

and its probability density is a Gaussian distribution.

In Figure 3.1**A** the steady states of the fast system proposed in chapter 2 (i.e., $\sigma = 0$ in equation 3.2) are grouped in 4 categories delimited by the bifurcation diagram of applied current vs. extracellular potassium.

1.) For low values of applied current and low values of extracellular potassium (subthreshold regime in Figure 3.1**A**), the spiking model has only one steady state, a stable node or fixed point. In this regime, the neuron model stays close to the steady node, fluctuating around it when perturbations are injected.

2.) For very high values of extracellular potassium and any applied current, the model has one steady state as well. A depolarized resting state (depolarization block regime in Figure 3.1**A**). The response of the model to noise in this regime, is similar to the one in the subthreshold regime, but the membrane potential is depolarized.

3.) For high values of applied current, the spiking model has a phase plane with one stable solution, a limit cycle (regular spiking regime in Figure 3.1**A**). When noise is

applied (non-zero σ in equation 3.2), trajectories deviate slightly from the stable limit cycle (see Figure 3.1**C**), and the spike timing jitters close to the natural period of the limit cycle (see Figure 3.1**E**).

4.) For low values of applied current and high values of extracellular potassium, two attractors coexist; a stable node and a stable limit cycle (bistable regime in Figure 3.1**A**). The response of the model to noise in this regime is more irregular than the one in the spiking regime (see Figure 3.1**D**). This irregularity comes from the perturbation dependent switch between both stable states (see Figure 3.1**B**). When the system is close to the limit cycle, trajectories deviate slightly from the limit cycle and the interspike interval jitters close to the natural period of the orbit. When the system is close to the stable node and noise is strong enough, it could jump away from the stable node to the limit cycle and vice versa (see Figure 3.1**B**).

A comparison of the spike trains produced from noisy stimulation in the spiking (3) and the bistable (4) regime are shown in Figure 3.1**D,E**. In the regularly spiking regime, most interspike intervals have similar lengths. In the bi-stable regime on the other hand, some interspike intervals are very long, and some are very short. Notice that the interspike interval (ISI) distribution in the spiking regime (see Figure 3.2**B**) is much more symmetric than the one in the bistable regime (see Figure 3.2**A**).

In the next sections I describe in detail where all the features of the ISI distribution in the bistable and the spiking region come from. I apply the formulation derived in (Schleimer et al., 2021) for a 2D model adapting it in the 4D model described in chapter 2 (i.e., the neuron model with fixed ionic concentrations). Simulations were performed in python and the code is available in *this repository*.

3.3 Spiking statistics in the bistable region

It is useful to describe the spiking statistics in terms of the interspike interval (ISI) distribution because the simulations can be directly compared to experimental observations. In experimental setups it is not possible to access all the state variables. Thus, it is not possible to understand trajectories in terms of their phase portraits, or their steady states. Instead, it is feasible to measure spike timing. And with enough observations, ISI distributions.

In the bistable region, the ISI distribution has different features than in the spiking region. In the bistable region, ISI distributions (Figure 3.2**A**) typically have long tails (positive skewness). These tails correspond to the long visits to the stable node.

The duration of the visits to the stable node vary depending on how close the attraction domain of the limit cycle is. The closer it is, the more likely it is to reach it, given an incoming perturbation. Another important feature of the duration of the visits to the stable node, they are independent of the spike history (markov process). This holds in the simplified model that we are analysing here (no adaptation currents, and no ionic concentration dependence on spiking).

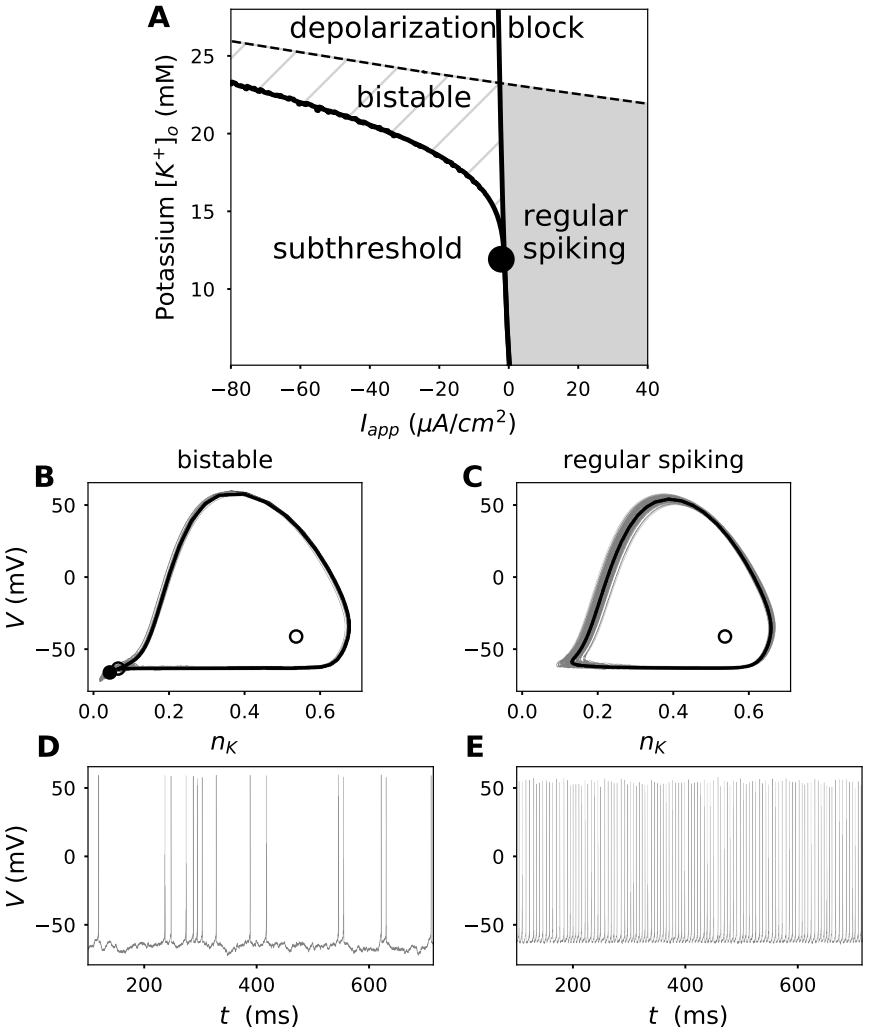

FIGURE 3.1: Single neuron dynamical regimes relative to extracellular potassium ($[K^+]_o$) and applied current (I_{app}). **A**: Extracellular potassium vs. input current bifurcation diagram, the different dynamical regimes being denoted with the different backgrounds. **B,C**: Single neuron response to white noise (grey trajectories), and the attractors of the system given the same input current without noise (black). The black dot represents the stable node, the empty dots represent unstable nodes, and the black orbit represents a stable limit cycle.**B** Shows an example trajectory in the bistable regime. **C** Shows an example trajectory in the regular spiking regime. **D,E**: Same trajectories plotted in (**B,C**), but with respect to time. **D** Membrane potential trajectory for the model in the bistable state. **E** Membrane potential trajectory for the model in the regularly spiking state.

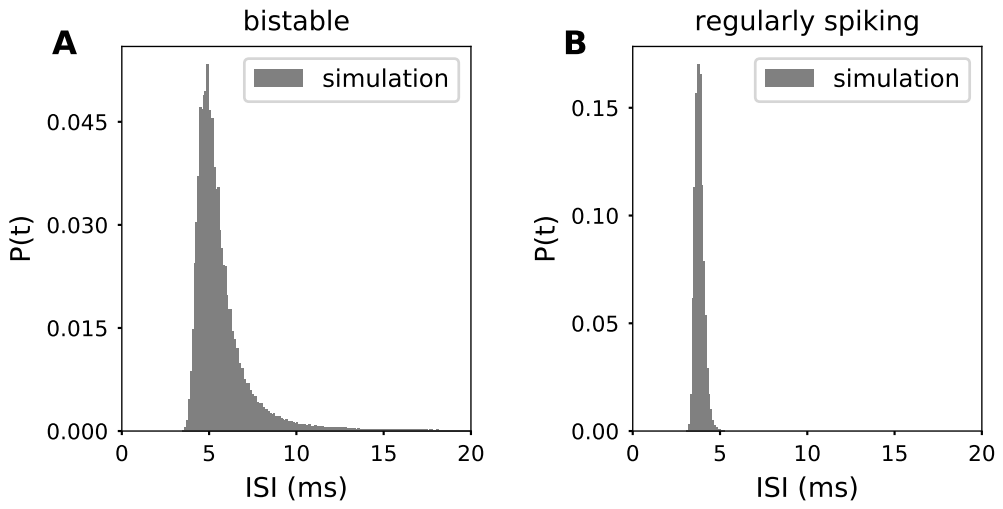

FIGURE 3.2: Interspike interval (ISI) distribution depends on the dynamical regime of the neuron model. **A**: Shows an ISI distribution of the model in the bistable regime. **B**: Shows an ISI distribution of the model in the regularly firing regime. Histograms are the ISI distributions, from 2000 realizations of 20 second long simulation of the neuron model with fixed ionic concentrations described in chapter 2. Both simulations have $[K^+]_o = 14$ mM and input current $I_{in} = I_{app} + \sigma\eta(t)$, where $\sigma = 1\mu A/cm^2$ and $\eta(t)$ is a Gaussian random variable with mean 0 and standard deviation 1 (white noise). $I_{app} = -1.66\mu A/cm^2$ in **A**, and $I_{app} = 0.41\mu A/cm^2$ in **B**.

The duration of the visits to the limit cycle are also independent of the previous time spent on the vicinity of the stable node. Thus, the ISI distribution in the bistable region could be regarded as a mixture of ISIs generated from trajectories going around the limit cycle ($P_{lc}(t)$), and trajectories lying in the attraction domain of the stable node ($P_{fp}(t)$).

$$P_{ISI}(t) = (1-\omega)P_{lc}(t) + \omega P_{fp}(t) \tag{3.4}$$

Where ω is the proportion of ISIs produced by visits to the fixed point, and $(1-\omega)$, the proportion of ISIs produced by visits to the limit cycle.

In the next sections I will show how the features of the steady states of the system could be used to derive the ISI distributions that result from trajectories visiting each steady state.

3.3.1 Trajectories visiting the stable node

When the system enters the attraction domain of the stable node, it gets pulled towards the stable node. An incoming perturbation could make the system deviate from the stable node. If the perturbation is weak relative to the strength of attraction of the stable node, the system would stay in its attraction domain. However, if the perturbation is strong enough, the system would leave the attraction domain of the stable node and enter the one of the limit cycle.

The ISI produced from a visit to the stable node can be described as:

$$t_{fp} = t_e + t_{lc} \tag{3.5}$$

Where t_e represents the time spent on the attraction domain of the stable node, and t_{lc} represents the time needed to generate one spike after escaping the attraction domain of the stable node. Assuming that trajectories in the attraction domain of the stable node and in the attraction domain of the limit cycle are independent of each other, t_e and t_{lc} are independent as well. The distribution of the sum of independent stochastic variables is the convolution of their distributions, so we can write the probability distribution of t_{fp}, $P_{fp}(t)$ as:

$$P_{fp}(t) = (P_e * P_{lc})(t) = \int_0^t P_e(r)P_{lc}(t-r)dr \tag{3.6}$$

First I will describe the distribution of t_e, $P_e(t)$:

3.3.1.1 Distribution of time spent on the basin of attraction of the stable node: $P_e(t)$

The stable node's attraction domain is bounded by a separatrix. This means that as soon as the system crosses the separatrix (coming from the stable node), it enters the attraction domain of the limit cycle.

Even though the separatrix is non-local, simulations showed that most of its crossings occur through the saddle node (see Figure 3.3**B**). In other words, if the system is in the stable node and receives a perturbation strong enough to make the system move pass the saddle node, it crosses the separatrix (saddle node), and enters the attraction domain of the limit cycle.

Most separatrix crossings are aligned in the same direction. They are perpendicular to the separatrix. The separatrix of the 4D system we are analyzing is a hyperplane. But luckily, right at the saddle node the separatrix is tangential to its stable manifold. So the orthogonal vector to the saddle's stable manifold yields the orientation of the separatrix crossings at the saddle node. This will be explained in more detail below.

When the noise has a large amplitude, the separatrix crossings from the limit cycle to the stable node could go through different locations than the saddle node. The scope of this work is limited to a noise intensity regime where separatrix crossings occur through the saddle node.

Dimensionality reduction

The derivation of the probability density $p_e(t)$ produced by the dynamics proposed above is not simple, mainly due to the high dimensionality of the system. However, given that the main goal here is to get an approximation for the interspike interval distribution, it is enough to get a good prediction for the dynamics close to the separatrix which in this case is right at the saddle node.

The dimensionality reduction requires the linearization of dynamics at the saddle node (x_s). The linearized dynamics are given by the Jacobian of the 4 dimensional spike generating dynamics evaluated at x_s.

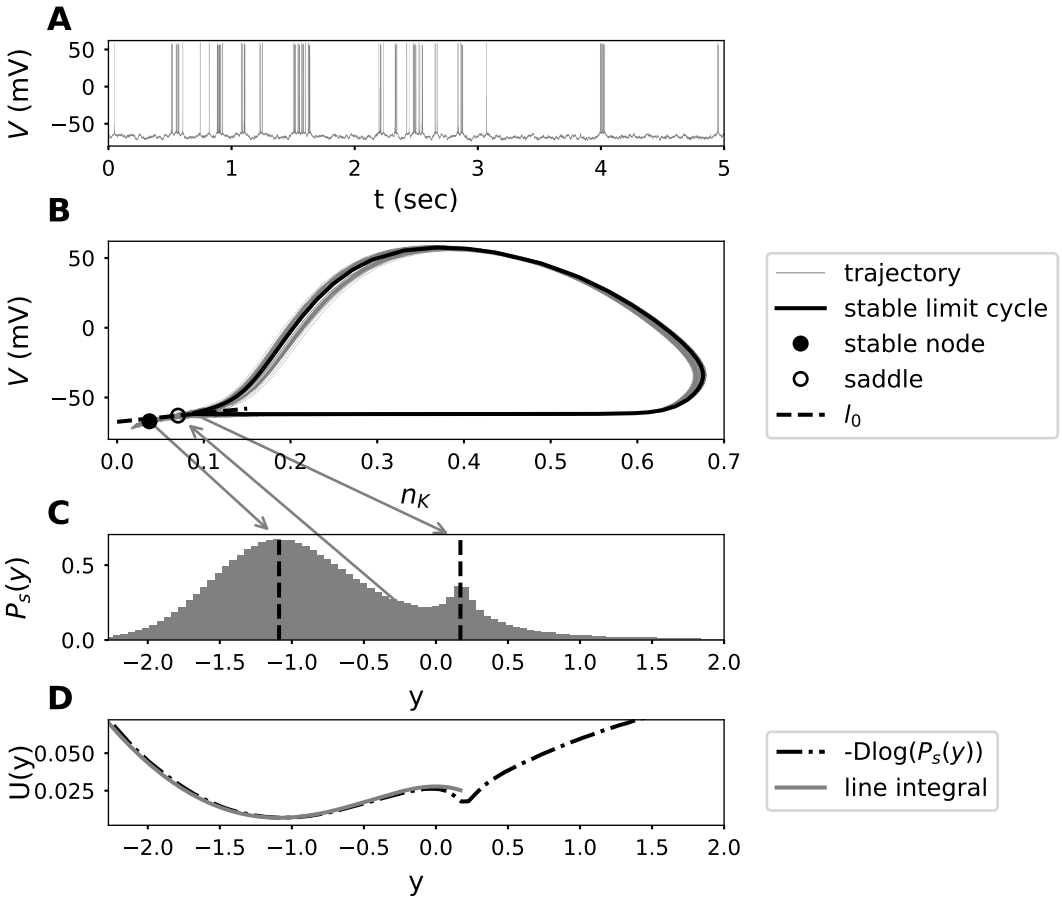

FIGURE 3.3: Illustration of l_0 relative to the attractors of the dynamical system. **A**: Example membrane potential trace (grey) of a neuron-model in the bistable region when receiving irregular input. **B**: Example trajectory (grey) relative to two state variables (out of four) together with the phase portrait containing the stable node (black dot), the saddle node (empty dot), the stable limit cycle (Black orbit), and l_0. l_0, the left eigenvector associated to the unstable manifold of the saddle node, is shown in a dashed line. **C**: Stationary distribution $P_s(y)$ of multiple realizations of the trajectory shown in **A** and **B**, projected into l_0. The first peak of the distribution from left to right matches the position of the stable node (d_{fp}), the second peak matches the minimum distance between the limit cycle and the saddle node (d_{lc}). Dashed lines coincide with the position of the fixed point (d_{fp}), and the minimum distance between the limit cycle and the saddle node (d_{lc}). **D**: Double well potential ($U(y)$) of the dynamical system shown in the bottom panel. Comparison between $U(y)$, calculated with equation 3.17, and with the steady state distribution $p_s(y)$ shown in **B**: $U(y) = -\sigma^2 \log(p_s(y))$ (see equation 3.24).

$$\mathbb{J}_{x_s} = \begin{bmatrix} \frac{\partial \dot{V}}{\partial V} & \frac{\partial \dot{V}}{\partial m_{Na}} & \frac{\partial \dot{V}}{\partial h_{Na}} & \frac{\partial \dot{V}}{\partial n_K} \\ \frac{\partial \dot{m}_{Na}}{\partial V} & \frac{\partial \dot{m}_{Na}}{\partial m_{Na}} & \frac{\partial \dot{m}_{Na}}{\partial h_{Na}} & \frac{\partial \dot{m}_{Na}}{\partial n_K} \\ \frac{\partial \dot{h}_{Na}}{\partial V} & \frac{\partial \dot{h}_{Na}}{\partial m_{Na}} & \frac{\partial \dot{h}_{Na}}{\partial h_{Na}} & \frac{\partial \dot{h}_{Na}}{\partial n_K} \\ \frac{\partial \dot{n}_K}{\partial V} & \frac{\partial \dot{n}_K}{\partial m_{Na}} & \frac{\partial \dot{n}_K}{\partial h_{Na}} & \frac{\partial \dot{n}_K}{\partial n_K} \end{bmatrix}_{x=x_s} \tag{3.7}$$

where x is a vector containing the position in the 4 dimensional space $[V, m_{Na}, h_{Na}, n_K]$, and x_s denotes the position of the saddle in the 4 dimensional space,

$$x_s = [V_s, m_{Na_s}, h_{Na_s}, n_{K_s}]. \tag{3.8}$$

The eigenvalues (λ) of the Jacobian evaluated at x_s,

$$(\mathbb{J}_{x_s} - \lambda I)\mathbb{X}_R = 0, \tag{3.9}$$

fulfill $\lambda_0 \geq 0 > \lambda_1 > .. > \lambda_{n-1}$. And $\mathbb{X}_R$ are the right eigenvectors. The stable manifold is tangential to the right eigenvectors associated to the eigenvalues $\lambda_1, .., \lambda_{n-1}$.

Similarly the left eigenvectors ($\mathbb{X}_L$) can be calculated as:

$$(\mathbb{J}_{x_s}^T - \lambda I)\mathbb{X}_L^T = 0. \tag{3.10}$$

The unstable direction l_0, is given by the left eigenvector corresponding to λ_0 (the unstable manifold of the saddle see Figure 3.3**B**).

Now that the orientation of separatrix crossings is defined, it is convenient to project the 4 dimensional dynamics into this vector l_0. Given that the saddle node separates trajectories on the basin of attraction of the stable node from the ones in the basin of attraction of the limit cycle, it is also helpful to set the reference for the trajectory right there:

$$y(t) = l_0 \cdot (x(t) - x_s), \tag{3.11}$$

where $x(t)$, represents the trajectory in the 4 dimensional space

$$x(t) = [V(t), m_{Na}(t), h_{Na}(t), n_K(t)], \tag{3.12}$$

Double well potential

The projection of the 4D trajectories on l_0 ($y(t)$) allows the calculation of the probability of staying in the stable node through a double well potential (Chow and White, 1996; Schleimer et al., 2021). In a double well potential there are 2 local minima, and a barrier separating them. Here, the two local minima are the stable node and the limit cycle positions in l_0 (the attractors), and the barrier is the saddle position (the separatrix).

The deterministic potential $U(y)$, can be calculated with the line integral along l_0:

$$U(y(b)) = \int_a^b f(y(t)) \cdot y'(t) dt. \tag{3.13}$$

$f(y(t))$ is the vector field and can also be expressed as:

$$f(x(t) \cdot l_0) = x'(t) \cdot l_0. \tag{3.14}$$

And, manipulating equation 3.11,

$$y'(t) = x'(t) \cdot l_0, \tag{3.15}$$

$$\bar{x}'(t) \cdot l_0 dt = dy, \tag{3.16}$$

$$U(y*) = \int_a^{y*} x'(t) \cdot l_0 dy. \tag{3.17}$$

Given the complexity of the dynamical system, equation 3.17 can only be calculated numerically (See Figure 3.3**D**). It is convenient to separate the integral into 3 sections; 1. From a point to the left of the stable node, 2. from the stable node to the saddle (integrating backwards), and, 3. from the saddle to the limit cycle. Evaluating the right hand side of equations 2.1, and equations in table 2.3, along the trajectories for each of the sections (1.,2., and 3.), yields the term $x'(t) \cdot l_0$.

$U(y)$ is useful to predict the probability of finding a particle in any location y given that an irregular input is injected. The movement of a particle along a potential can be described as follows,

$$\frac{dy}{dt} = -U'(y) + \sqrt{2D}\xi(t), \tag{3.18}$$

here $U(y)$ is the potential, and, D is the effective noise strength in l_0 (note that the noise is only injected on the voltage dimension (equation 3.2)):

$$\sqrt{D} = l_0 \cdot ([\sigma, 0, 0, 0]). \tag{3.19}$$

The barrier is the potential energy needed to cross the saddle node (see Figure 3.3**D**). The local minima are located at d_{fp} and d_{lc},

$$d_{fp} = l_0 \cdot (x_n - x_s), \tag{3.20}$$

$$d_{lc} = min_{x \in \Gamma}\{l_0 \cdot (x - x_s)\}, \tag{3.21}$$

where x_n is the position of the stable node (fixed point) and Γ denotes the stable limit cycle in the 4 dimensional space.

Notice from Figure 3.3 that when a particle is to the left of the potential barrier (the saddle), it is pulled to the local minimum, the stable node (at $y = d_{fp}$). When a particle is to the right of the potential barrier, it is pulled towards the limit cycle (at $y = d_{lc}$).

The position Yt is a stochastic variable, different realizations of the same process (equation 3.18) will yield different trajectories. Thus, to describe them, it is useful to understand the probability density over many realizations. The probability density $p(y, t)$ can be described by a simple 1D form of the Fokker-Planck equation:

$$\partial_t p(y,t) = \partial_y[U'(y)p(y,t)] + D\partial_y^2[p(y,t)]. \tag{3.22}$$

Since here we assume that $U(y)$, and D are time invariant, the previous is an homogeneous process. We are only interested in the stationary distribution $p_s(y)$. Thus,

$$0 = \partial_y[U'(y)p_s(y)] + D\partial_y^2[p_s(y)]. \tag{3.23}$$

The stationary solution when motion is on an infinite range:

$$p_s(y) = \mathcal{N} \exp \frac{-U(y)}{D}, \tag{3.24}$$

where $\mathcal{N}$ is a normalization constant,

$$\mathcal{N} = \frac{1}{\int_{-\infty}^{\infty} \exp \frac{-U(y)}{D}}. \tag{3.25}$$

Now that we have an expression for the steady state distribution $p_s(y)$, and the potential $U(y)$, we can continue to find the distribution of times spent in the left well, y from $-\infty$ to 0 (the saddle node position). So we need to calculate the mean escape time from the left well to the right. Or the mean first passage time from d_{fp} to d_{lc}. The derivation of the expression for the mean first passage time from one attractor to the other can be found in (Gardiner, 2009);

$$T(d_{fp} \to d_{lc}) \approx \frac{1}{D} \int_{d_{fp}}^{d_{lc}} dy \exp \frac{U(y)}{D} \int_{-\infty}^{y} \exp \frac{-U(z)}{D} dz \tag{3.26}$$

When the potential has a high barrier ($U(0)$ is large relative to $U(d_{fp})$ and $U(d_{lc})$), and D is small, the term $\int_{-\infty}^{y} \exp \frac{-U(z)}{D} dz$ has a narrow peak at 0 and decays rapidly around it. Thus, equation 3.26 can be approximated to:

$$T(d_{fp} \to d_{lc}) = \frac{1}{D} \left(\int_{d_{fp}}^{d_{lc}} \exp \frac{U(y)}{D} dy \right) \left(\int_{-\infty}^{0} \exp \frac{-U(y)}{D} dy \right). \tag{3.27}$$

Equation 3.27 can be simplified even further, approximating the potential decay near the barrier ($U(0)$) and the potential increase from the fixed point ($U(d_{fp})$ to a quadratic function, which yields:

$$T(d_{fp} \to d_{lc}) \approx \frac{2\pi}{\sqrt{|U''(y_{d_{fp}})||U''(0)|}} e^{(U(0)-U(d_{fp}))/D}. \tag{3.28}$$

Which is also known as the Kramers rate (Kramers, 1940). The Kramers rate will be close to equation 3.26 when D is very small relative to the potential height (the derivation of equations 3.24, 3.26, 3.27, and 3.29 is explained in detail in (Gardiner, 2009) section 5.2.b). For convenience from here on $T(d_{fp} \to d_{lc})$ will be referred to as the escape time or τ_e. The distribution of escape times from the basin of attraction of the fixed point to d_{lc}, can be described by:

$$\tau_e = \approx \frac{2\pi}{\sqrt{|\lambda_{fp}||\lambda_0|}} e^{(U(0)-U(d_{fp}))/D}. \tag{3.29}$$

$$P_e(t) = \frac{e^{-t/\tau_e}}{\tau_e}, \tag{3.30}$$

Where $U(y)$ can be obtained from the numerical solution of equation 3.17 for each combination of parameters studied. Calculating derivatives numerically introduces errors, so $U''(d_{fp})$ was approximated to λ_{fp} (the less negative eigenvalue of the Jacobian evaluated at the stable node), and $U''(0)$ is approximated to λ_0 the only positive eigenvalue of the Jacobian evaluated at the saddle.

The mean time spent on the attraction domain of the stable node (τ_e) depends on the potential difference between saddle and node in l_0 (see Figure 3.4 and 3.5). Notice that in Figure 3.4 left panel (trajectories in the phase plane), the stable node and the saddle are further away than in the right panel. The further the stable node and the saddle node are, the bigger the basin of attraction of the stable node, and the higher the density of long waiting times (see Figure 3.4 bottom panel).

In (Schleimer et al., 2021), a different formulation for $U(y)$ was proposed, based on the concavity of the voltage dimension. That formulation is valid very close to the SNL bifurcation for simpler models. Here, we are interested in a broader range of the bistable region, and given that the model analyzed here is four dimensional, the concavity in the voltage dimension doesn't capture $U(y)$ for parameters far away from the SNL. Another issue was that right at the bifurcations some approximations fail.

The regime where the Kramers rate (equation 3.30) fails is at very small distances between saddle and node (see Figure 3.5). The reason for this is that the potential barrier is too small relative to the noise intensity (see the potential for very low d_{fp} in the appendix, Figure 3.16, and τ_e for different noise intensities Figure 3.16). As mentioned above, one of the assumptions needed to derive a simple τ_e expression (equation 3.29), was that the potential barrier should be big relative to the noise intensity (D) Kramers (1940). Escape times are not precisely estimated for small barriers because particles freely diffuse from the stable node to the saddle. Also, particles that touch the barrier and come back to the fixed point are underestimated.

τ_e varies along the bistable region. This is due to the fact that the distance between the saddle and the node (d_{fp}) is not constant along the bistable region (See Figure 3.6). The distance between both increases for more hyperpolarizing mean input currents. The stable node position acquires more negative voltages. This hyperpolarization of the stable node would be straightforward to identify in patch clamp recordings, where the membrane potential in the steady state hyperpolarizes or depolarizes depending on the magnitude of the input current. Towards higher values of mean input current, the stable node acquires more depolarized values and comes closer to the saddle node. Close to the bifurcation, where the stable node loses stability, the distance between saddle and stable node is minimal (See Figure 3.4, right panel).

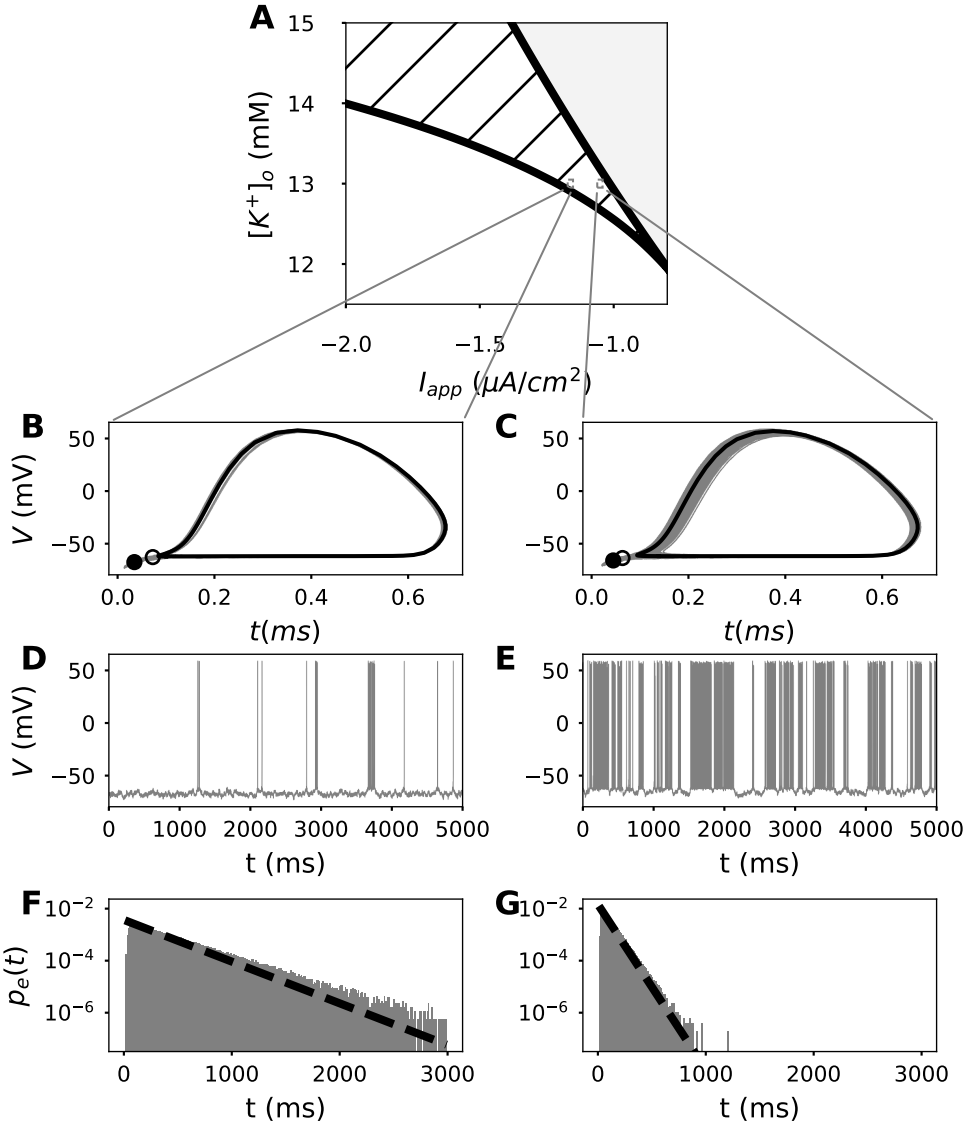

FIGURE 3.4: Distance between saddle and node (d_{fp}) determines τ_e. Simulations are shown for 2 different d_{fp}. **A**: Locations of the phase planes are indicated in a zoom to the bifurcation diagram. **B**: Phase portrait in the potassium inactivation - membrane potential ($n_K - V$) plane for large d_{fp}, and example trajectory (gray) when irregular input is injected. **C**: Phase portrait in the potassium inactivation - membrane potential ($n_K - V$) plane for small d_{fp} , and example trajectory (gray) when irregular input is injected. **D**: Trajectory portrayed in **B**, but relative to time. **E**: Trajectory portrayed in **C**, but relative to time. **F**, shows the distribution of time spent on the attraction domain of the stable node ($P_e(t)$) for large d_{fp}. Dashed line shows the prediction (equation 3.26 with potential from the line integral in l_0). **G** shows the distribution of time spent on the attraction domain of the stable node ($P_e(t)$) for small d_{fp}. Dashed line shows the prediction (equations 3.26 and 3.30). Simulations with parameters $K_o = 13.0$ mM, $\sigma = 0.5(\mu\text{A/cm}^2)$, $I_{app} = -1.16\mu\text{A/cm}^2$, (**B,D,F**), $I_{app} = -1.05\mu\text{A/cm}^2$ (**C,E,G**)

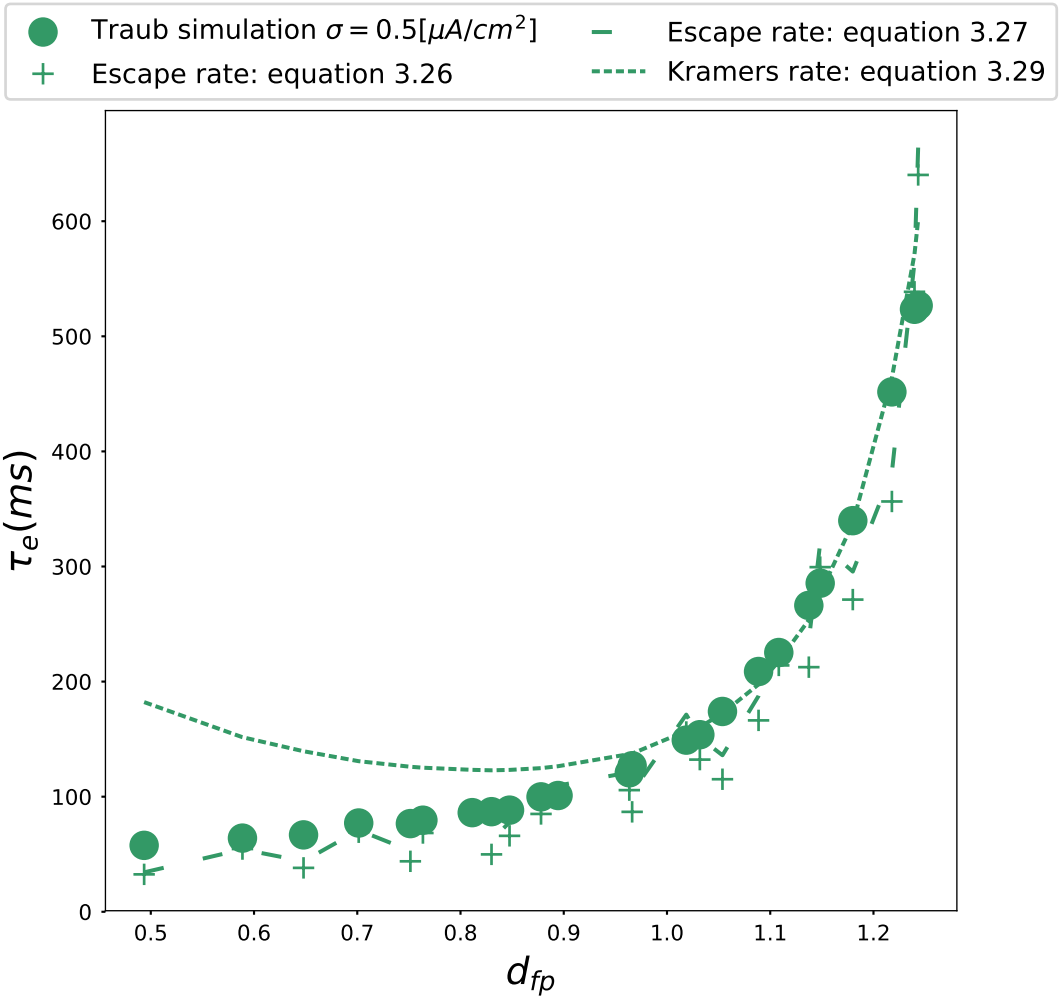

FIGURE 3.5: Average duration in the attraction domain of the stable node vs. distance between saddle and node projected in l_0. Simulations are compared to the predictions described in equations 3.26, 3.27 and 3.29. Simulations were performed with noise intensity $\sigma = 0.5\ \mu A/cm^2$.

Now that $P_e(t)$ has been derived, $P_{lc}(t)$ is the only missing piece to complete $P_{fp}(t)$ (Equation 3.6).

3.3.1.2 Distribution of time needed to produce one spike: $P_{lc}(t)$

The distribution of time needed to complete a lap around the limit cycle can be approximated as a function of the natural frequency of the stable limit cycle, and its susceptibility to perturbations. For the derivation of such function, a phase reduction, mapping the process to a one-dimensional Brownian motion in the phase with constant drift is needed (Schleimer et al., 2021; Schleimer, 2013).

$$\dot{\varphi} = \frac{1}{\tau_{lc}} + \sqrt{2\bar{D}_{lc}}\xi(t) \tag{3.31}$$

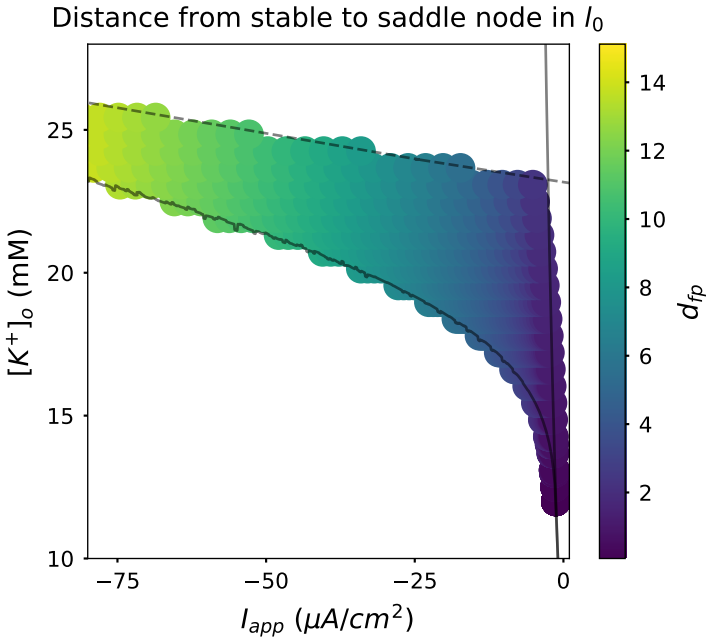

FIGURE 3.6: Distance between saddle node and stable node in the extracellular potassium - applied current plane. The distance between both nodes is calculated as the difference between the stable node and saddle node positions projected into l_0. l_0 is the left eigenvector corresponding to the unstable manifold of the saddle.

Here $\frac{1}{\tau_{lc}}$ is the natural frequency of the limit cycle, and $\xi(t)$ is a stochastic white noise Gaussian process with effective diffusion matrix $\bar{D}_{lc}$. Such a simple approximation relies on three assumptions: 1) perturbations are small enough so that trajectories stay in the attraction domain of the limit cycle. 2) Noise is white or at least much faster than τ_{lc}. 3) The radial attraction of the limit cycle is almost instantaneous. First, I will explain in detail each term and afterwards, I will discuss the accuracy of the assumptions.

$\bar{D}_{lc}$ can be approximated by averaging the noise with a weighting function $(Z_0(\varphi))$ over the time scale of an ISI. $Z_0(\varphi)$ introduces the susceptibility to perturbations as a function of the phase in the cycle in which the perturbation is injected (Schleimer, 2013; Schleimer et al., 2021).

$$\bar{D}_{lc} = \int_0^1 d\varphi Z_o(\varphi) \cdot D(x_{lc}(\varphi)) Z_o(\varphi) \tag{3.32}$$

$Z_o(\varphi)$ is the phase response curve (PRC) (Schleimer and Schreiber, 2018). Here it is calculated as the periodic solution to the adjoint of the first variational equation of the unberturbed dynamics (Hesse et al., 2017).

$$\frac{dZ_0}{d\varphi}(\varphi) = -J^T(\varphi) Z_0(\varphi) \tag{3.33}$$

Where J^T is the transposed Jacobian of the dynamical system evaluated on the limit cycle. Note that when noise is slower than an ISI timescale in equation. 3.32, this average does not convey the effective diffusion of the system.

Here, the only noise that is injected is in one dimension, so the effective diffusion could be reduced to:

$$\bar{D}_{lc} = \int_0^1 d\varphi Z_o(\varphi) \cdot \begin{bmatrix} \sigma^2_{\mathbf{inp}} & 0 & 0 & 0 \\ 0 & 0 & 0 & 0 \\ 0 & 0 & 0 & 0 \end{bmatrix} Z_o(\varphi) \tag{3.34}$$

$$\bar{D}_{lc} \approx \sigma^2_{inp} \int_0^1 d\varphi Z_o(\varphi)^2 \tag{3.35}$$

The probability density of equation 3.31 can be exactly calculated:

$$P_{lc}(t) \approx \frac{\exp(-\frac{(t-\tau_{lc})^2}{2\tau^2_{lc}\bar{D}_{lc}t})}{\sqrt{2\pi\bar{D}_{lc}t^3}}. \tag{3.36}$$

Notice the resemblance of equation 3.36 to the probability density solution of a perfect integrator receiving noisy input (Gerstein and Mandelbrot, 1964). Perfect integrator models have been used to approximate the probability densities of more complicated neuron models. Such approximations are close to the complex dynamics when the input current is strong enough (Lindner, 2004).

The reduction of the 4D system shown here, is only strictly valid when the radial attraction to the limit cycle is almost instantaneous (Schleimer, 2013). This assumption is not strictly fulfilled in any of the combinations of parameters shown here (see Figure 3.7). However, for fast radial attraction, the approximation yields satisfactory results. The higher the attractiveness of the limit cycle, the faster the radial attraction. The attractiveness of the limit cycle increases with input current. Notice that the predicted distribution comes closer to the numerical simulations in the right panel of Figure 3.7 compared to the left one. On the right panel the input current is more depolarized than on the left panel. Thus, in the right panel, trajectories converge faster to the limit cycle than on the left panel, and the theoretical approximation is better.

3.3.2 Time spent around the limit cycle

When a particle is in the basin of attraction of the limit cycle, its trajectories will orbit the limit cycle unless a perturbation is strong enough to make the particle cross the separatrix and enter the basin of attraction of the stable node. In the vast majority of cases, particles cross the separatrix right after the spike downstroke, where the separatrix (the saddle node) is closest. It is worth highlighting that when perturbations are much bigger than the ones we are showing here, the crossings of the separatrix could also occur in locations different than the saddle, but here we will assume the small noise regime.

Right after spike downstroke, particles are closest to the saddle node (separatrix). This distance is denoted as d_{lc} (equation (3.21);

d_{lc} has a strong influence on the time spent on the limit cycle. When d_{lc} is very small, every time there is a spike, particles come very close to the separatrix right after

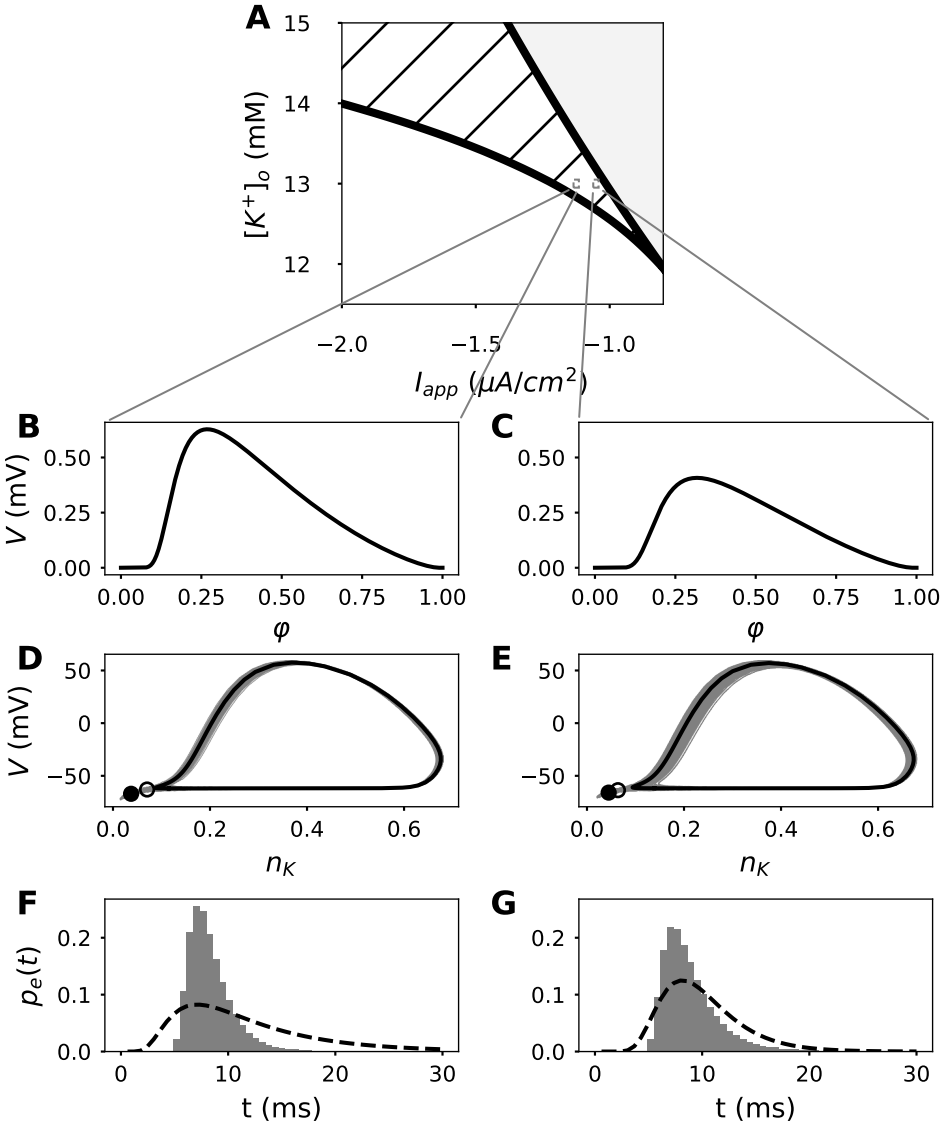

FIGURE 3.7: $P_{lc}(t)$ approximation given slightly different limit cycles. Simulations are shown for the system in 2 different parameter combinations.**A**: Locations are indicated in a zoom to the bifurcation diagram. **B,C**: $Z(\varphi)$ is shown for each parameter combination. **D,E**: Phase portraits, and trajectories projected in the potassium inactivation - membrane potential ($n_K - V$) plane. **F,G**: shows the distribution of time needed to complete a lap around the limit cycle ($P_{lc}(t)$). Simulations are shown in grey, and the theoretical derivation is shown in black. Simulations with parameters $K_o = 13.0$ mM, $\sigma = 0.5$ (μA/cm^2), applied current$=-1.12\mu$A/cm^2 (**B,D,F**), and applied current$=-1.05\mu$A/cm^2 (**C,E,G**).

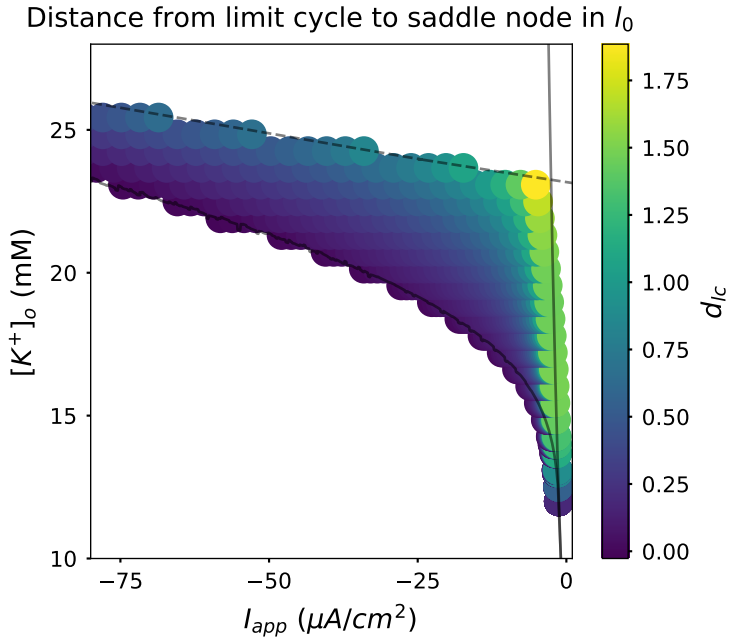

FIGURE 3.8: Minimal distance between saddle node and limit cycle in the extracellular potassium - applied current plane. The distance is calculated as the minimum difference between the limit cycle and saddle node projected into l_0. Where l_0 is the left eigenvector corresponding to the unstable manifold of the saddle.

spike downstroke, thus, even small perturbations are enough to make them cross the separatrix.

Similarly to d_{fp}, d_{lc} varies in the bistable region (See Figure 3.8). Depolarizing mean input currents increase d_{lc}. Large d_{lc} produce longer visits to the the limit cycle. Notice that d_{lc} follows an inverse trend than d_{fp} (compare Figures 3.8 and 3.6). Consequently, the time spent on the limit cycle is negatively correlated to the time spent on the stable node.

3.3.3 Mixing factor: ω

After spike downstroke the particle is relatively close to the saddle ($y = d_{lc}$, equation 3.21), thus at this location a perturbation can push a particle to cross the barrier and visit the fixed point. The mixing factor is the probability ω that a particle starting at d_{lc} crosses the barrier and reaches the basin of attraction of the stable node (d_{fp}) depends on d_{lc}. If the minimal distance d_{lc} is very small, then the probability of crossing the barrier is high. If d_{lc} is big, the probability of crossing the barrier is smaller. Here I will explain how this dependence can be derived.

The probability ω to end up in d_{fp} after spike downstroke can be calculated with the "splitting probability" defined in (Gardiner, 2009) in section 9.1,

$$\omega = \frac{\left[\int_{d_{lc}}^{\infty} dy p_s(y)^{-1}\right]}{\left[\int_{d_{fp}}^{\infty} dy p_s(y)^{-1}\right]}. \tag{3.37}$$

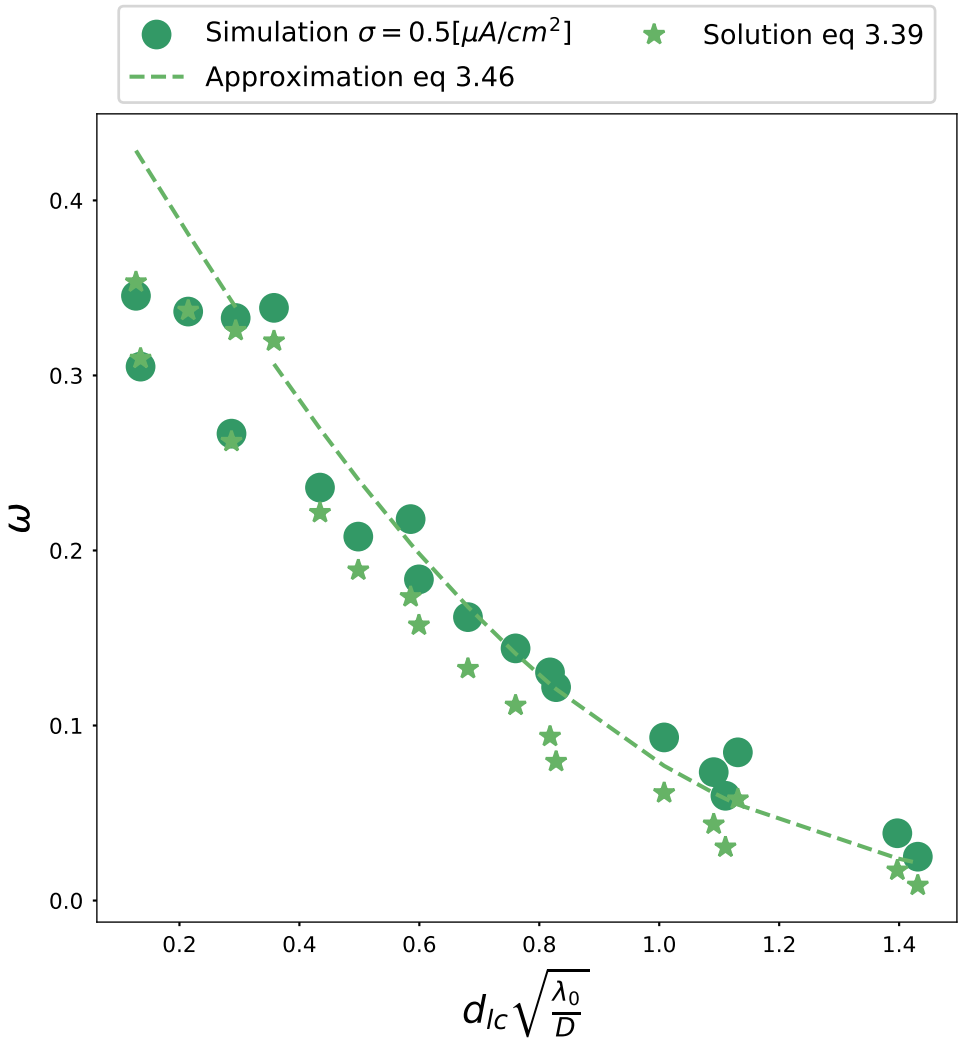

FIGURE 3.9: Mixing factor w or the probability of visiting the fixed point right after spike downstroke. Simulations are compared to the predictions from equations 3.39 and 3.46.

Using equation 3.24,

$$\int_a^b dy p_s(y)^{-1} = \int_a^b dy \mathcal{N}^{-1} \exp \frac{U(y)}{D}, \tag{3.38}$$

and,

$$\omega = \frac{\int_{d_{lc}}^{\infty} \exp \frac{U(y)}{D} dy}{\int_{d_{fp}}^{\infty} \exp \frac{U(y)}{D} dy}. \tag{3.39}$$

Equation 3.39 can be solved numerically, with $U(y)$ from equation 3.17 and replacing the upper integration boundary (∞) with a value $y*$ such that $y* >> d_{lc}$ (see Figure 3.9).

Equation 3.39 can be simplified assuming $U(y)$ decays as a squared function of y from the barrier at $y = 0$,

$$U(y) \approx U(0) - |U''(y_s)|(0-y)^2, \tag{3.40}$$

where $U(0)$ is the potential at $y = 0$, or the barrier height. When D is very small relative to the barrier height $U(0)$ the integration limits of the denominator of equation 3.39 can be assumed to recede to $-\infty$ and $+\infty$ thus,

$$\int_{d_{fp}}^{\infty} \exp \frac{U(y)}{D} dy \approx \int_{-\infty}^{\infty} \exp \frac{U(0) - |U''(0)|y^2}{D} dy, \tag{3.41}$$

$$\approx \sqrt{\frac{\pi D}{|U''(0)|}} \exp \frac{U(0)}{D}. \tag{3.42}$$

When d_{lc} is small, it is possible to use the quadratic approximation for $U(y)$ in the nominator of equation 3.39 as well. It is also useful to change the integration boundary $d_{lc} = y_o\sqrt{D}$, which then yields:

$$\int_{d_{lc}}^{\infty} \exp \frac{U(y)}{D} dy \approx \int_{y_o\sqrt{D}}^{\infty} \exp \frac{U(0) - |U''(0)|y^2}{D} dy \tag{3.43}$$

$$\approx \frac{1}{2}\sqrt{\frac{\pi D}{|U''(0)|}} \exp \frac{U(0)}{D} \left(1 - \mathrm{erf}(\sqrt{|U''(0)|}y_o)\right) \tag{3.44}$$

Substituting back $y_o = d_{lc}/\sqrt{D}$,

$$\approx \frac{1}{2}\sqrt{\frac{\pi D}{|U''(0)|}} \exp \frac{U(0)}{D} \left(1 - \mathrm{erf}\left(d_{lc}\sqrt{\frac{|U''(0)|}{D}}\right)\right). \tag{3.45}$$

Replacing this terms back to equation 3.39 and $U''(0) \approx \lambda_0$, the probability ω can be approximated to a function of d_{lc}, λ_0, and D:

$$\omega \approx \frac{1}{2}\left(1 - \mathrm{erf}\left(d_{lc}\sqrt{\frac{\lambda_0}{D}}\right)\right). \tag{3.46}$$

Therefore, when the distance between the saddle node and the limit cycle is 0 ($d_{lc} = 0$), after every spike the probability of staying in the limit cycle tends to 0.5. When d_{lc} is large, it is less likely to switch from the limit cycle basin of attraction to the one of the stable node, ω yields values smaller than 0.5 and the $P_{ISI}(t)$ in equation 3.4 has a more prominent contribution from $P_{lc}(t)$ than from $P_{fp}(t)$.

The approximation for the mixing factor in equation 3.46, overestimates the proportion of trajectories that end up in the fixed point after crossing the barrier. This is the case particularly when the potential $U(0)$ is not very high relative to $U(d_{lc})$ (see appendix Figure 3.19). When the difference between the potential $U(0)$ and $U(d_{lc})$ is very small, particles freely diffuse back and forth through $y = 0$, and might not visit d_{fp} as often as expected from the asymptotic evaluation of $U(y)$ (equation 3.40). For those cases it is necessary to solve equation 3.39 in order to get a better estimate for ω.

d_{lc} and λ_0 are not constant along the bistable plane, thus ω varies as well. ω reaches a maximum close the limit cycle onset bifurcation, where d_{lc} is smaller (more hyperpolarized currents in the bistable region, see Figure 3.8).

3.3.4 Result: Theoretical prediction of ISI in the bistable region

In the previous sections, an approximation for $P_{ISI}(t)$ was derived. The parameters that go into the approximation can either be obtained from the deterministic potential (equation 3.17), or from a simpler approximation coming from the features of the attractors of the dynamical system. The features used were: the position of the fixed point relative to the saddle (d_{fp}), the position of the limit cycle (d_{lc}) relative to the saddle, the limit cycle natural period (τ_{lc}), the curvature of the potential at the saddle (λ_0), the curvature of the potential at the fixed point (λ_{fp}), the potential height, and the limit cycle phase response curve (PRC). These are all parameters fully determined by the steady state of the system when the input is completely deterministic. Finding those steady states (for noiseless input current) is much faster than simulating all the noise realizations needed to find $P_{ISI}(t)$. Which is why the theory we proposed in (Schleimer et al., 2021), and implemented here is an effective way of generating multiple spike trains that resemble the spiking of a neuron in the bistable dynamical regime described here. When more precise approximations are needed however, specially close the bifurcations, it is better to directly use the deterministic line integral (equation 3.17), which yields more exact results. Calculating the line integral in equation 3.17 to obtain the potential is not computationally expensive and yields very satisfactory predictions for the interspike interval distribution (see Figure 3.10).

Moments of the distribution

The uncentered moments of $P_{ISI}(t)$ can be obtained from its Laplace transform ($P_{ISI}(s)$):

$$P_{ISI}(s) = (1-\omega)P_{lc}(s) + \omega P_{fp}(s). \tag{3.47}$$

$P_{lc}(s)$ is the Laplace transform of equation 3.36,

$$P_{lc}(s) = \exp\left[\frac{1-\sqrt{2D_{lc}\tau_{lc}^2 s+1}}{\tau_{lc}D_{lc}}\right], \tag{3.48}$$

and $P_{fp}(s)$ is the Laplace transform of equation 3.6 where the convolution $(P_e * P_{lc})(t)$ turns into a multiplication in the Laplace domain;

$$P_{fp}(s) = P_{lc}(s)P_e(s), \tag{3.49}$$

$$P_e(s) = \frac{1}{1+s\tau_e}. \tag{3.50}$$

Thus,

$$P_{ISI}(s) = (1-\omega)P_{lc}(s) + \frac{\omega}{1+s\tau_e}P_{lc}(s). \tag{3.51}$$

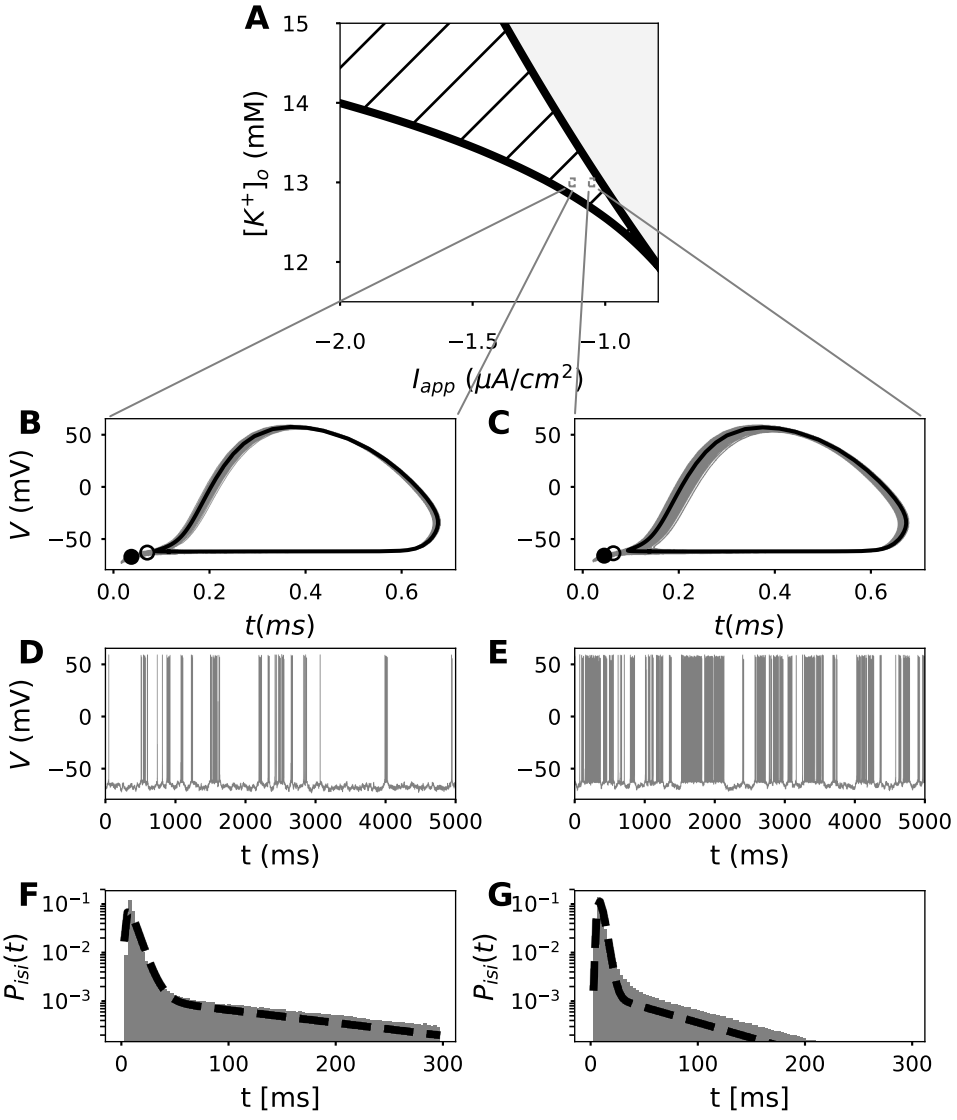

FIGURE 3.10: $P_{ISI}(t)$ approximation in the bistable region, theory compared to simulations. Simulations are shown for the system in two different parameter combinations. **A** Locations are indicated in a zoom to the bifurcation diagram. **B,C**: Phase portraits, and trajectories projected in the potassium inactivation - membrane potential ($n_K - V$) plane. **D,E**: Evolution of the membrane potential (V) in time. **F,G**: Distribution of ISIs ($P_{isi}(t)$) from simulations (grey), and prediction (dashed line). For τ_e, equation 3.26 was used, and for ω equation 3.39 was used. Simulations with parameters $K_o = 13.0$ mM, applied current$=-1.12\mu$A/cm^2, $\sigma = 0.5(\mu$A/cm$^2)$ (left), and $K_o = 13.0$ mM, applied current$=-1.05\mu$A/cm^2, $\sigma = 0.5(\mu$A/cm$^2)$ (right).

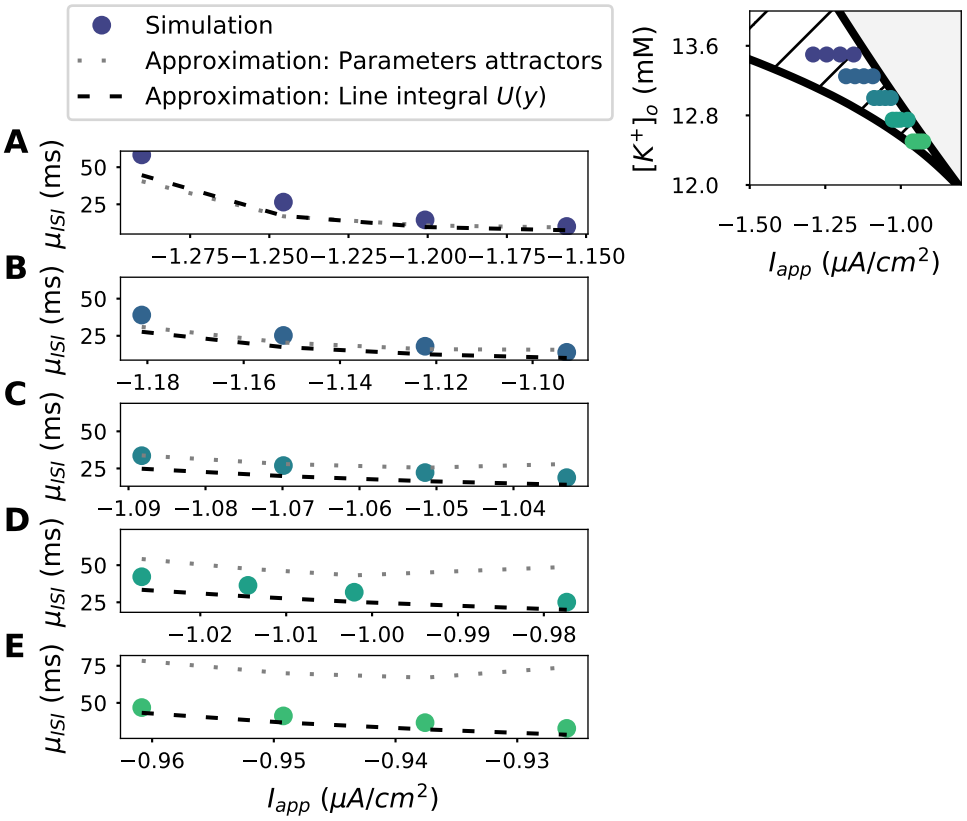

FIGURE 3.11: $\mu_{ISI}(t)$ approximation compared to simulations in the bistable region. **A-E** Comparison of μ_{ISI} from simulations and from equation 3.53 evaluated with the simplified parameters i.e the features of the attractors (τ_e and ω from equations 3.29 and 3.46) and the parameters coming from the numerical integration of the potential $U(y)$ with parameters obtained from $U(y)$ (τ_e from equation 3.26 and ω from equation 3.39). The parameters used for each simulations are represented in the bifurcation diagram on the top right. The intensity of the input noise was set to $\sigma = 0.5(\mu\text{A/cm}^2)$ in all simulations shown here. Each panel shows a different $[K^+]_o$ as follows: **A** $[K^+]_o = 13.5$, **B** $[K^+]_o = 13.25$, **C** $[K^+]_o = 13.0$, **D** $[K^+]_o = 12.75$, and **E** $[K^+]_o = 12.5$.

The uncentered moments of P_{ISI} are:

$$v_k = (-1)^k \frac{d^k}{ds^k} P_{ISI}(s)|_{s=0}. \tag{3.52}$$

The mean of the interspike interval distribution μ_{ISI} is the first moment $k = 1$, thus:

$$\mu_{ISI} = \tau_{lc} + \omega\tau_e \tag{3.53}$$

And, the variance is the second moment $k = 2$:

$$\sigma^2_{ISI} = \tau^2_{lc}(1 + D_{lc}\tau_{lc}) + 2\omega\tau_e(\tau_{lc} + \tau_e) \tag{3.54}$$

The spiketrain spectrum can also be calculated from $P_{ISI}(s)$ (Franklin and Bair, 1995; Schleimer, 2013):

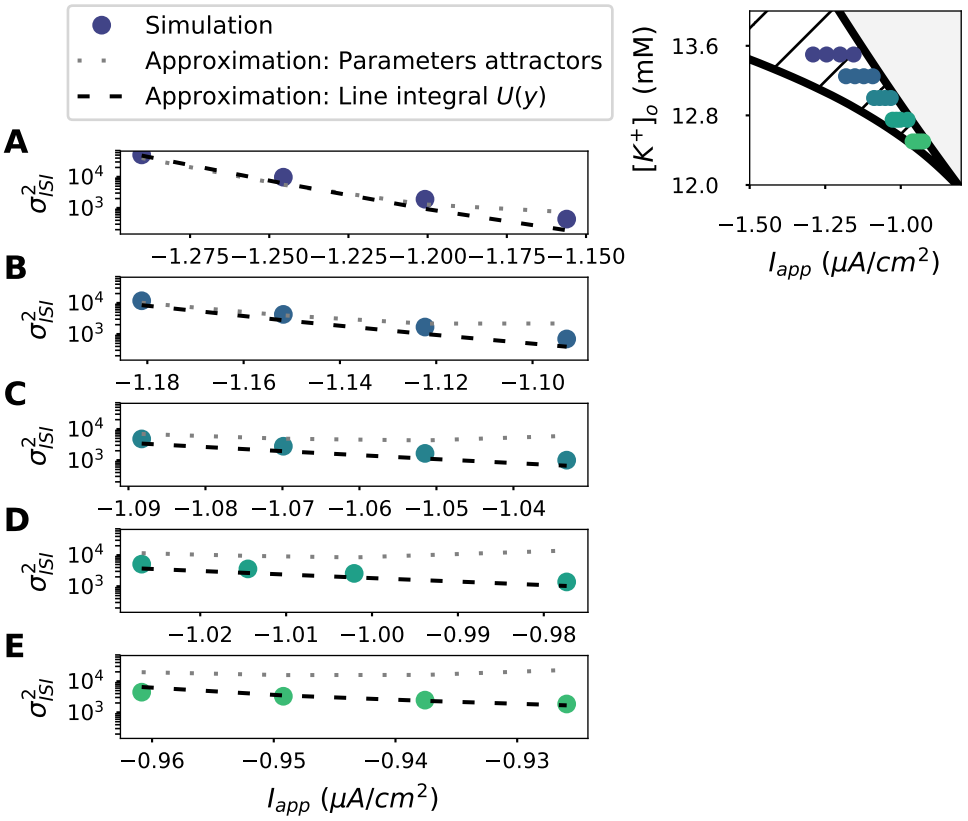

FIGURE 3.12: $\sigma^2_{ISI}(t)$ approximation compared to simulations in the bistable region. **A-E** Comparison of σ^2_{ISI} from simulations and from equation 3.54 evaluated with the simplified parameters i.e the features of the attractors (τ_e and ω from equations 3.29 and 3.46) and the parameters coming from the numerical integration of the potential $U(y)$ with parameters obtained from $U(y)$ (τ_e from equation 3.26 and ω from equation 3.39). The parameters used for each simulations are represented in the bifurcation diagram on the top right. The intensity of the input noise was set to $\sigma = 0.5(\mu\text{A/cm}^2)$ in all simulations shown here. Each panel shows a different $[K^+]_o$ as follows: **A** $[K^+]_o = 13.5$, **B** $[K^+]_o = 13.25$, **C** $[K^+]_o = 13.0$, **D** $[K^+]_o = 12.75$, and **E** $[K^+]_o = 12.5$.

$$P(f) = \frac{1}{\mu_{ISI}} \left(1 + \frac{P_{ISI}(s)}{1 - P_{ISI}(s)}\bigg|_{s \to if} + \frac{P_{ISI}(s)}{1 - P_{ISI}(s)}\bigg|_{s \to -if} \right) \tag{3.55}$$

In Figures 3.11 and 3.12 it can be observed that in general when the system is closer to the limit cycle onset biburcation, the higher is the mean and variance of the interspike interval (μ_{ISI} and σ_{ISI}). This is due to the fact that the distance between saddle and node d_{fp} is highest right at the limit cycle bifurcation. However, there are differences among different locations on the $[K^+]_o - I_{app}$ plane. Locations at high $[K^+]_o$, are characterized by more abrupt changes in μ_{ISI} and particularly in σ_{ISI}. Furthermore, the spiketrain spectrum also changes more abruptly at higher extracellular potassium concentrations; see Figures 3.13 and 3.21, notice that the power in the low frequencies is

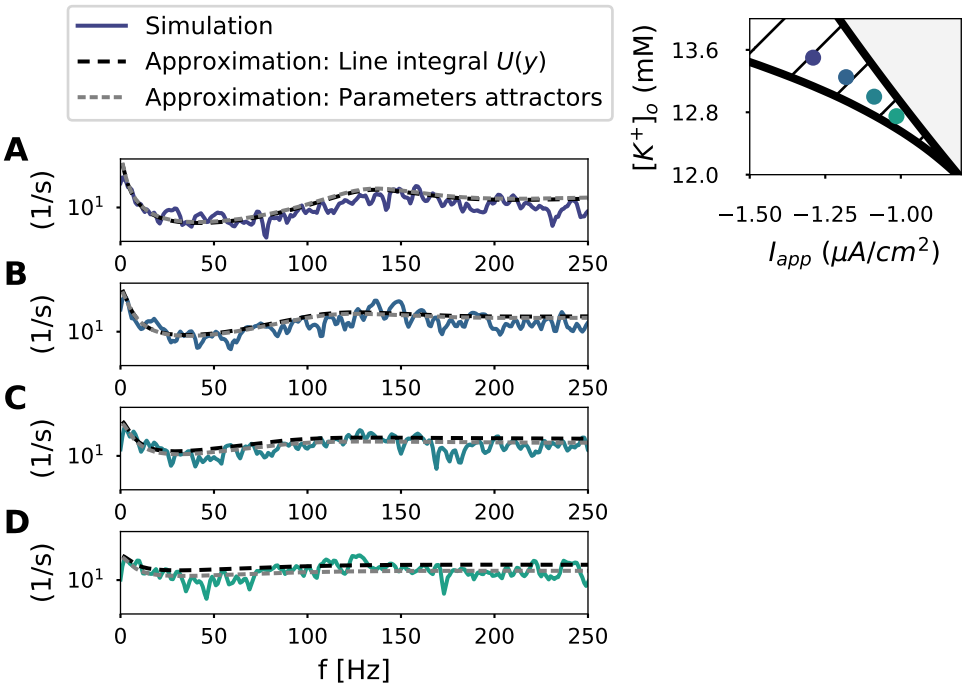

FIGURE 3.13: Spiketrain spectrum in the bistable region. **A-E** Comparison of Spiketrain spectrum from simulations and from equation 3.55 evaluated with the simplified parameters i.e the features of the attractors (τ_e and ω from equations 3.29 and 3.46) and the parameters coming from the numerical integration of the potential $U(y)$ with parameters obtained from $U(y)$ (τ_e from equation 3.26 and ω from equation 3.39). The parameters used for each simulations are represented in the bifurcation diagram on the top right. The intensity of the input noise was set to $\sigma = 0.5(\mu\text{A/cm}^2)$ in all simulations shown here. Each panel shows a different $[K^+]_o$ as follows: **A** $[K^+]_o = 13.5$, **B** $[K^+]_o = 13.25$, **C** $[K^+]_o = 13.0$, and **D** $[K^+]_o = 12.75$.

higher for higher extracellular potassium concentrations. The increased variance of spike production of single neurons and the distortion of the spiketrain spectrum might have very strong effects on the dynamics of a microcircuit of interacting neurons.

Accuracy of approximations

Notice that close to the limit cycle onset bifurcation (see Figure 3.11) **D,E**, the simplification calculated with the features of the attractors (τ_e and ω from equations 3.29 and 3.46) diverges from the simulations. This is partly because the escape rate τ_e, and the mixing factor ω are over estimated (see Figures 3.5 and 3.9, and explanation in sections 3.3.1.1 and 3.3.4), and partly because trajectories that cross the barrier but don't reach the local minimum (the fixed point) are assumed to be shorter in duration than they are.

Furthermore, when the saddle is very close to the limit cycle, the approximation for P_{lc} does not capture well the interspike interval, as discussed in section 3.3.1.2 (see Figure 3.7). The assumption to derive P_{lc} is that when a particle is perturbed in the basin of

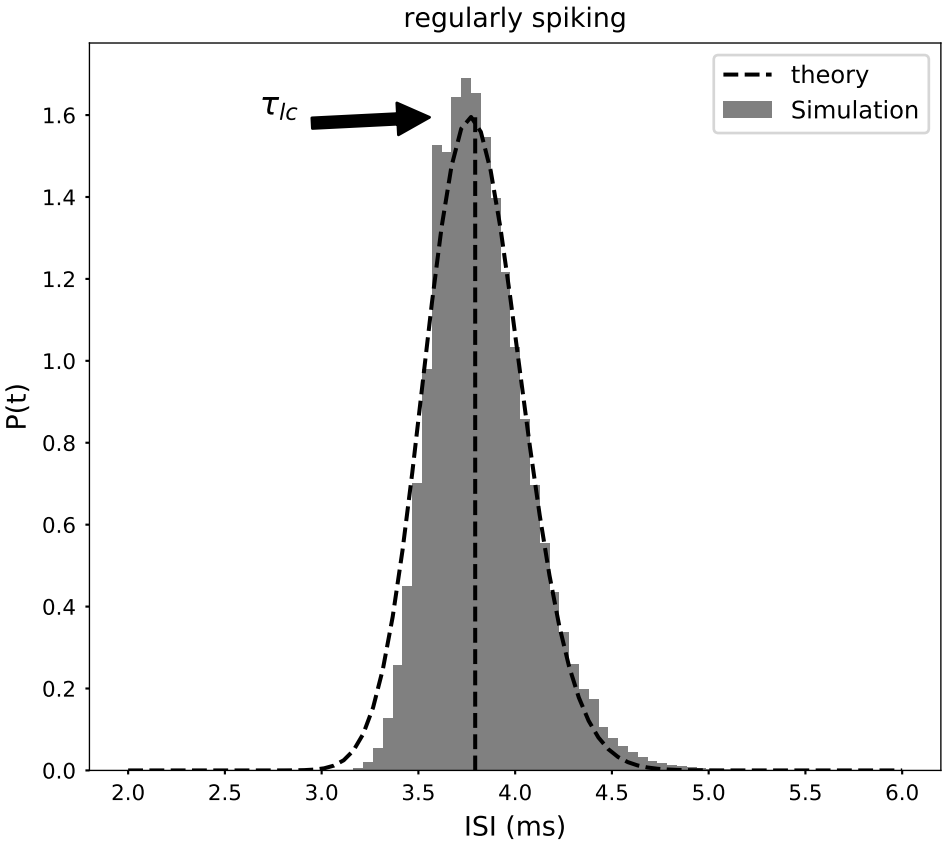

FIGURE 3.14: Spiking statistics in the regularspiking region, theory compared to simulations.

attraction of the limit cycle, it is radially attracted back to the orbit instantaneously. This assumption is very close to the actual dynamics when particles are radially attracted very rapidly to the limit cycle, however, when the saddle is very close to the limit cycle this is not the case.

3.4 Spiking statistics in the regularly spiking region

In the regularly spiking region the only attractor is a stable limit cycle. Thus, the ISI distribution produced when the system lies in this dynamical regime, is given by trajectories going around the limit cycle. In the previous section, an expression for the ISI (equation 3.4) in the bistable region was derived. This expression holds for the spiking region by fixing the probability of crossing the barrier towards the fixed point to $\omega = 0$, which yields:

$$P_{ISI}(t) = P_{lc}(t) \tag{3.56}$$

Where $P_{lc}(t)$ is the same distribution derived in section 3.3.1.2, equation 3.36. See Figure 3.14.

3.5 Spiking statistics in the subthreshold region

In the subthreshold region the only attractor is a stable node. However, in the presence of noise, spikes could be generated as well. If the stable node and the saddle are not far from each other (small d_{fp}), a particle could cross the saddle and go around the ghost of the limit cycle. However, because the limit cycle is not stable, trajectories would always return to the stable node.

Thus, the expression derived for the ISI in the bistable region (equation 3.4) holds by fixing $\omega = 1$, which yields:

$$P_{ISI}(t) = P_{fp}(t), \tag{3.57}$$

where P_{fp}, is the same as the one described in section 3.3.1.1 equation 3.30 for the bistable regime.

To calculate $P_{fp}(t)$, one needs a stable limit cycle to describe $P_{lc}(t)$. Given that there is no stable limit cycle in the subthreshold region, the one used to derive $P_{lc}(t)$ is the first stable limit cycle right at the SNIC bifurcation (which varies as a function of extracellular potassium concentration $[K^+]_o$).

3.6 Discussion

In this chapter it was shown how the analytical derivation for the ISI distribution depends on the dynamical system's features particular for the bistable dynamical regime (HOM), regularly spiking and subthreshold regimes. The ideas portrayed here hold true for different models, given that they undergo the same bifurcations.

Furthermore, predictions were made on how the spiking statistics could be distorted with extracellular potassium accumulation in an experimental setup, where the extracellular potassium and the input current are controlled. Given that extracellular potassium accumulation $[K^+]_o$ could make a neuron transition in between the regimes described in this chapter, it alters the neuronal spiking statistics as described here.

In this chapter an expression for the ISI probability distribution of the model proposed in chapter 2 was derived. Simplifications where made in order to have a compact expression with interpretable parameters. Altogether, the technique we proposed in (Schleimer et al., 2021) and applied in this chapter, serves as a model reduction that captures the essence of complex, biophysically more realistic conductance-based models, preserving accuracy.

The analytical ISI expression could be used to test hypothesis of homoclinic spiking experimentally. As was portrayed in Figure 3.2, ISI distributions in the bistable and the spiking region are very different. Thus, ISI distributions measured experimentally could be compared with the ones derived here, and the most probable regime where the

neuron was during the experiment could be determined. Importantly, it is possible to relate specific experimentally measurable parameters with the parameters used to derive the ISI expression, like the average firing rate of the neuron, the interspike interval variability, and the spiketrain spectrum.

Another potential application for the dimensionality reduction implemented in this chapter is the analysis of neuronal-microcircuit dynamics. The simplification proposed here, allows the analysis of the population dynamics of sparsely connected neurons exposed to extracellular potassium accumulation (or any parameter that could induce the co-dimension 2 bifurcation described in this chapter as well as in chapter 2). Simplifying multidimensional dynamics allows analytical descriptions and more efficient trackability of simulations.

3.7 Appendix

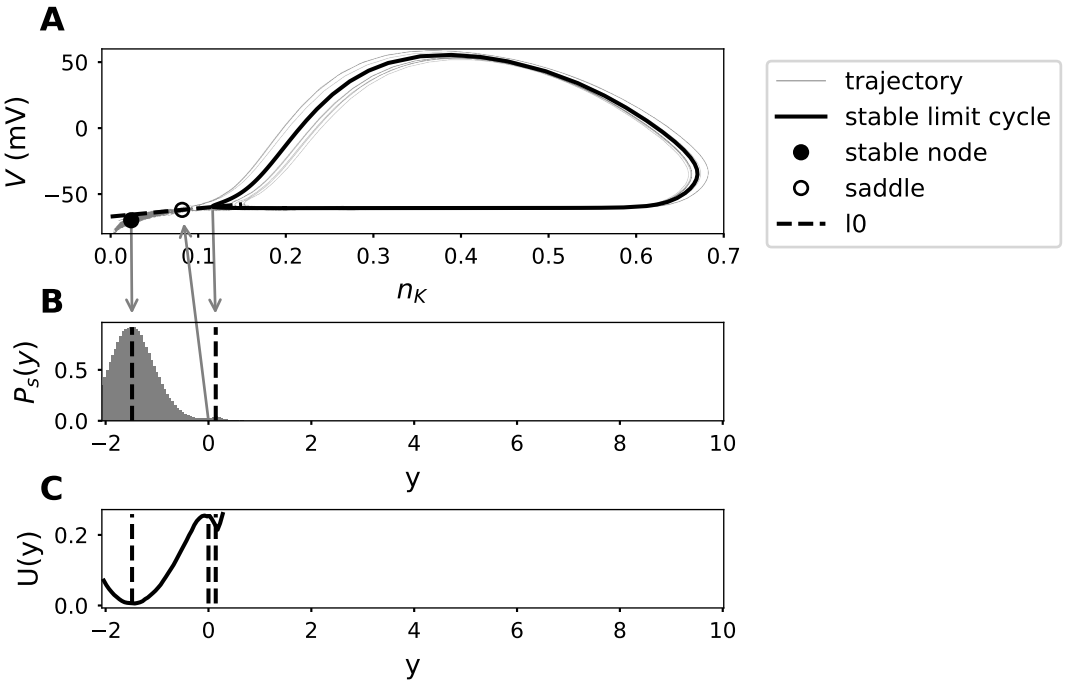

FIGURE 3.15: Double well potential with very low d_{lc}. **A**: Example trajectory together with the phase portrait containing the stable node (black dot), the saddle node (empty dot) and the stable limit cycle (Black orbit). Left eigenvector associated to the unstable manifold of the saddle node (l_0) is shown in a dashed line. **B**: Stationary distribution $P_s(y)$, calculated as the distribution of the trajectory shown in **A**, projected into l_0. The first peak of the distribution from left to right matches the position of the stable node (d_{fp}), the second peak matches the minimum distance between the limit cycle and the saddle node (d_{lc}). **C**: Double well potential ($U(y)$) of the dynamical system shown in the bottom panel, calculated as $U(y) = -\sigma^2 \log(P_s(y))$. Dashed lines coincide with the position of the fixed point, the saddle node and the minimum distance between the limit cycle and the saddle node.

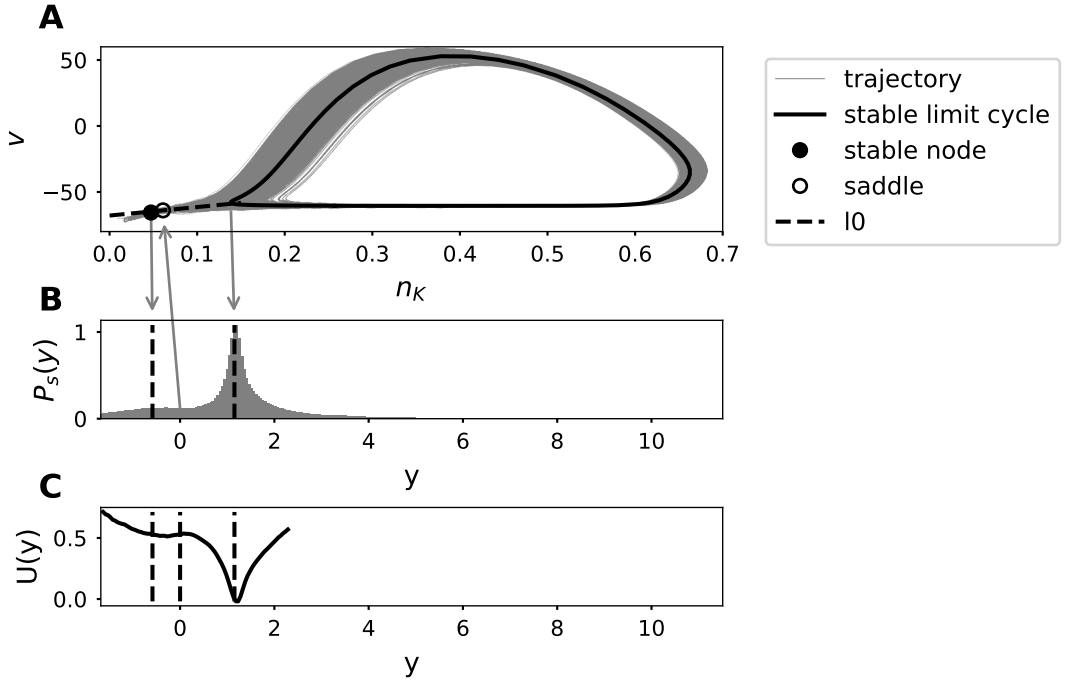

FIGURE 3.16: Double well potential with very low d_{fp}. **A**: Example trajectory together with the phase portrait containing the stable node (black dot), the saddle node (empty dot) and the stable limit cycle (Black orbit). Left eigenvector associated to the unstable manifold of the saddle node (l_0) is shown in a dashed line. **B**: Stationary distribution $P_s(y)$, calculated as the distribution of the trajectory shown in **A**, projected into l_0. The first peak of the distribution from left to right matches the position of the stable node (d_{fp}), the second peak matches the minimum distance between the limit cycle and the saddle node (d_{lc}). **C**: Double well potential ($U(y)$) of the dynamical system shown in the bottom panel, calculated as $U(y) = -\sigma^2 \log(P_s(y))$. Dashed lines coincide with the position of the fixed point, the saddle node and the minimum distance between the limit cycle and the saddle node.

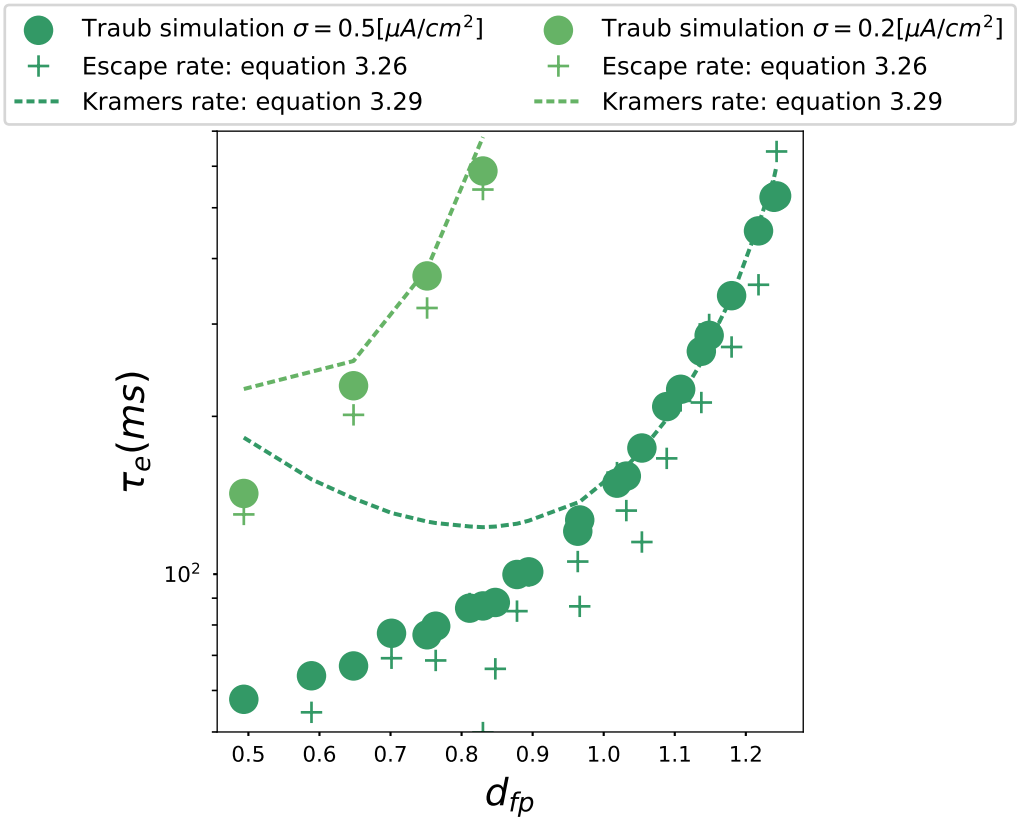

FIGURE 3.17: Average duration in the attraction domain of the stable node vs. distance between saddle and node projected in l_0 for different noise input intensities. Simulations are compared to the predictions described in equations 3.26 and 3.29. Simulations were performed with noise intensity $\sigma = 0.2$ and 0.5 $\mu A/cm^2$.

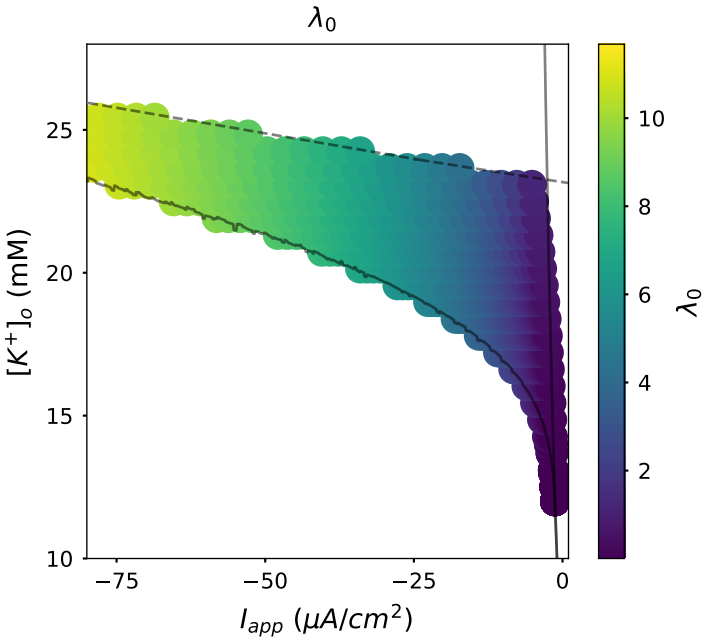

FIGURE 3.18: Magnitude of the eigenvalue associated with the unstable manifold of the saddle node lam_0

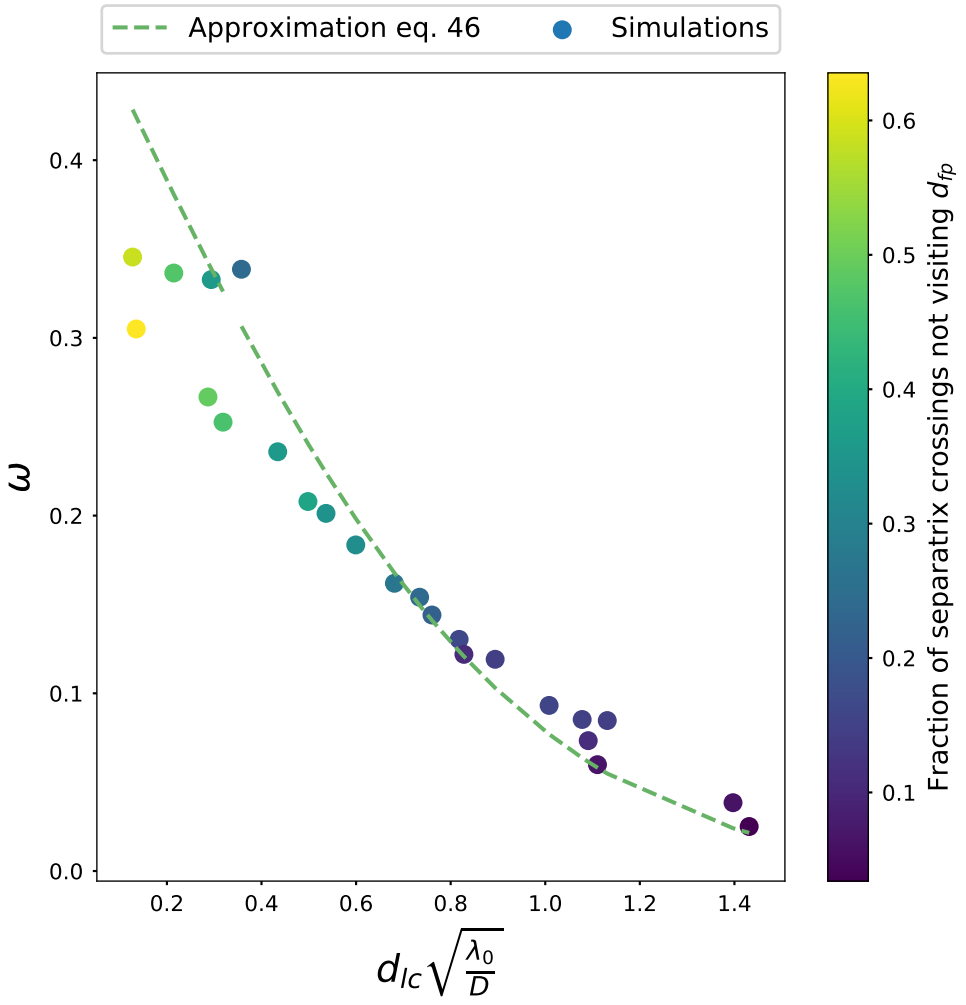

FIGURE 3.19: The simplified expression for the mixing factor w vs. simulations. The color of the simulations denotes the proportion of trajectories that did not visit the fixed point after crossing the separatrix (right after spike downstroke).

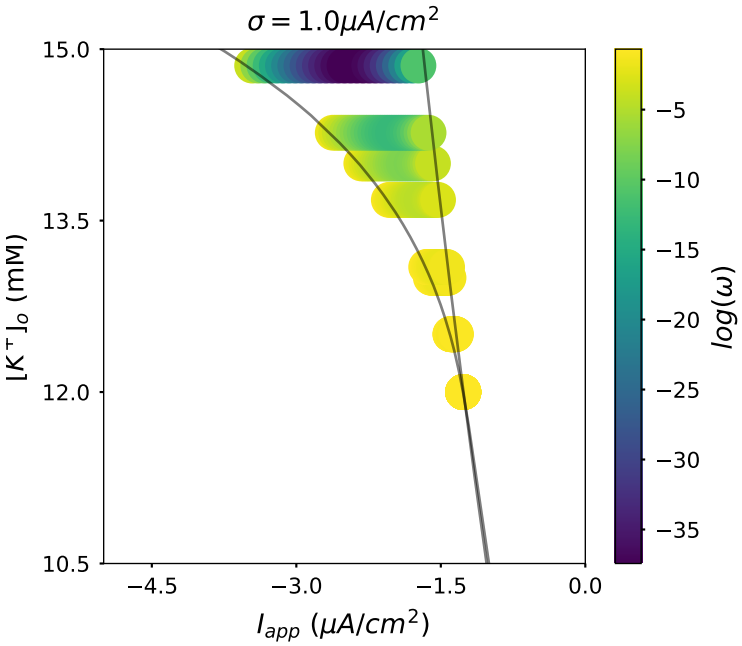

FIGURE 3.20: Log of Mixing factor in the bistable plane. Notice that the more negative the input current, close to the limit cycle onset bifurcation, the higher omega. Then it decreases half way between both bifurcations, and then it increases again towards the saddle node bifurcation.

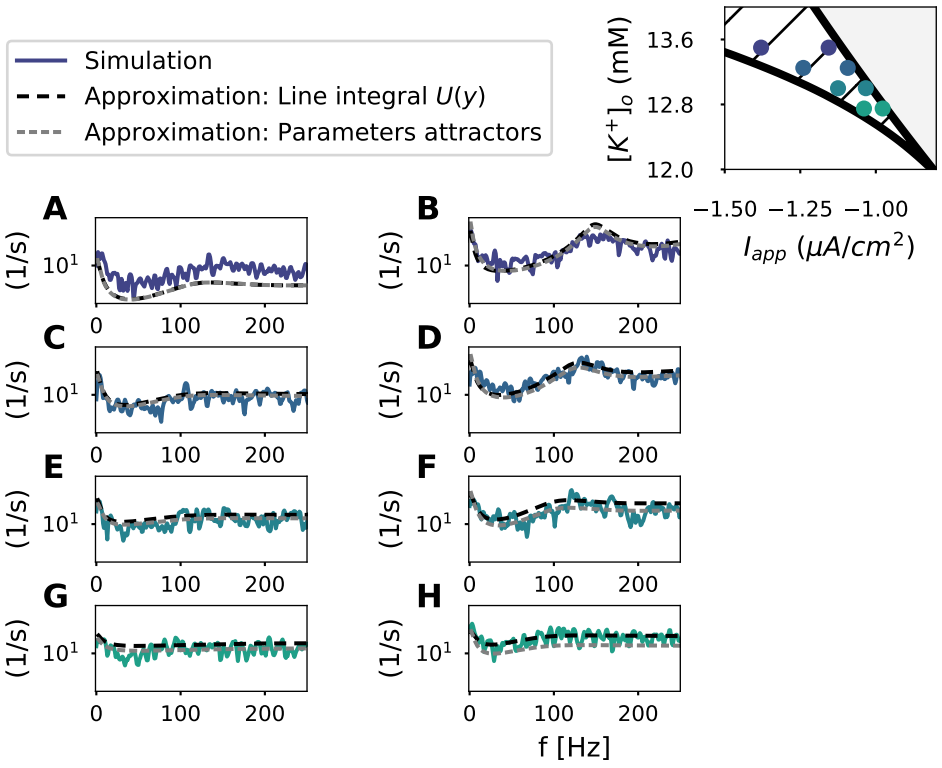

FIGURE 3.21: Spiketrain spectrum close to the bifurcation lines. **A-E** Comparison of Spiketrain spectrum from simulations and from equation 3.55 evaluated with the simplified parameters i.e the features of the attractors (τ_e and ω from equations 3.29 and 3.46) and the parameters coming from the numerical integration of the potential $U(y)$ with parameters obtained from $U(y)$ (τ_e from equation 3.26 and ω from equation 3.39). The parameters used for each simulations are represented in the bifurcation diagram on the top right. The intensity of the input noise was set to $\sigma = 0.5(\mu\text{A/cm}^2)$ in all simulations shown here. Each panel shows a different $[K^+]_o$ as follows: **A** $[K^+]_o = 13.5$, **B** $[K^+]_o = 13.25$, **C** $[K^+]_o = 13.0$, and **D** $[K^+]_o = 12.75$.

4 | Ion-dependent network dynamics

In the previous chapter an analytical approximation for the interspike interval distribution of a neuron model exposed to different extracellular potassium concentrations and irregular input was derived. The main assumption needed for the approximation was that the neuron model only received white noise.

The assumption of neurons receiving solely white noise is not fulfilled in an *in-vivo* setup, where the input has some degree of temporal correlations due to synaptic filtering (Brunel et al., 2001) and network activity (Pena et al., 2018). In particular, if one focuses on cortical networks, where neurons are recurrently connected, the input to an individual neuron will have frequency components related to the ones produced by the other neurons in the network (Pena et al., 2018; Dummer et al., 2014). In the previous chapter (chapter 3) it was evident that neurons in the bistable dynamical regime, display firing rates with high power in the low frequencies. Thus, it is not realistic to assume that the input produced by the network, and fed into its units will have a flat power spectrum. Consequently, the white noise approximation proposed in chapter 3 needs to be adapted.

In this section, a feasible semi-analytical approach to describe the response of conductance-based neuron models to colored (slow) noise is proposed. Furthermore, dynamics of sparsely and recurrently connected neurons that share the extracellular medium are described in a balanced network.

4.1 Introduction

In the brain's cortex, neurons are recurrently connected through synapses. Synaptic dynamics, together with the response properties of each neuron, give rise to collective circuit dynamics. Such collective dynamics have been measured extensively in the cortex of the brain. An interesting feature of cortical collective dynamics is that the intensity of fluctuations in specific frequency bands can be linked to behavioral states. For instance, slow-wave sleep is characterized by its strong low-frequency (1 Hz) fluctuations of cortical activity (Young et al., 1978). Other physiological process are associated with a decrease in the intensity of low-frequency fluctuations, like attentive states (Harris and Thiele, 2011).

It has been observed that slow dynamics can emerge from the interaction of multiple units whose individual time scales are orders of magnitude faster. Understanding how

such slow dynamics are generated could be the key to explain the mechanisms that induce deep sleep in the cortex, or how to speed up cortical dynamics to induce attentive states.

Slow time-scales have been reproduced in rate models of balanced networks by increasing the connectivity strength (Sompolinsky et al., 1988). Even though it has been challenging to reproduce those results in spiking neuronal networks (Engelken et al., 2016), it has been shown that if clusters of higher connection probability are activated, slow oscillations can emerge for finite cluster size (Litwin-Kumar and Doiron, 2012).

An alternative mechanism to generate slow dynamics in a spiking neuronal network is the regulation of the neuronal excitability. As shown in chapter 3, altering the excitability of single neurons through extracellular potassium ($[K^+]_o$) accumulation, can modify several features of the spiking statistics. For instance, the spectral composition of the neuronal spiking activity. Given that $[K^+]_o$ accumulation can alter the spectral composition of single cell spiking statistics, microcircuit dynamics can undergo similar transitions when its units are exposed to high $[K^+]_o$.

In line with the previous idea, Bellot et al., (Bellot-Saez et al., 2018) propose that by regulating the composition of the extracellular environment, astrocytes promote slow network dynamics. Specifically they hypothesize that astrocytes, by controlling the extracellular potassium concentration, can alter the time scale of cortical activity. Another interesting observation is that the extracellular potassium concentration is dynamic, and its fluctuations are locked to network dynamics. Amzica and colleagues (Amzica and Steriade, 2000) observed that extracellular potassium concentration oscillated locked to slow wave sleep cortical oscillations, with the highest concentration coinciding with the up-state of cortical activity. The up-state that corresponds to the surface-positive half-wave of the slow oscillation coincides with depolarized neuronal membrane potentials. Thus, it is thought of as a window of neuronal activity facilitation. Together, these studies provide evidence that favor the hypothesis of extracellular potassium concentration modulating cortical dynamics.

Mechanistically understanding the effect of this ionic concentration in the cortical dynamics is not straightforward. Extracellular potassium concentration sets the Nernst potential for potassium which is very close to the resting membrane potential of neurons. Thus, it has the potential to alter single neuron excitability, and consequently alter single neuron spiking statistics. However, given that slow synaptic activity can average out the effect of single cell spiking, it is not clear whether the concentration by itself can induce a change in the microcircuit dynamics.

In this chapter, I will attempt to explain the observations of Bellot et al. (Bellot-Saez et al., 2018) from a theoretical perspective. In the cortical model proposed here, slow dynamics emerge as a consequence of extracellular potassium accumulation. The power spectral density in the slow frequency bands (2-6Hz) is correlated with the extracellular potassium concentration. The theoretical prediction is consistent with the observations reported by Bellot and colleagues (Bellot-Saez et al., 2018), showing that impaired astrocytic extracellular potassium uptake could lead to higher power in the slow bands of the cortical local field potentials.

The work shown here proposes a technique that combines simulations and an analytical approach to study spiking networks of conductance based units exposed to different extracellular potassium concentrations. These findings fill a gap in the understanding of how specific parameters, like the extracellular potassium concentration, by altering the single neuron response can alter the network dynamics.

4.2 Results

The aim of this chapter is to understand how increases in the extracellular potassium concentration alter the microcircuit dynamics. In chapters 2, and 3 it was shown how extracellular potassium concentration modulates single neuron spiking statistics. High extracellular potassium concentrations in the extracellular space increase the spiking probability by making neurons more excitable. Extracellular potassium can also change the spike generating mechanism (refer to chapter 2). Although the effect of high extracellular potassium concentration on the spiking statistics is very drastic at the single cell level, it is not clear whether such change in the single-cell spiking statistics is enough to alter the network dynamics.

Here, I use a balanced network model to investigate the dynamical consequences of increased extracellular potassium concentration. Balanced networks are capable of reproducing the temporal irregularity of firing patterns, as well as the low firing rates elicited by cortical neurons, which makes them a convenient model to understand cortical network dynamics (Amit and Brunel, 1997; Van Vreeswijk and Sompolinsky, 1998). The network consists of N=4000 (or 2000) identical conductance based units (see section 4.4), 50% excitatory (E) and 50% inhibitory (I)[1]. Connections are nonspecific, e.g the probability of an inhibitory or an excitatory neuron of connecting to any other neuron is $p^{EI} = p^{II} = p^{IE} = p^{EE} = 5\%$ (10% when $N = 2000$), where $p^{i,j}$ denotes the probability of a neuron in population j to connect to a neuron in population i. Excitatory synapses have faster exponential decay than inhibitory ones, and the synpatic efficacy of inhibitory synapses is higher than the excitatory efficacy (see section 4.4).

When a constant identical input is injected to each unit, the network exhibits asynchronous spontaneous activity (consistent with the work by Brunel (Brunel, 2000) given that inhibition dominates excitation). The asynchronous state emerges and is sustained by the network. Every single unit fires irregularly, thus generates irregular excitatory/inhibitory postsynaptic inputs. The average input to a unit is below its threshold or limit cycle onset (when inhibition is stronger than excitation), thus spiking is fluctuation-driven (spikes occur due to an input intensity slightly above threshold during brief periods).

[1] Although most balanced network models use the default state of 80% excitatory and 20% inhibitory cells, there is no concrete evidence showing that these proportions are a general property of cortical circuits. In fact there is evidence suggesting that these quantities might vary throughout the cortex and across species (Mitra, 1955). Although the 50% -50% case is not the most likely case, here it is used as an arbitrary value because the results presented here are not dependent on the choice of this proportion.

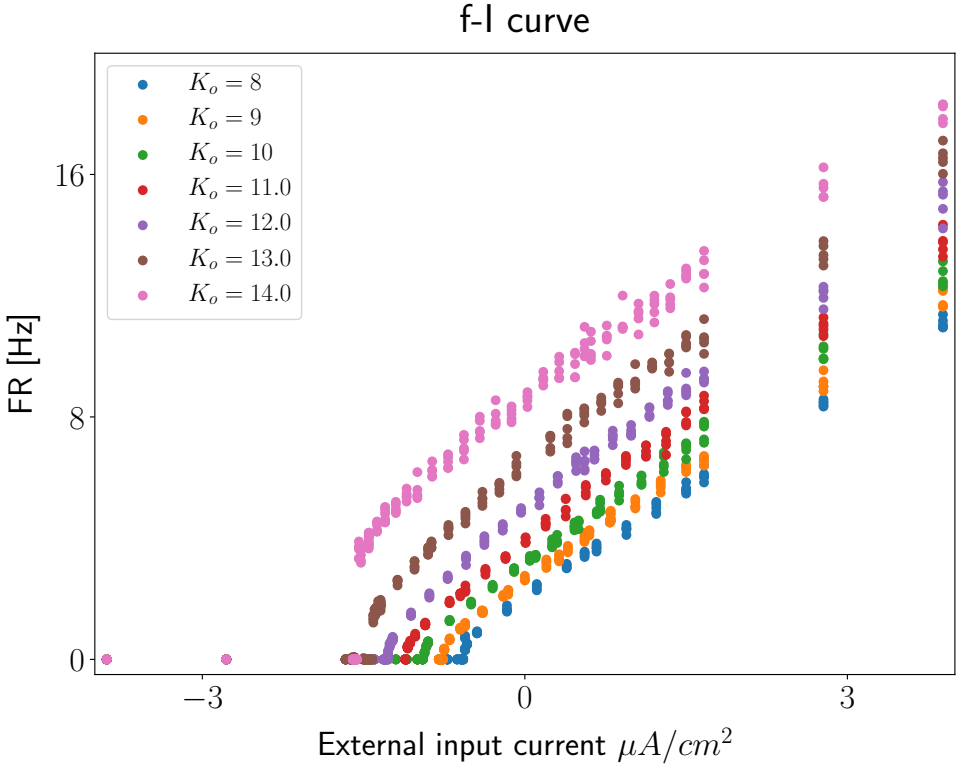

FIGURE 4.1: Extracellular potassium modulates the f-I curve of the network. Mean population firing rate (A) as a function of input current for different extracellular potassium concentrations. The threshold of the f-I curve is shifted with extracellular potassium concentration. Each realization is a simulation with $N = 2000$, and a random connectivity with in degree (K) =10%.

The mean firing rate of the network increases the higher the extracellular potassium concentration. Given a fixed external input current to the neurons in the network, increasing the extracellular potassium concentration increases the firing rate of the network. In Figure 4.1, the mean firing rate of the network is plotted against the network input current (f-I curve) for different extracellular potassium concentrations. Notice that networks with higher extracellular potassium concentrations need less external depolarization to generate spikes. This shift in the network f-I curve comes about from the single neuron increased excitability elicited by higher extracellular potassium concentrations (refer to chapters 2 and 3).

As shown in chapter 2, besides increasing single unit excitability, extracellular potassium can change the spike generating mechanism shifting it from the saddle-node-on-invariant-cycle (SNIC) to the homoclinic orbit (HOM). When the neuron model receives a current slightly above the spike generating current threshold (similar to the one received by a neuron in a balanced network during spike generation), its dynamics are remarkably different in both spike generating bifurcations (refer to Figure 4.2). When a neuron has a HOM spike generating bifurcation (high extracellular potassium concentrations), it displays bi-stability when it receives a current slightly above threshold. The bi-stability consists of a stable fixed point coexisting with a stable limit cycle orbit. When a neuron

has a SNIC spike generating bifurcation (lower extracellular potassium concentrations), only the limit cycle orbit attractor is present when it receives current above threshold. The critical value where the transition between SNIC and HOM occur is denoted with a black dot in the top panel of Figure 4.2, and is known as the SNL codimension two bifurcation, refer to chapter 2, chapter 3 and (Hesse et al., 2017).

In order to fully understand the network dynamics, another important feature that needs to be characterized is the spike timing variability. The dependence of spiking variability on the extracellular potassium concentration was characterized in detail for single neurons receiving white noise in chapter 3 and is summarized here. The bi-stability induced by extracellular potassium concentration ($[K_o]^+$), has a strong effect on spiking variability. In the bottom panels of Figure 4.2, it is evident that spiking variability of single neurons is higher in the bi-stable region when white noise is injected. At the network level, it is not straightforward to draw the same conclusion. The input that a single neuron receives in a recurrently connected network is not uncorrelated in time (the input is not white), it has frequency components related to the ones generated by each unit (Pena et al., 2018; Dummer et al., 2014). Thus, to understand the effect of extracellular potassium concentration on the network activity, further analysis is needed.

To investigate the consequences of extracellular potassium concentration on the network dynamics, the first approach is to simulate different networks exposed to different extracellular potassium concentrations. The parameter representing the extracellular potassium concentration surrounding each unit is identical across all the units of the network (see methods 4.4). This implies the assumption of a well stirred bath, in other words, every single unit in the network is exposed to an identical extracellular environment. The validity of this assumption will be discussed further in section 4.3.

A comparison of the network dynamics exposed to extracellular potassium concentration below and above the critical value (SNL) are shown in Figure 4.3. The external input (I_{app}) is adjusted so that the mean population rate is ~ 10 spikes per second or Hz (see section 4.4.3). Notice that both networks exhibit irregular asynchronous firing, with a similar average firing rate (Figure 4.3, first and second panels). The main difference between both, is that for the network with $[K_o]^+$ above the bifurcation (right column in Figure 4.3, third and fourth panel), slow dynamics in the membrane potential are more prominent than in the network with extracellular potassium below the bifurcation (left column in Figure 4.3, third and fourth panel). These slow dynamics emerge from the transitions between high-frequency spiking intervals and relatively long periods of silence. The intermittent activity, consequently generates intermittent post synaptic potentials at a frequency set by the rate of the silent-to-active transition.

4.2.1 Spiking statistics as a function of extracellular potassium concentration

To characterize the effect of $[K_o]^+$ concentration on the network dynamics, the spiking statistics of networks exposed to different $[K_o]^+$ are compared (same networks shown in

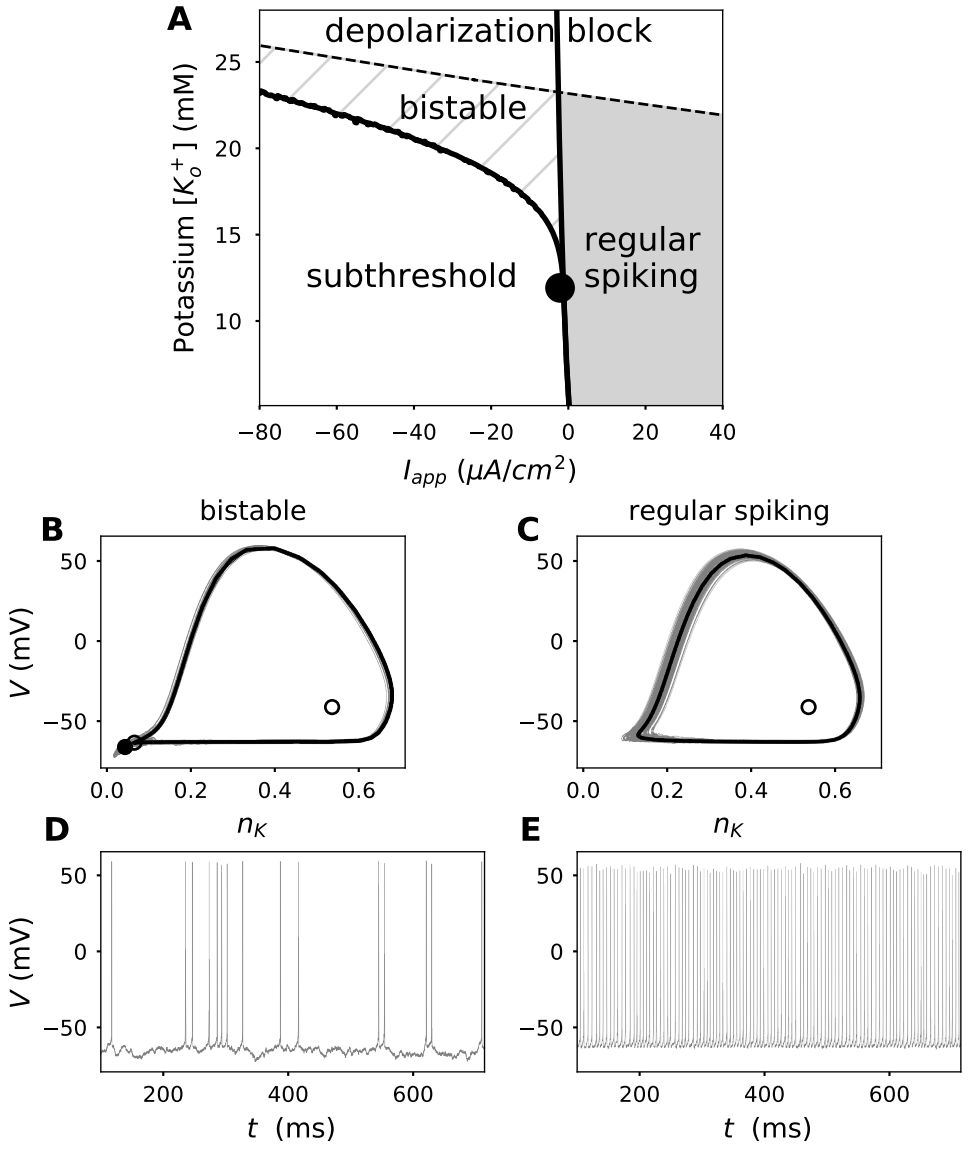

FIGURE 4.2: Extracellular potassium has the potential to alter the spike generating mechanism of single neurons. **A**: Extracellular potassium vs. input current bifurcation diagram, the different dynamical regimes are denoted with the different backgrounds. **B,C**: Single neuron response to white noise (grey trajectories), and the attractors of the system given the same input current without noise (black). The black dot represents the stable node, the empty dot represents a saddle node, and the black orbit represents a stable limit cycle orbit.**B** Shows an example trajectory in the bistable regime. **C** Shows an example trajectory in the regular spiking regime. **D,F**: Same trajectories plotted in **B,C**, but shown against time.

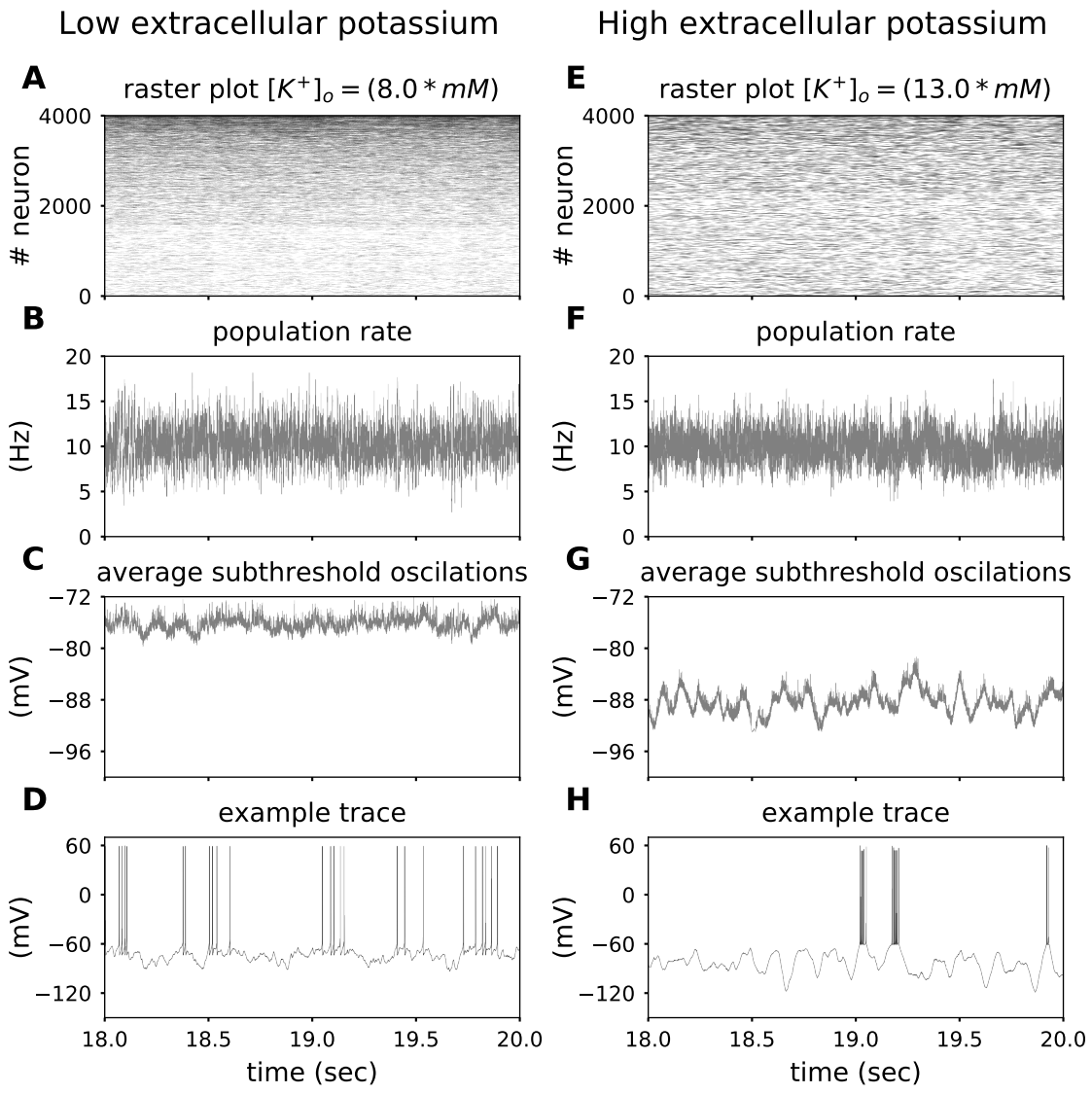

FIGURE 4.3: Contrast between the dynamics of a network with extracellular potassium below the critical (codimension two bifurcation) concentration vs extracellular potassium concentration above the critical (codimension two bifurcation) concentration. Left column (**A, B, C, D**) neurons with $[K_o]^+ = 8$ mM, concentration below the critical single cell phase transition (SNL bifurcation). Right column (**E, F, G, H**) neurons with $[K_o]^+ = 13$ mM, concentration above the SNL bifurcation. **A,E**: Raster plots of 4000 sparsely connected neurons (5% probability of connection) sorted by total number of spikes fired during the first 3000 milliseconds of simulation. **B,F**: Population activity as calculated in equation 4.22. Notice that in both networks the mean population activity is $\sim$ 10 spks/sec, this is set by adjusting the external constant input to the network (for $[K^+]_o = 8$ mM, external input is set to $I_{app} = 3.45\ \mu A$. For $[K^+]_o = 13$ mM, external input is set to $I_{app} = 0.92\ \mu A$). **C,G**: Average membrane potential across the population. **D,F**: Example of a single unit voltage trace. For both traces the steady state is shown (second 18 to 20 of the whole 20 seconds long simulation)

Figure 4.3). Firing rate distributions across all units in the network are very similar for both networks (with mean $\sim$ 10 spks/sec) see methods section 4.4.3. For the network with an extracellular potassium concentration of $[K_o]^+ = 8$ mM, the mean firing rate is 10.21Hz, and the standard deviation 11.57Hz, for the one with $[K_o]^+ = 13$ mM the mean is 9.9Hz and the standard deviation 8.71Hz (see Figure 4.4**A**). Notice that both networks have firing rate distributions with low mean and a broad distribution.

Spiking variability increases with extracellular potassium concentration. Compare the voltage traces displayed in the bottom panels of Figure 4.3, notice that the example trace corresponding to the network with $[K_o]^+$ below the critical (single unit bifurcation) value ($[K_o]^+ = 8$ mM) exhibits a more uniform distribution of interspike intervals (ISIs) than the one with the higher extracellular potassium. In the latter one, long silent periods combined with bursts of high frequency spiking, give rise to very broad ranges for the ISI distribution. The transitions between high frequency spiking and silent periods, give rise to large spiking variability. Spiking variability is quantified with the inter-spike interval coefficient of variation (CV). In Figure 4.4**B** a distribution of the CV across the networks is portrayed, the $[K_o]^+ = 13$ mM networks have a higher mean and a broader distribution of CVs than the $[K_o]^+ = 8$ mM networks. Spiking varibility is also quantified with the average Fano factor for networks with different extracellular potassium concentrations (shown in the appendix Figure S.4.17), notice that the increase in spiking variability produced by the increased extracellular potassium concentration is consistent for different window lengths.

Variability within the units in the network was quantified with the (pearson) correlation of the spike count over windows of 50 ms across neuron pairs (Figure 4.4**C**). Both networks have distributions of correlation coefficients around 0, similar to the ones measured in the brain cortex (Renart et al., 2010; Greenberg et al., 2008; Renart et al., 2010).

In Figure 4.4**D**, the normalized auto-correlation of the population activity is shown. The network with higher extracellular potassium concentration, has a longer timescale of decay. This suggests the emergence of a slower process induced by high extracellular potassium concentrations.

4.2.2 The power of the population activity in low frequency bands increases with the extracellular potassium concentration

In this section, the power of the population activity in the low frequency bands is characterized for different extracellular potassium concentrations ($[K_o]^+$). The power spectral density of the population activity strongly depends on the mean firing rate of the network. In order to compare networks with different extracellular potassium concentrations (due to the effect this ion has on the neuron's excitability), the external input to the units is adjusted as mentioned above.

The power in the low frequency bands (2-6Hz) increases with extracellular potassium

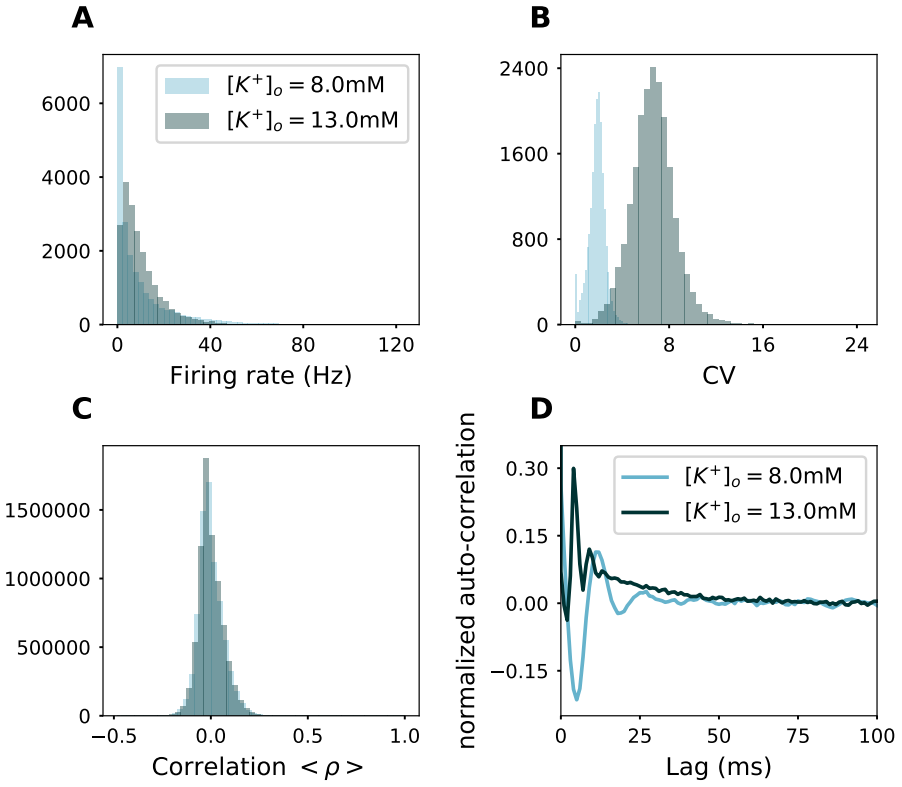

FIGURE 4.4: Elevation in extracellular potassium concentration increase spiking variability. Spiking statistics comparison for the networks exposed to 8 and 13 mM extracellular potassium $[K_o]^+$, the external applied current is adjusted so that the average population rate is $\sim$ 10Hz; $I_{app,10spks/sec} = 3.45\ \mu A$ and $I_{app,10spks/sec} = 0.92\ \mu A$ respectively, refer to methods 4.4.3. Statistics were obtained from 5 realizations of 20 seconds simulations after reaching the steady state. The networks where N=4000, 50% excitatory and 50% inhibitory units with identical intrinsic parameters and different synaptic kernels as described in the section 4.4, the average in-degree for all the units in the population is 200 (with random connectivity). **A** Histogram of individual unit's firing rate across the network. **B** Histogram of coefficient of variation of inter-spike intervals (CV) for every unit in the network. **C** Histogram of Pearson correlation coefficients of spiking in windows of 50 ms calculated over all the combinations of pairs in the network. **D** Normalized autocorrelation of population activity (as described in section 4.4), averaged over the 5 realizations.

concentration. The power spectral density of the population activity for networks exposed to different extracellular potassium concentrations is shown in Figure 4.5. Notice that the population activity of the network exposed to $[K_o]^+ = 8$ mM, has a relatively high power in the high frequency band 50-100Hz, but a relatively low power on the slow frequency band 2-6Hz. In contrast the network exposed to $[K_o]^+ = 13$ mM, has a relatively high power in the low frequency band. The ratio of the power in the slow frequency band and the high frequency band is independent of the network size N (refer to appendix Figure S.4.18). In Figure 4.6, the power at the peak of the power spectral density in the low frequency range (2-6Hz) for different $[K_o]^+$, is shown. The higher

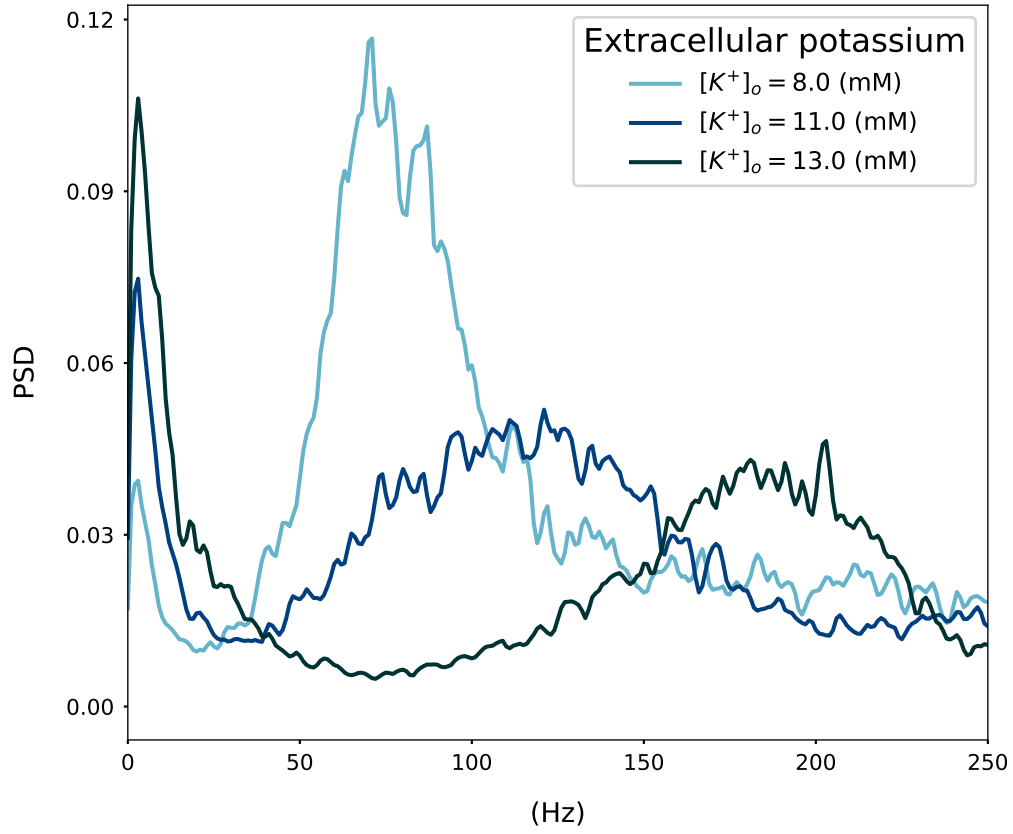

FIGURE 4.5: Population activity - Power spectrum for different values of Ko, mean in-degree=200 and N=4000. Power spectral density of population activity, averaged over 5 realizations of random networks with identical connectivity statistics. Population activity for all the networks $\sim$ 10Hz.

extracellular potassium concentration, the higher the power on the low frequency bands (2-6Hz). The relatively high power in the low frequency band is also observed at the single cell level (Figure 3.13), and, in fact, the magnitude of the effect correlates with extracellular potassium concentration. However, in this case, the single cell effect is enhanced by the recurrent interactions in the network. The model response is in line with experimental observations describing how impaired astrocytic potassium uptake, causes a higher power on the low frequency bands reported by (Bellot-Saez et al., 2018). Because impaired astrocytic potassium uptake leads to increased extracellular potassium concentration $[K_o]^+$, the power in the slow bands intensifies. It is worth highlighting that the slow oscillations displayed by the model, remain for a broad range of in-degrees K (refer to the appendix section 4.5.0.2, Figure S.4.19). It is worth highlighting, however, that the slow oscillations displayed by the model depend on a finite in-degree. Thus, the explanation proposed here is not valid in the thermodynamic limit.

The power increase in the low frequency bands is a consequence of the change in the single unit spiking statistics induced by extracellular potassium concentration changes.

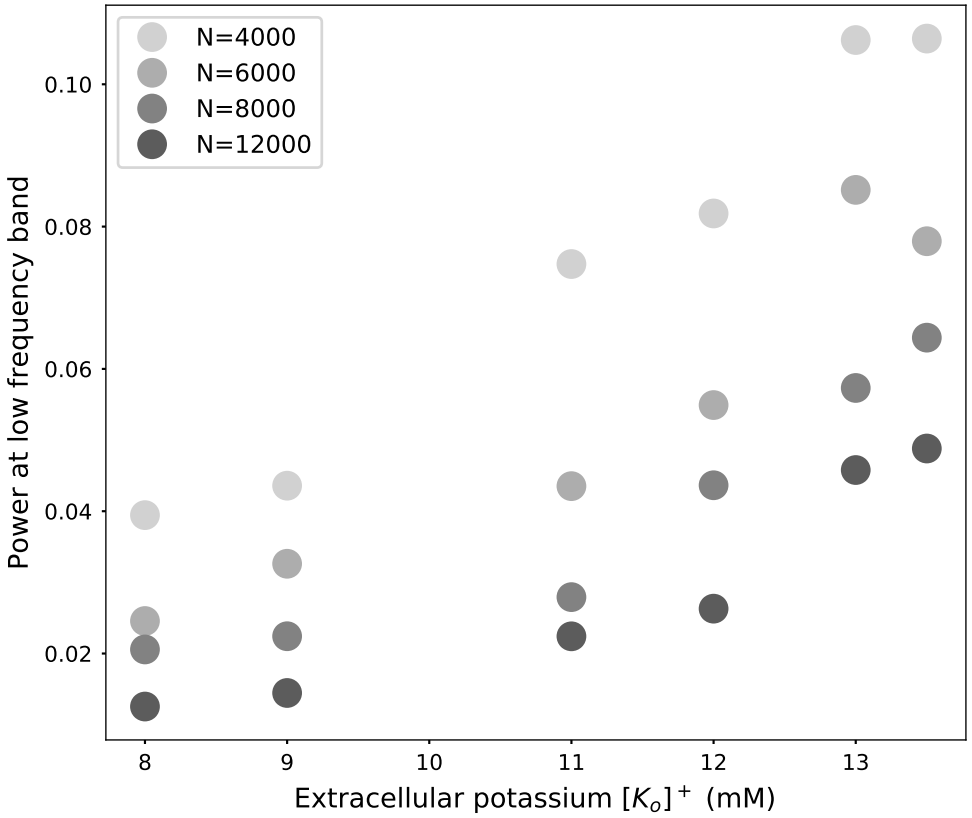

FIGURE 4.6: Relative power in the slow frequency bands (2-6 Hz) increases with extracellular potassium concentration. Population activity - Power spectrum for different values of Ko, mean in-degree=200 and N=4000, 6000 and 8000. Population activity for all the networks $\sim$ 10Hz.

The only effect of the parameter representing the extracellular potassium concentration in the model shown here, is on the single cell spiking dynamics. As was shown in chapter 3, the attractors of the single cell dynamics, are altered with extracellular potassium concentration changes, and this is reflected on the spiking statistics.

In the following section, the single unit spiking statistics will be related to the extracellular potassium concentration $[K_o]^+$ through the dependence of the attractors of the dynamical system on this parameter. Furthermore, dimensionality reduction of single unit dynamics, allows a simple interpretation of the whole network activity, specifically the emergence of slow dynamics.

4.2.3 Analysis

In this section a method that combines simulations and analysis is used to predict features of the dynamics from networks that contain conductance-based units. Specifically, the impact on the network collective dynamics caused by the alteration of the single unit

dynamics due to changes in parameters (here $[K_o]^+$) will be mechanistically explained. Firstly, the single neuron response to irregular input is approximated based on features from the phase plane. Secondly, a collective mean field representation of the network dynamics is obtained. And finally the features like the power spectral density of the population activity are related to the single neuron dynamics.

The single neuron response to irregular input can be approximated based on features from the phase plane of the dynamical system given a constant input that equals the mean of the irregular input. The phase portrait of the dynamical system contains information related to the spike generation dynamics. Knowing the phase portrait of the dynamical system makes it possible to predict which trajectories are more likely to generate a spike given their distance to a limit cycle attractor, for instance. Those distances can be calculated from projections of the multi-dimensional dynamics into lower dimensional representations. The projections are constructed from features of the phase plane morphology, for example, one useful projection is the closest path between a stable node attractor (stable silent state), and a stable limit cycle attractor (regular spiking state).

In chapter 3, it was shown that the single neuron response to white noisy input can be approximated when the phase plane of the dynamical system is known. In the sparsely connected network that is being analyzed here, each neuron receives colored noisy input that results from the activity of the other neurons. Thus, the description obtained in chapter 3 for white noise is not valid. In this chapter, the analysis made in chapter 3 is adapted to colored input noise.

4.2.3.1 Input to neuron i in the network

The total input that neuron i in the network receives is the sum of the external input I_{app} and the synaptic input $I_{syn_i}(t)$. I_{app} is constant throughout the simulation, but $I_{syn_i}(t)$ fluctuates due to the irregularity of the spike trains of presynaptic neurons projecting to neuron i. In order to understand the response of neuron i, it is convenient to first describe the features of the input it receives.

The total input received by neuron i is shown in Figure 4.7**A**, notice that it does not have a flat power spectral density (Figure 4.7**B**), thus, the white noise assumption made in chapter. 3 to derive the output is not valid. However, the power in the very low frequency bands ($< 6Hz$) is much larger than the one in high frequency bands. Therefore, it is possible to make a slow/fast time scale separation. The input to neuron i (I) can be approximated to a very slow signal $I_i(t)$, plus Gaussian white noise ($\sigma\eta(t)$).

$$I(t) = I_i(t) + \sigma\eta(t). \tag{4.1}$$

Where the averaged autocorrelation function of $\eta(t)$ yields a delta function,

$$\langle \eta(t)\eta(t') \rangle = \delta(t - t'). \tag{4.2}$$

And $I_i(t)$ changes very slowly compared to $\eta(t)$.

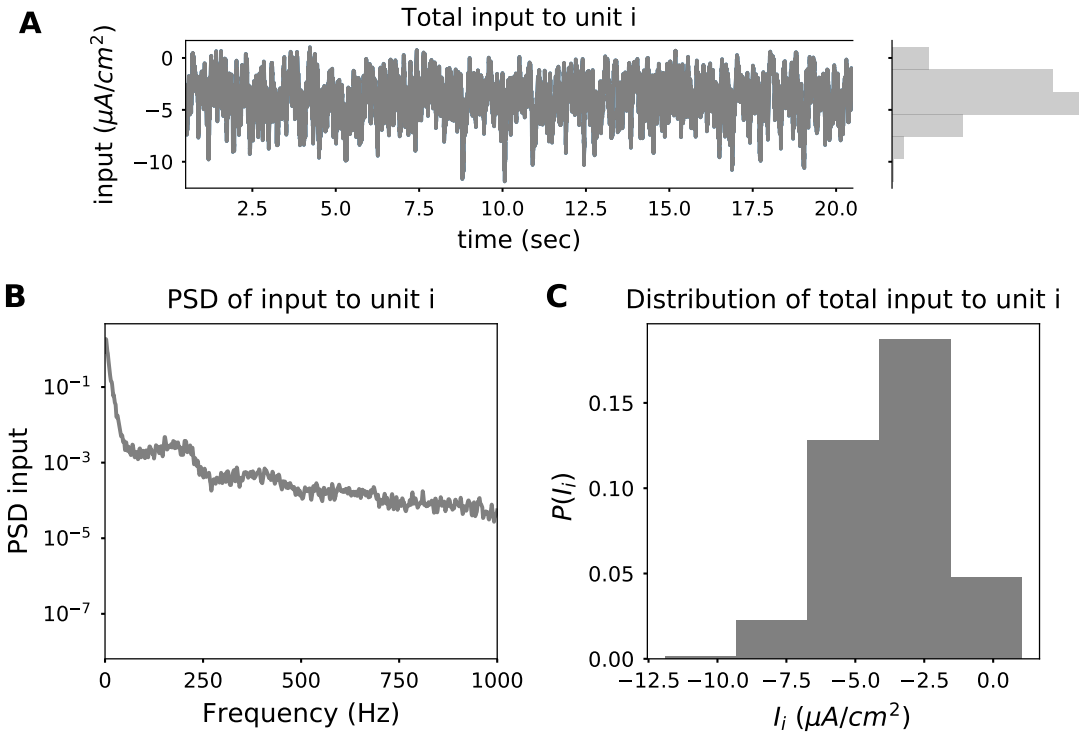

FIGURE 4.7: The input that neuron i receives can be split into a slow component and fast components. **A**: Total input to neuron i, where total input is the sum of the external input I_{app} and the synaptic input I_{syn_i} to neuron i. **B**: Power spectral density of the signal total input (signal shown in **A**). **C**: Distribution of the total input to neuron i. (same histogram as the one shown in the right of the **A**.

An approximation of the response of neuron i to the input $I(t)$ (equation 4.1), is calculated by assuming that the response of neuron i to the input $I(t_i)$ is independent of the response of neuron i to the input $I(t_{i+1})$. Where t_i and t_{i+1} represent points in time that are sufficiently far apart, such that $\Delta t = t_{i+1} - t_i$ is larger than the time scale needed for the fast spike generating dynamics to converge. Given that $I_i(t)$ changes very slowly relative to the time in which the fast spike generating dynamics reach an equilibrium, the response of neuron i to the input $I(t_i)$ is independent of the response of neuron i to the input $I(t_{i+1})$ after the fast dynamics reached the steady state. Thus, it is possible to remove the time dependence of I_i by replacing it with its average between t_i and t_{i+1}. In the next section the response of neuron i will be predicted in this interval.

4.2.3.2 Response of a unit to a mean input I_i

The response of a unit i is represented with a variable (y) denoting a position relative to the attractors of the dynamical system. $y(t)$ represents a trajectory lying in a lower dimensional space than the spike generating dynamics of neuron i. The dimensionality reduction is convenient because it links the information gathered from the phase portraits, into features of the spiking statistics.

More specifically, y is the projection of the dynamics of each unit, $x(t)$ (4 dimensional space; membrane potential, potassium activation channel and the sodium activation and

inactivation channels), onto a vector l_0. This vector is to be chosen such, that it separates trajectories in the basin of attraction of the stable node from the ones in the basin of attraction of the limit cycle. The purpose is to clearly classify trajectories lying in each of the attractor's basins.

For the particular dynamical system that is studied here (with a HOM bifurcation), it is convenient to choose l_0 as the left eigenvector of the unstable manifold of the saddle node (see methods 4.4.4). Refer to Figure 4.8**B** for a graphical description, where the 4 dimensional trajectories are portrayed in a 2D plane for clarity. The basin of attraction of the stable node is bounded by the separatrix which is non-local, however, most trajectories cross it through the saddle node. The tangent space to the separatrix at the saddle is given by the left eigenvector of its unstable manifold (l_0), thus most trajectories are aligned to it.

Given that the separatrix is located at the saddle node, it is helpful to set the reference for the trajectory right there:

$$y(t) = l_0 \cdot (x(t) - x_s), \tag{4.3}$$

where $x(t)$, represents the trajectory in the 4 dimensional space

$$x(t) = [V(t), m_{Na}(t), h_{Na}(t), n_K(t)], \tag{4.4}$$

and x_s denotes the position of the saddle in the 4 dimensional space,

$$x_s = [V_s, m_{Na_s}, h_{Na_s}, n_{K_s}]. \tag{4.5}$$

Notice, from Figures 4.8**B, C** that $y(t) < 0$ corresponds to trajectories in the basin of attraction of the stable node, and $y(t) > 0$, trajectories in the basin of attraction of the limit cycle. Consequently, the projection results are informative regarding silent vs. spiking periods.

The steady state distribution of y given an input that consists of white noise $\eta(t)$ plus a static input I_i,

$$P_s(y|I = I_i + \sigma\eta(t)), \tag{4.6}$$

is shaped by the phase portrait of the system when $\sigma = 0$. Refer to Figure 4.8**B, C**, notice that the peaks of the distribution $P_s(y|I = I_i + \sigma\eta(t))$, are located on the stable node (d_{fp}) and the limit cycle (d_{lc}) position.

$$d_{fp} = l_0 \cdot (x_n - x_s) \tag{4.7}$$

$$d_{lc} = argmin_{x\in\Gamma}\{l_0 \cdot (x - x_s)\}, \tag{4.8}$$

where x_n is the position of the stable node, and Γ denotes the stable limit cycle, both in the 4 dimensional space.

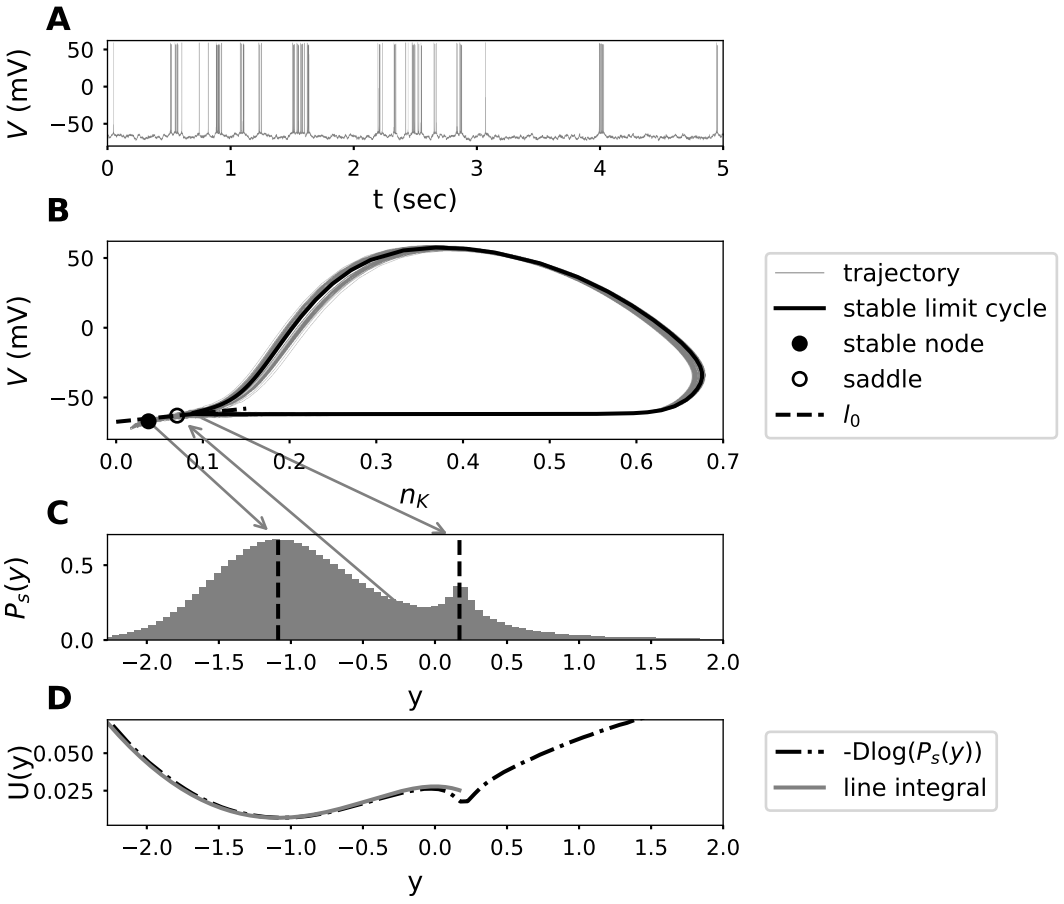

FIGURE 4.8: Example trajectory of a unit when receiving an input $I_i + \sigma\eta(t)$. **A** Time evolution of the membrane potential of the unit in response to the input $I_i + \sigma\eta(t)$. **B** Trajectory in response of white noisy stimuli projected into the membrane potential vs. potassium activation channel plane (grey) on top of the phase portrait (stable state when $\sigma\eta(t) = 0$) containing the stable node (black dot), the saddle node (empty dot) and the stable limit cycle (Black orbit). Left eigenvector associated to the unstable manifold of the saddle node (l_0) is shown in a dashed line. **C**: Stationary distribution $P_s(y)$ of multiple realizations of the trajectory shown in **A** and **B**, projected into l_0. The first peak of the distribution from left to right matches the position of the stable node (d_{fp}), the second peak matches the minimum distance between the limit cycle and the saddle node (d_{lc}). Dashed lines coincide with the position of the fixed point (d_{fp}), and the minimum distance between the limit cycle and the saddle node (d_{lc}). **D**: Double well potential ($U(y)$) of the dynamical system shown in the bottom panel. Comparison between $U(y)$, calculated with equation 3.17, and with the steady state distribution $p_s(y)$ shown in **B**: $U(y) = -\sigma^2 \log(p_s(y))$ (see equation 3.24).

4.2.3.3 Neuron i response dependence on I_i

In Figure 4.9, the steady state distribution $P_s(y|I = I_i + \sigma\eta(t))$ is shown relative to the phase portrait of the system. This Figure illustrates how the peaks of the distribution coincide with the relative positions of the attractors portrayed in the phase portraits. Notice that when the system is bistable (stable node and stable limit cycle attractors coexist), two peaks emerge in the y distribution, which coincide with d_{fp} and d_{lc} (refer to Figure 4.8). When the system has only a stable node (subthreshold region) there is only one peak in the y distribution located in d_{fp}. Consequently, when the phase portrait is in the regularly spiking region there is only one peak in the y distribution at d_{lc}.

Notice that for the distribution of mean values (I_i) of the total input received by neuron i (I_i in Figure 4.7**C**) most phase portraits lie on the subthreshold region (relate to Figure 4.9). This is not surprising considering that the network has much stronger inhibition than excitation, thus the mean input to this unit is subthreshold.

The $P_s(y)$ distribution in Figure 4.9 can be approximated to one or two Gaussian distributions (depending on whether the phase portrait is stable or bistable), by parametrizing the mean with respect to the stable node (d_{fp}) and/or limit cycle position (d_{lc}). The variance of the Gaussian located at $y < 0$, can be parametrized with respect to the eigenvalue associated with the unstable manifold of the saddle node (λ_0). The variance of the Gaussian located at $y > 0$ is proportional to $\bar{D}_{lc}$, described in chapter 3 (section 3.3.1.2).

4.2.3.4 Parametrization of $P_s(y)$ relative to I_i

Figure 4.9 illustrates the dependence of the stable node d_{fp} position on the mean input I_i. The more depolarizing I_i is, the closer the stable node gets to the saddle node, thus the mean of the y distribution moves closer to zero. The variance of the distribution also increases towards less negative input currents, because the saddle node becomes less repulsive, in other words particles are not repelled as fast as for more negative currents. The speed at which particles are repelled by the saddle node, into the basin of attraction of the stable node, is proportional to λ_0 (for detailed derivation of λ_0, refer to methods 4.4.4).

The relation between the mean of the Gaussian for $y < 0$ and d_{fp}, together with its standard deviation σ relative to λ_0 are shown in Figure 4.10. Notice that both are continuous functions, what makes parametrization feasible. The parametrization could well be done relative to the applied current I_i, because both d_{fp}, and λ_0 depend on I_i.

4.2.3.5 Approximation of the response of a neuron

The distribution $P_s(y)$ of a neuron when receiving colored noise can be approximated with the weighted average response of neuron i to the inputs $I_i + \sigma\eta(t)$ (white noise), for I_i in $I_i([t_0, t_1, .., t_n, t_{n+1}])$. The weight assigned to each response is given by the frequency of occurrence of I_i along the 20s simulation (normalized histogram of I_i in Figure 4.7**C**, $P(I_i)$).

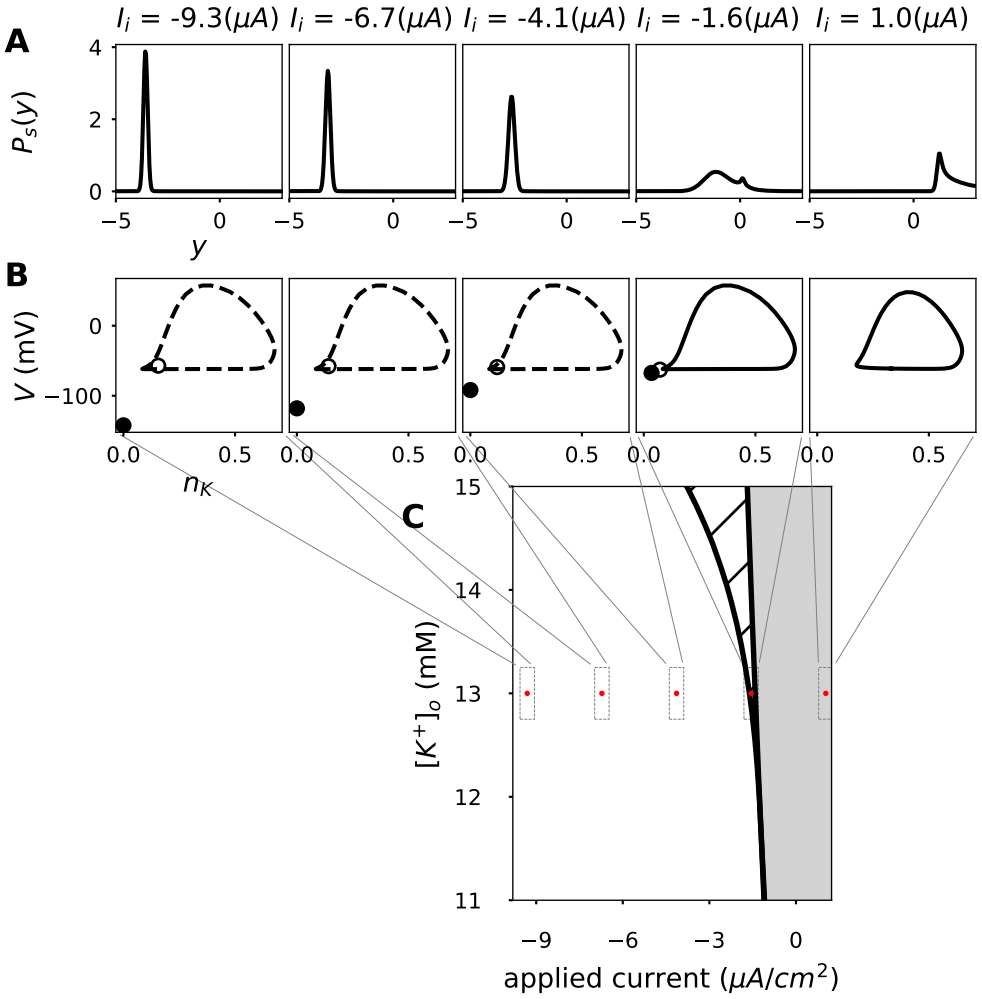

FIGURE 4.9: Stationary distribution of y in response to I_i plus white noise ($\sigma\eta(t)$). $P_s(y)$ is portrayed on top of the phase portraits of the neuron model for different static input currents I_i. **A**: $P(y|I = I_i + \sigma\eta(t))$ for different I_i, from left to right $I_i = -11.9$ $\mu A/cm^2$, $I_i = -9.3$ $\mu A/cm^2$, $I_i = -6,7$ $\mu A/cm^2$, $I_i = -4.1$ $\mu A/cm^2$, $I_i = -1.6$ $\mu A/cm^2$ and $\sigma = 1$ $\mu A/cm^2$. **B**: Phase portraits of neuron i when receiving a static input I_i (same input of **A**). The phase portraits show the stable node (black dot), the unstable node (empty dot), the stable limit cycle (black orbit), and the ghost of the limit cycle (dashed orbit). All the phase portraits shown share $K_o = 13.0$ mM. **C**: Bifurcation diagram representing the subthreshold region (white), the bistable region (dashed), and the regularly spiking region (grey). Locations of the phase portraits (red dots) relative to the different qualitative behaviors of the neuron are portrayed.

Parametrization of $P_s(y)$ in the basin of attraction of the stable node

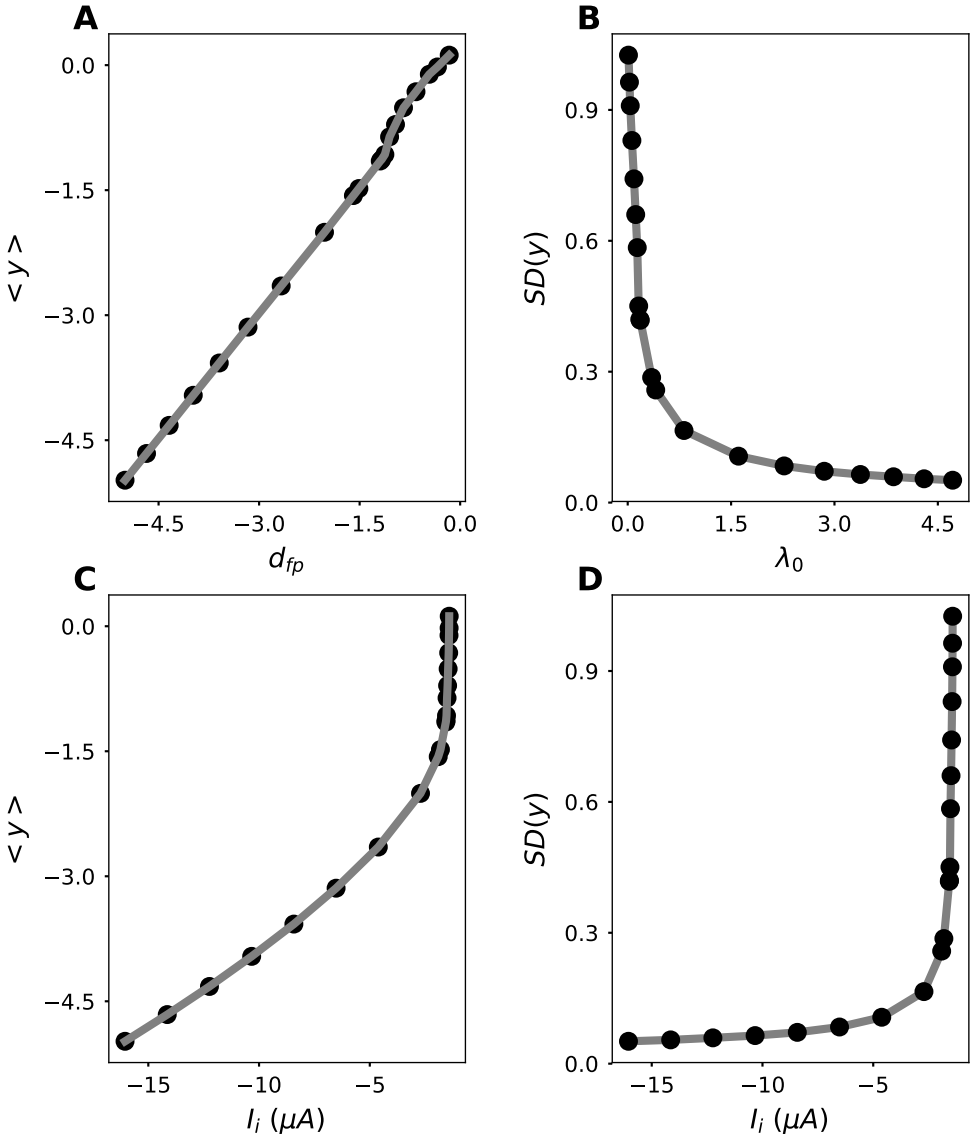

FIGURE 4.10: Parametrization of the y distribution. In **A, B** panels, parametrization is with respect to the stable node position d_{fp} and the eigenvalue of the unstable manifold of the saddle node λ_0, and in the bottom panels with respect to I_i. Top Left: Mean of the y distribution vs. stable node position d_{fp}. Top Right: Variance of the y distribution vs. λ_0. Bottom left: Mean of the y distribution vs. mean input I_i. Bottom right: Variance of the y distribution vs. mean input I_i

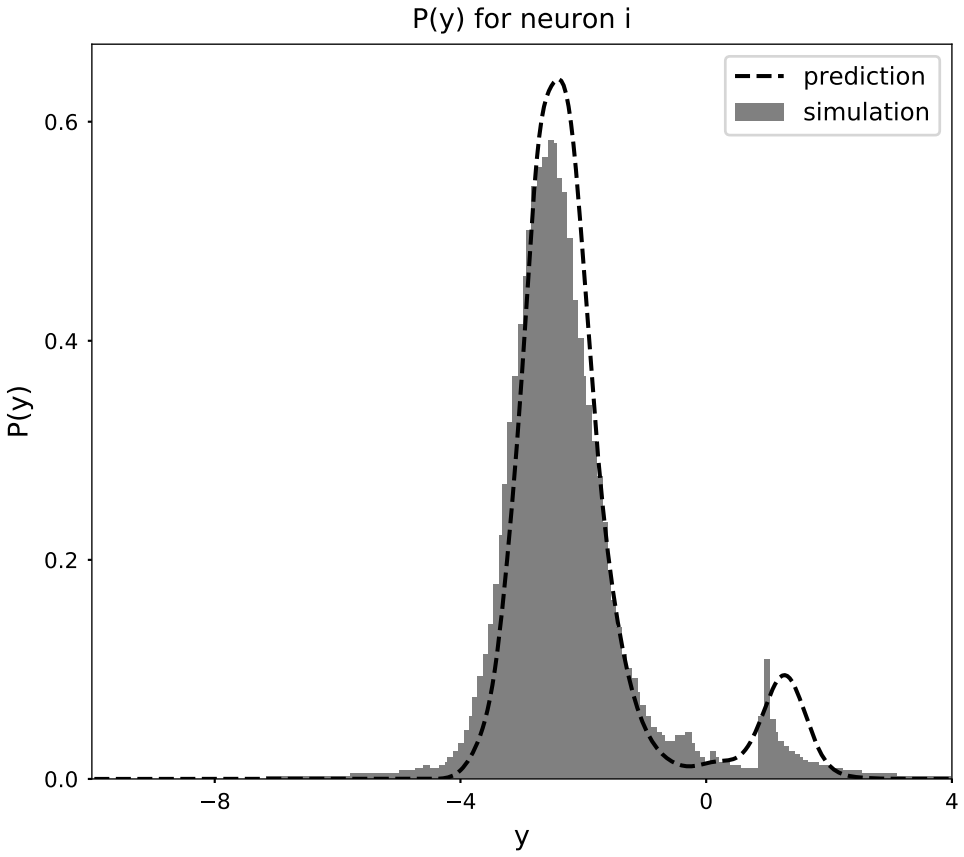

FIGURE 4.11: Distribution $P(y)$ for neuron i. Dashed line shows the prediction, and the grey histogram portrays the simulation.

$$P_s(y) = \sum_{I_i} P(I_i) P_s(y| < I >= I_i). \tag{4.9}$$

Notice that $P_s(y| < I >= I_i)$ can be constructed with the dependence found in Figure 4.10.

After all the the necessary terms to solve equation 4.9 have been defined, it is possible to draw a prediction of the distribution $P_s(y)$ (find a summary of the requirements to solve equation.4.9 in Table. 4.1). In Figure 4.11 the resulting prediction for the distribution of y, $P_S(y)$, is portrayed. The prediction is a very good estimate for the relative proportion of particles in the silent state against the ones in the spiking state. However, it underestimates the density close to the saddle node, where the dynamics slow down and the initial assumption of having a much slower input than the dynamics of the system breaks.

Given that all the units in the network are identical, the distribution $P_s(y)$ of each unit only depends on the input distribution $P(I_i)$. Figure 4.12 shows two extreme examples of $P(I_i)$, and the respective $P(y)$ are shown. One is a unit receiving a very hyperpolarized input distribution $P(I_i)$, and another unit receiving a very depolarized input distribution

TABLE 4.1: Algorithm to predict the distribution $P(y)$ of neuron i.

(i) Classification of the input to neuron i
(i-a) Extract the total input to neuron i, e.g the sum of all the synaptic currents $I_{syn,i}(t)$ and the external input I_{app} (Figure 4.7**A**).
(i-b) Calculate the power spectral density of the total input, check what is the relative power of slow (<6Hz) vs. fast components. When the slow component is stronger than the fast components, the approximation proposed here is appropriate (Figure 4.7**B**).
(i-c) Estimate the probability density of the total input to neuron i throughout the simulation, $P(I_i)$ (normalized histogram of I_{tot}, Figure 4.7**C**).
(ii) Characterize the steady-state distribution of y for every mean input I_i throughout the simulation (Figure 4.9).
(ii-a) For every mean input current (bins in i-c, I_i) calculate the phase portrait of neuron i.
(ii-b) Calculate an approximation of the y distribution for each bin in i-c (I_i). (ii-b-1) Define the overall shape of the distribution of y. The number of stable states in the phase portrait equals the number of Gaussians of the distribution of y. (ii-b-2) Use the parametrization of the mean μ and the standard deviation σ of the Gaussians, to approximate the distribution of y relative to I_i, $P_s(y\| < I >= I_i)$.
(iii) Calculate $P(y)$ from the weighted average of all the distributions. (equation 4.9) (iii-a) Calculate $\sum_i P(I_i)P_s(y\| < I >= I_i)$

$P(I_i)$. As expected, the density of particles in the basin of attraction of the limit cycle ($y > 0$) increases for more depolarized input distributions.

4.2.3.6 Distribution y across the network

The same approach used for a single neuron can be employed to solve the mean field of the network, by calculating $P(I_i)$ from the theoretical mean field of the network (mean field detailed description in section 4.4.6, equations 4.25, and 4.26). The procedure listed in Table 4.1 is performed to calculate $P_s(y)$ for the whole network, but the distribution of inputs $P(I_i)$ is replaced by the distribution of inputs throughout the network.

The distribution of $P(I_i)$ for the network, can be assumed to be the mean distribution of inputs that all the neurons receive across the network. Thus $P(I_i)$ for the network can be approximated by a Gaussian with mean given by equation 4.25 and standard deviation given by equation 4.26 (Amit and Brunel, 1997; Brunel, 2000).

Thus, in order to calculate the network $P(y)$, the same procedure shown in Table.4.1 can be used by replacing $P(I_i)$ for each unit, with the mean $P(I_i)$ of the whole network.

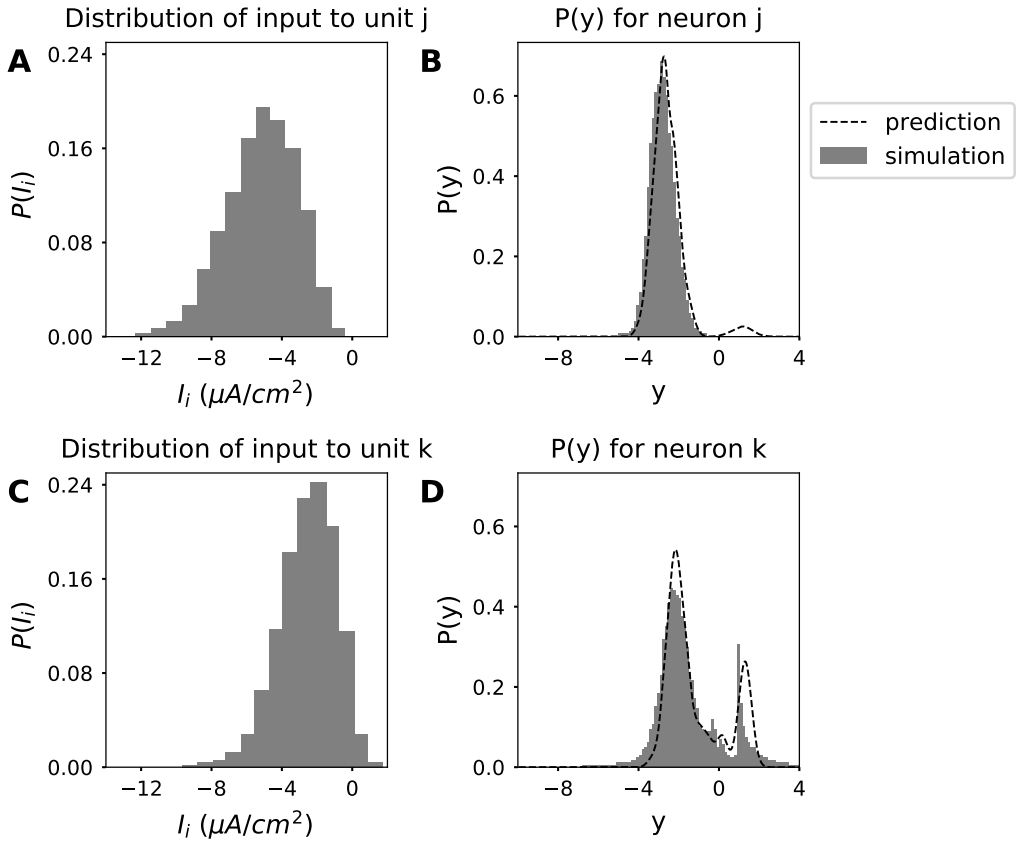

FIGURE 4.12: Distribution $P(y)$ for different neurons in the network. The relative density of particles above 0 increases when the input distribution is located at more depolarized values. **A,B**: $P(I_i)$ (**A**), and $P(y)$ (**A**) for an example unit j receiving a hyperpolarized input distribution ($\int_i I_i P(I_i) = -5.2\ \mu A/cm^2$). **C,D**: $P(I_i)$ (**C**), and $P(y)$ (**D**) for an example unit k receiving a depolarized input distribution ($\int_i I_i P(I_i) = -2.6\ \mu A/cm^2$).

More specifically, replacing step (i-c) of Table.4.1, with a Gaussian with mean given by equation 4.25 and standard deviation given by equation 4.26.

The resulting distribution $P_s(y)$ for the network (Figure 4.13 right panel) has two prominent peaks, one around $y = -2.5$ and another around $y = 1.5$. The first ($y < 0$) corresponds to particles in the basin of attraction of the stable node, and the second one ($y > 0$) corresponds to particles in the basin of attraction of the limit cycle.

An estimate for the population activity of the network can be expressed in terms of $P_s(y)$. The probability of finding a particle in one of the basins of attraction can be calculated by integrating $P_s(y)$. The integral of the probability distribution of $P(y)$, $\int_{-\infty}^{0} P(y)dy$, is the probability of finding a particle in the basin of attraction of a stable node. Similarly, $P_s(y)$, $\int_{0}^{\infty} P_s(y)dy$, corresponds to the probability of finding a particle in the basin of attraction of the limit cycle. Thus, the population activity of the network

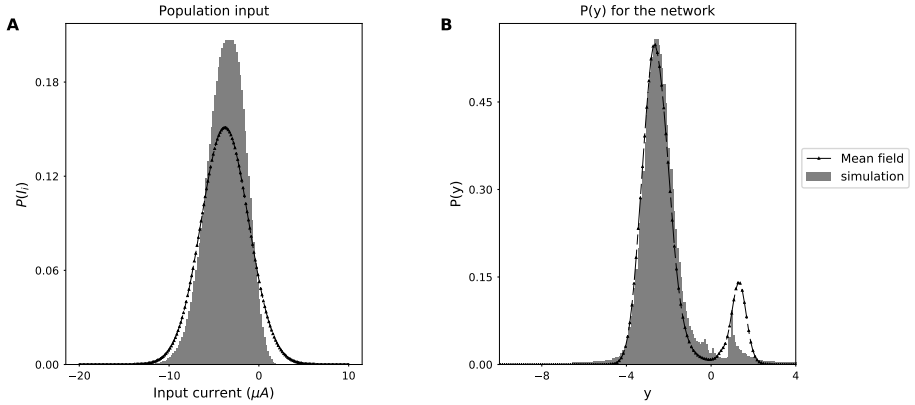

FIGURE 4.13: Distribution $P(y)$ for the network. **A**: Input distribution across the population, dashed line shows the mean field approximation, and the grey histogram shows the simulation. **B**: Distribution of $P(y)$ across the network. Dashed line shows the approximation obtained from assuming the mean field input, and the grey histogram shows the simulation.

is related to $P_s(y)$ as follows,

$$< A >= \frac{\int_0^\infty P(y)dy}{< \tau_{lc}(I_i) >}, \tag{4.10}$$

Where $< \tau_{lc}(I_i) >$ is the mean limit cycle period, the latter varying as a function of I_i. The more depolarized I_i, the lower the period (higher firing rate).

The approximation obtained from the mean field yields a fairly good estimate of the distribution of y across the population, although the probability of being in the basin of attraction of the limit cycle is overestimated. This overestimation is due to the fact that the mean field approximation does not capture the negative skewness of the input distribution (Figure 4.13 left panel).

Notice that the two attractors of the network proposed in section.4.2.2 are already evident from $P(y)$, Figure 4.13 right. Particles tend to segregate in low energy states, and disperse from high energy states. Thus, peaks in the distribution coincide with low energy states, and minima coincide with barriers or high energy states.

The potential energy landscape $U(y)$ can be calculated from $P_s(y)$ in a fairly simple way (if $P_s(y)$ is indeed stationary in time (Gardiner, 2009)),

$$U(y) = \sigma^2 \log(P_s(y)), \tag{4.11}$$

where σ is the standard deviation of the distribution of the inputs throughout the network projected to l_0, refer to Figure 4.14.

The higher power in the low frequency bands for high extracellular potassium concentrations (Figure 4.5, and 4.6) can be explained by the rate of escape from the silent state.

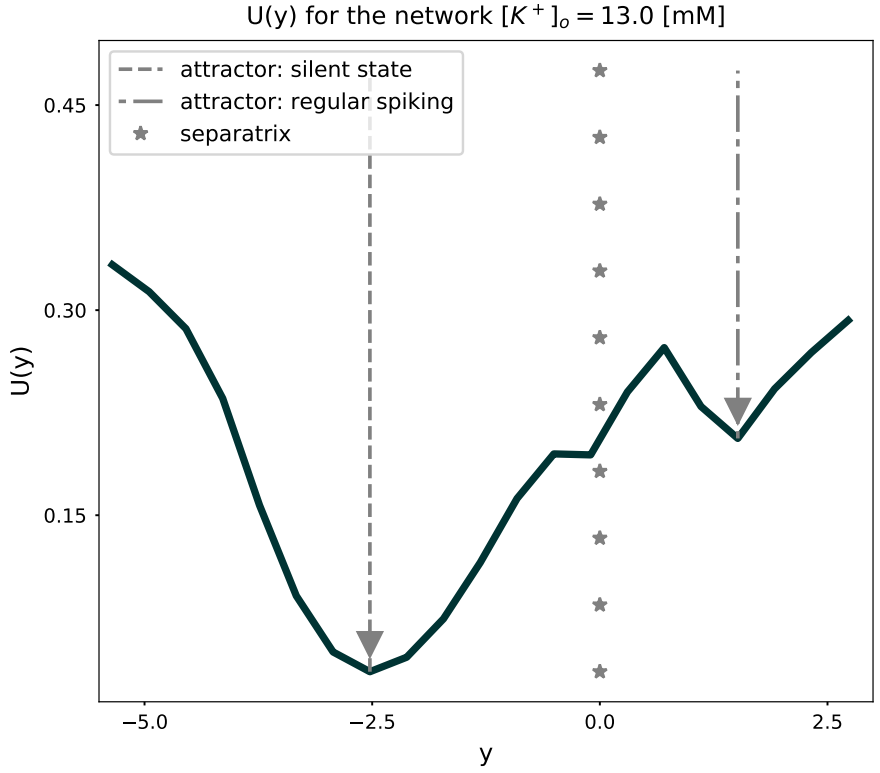

FIGURE 4.14: Potential $U(y)/c$ for the population portrays the two strong attractors, the silent state ($y = -2.54$) and the spiking state ($y = 1.26$). Potential calculated as $U(y) = \sigma^2 \log(P_s(y))$, where σ is the projection of the standard deviation of the distribution of inputs throughout the network projected into l_0.

Namely, the rate at which neurons escape from the basin of attraction of the stable node and cross the separatrix (τ_e). The escape rate, τ_e, depends on the height ΔU (Gardiner, 2009),

$$\tau_e \propto e^{\Delta U/\sigma}. \tag{4.12}$$

The previous holds from the silent state attractor to $y = 0$ (separatrix). see Figure 4.15.

Networks with different extracellular potassium concentrations yield different potential shapes $U(y)$. On the one hand the potential height ΔU increases with extracellular potassium concentration (Figure 4.15, and S.4.25). Therefore, the mean escape time from the basin of attraction of the stable node, τ_e, increases with an extracellular potassium concentration increase. On the other hand, the extracellular potassium concentration determines the number of attractors of the potential $U(y)$ (see Figure 4.16).

Below the critical extracellular potassium concentration (phase transition for single units, SNL bifurcation), the potential has one attractor located in the basin of attraction of the stable node. For those potentials, particles cross the separatrix (at $y = 0$) when fluctuations are large enough to push particles beyond the height ΔU. There is no other

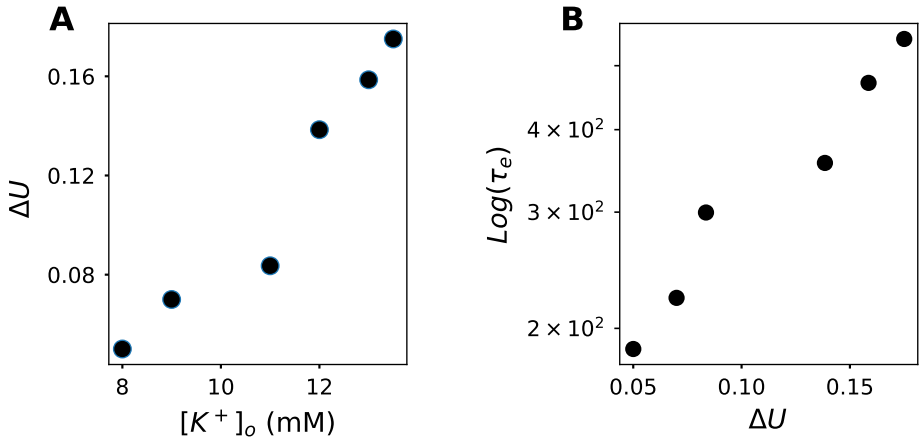

FIGURE 4.15: Potential height ΔU from the stable node attractor to the separatrix crossing depends on extracellular potassium. Left: Potential height ΔU to exit the basin of attraction of the stable node for the network, for networks exposed to different $[K^+]_o$. Right: Average escape time from the basin of attraction of the stable node τ_e (See Figure S.4.25 to find the distribution t_e).

attractor, thus particles go back to the lowest energy state. For extracellular concentrations above the critical value (phase transition for single units, SNL bifurcation), the potential $U(y)$ has two attractors, one in the basin of attraction of the stable node and one in the basin of attraction of the limit cycle. When particles receive a perturbation strong enough to cross the barrier at $y \approx 0.7$, they are attracted to the regularly spiking attractor (high frequency spiking) until they receive a perturbation strong enough to push them back to the attractor located in the basin of attraction of the stable node.

4.3 Discussion

In this chapter it was shown that extracellular potassium concentration has the potential to distort network dynamics. In agreement with previous experimental observations (Bellot-Saez et al., 2018), membrane potential and population activity fluctuations in the low-frequency bands increase with extracellular potassium concentration.

One of the striking results from this analysis is that the network reshapes its potential landscape, $U(y)$, with extracellular potassium concentration changes. The extracellular potassium concentration can switch the spike generating mechanism of single neurons, which has a strong effect on the neuronal spiking statistics. The single cell phase transition caused by the ionic concentration, results in the emergence of a new attractor in the potential landscape of the network, located in the basin of attraction of the limit cycle.

The distortion of the potential landscape could explain why during slow wave sleep neurons tend to fire at high rates during the up-state and reduce firing during the down state. Amzica and colleagues (Amzica and Steriade, 2000), showed that an extracellular

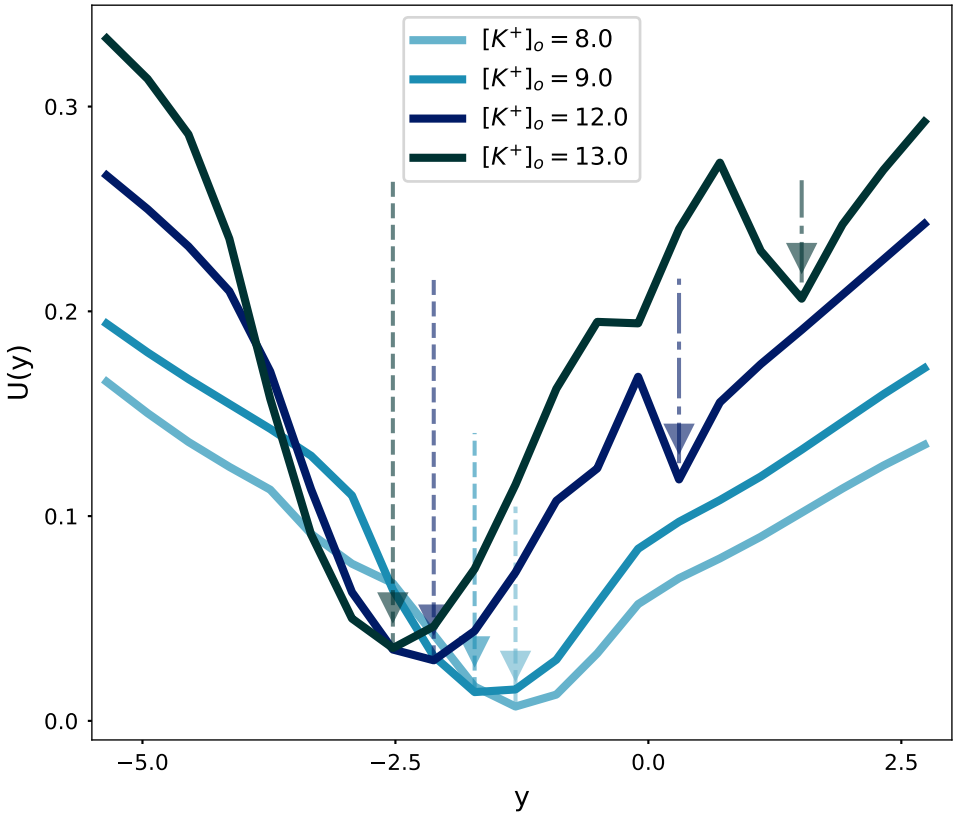

FIGURE 4.16: The potential $U(y)$ for the population depends on the extracellular potassium concentration ($[K^+]_o$). Potential $U(y)$ for each network changes with $[K^+]_o$. For Networks with extracellular potassium concentrations $[K_o]^+$ below the SNL bifurcation, the network has only one attractor. Networks with $[K_o]^+$ higher than the SNL bifurcation, have two attractors (notice the two local minima in the $U(y)$ for $[K^+]_o \geq 12$ mM, compared to one local minima for $[K^+]_o < 12$ mM).

potassium oscillation is locked to the slow LFP oscillation measured during slow wave sleep, and that the highest concentration co-occurs with the up-state. If the highest concentration is big enough to induce a phase shift in single neurons, then the cortex can develop a new attractor temporarily, that would drift a fraction of neurons into high frequency spiking. This effect would explain the high power in the gamma frequencies measured during the up states of slow wave sleep (Valderrama et al., 2012; Compte et al., 2008).

A prediction of the model is that stimulation-induced reduction of the Fano factor has different dynamics in both conditions, low vs high extracellular potassium concentrations (below and above the concentration where the phase transition occurs). In the lower extracellular potassium concentration, the reduction of the Fano factor would be transient, and it would last as long as the fluctuations take to adapt to the new mean input of the distribution. Afterwards it would come back to baseline as predicted by

(Farkhooi et al., 2013). In the condition with higher extracellular concentration (above the critical SNL concentration), the Fano factor would go down with a depolarizing stimulus, and it would stay at the lower value until stimulus is removed. The mechanistic explanation for this difference is that for depolarizing stimuli, the second attractor lying in the basin of the limit cycle, increases its attractiveness, thus, more units enter the basin of attraction of the limit cycle which would give rise to highly regular firing. This mechanism is similar to the one reported by (Litwin-Kumar and Doiron, 2012), where depolarizing stimuli biased the cluster-attractors making high frequency spiking more probable. Instead of a cell intrinsic effect, Litwin and Kumar (Litwin-Kumar and Doiron, 2012), induced the attractor perturbation by increasing the excitatory efficacy in sub-populations of neurons, resulting in highly active sub-clusters in the network.

It is unclear if such spiking variability increase with extracellular potassium concentration is feasible under physiological conditions. Softky and Koch (1993) report coefficients of variation (CV) close to one, consistent with a Poisson process, however, they remove from their analysis bursting neurons which are indeed present in physiologically realistic settings. Further *in-vivo* experimental observations are needed to answer this question. However, it is not a strightforward answer given that extracellular potassium concentration most likely fluctuates locked to neuronal activity. Long recordings would be needed to define if the short windows of high extracellular potassium concentrations display high interspike interval coefficients of variation.

The results shown in this chapter rely on two simplifications that are unphysiological. The first is that every single neuron is exposed to the same extracellular potassium concentration and the second is that the concentration does not change with time. Amzica and colleagues (Amzica and Steriade, 2000) observed that stimulus induced activity in the cat visual cortex was followed by extracellular potassium accumulation in the vicinity of active neurons, while remaining constant further away. Thus, future work is needed to include both activity-dependent and spatially specific concentration changes.

The second simplification that is unphysiological is that synaptic efficacy is not altered by extracellular potassium alterations. An increase in extracellular potassium caused, for instance, by a decrease in excitatory synaptic transmission could alter the network activity. Rimmele and colleagues reported extracellular potassium dependent inhibition of glutamate transporters (Rimmele et al., 2017). Indirectly, extracellular potassium could also alter inhibitory efficacy. GABA-A and GABA-B efficacy might be changed by a shift in the resting membrane potential to a slightly more depolarized potential. The shift in the depolarization level can be a consequence of extracellular potassium accumulation (Fertziger and Ranck, 1970). Further experimental observations are needed to quantify the change of synaptic efficacy, and the single unit spiking statistics relative to extracellular potassium accumulation in order to draw informed conclusions.

Taken together, this work links the effect of parameters in the single neuron response with microcircuit dynamics. The approach used here can be implemented to understand the effect of a variety of parameters, like temperature, capacitance, and membrane leakage on the network state, presumably drawing similar conclusions (Hesse et al., 2017).

It can be used as well for different conductance based models, as long as a principal component exists that permits a separation of silent vs. spiking states.

4.4 Methods

4.4.1 Network setup

We consider networks of N conductance based neuron models: (50%) excitatory and (50%) inhibitory neurons. Excitatory and inhibitory units have identical membrane potential dynamics described in equation 4.13. The only distinction between both populations comes from the effect they have on the postsynaptic neurons they target.

Membrane potential dynamics are similar to the ones described in chapter 2, however we add a synaptic current I_{syni}, that results from the sum of all the excitatory and inhibitory postsynaptic potentials that project to the neuron model:

$$\frac{dV_i}{dt} = \frac{1}{C}(I_{app} - I_L - I_{Na} - I_K - I_{pump} + I_{syn_i}(t)). \tag{4.13}$$

Recall that $I_{Na}(t)$ and $I_K(t)$ depend on the dynamics of the activation and deactivation gates for those channels. Thus, the number of state variables that shape the dynamics of each unit is 4. For simplicity we fix ionic concentrations (similar to what was shown in chapter 2), and turn them into parameters.

When an excitatory presynaptic unit j fires a spike ($s_j = 1$), the postsynaptic neuron i receives an excitatory post synaptic potential (F^E) described by an exponential decay if the excitatory presynaptic neuron j is connected to the postsynaptic neuron i, e.g. $J_{ij} \neq 0$. Similarly, when an inhibitory presynaptic unit fires a spike, neuron i receives an inhibitory post synaptic potential (F^I) if the inhibitory presynaptic neuron j is connected to the postsynaptic neuron i, e.g. $J_{ij} \neq 0$. This can be expressed as follows,

$$I_{syn_i}(t) = \sum_{j \in E} J_{ij} F^E * s_j(t) + \sum_{j \in I} J_{ij} F^I * s_j(t) \tag{4.14}$$

$$F^E(t) = \frac{1}{\tau_E} \mathrm{e}^{-t/\tau_E}, \tag{4.15}$$

$$F^I(t) = \frac{1}{\tau_I} \mathrm{e}^{-t/\tau_I}. \tag{4.16}$$

The networks shown here are inhibition dominated, thus $J^{II} = J^{IE} >> J^{EE} = J^{EI}$:

$$J^{EE} = J^{EI} = 0.035mV, \tag{4.17}$$

$$J^{II} = J^{IE} = 0.27mV. \tag{4.18}$$

The in-degree (K) is on average 200 (Erdös Rényi graph), regardless of N. All results are repeated for different N. The input I_{app} is adjusted, so that the resulting population rate of the networks is 10Hz on average.

In these simulations I assume that the synaptic activity is not varied with changes in extracellular potassium concentration. Thus, the f-I curve modulation of extracellular potassium is a consequence of the effect it has on the single cell spiking statistics exclusively.

4.4.2 Simulations

All network simulations where performed in python 3, with the package Brian 2 (Stimberg et al., 2019). The second order Runge-Kutta numerical integration method was used with maximal integration time steps of 0.01 ms. The code is available in *this repository.*

4.4.3 Tuning the networks

In order to compare networks with different extracellular potassium concentrations on the same regime, the population activity of the networks is adjusted through the external input current.

The input-output curve is obtained from simulations (see Figure 4.1). For every combination of $[K_o]^+$ and external input current (I_{app}), 5 random realizations of connectivity patterns with the same mean in-degree (200) are simulated. The population activity (A) in the steady state is shown. For every $[K_o]^+$, the external input ($I_{app,10spks/sec}$) that yields a mean population rate of 10 spks/sec ($\pm 0.1 spks/sec$) is obtained from the input-output curve (Figure 4.1). Notice that larger $[K_o]^+$, require more hyperpolarized $I_{app,10spks/sec}$ than lower $[K_o]^+$.

4.4.4 Dimensionality reduction

The dimensionality reduction requires the linearization of dynamics in the saddle node (x_s). The linearized dynamics are given by the Jacobian of the 4 dimensional spike generating dynamics evaluated at x_s.

$$\mathbb{J}_{x_s} = \begin{bmatrix} \frac{\partial \dot{V}}{\partial V} & \frac{\partial \dot{V}}{\partial m_{Na}} & \frac{\partial \dot{V}}{\partial h_{Na}} & \frac{\partial \dot{V}}{\partial n_K} \\ \frac{\partial \dot{m}_{Na}}{\partial V} & \frac{\partial \dot{m}_{Na}}{\partial m_{Na}} & \frac{\partial \dot{m}_{Na}}{\partial h_{Na}} & \frac{\partial \dot{m}_{Na}}{\partial n_K} \\ \frac{\partial \dot{h}_{Na}}{\partial V} & \frac{\partial \dot{h}_{Na}}{\partial m_{Na}} & \frac{\partial \dot{h}_{Na}}{\partial h_{Na}} & \frac{\partial \dot{h}_{Na}}{\partial n_K} \\ \frac{\partial \dot{n}_K}{\partial V} & \frac{\partial \dot{n}_K}{\partial m_{Na}} & \frac{\partial \dot{n}_K}{\partial h_{Na}} & \frac{\partial \dot{n}_K}{\partial n_K} \end{bmatrix}_{x=x_s} \tag{4.19}$$

where x is a vector containing the position in the 4 dimensional space $[V, m_{Na}, h_{Na}, n_K]$, and x_s denotes the position of the saddle in the 4 dimensional space $[V_s, m_{Na_s}, h_{Na_s}, n_{K_s}]$.

And the eigenvalues (λ) of the Jacobian evaluated at x_s,

$$(\mathbb{J}_{x_s} - \lambda I)\mathbb{X}_R = 0, \tag{4.20}$$

fulfill $\lambda_0 \geq 0 > \lambda_1 > .. > \lambda_{n-1}$. And $\mathbb{X}_R$ are the right eigenvectors. The stable manifold is tangential to the right eigenvectors associated to the eigenvalues $\lambda_1, .., \lambda_{n-1}$.

Similarly the left eigenvectors ($\mathbb{X}_L$) can be calculated as:

$$(\mathbb{J}_{x_s}^T - \lambda I)\mathbb{X}_L^T = 0. \tag{4.21}$$

The unstable direction l_0, is given by the left eigenvector corresponding to λ_0 (the unstable manifold of the saddle).

4.4.5 Spiking statistics

The population activity A is defined as the spike rate of the network in a window of time Δt as follows:

$$A(t*) = \sum_{t=t*}^{t*+\Delta t} \frac{\sum_{j=0}^{N} s_j(t)}{N\Delta t}, \tag{4.22}$$

where s_j refers to the spike train of neuron j, and N is the total number of neurons in the network.

The autocorrelation of the population activity is defined as:

$$C(\tau) = \frac{1}{T}\sum_{t=0}^{T} A(t)A(t+\tau). \tag{4.23}$$

The mean firing rate of the network is given by:

$$< fr >= \frac{1}{T}\sum_{t=0}^{T} A(t)\Delta t. \tag{4.24}$$

4.4.6 Mean-field

The mean and the variance of the distribution of inputs over the population can be estimated (Brunel, 2000):

$$\mu = \tau_E v_E K J^E - \tau_I v_I K J^I + I_{app}, \tag{4.25}$$

$$\sigma^2 = \tau_E v_E K {J^E}^2 + \tau_I v_I K {J^I}^2. \tag{4.26}$$

K is the average number of presynaptic neurons projecting into one postsynaptic neuron across the network, v_E is the population activity of the excitatory population, and v_I of the inhibitory one.

4.5 Appendix

4.5.0.1 Spiking variability

Spiking variability increases with extracellular potassium concentration, see Figure S.4.17.

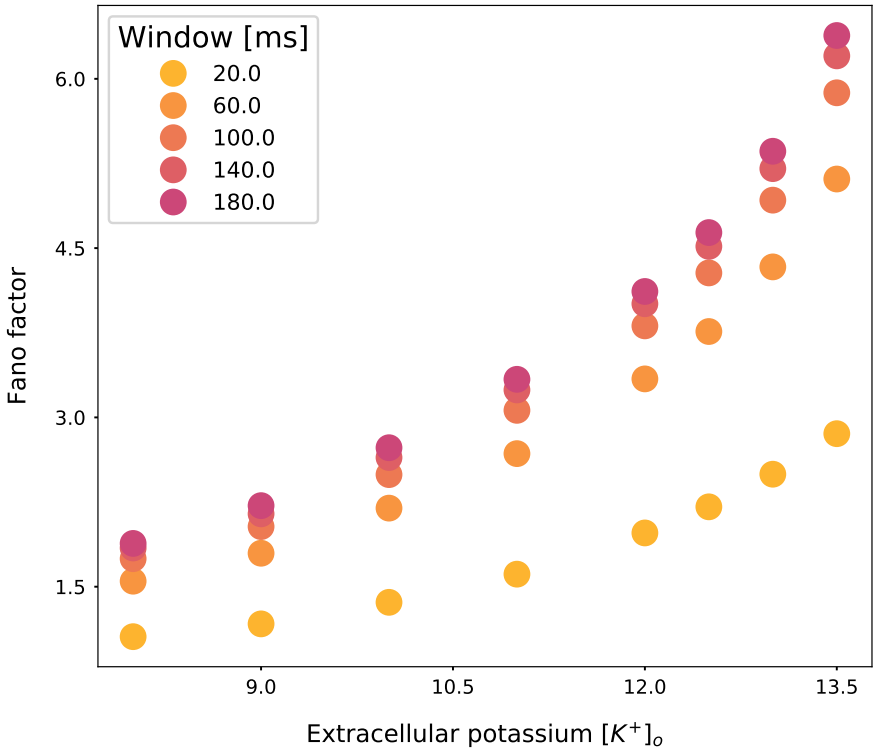

FIGURE 4.17: Spiking variability increases with extracellular potassium concentration. Average Fano factor vs. extracellular potassium concentration ($[K_o]^+$). The Fano factor resulting from using different windows of time to define one trial: 20, 60, 100, 140, and 180 ms

4.5.0.2 PSD dependence on network size and in-degree

Ratio of peak power in the slow frequency bands (2-6 Hz) relative to the peak power in the high frequency band (>50 Hz) increases as the extracellular potassium concentration increases regardless of the network size N, see Figure S.4.18.

This ratio it is also independent of the in-degree K, for a broad range of in-degrees, see Figure 4.19.

Population activity for all the networks in Figure S.4.19 are shown in Figure S.4.20.

For the simulations shown in Figures S.4.19, and S.4.20, the synaptic conductances and the external applied current were scaled as follows:

$$g_E = \bar{g_E}\sqrt{\frac{K_{ref}}{K}}, \tag{4.27}$$

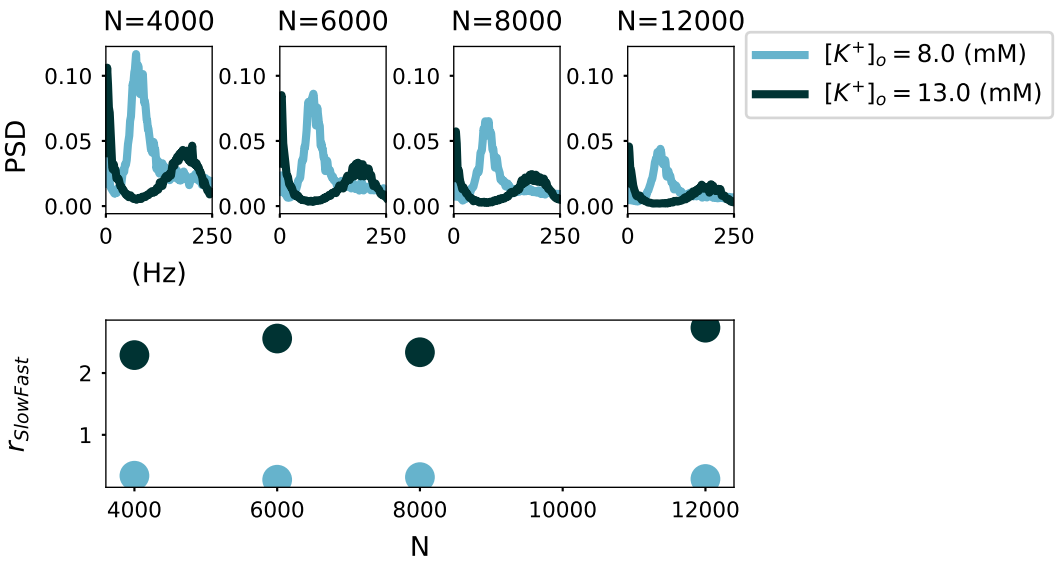

FIGURE 4.18: Ratio of peak power in the slow frequency bands (2-6Hz) relative to the peak power in the high frequency band (>50Hz). Top panel: PSD for networks with different $[K_o]^+ = 8$ mM and $[K_o]^+ = 13$ mM, and different network sizes (N). Bottom panel:Ratio of peak power in the slow frequency bands (2-6 Hz) relative to the peak power in the high frequency band (>50Hz) for different N. Mean in-degree=200 and N=4000, 6000, 8000 and 12000. Population activity for all the networks $\sim$ 10Hz.

$$g_I = \bar{g_I}\sqrt{\frac{K_{ref}}{K}}, \tag{4.28}$$

$$I_{app} = \bar{I_{app}}\sqrt{\frac{K}{K_{ref}}}. \tag{4.29}$$

Where $\bar{I_{app}}$ is the external input, and $\bar{g_I}$ and $\bar{g_E}$ are the excitatory and inhibitory synaptic maximal conductances for the network setup with $K_{ref} = 200$. The limit when $K \to \infty$ (given $N >> K$) is derived as follows:

The mean input to the excitatory population is given by,

$$\mu_E = \tau_E v_E \sqrt{K} g_E \sqrt{K_{ref}} - \tau_I v_I \sqrt{K} g_I \sqrt{K_{ref}} + I_{app}\sqrt{\frac{K}{K_{ref}}}, \tag{4.30}$$

where v_E and v_I are the rates of the excitatory and inhibitory populations respectively. Considering that in the large K limit $\mu_E - \frac{\theta_E}{\sqrt{K}}$ should be finite (given that θ_E is the excitatory threshold),

$$\mu_E(K \to \infty) = 0. \tag{4.31}$$

And because $J_{EE} = J_{II} = J_{EI} = J_{IE}$, and K are the same for the inhibitory and excitatory populations,

$$v_E(K \to \infty) = v_I(K \to \infty). \tag{4.32}$$

Thus,

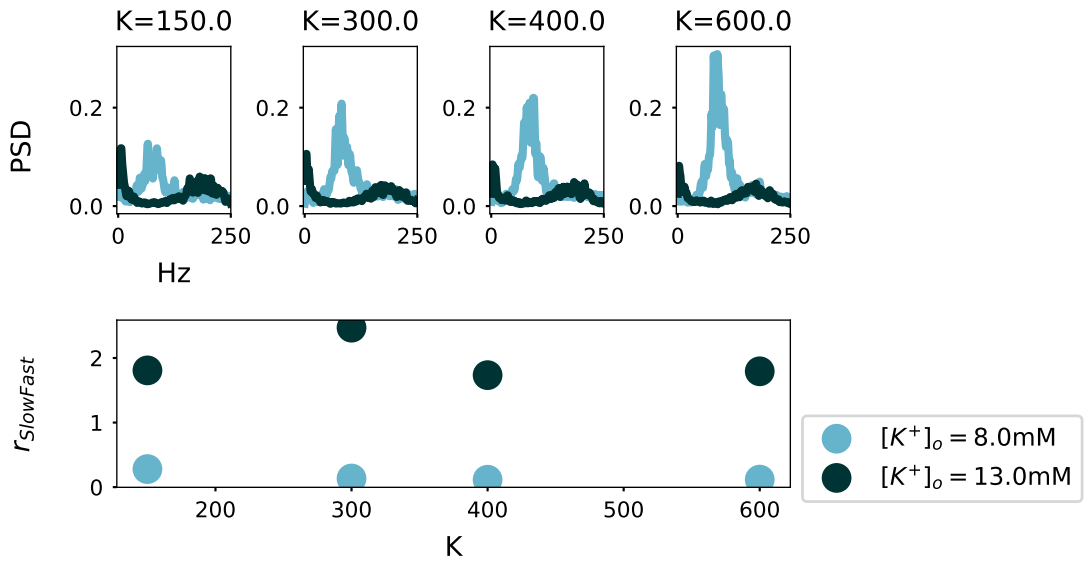

FIGURE 4.19: Ratio of peak power in the slow frequency bands (2-6Hz) relative to the peak power in the high frequency band (>50Hz). Top panel: PSD for networks with different $[K_o]^+ = 8$ mM and $[K_o]^+ = 13$ mM, and different mean in-degree (K). Bottom panel:Ratio of peak power in the slow frequency bands (2-6 Hz) relative to the peak power in the high frequency band (>50Hz) for different K, and N=4000.

$$v_E(K \to \infty) = \frac{-I_{app}}{K_{ref}(\tau_E g_E - \tau_I g_I)}. \tag{4.33}$$

Where v_E and v_I are the rates of the excitatory and inhibitory populations respectively.

The slow oscillations are also stronger for networks with $[K^+]_o$ above the SNL bifurcation relative to networks with $[K^+]_o$ below the SNL bifurcation, when all the networks have the same $v_E(K \to \infty)$. In Figure 4.21, I_{app} is set such that networks have $v_E(K \to \infty) = 5Hz$.

The power spectral density of the networks sown in Figure 4.21, are displayed in Figure 4.22.

4.5.1 Dependence of the parametrization on the amplitude of the input irregularity

In Figure S.4.23, the parametrization of the mean and the standard deviation of the distributions is shown for different white noise intensities (σ). Notice that the mean of the y distribution is insensitive to the noise intensity. The standard deviation of the y distribution depends on the white noise intensity only moderately. This is why the white noise intensity is assumed constant in equation 4.9.

4.5.2 Spiking statistics for networks with different $[K^+]_o$

$P(y)$ distributions for networks with different $[K^+]_o$, are shown in Figure S.4.24.

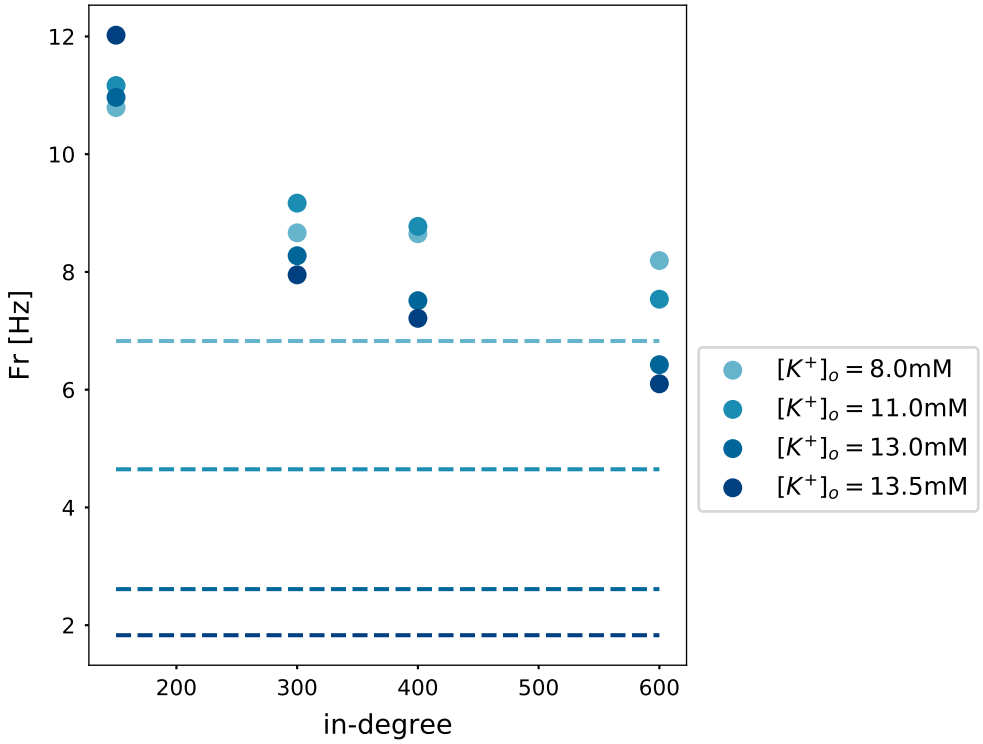

FIGURE 4.20: Population mean firing rate for networks with different $[K_o]^+$, and different mean in-degree (K). The dots show the average firing rate of the simulated networks, and the dashed lines show the theoretical firing rate for the limit $K \to \infty$.

Distribution of escape times for the networks shown in Figure S.4.24, are portrayed in Figure S.4.25. ISI distributions of the same networks are portrayed in Figure S.4.26.

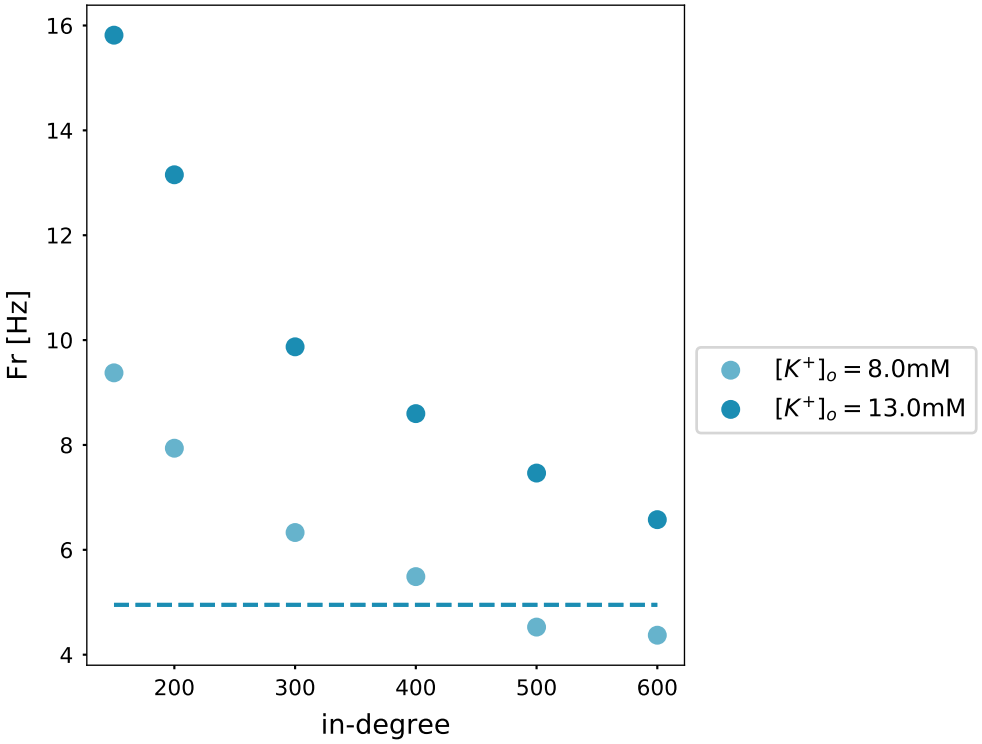

FIGURE 4.21: Population mean firing rate for networks with different $[K_o]^+$, and different mean in-degree (K), but same I_{app} such that $v_E(K \to \infty) = 5Hz$. The dots show the average firing rate of the simulated networks, and the dashed lines show the theoretical firing rate for the limit $K \to \infty$.

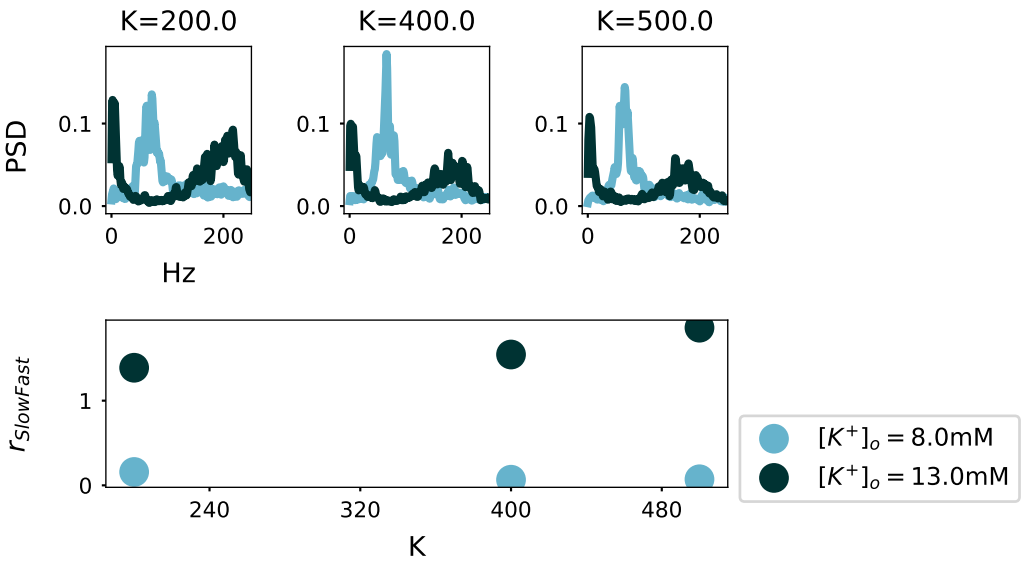

FIGURE 4.22: Ratio of peak power in the slow frequency bands (2-6Hz) relative to the peak power in the high frequency band (>50Hz) for networks with I_{app} such that $v_E(K \to \infty) = 5Hz$. Top panel: PSD for networks with different $[K_o]^+ = 8$ mM and $[K_o]^+ = 13$ mM, and different mean in-degree (K), and N=4000. Bottom panel:Ratio of peak power in the slow frequency bands (2-6 Hz) relative to the peak power in the high frequency band (>50Hz) for different K, and N=4000.

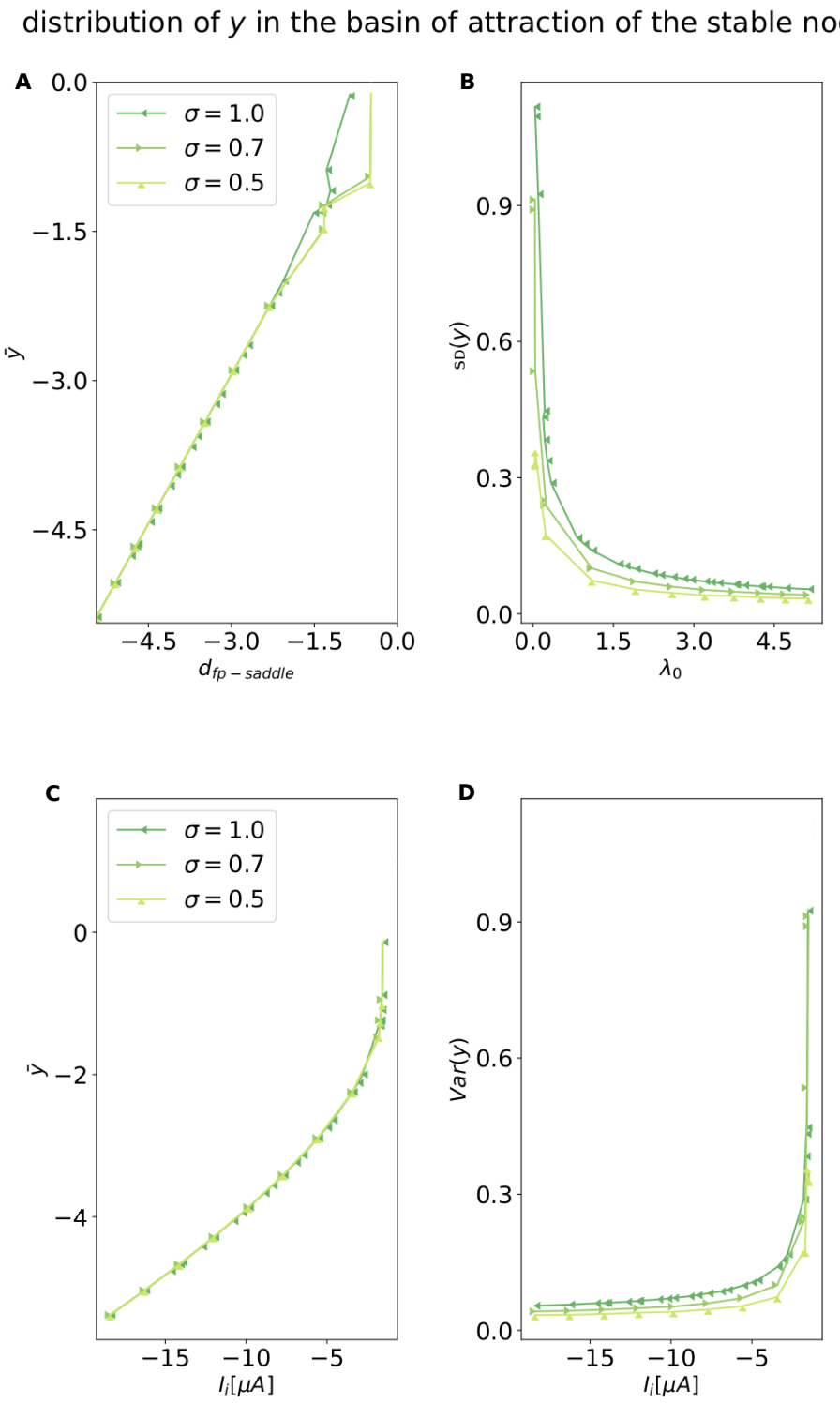

FIGURE 4.23: Parametrization of the y distribution for different white noise intensities (σ). **A**: Mean of the y distribution vs. stable node position d_{fp}. **B**: Variance of the y distribution vs. λ_0. **C**: Mean of the y distribution vs. mean input I_i. **D**: Variance of the y distribution vs. mean input I_i

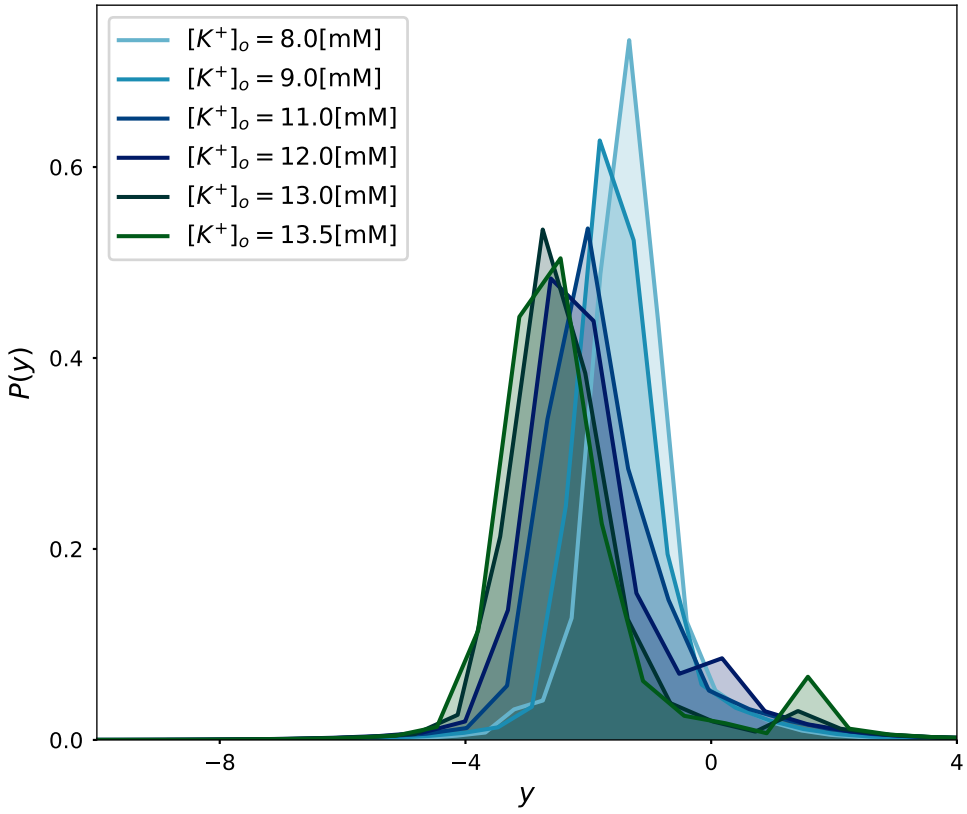

FIGURE 4.24: The modality of distribution $P(y)$ depends on the extracellular potassium concentration. The distributions $P(y)$ for extracellular potassium concentrations $[K_o]^+$ below the critical (phase transition for single units, SNL bifurcation) are uni modal ($[K^+]_o < 12$ mM). For $[K_o]^+$ values higher than the critical value, the $P(y)$ distributions are bimodal ($[K^+]_o \geq 12$ mM).

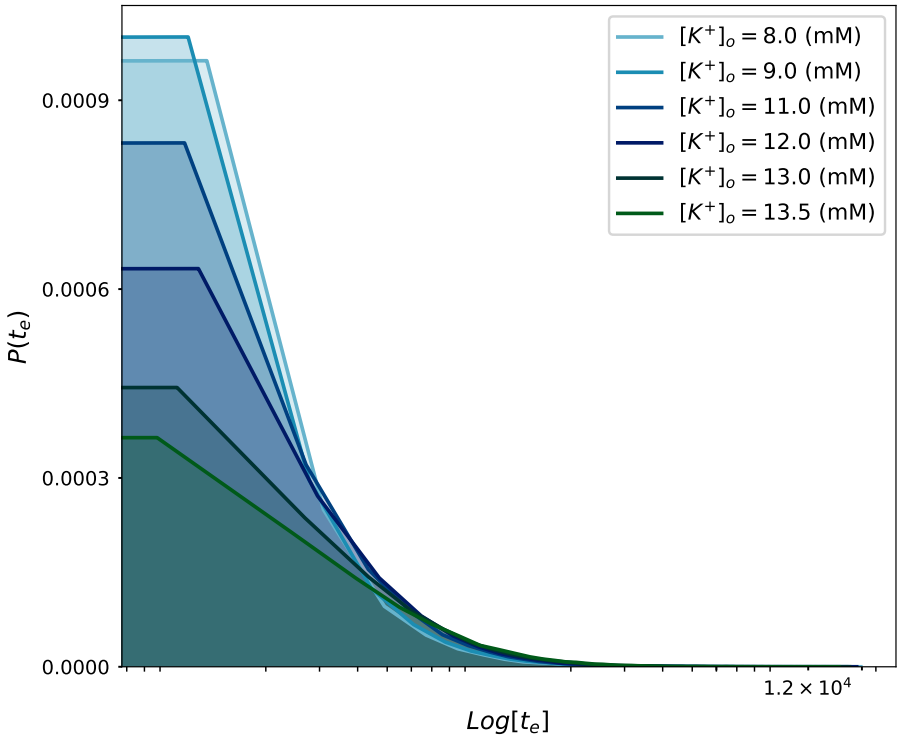

FIGURE 4.25: Distribution of escape times t_e from the stable node basin of attraction for each neuron in the network depends on the extracellular potassium concentration.

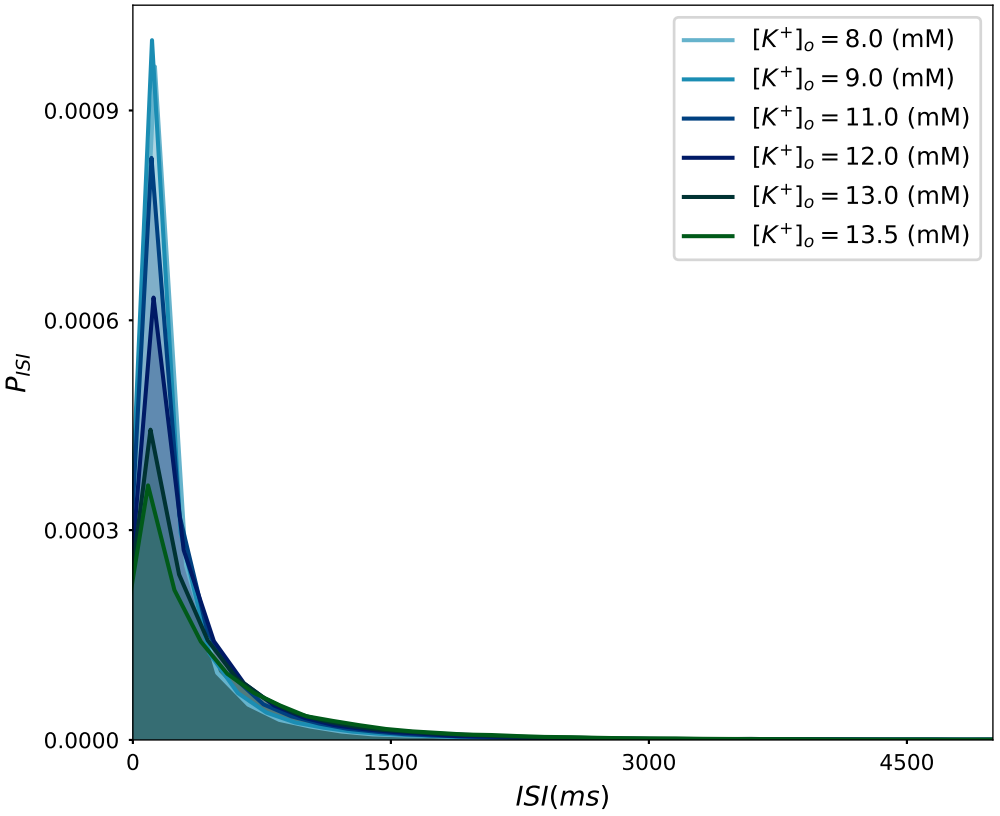

FIGURE 4.26: Interspike interval (ISI) distributions for networks with different extracellular potassium concentrations $[K^+]_o$. Longer tails are observed for higher extracellular potassium concentrations.

Part III

Synthesis

5 | Thesis conclusion

5.1 Thesis summary and conclusions

In this work, the interplay between neuronal spiking and ionic concentration dynamics is investigated from a theoretical perspective. This problem was addressed using a combination of conductance based modelling and spiking neural network analytical tools. Such combination was adequate to explain several features of empirical data obtained from pyramidal neurons of mice. Altogether, this thesis highlights the relevance of considering ionic concentration dynamics to understand neuronal activity, and provides technical insights on how to model and analyze the interactions between them.

First, I explained how neuronal action potentials, are generated, modelled, and analyzed. I then showed how ionic concentrations are distributed in the brain, how they are regulated, and how neuronal activity perturbs them. Next, I reviewed the literature that illustrates how ionic concentration dynamics can alter spike generation both from an experimental, and a theoretical perspective (chapter 2). Inspired by previous theoretical approaches Hübel and Dahlem (2014); Zandt et al. (2011), I proposed a model of a conductance based neuron that contains ionic concentration dynamics. Compared to other models, the one proposed here, combines fast spike generating dynamics with slow ionic concentration dynamics. Thus, the model is capable of illustrating how ionic concentration dynamics could explain multiple features observed on pyramidal patch clamp data, like spike frequency adaptation, slow after-hyperpolarization, and spike amplitude reduction. The model predicts as well that a neuron that displays regular firing, can transition to a burst-like intermittently interrupted firing due to extracellular potassium accumulation caused by its own activity (chapter 2). Later, I applied the theory we proposed in Schleimer et al. (2021), to quantitatively describe ionic concentration dependent spiking statistics (chapter 3). Finally, I used those spiking statistics to explain the dynamics of a spiking neural network composed of conductance based neurons whose spike generation is altered by ionic concentration dynamics (chapter 4).

In conclusion, I proposed a mechanistic explanation of how ionic concentration dynamics can alter single neuron and microcircuit activity. This thesis shows that activity-dependent changes in ionic gradients during prolonged neuronal activation can impact the pattern of ongoing action potential generation. This theoretical prediction challenges the view of neurons as static uni-functional computational elements. Furthermore, this

work shows that ionic concentrations can alter enormously the network dynamics, by modifying the single neuron spiking statistics.

5.1.1 Main theoretical contribution

The model proposed. The proposed single-compartment neuron model displays multiple features that coincide with experimental observations (chapter 2). It displays spike frequency adaptation, which results from the sodium pump activity. This feature has been observed in the response of leech mechanoreceptor neurons Arganda et al. (2007) as well as in rodent cortical neurons Gulledge et al. (2013). The model exhibits spike amplitude shrinkage as a consequence of slow intracellular sodium accumulation. Extracellular potassium accumulation may induce a bi-stability in the model, that is observable as intermittently interrupted firing, consistent with experimental observations Hounsgaard and Nicholson (1983).

Dimensionality reduction. The model proposed in chapter 2 reproduces closely diverse experimental observations linking ionic concentrations with neuronal dynamics. However, its multiple dimensions, make analysis unfeasible. Thus, in chapter 3 dynamical systems theory is used find a one dimensional projection, that explains the most relevant features of the neuronal activity.

Network dynamics made simple. Projecting the multi dimensional activity of a big population (N=4000) of neurons into a one dimensional vector, simplifies the analysis of the network dynamics (chapter 4). With simplified network dynamics, a clear and intuitive understanding of the interplay between the effect of parameters altering the single neuron response and the microcircuit dynamics, turns out feasible.

Multiple-use Technique. The approach used here can be implemented to understand the effect of a variety of parameters, like temperature, capacitance, and membrane leakage on the network dynamics. Given that such parameters have similar qualitative effects on neuron models Hesse et al. (2017); Franci et al. (2013).

5.1.2 Future work

Even though the model proposed shares multiple features observed experimentally. There are still broader questions that it failed to address.

In-homogeneous distribution of extracellular potassium. Amzica and colleagues Amzica and Steriade (2000) observed that stimulus induced activity in the cat visual cortex was followed by extracellular potassium accumulation only in the vicinity of active neurons. Thus, including activity dependent, spatial specific concentration changes could provide a good intuition on how spatial ionic gradients could alter the microcircuit activity. One possible outcome is the emergence of spatial waves, a phenomenon observed during spreading depolarization.

Broad range of $[K]^+$ homeostatic mechanisms. As mentioned early on this thesis, glial cell uptake of the extracellular potassium, and potassium diffusion along the glial network, are active homeostatic regulatory mechanisms. It has been suggested

that both act upon different time-scales. In the model shown here the dynamics of glial potassium regulation was ignored, but including it might improve our understanding of slow synchronization of distant neuronal populations Amzica and Steriade (2000).

Considering other ionic species might drastically change the dynamics of the system. Chloride $[Cl]^-$, and Calcium $[Ca]^{2+}$ are known to alter neuronal excitability. There are multiple calcium dependent depolarizing currents known to be active on cortical pyramidal cells. Including the dynamics of those ionic species might alter the bifurcation structure derived in chapter 2. It has been suggested, for instance that hyperpolarization activated currents I_h might annihilate the bistability reported here Hahn and Durand (2001). This conjecture remains to be shown, and a feasible approach to do so is the one proposed in the work by Franci et. al Franci et al. (2013).

Conductance based synapses. Chloride $[Cl]^-$, calcium $[Ca]^{2+}$, potassium $[K]^+$, and sodium $[Na]^+$ concentration changes can alter synaptic excitatory and inhibitory currents. Including such effects on conductance based synapses, would allow comparing the contribution of the ionic dependent synaptic change and the intrinsic neuronal response change to the network dynamics.

Abstracting the relevant dynamics in simpler models. The dimensionality reduction shown in chapter 3 makes evident that simpler models, like the quadratic-integrate and fire model, could capture the most relevant spiking dynamics. The quadratic-integrate and fire model has fewer parameters than the model proposed in chapter 2, and conveniently displays qualitatively similar dynamics. Modifying only one parameter in the quadratic-integrate and fire model, the reset value, makes it possible to set the model in the regular spiking regime or in the intermittently interrupted firing regime. Given the vast amount of analytical work developed for networks containing quadratic-integrate and fire units, using this model makes it feasible to generate analytical predictions, thus, more general intuitions than the ones obtained with constrained simulations as the ones performed in this work.

6 | Outlook

6.1 Outlook

This work showed how ionic concentration dynamics can alter cortical activity, by reshaping the single neuron spiking statistics. Cortical activity of behaving animals has been widely studied. Thus, there are enough phenomenological observations to draw a link between different behavioral states and the characteristic cortical activity. In this section, I will give an outlook of different cortical states contextualized by their respective behavioral state. I will speculate, based on what was found in this work, how ionic concentrations could be involved in generating behavioral state changes.

6.2 Brain states

The broad environmental changes challenge animals to constantly switch between different behavioral states in order to react optimally. When an animal is resting and receives a stimulus that has been linked with danger before, probably its attention would automatically focus on the source of the stimulus. If after a while, there are enough cues to rule out danger, its attention would be shifted again and the vigilant state would probably be substituted by a resting state. Such behavioral states, can be associated to specific traits of neural activity.

Neural activity can be measured electrophysiologically and is remarkably different during resting and vigilant states. Widespread techniques to measure the brain's electrical activity are the electroencephalogram (EEG), and local field potential (LFP). The EEG is a noninvasive technique in which scalp electrodes record the electrical activity of the brain cortex. The LFP is an invasive technique that places electrodes in the brain tissue, close to the region of interest, and records the electrical field generated by the neighboring cells. When an animal is quietly resting, there is high activity in EEG and LFP on the frequency band between 1-4Hz. The power on this frequency band further increases when the animal falls asleep Lee and Dan (2012). However, during attentive states cortical activity measured with the LFP is desynchronized in the low frequencies Niell and Stryker (2010), which leads to a measured signal with very low power in the 1-4Hz frequency band.

There are different degrees of rest, and vigilance. One of the most widely studied states among the resting states is sleep. Sleep makes animals vulnerable since they are

not able to detect changing environmental conditions. During sleep, animals sacrifice foraging and mating opportunities. Nevertheless, it is a universal behavior across the animal kingdom. Sleep is a systemic state, thus, it has been linked with a broad range of functions. There is a tight link between the sleeping cycle and the immune system Besedovsky et al. (2012), and homeostatic mechanisms for breathing, cardiovascular and gastrointestinal function and thermoregulation happen during sleepSteriade and McCarley (2005).

Several studies have found strong evidence suggesting that memories are consolidated during sleep Girardeau et al. (2009); van de Ven et al. (2016); Lee and Dan (2012). In humans, for instance, motor skills in specific tasks can be enhanced by sleeping shortly after practicing Lee and Dan (2012). The potential that sleep has to catalyze learning and memory consolidation, makes it a very intriguing behavioral state from the computational perspective.

6.2.1 Sleep

To understand the link between sleep and learning processes, various studies conveniently split sleep into its characteristic electroencephalographic stages. Sleep is separated into two main categories: rapid eye movement (REM) sleep, and non-REM sleep. During REM sleep the EEG signal has very small amplitude, and resembles the signals recorded during awake periods. Another prominent feature of this sleep stage is that animals have rapid eye movements but, overall, low muscle tone. During non-REM sleep the power in the 1-4Hz frequency band is increased and no rapid eye movements are detected. Non-Rem sleep is often divided into 3 stages, Stage I, II, and III Purves (2004).

Stage I marks the transition from the awake state to the sleeping state. In humans the EEG recorded during this stage is characterized by a high power on the theta frequency band (4-8Hz). Stage II is a deeper sleep state and is characterized by the occurence of multiple sleep spindle[1] events. Stage III, or slow wave sleep (SWS), is characterized by high-amplitude slow oscillations with the highest power on the 0.5-2Hz frequency band Purves (2004). Slow wave sleep is the deepest sleep stage, thus, is often hard to be awakened during this stage. The cortical activity during slow wave sleep resembles the activity during anesthesia, which is why many experimental setups use anesthetized animals as models to understand the brain activity during slow wave sleep.

Slow wave sleep. The slow cortical oscillation observed during slow waves is thought of a pacer for faster oscillations. During slow waves the membrane potential of pyramidal neurons alternates between depolarized, and hyperpolarized states with a $\sim 1Hz$ rhythmic fashion Steriade et al. (1993). The up-state that corresponds to the surface-positive half-wave of the slow oscillation coincides with depolarized neuronal membrane potentials. Thus, it is thought of a window of neuronal activity facilitation. During the up-phase the sleep spindle occurrence increases. Furthermore, sleep spindles have

[1] Spindles are oscillations on the frequency range of 12-14Hz that last 0.5-1.5 seconds. Are generated with thalamo-cortical circuits. These oscillations are thought to be involved in sensory processing and long-term memory consolidation.

been shown to be temporally locked to hippocampal (CA3) sharp wave-ripples[2] (SWR) Clemens et al. (2007). The co-ocurrence of spindles and sharp wave ripples is thought of a mechanism for information transfer between hippocampus and neocortex which could underly long term memory consolidation Axmacher et al. (2006). In fact, the length of Stages II and III are correlated with performance of learning motor tasks Huber et al. (2004).

Sleep spindles occur after cortical (layer 4) pyramidal neurons receive excitatory post synaptic potentials from bursting thalamocortical neurons. Some of these excitatory post synaptic potentials trigger spikes in cortical neurons, and often just a subthreshold deflection of their membrane potential Amzica and Steriade (2001); Adamantidis et al. (2019). Here I hypothesize that extracellular potassium may facilitate cortical spikes during spindle occurrence, which is more likely at the up-state of the slow wave. Extracellular potassium concentration during slow wave sleep is dynamic, and its fluctuations are locked to the LFP slow oscillation Amzica and Steriade (2000); Amzica et al. (2002); Amzica (2002); Seigneur et al. (2006). Amzica and colleagues observed that extracellular potassium concentration oscillation has a spectral composition with a peak at 1Hz. The peak of the extracellular potassium concentration oscillation coincides with the up-state of cortical activity. Amzica and colleagues hypothesize that the extracellular potassium oscillation is paced by glial cells, given that it is highly correlated ($\sim$97%) with a glial membrane potential oscillation (with a short time lag $< 7ms$). If this hypothesis is true, such oscillation could have the purpose of modulating cortical activity during slow wave sleep.

In this thesis, it was shown that extracellular potassium concentration can modulate the network dynamics, by altering the single neuron spiking statistics. In chapter 4, it was shown that the potential landscape of the network can be reshaped with extracellular potassium accumulation. Thus, a natural question that follows is whether the extracellular potassium oscillation is dynamically shaping the potential landscape of the cortex during slow wave sleep. Stabilizing, and destabilizing certain neuronal activity states dynamically. And for instance,facilitating cortical spikes during sleep spindles which may elicit synaptic strengthening.

There is ample evidence of the potential implication of slow wave sleep in behaviorally crucial processes as learning and memory consolidation. Multiple measurements of single neurons, and population activity (LFP, and EEG) have characterized the overall change of the brain activity as well. Nevertheless, how the transition to slow wave sleep occurs, and how are the different sleep stages maintained, are still open questions.

[2]Sharp wave-ripples (SWR) are transient deflections (sharp wave) overlaid by fast (ripple) oscillations (120-250 Hz) of the LFP measured in the hippocampus (CA areas), with a duration of 50-100ms. SWRs are thought to mediate the consolidation of explicit memories

6.3 Modulation of cortical states through extracellular ionic concentrations

Neuromodulators are known to play a big role in inducing brain state changes. For instance, the coordinated release of some neuromodulators [3], has been shown to induce the arousal state Seigneur et al. (2006). Several studies have attempted to understand the particular effect of neuromodulators on glial cells, neurons, and interneurons. From these studies we now know that the effect of each neuromodulator is highly diverse across the different cell populations, and even across brain circuits (See this review for an example of the effect of norepinephrine O'Donnell et al. (2012)). Given the broad and diverse effect of neuromodulators on the brain activity, it is still not clear how they give rise to the stereotypical cortical activity observed during different brain states.

By studying the transition between sleep and awake states, Ding and colleagues proposed that neuromodulators can alter the cortical activity by effectively altering the extracellular ionic concentrations Ding et al. (2016). They confirmed the hypothesis by first observing that neuromodulators can alter the extracellular concentrations before and after blocking neuronal activity. Afterwards, they measured the extracellular concentrations of different ions[4] when mice where awake and right after they fell asleep. The authors reported significant differences in the concentrations of those ions in both brain states. Extracellular potassium concentrations of $[K_o]^+$ decreased, calcium increased $[Ca_o]^{2+}$, and magnesium $[Mg_o]^{2+}$ decreased when the mouse fell asleep. Even more striking, was that when infusing solutions with the same extracellular concentrations as the ones measured during awake periods, they could induce the awake state. On the same line of experiments, earlier, Korytova reported a similar accumulation of extracellular potassium K_o^+ when transiently waking rats Korytová (1977).

Given that extracellular concentrations are dynamic, and their variation coincide with sleep-wake transition, the natural question that follows is whether the direct ionic effect on the network dynamics is enough to explain such transition. Given that to date, there is no single circuit that generates the wake-active transition, but rather multiple circuits can generate the transition. A generic means by which those circuits could induce awakening is by altering extracellular concentrations through Glial activity for instance.

The theoretical insights presented throughout this thesis suggest that extracellular potassium can alter the microcircuit activity, as drastically as the observed changes of cortical activity during behavioral changes such as sleep-wake transitions. This alteration is evident at the single cell level, spiking statistics where shown to be drastically altered with extracellular potassium accumulation. This prediction is supported by previous modelling studies that have proposed that extracellular potassium can have a drastic effect on neuronal spiking dynamics Hahn and Durand (2001); Aihara and Matsumoto (1983); Fröhlich and Bazhenov (2006). By altering the single cell spiking statistics, the microcircuit dynamics are also altered. And the population activity exhibits different

[3] norepinephrine, acetylcholine, histamine, dopamine, orexin.

[4] Potassium, calcium and magnesium

spectral components when extracellular potassium accumulates. This prediction is supported by the work of Bellot-Saez and colleagues Bellot-Saez et al. (2018), who observed that perturbing slices from somatosensory cortical areas of mice, with high extracellular potassium concentration solutions, distort the frequency components of the local field potentials. As shown in this work, the extracellular potassium accumulation induced change in spiking dynamics could result in a strong alteration of network dynamics, that can explain the drastic change of the measured cortical activity across behavioral states.

Bibliography

Adamantidis, A. R., Gutierrez Herrera, C., and Gent, T. C. (2019). Oscillating circuitries in the sleeping brain. *Nature Reviews Neuroscience*.

Aihara, K. and Matsumoto, G. (1983). Two stable steady states in the Hodgkin-Huxley axons. *Biophysical journal*, 41(1):87–9.

Amit, D. and Brunel, N. (1997). Model of global spontaneous activity and local structured activity during delay periods in the cerebral cortex. *Cerebral Cortex*, 7(3):237–252.

Amzica, F. (2002). In vivo electrophysiological evidences for cortical neuron-glia interactions during slow ($<$ 1 Hz) and paroxysmal sleep oscillations. *Journal of Physiology Paris*, 96(3):209–219.

Amzica, F., Massimini, M., and Manfridi, A. (2002). Spatial buffering during slow and paroxysmal sleep oscillations in cortical networks of glial cells in vivo. *Journal of Neuroscience*, 22(3):1042–1053.

Amzica, F. and Steriade, M. (2000). Neuronal and glial membrane potentials during sleep and paroxysmal oscillations in the neocortex. *The Journal of neuroscience : the official journal of the Society for Neuroscience*, 20(17):6648–6665.

Amzica, F. and Steriade, M. (2001). 2 - Electrophysiology of Sleep. In Dinner, D. S. and Lüders, H. O., editors, *Epilepsy and Sleep*, pages 19–41. Academic Press, San Diego.

Arganda, S., Guantes, R., and de Polavieja, G. G. (2007). Sodium pumps adapt spike bursting to stimulus statistics. *Nature Neuroscience*, 10(11):1467–1473.

Axmacher, N., Mormann, F., Fernández, G., Elger, C. E., and Fell, J. (2006). Memory formation by neuronal synchronization.

Azarias, G., Kruusmägi, M., Connor, S., Akkuratov, E. E., Liu, X.-L., Lyons, D., Brismar, H., Broberger, C., and Aperia, A. (2012). A Specific and Essential Role for Na,K-ATPase 3 in Neurons Co-expressing 1 and 3 *. *The Journal of biological chemistry*, 288(4):2734–2743.

Barreto, E. and Cressman, J. R. (2011). Ion concentration dynamics as a mechanism for neuronal bursting. *Journal of Biological Physics*, 37(3):361–373.

Bazhenov, M., Timofeev, I., Steriade, M., and Sejnowski, T. J. (2002). Model of thalamocortical slow-wave sleep oscillations and transitions to activated states. *Journal of Neuroscience*, 22(19):8691–8704.

Bazhenov, M., Timofeev, I., Steriade, M., and Sejnowski, T. J. (2004). Potassium model for slow (2-3 Hz) in vivo neocortical paroxysmal oscillations. *Journal of neurophysiology*, 92(2):1116–1132.

Bellot-Saez, A., Cohen, G., van Schaik, A., Ooi, L., W Morley, J., and Buskila, Y. (2018). Astrocytic modulation of cortical oscillations. *Scientific Reports*, 8(1):11565.

Besedovsky, L., Lange, T., and Born, J. (2012). Sleep and immune function.

Blaesse, P., Airaksinen, M. S., Rivera, C., and Kaila, K. (2009). Cation-Chloride Cotransporters and Neuronal Function. *Neuron*, 61(6):820–838.

Blanco, G. (2005). Na,K-ATPase Subunit Heterogeneity as a Mechanism for Tissue-Specific Ion Regulation. *Seminars in nephrology*, 25(5):292–303.

Bromm, B. and Frankenhaeuser, B. (1972). Repetitive discharge of the excitable membrane computed on the basis of voltage clamp data for the node of Ranvier. *Pflügers Archiv: European Journal of Physiology*, 332(1).

Brunel, N. (2000). Dynamics of Sparsely Connected Networks of Excitatory and Inhibitory Spiking Neurons. *J Comput Neurosci*, 8:183–208.

Brunel, N., Chance, F. S., Fourcaud, N., and Abbott, L. F. (2001). Effects of synaptic noise and filtering on the frequency response of spiking neurons. *Physical Review Letters*, 86(10):2186–2189.

Chow, C. and White, J. (1996). Spontaneous action potentials due to channel fluctuations. *Biophysical Journal*, 71(6):3013–3021.

Clausen, M. V., Hilbers, F., and Poulsen, H. (2017). The Structure and Function of the Na,K-ATPase Isoforms in Health and Disease. *Frontiers in Physiology*, 8:371.

Clemens, Z., Mölle, M., Eross, L., Barsi, P., Halász, P., and Born, J. (2007). Temporal coupling of parahippocampal ripples, sleep spindles and slow oscillations in humans. *Brain*, 130(11):2868–2878.

Colbert, C. M., Magee, J. C., Hoffman, D. A., and Johnston, D. (1997). Slow recovery from inactivation of Na+ channels underlies the activity- dependent attenuation of dendritic action potentials in hippocampal CA1 pyramidal neurons. *Journal of Neuroscience*, 17(17):6512–6521.

Cole, K. S. and Moore, J. W. (1960). Ionic current measurements in the squid giant axon membrane. *The Journal of general physiology*, 44(1):123–167.

Compte, A., Reig, R., Descalzo, V. F., Harvey, M. A., Puccini, G. D., and Sanchez-Vives, M. V. (2008). Spontaneous high-frequency (10-80 Hz) oscillations during up states in the cerebral cortex in vitro. *Journal of Neuroscience*.

Crambert, G., Hasler, U., Beggah, A. T., Yu, C., Modyanov, N. N., Horisberger, J.-D., Leliè vre, L., and thi Geering, K. (2000). Transport and Pharmacological Properties of Nine Different Human Na,K-ATPase Isozymes*. *The Journal of biological chemistry*, 275(3):1976–1986.

Dallérac, G., Chever, O., and Rouach, N. (2013). How do astrocytes shape synaptic transmission? Insights from electrophysiology. *Frontiers in cellular neuroscience*, 7:159.

Dichter, M. A. and Ayala, G. F. (1987). Cellular mechanisms of epilepsy: A Status report. *Science*, 237(4811):157–164.

Ding, F., O'Donnell, J., Xu, Q., Kang, N., Goldman, N., and Nedergaard, M. (2016). Changes in the composition of brain interstitial ions control the sleep - wake cycle. *Science (New York, N.Y.)*, 352(6285):550–555.

Doedel, E. J., Champneys, A. R., Dercole, F., Fairgrieve, T., Kuznetsov, Y., Oldeman, B.,

Paffenroth, R., Sandstede, B., Wang, X., and Zhang, C. (2008). AUTO-07P: Continuation and Bifurcation Software for Ordinary Differential Equations.

Dummer, B., Wieland, S., and Lindner, B. (2014). Self-consistent determination of the spike-train power spectrum in a neural network with sparse connectivity. *Frontiers in Computational Neuroscience*, 8:104.

Engelken, R., Farkhooi, F., Hansel, D., van Vreeswijk, C., and Wolf, F. (2016). A reanalysis of "Two types of asynchronous activity in networks of excitatory and inhibitory spiking neurons" [version 1; referees: 2 approved]. *F1000Research*, 5.

Ermentrout, B. (1996). Type I Membranes, Phase Resetting Curves, and Synchrony. *Neural Computation*, 8(5):879–1001.

Farkhooi, F., Froese, A., Muller, E., Menzel, R., and Nawrot, M. P. (2013). Cellular Adaptation Facilitates Sparse and Reliable Coding in Sensory Pathways. *PLoS Computational Biology*, 9(10):e1003251.

Fertziger, A. P. and Ranck, J. B. (1970). Potassium accumulation in interstitial space during epileptiform seizures. *Experimental neurology*, 26(3):571–85.

Fink, C. G., Booth, V., and Zochowski, M. (2011). Cellularly-driven differences in network synchronization propensity are differentially modulated by firing frequency. *PLoS Computational Biology*, 7(5):e1002062.

Fleidervish, I. A., Friedman, A., and Gutnick, M. J. (1996). Slow inactivation of Na current and slow cumulative spike adaptation in mouse and guinea-pig neocortical neurones in slices. *The Journal of physiology*, 493:83–97.

Franci, A., Drion, G., Seutin, V., and Sepulchre, R. (2013). A Balance Equation Determines a Switch in Neuronal Excitability. *PLoS Computational Biology*, 9(5):e1003040.

Frankenhaeuser, B. and Hodgkin, A. L. (1957). The action of calcium on the electrical properties of squid axons. *The Journal of physiology*, 137:218–244.

Frankenhaeuser, B. and Vallbo, B. (1965). Accommodation in Myelinated Nerve Fibres of Xenopus Laevis as Computed on the Basis of Voltage Clamp Data. *Acta Physiologica Scandinavica*, 63(1-2):1–20.

Franklin, J. and Bair, W. (1995). The Effect of a Refractory Period on the Power Spectrum of Neuronal Discharge. *SIAM Journal on Applied Mathematics*, 55(4):1074–1093.

Fröhlich, F. and Bazhenov, M. (2006). Coexistence of tonic firing and bursting in cortical neurons. *Physical Review E*, 74(3):031922.

Fröhlich, F., Bazhenov, M., Iragui-Madoz, V., and Sejnowski, T. J. (2008). Reviews: Potassium dynamics in the epileptic cortex: New insights on an old topic.

Gardiner, C. W. C. W. (2009). *Stochastic methods : a handbook for the natural and social sciences*, volume 13. Springer.

Gerstein, G. L. and Mandelbrot, B. (1964). Random Walk Models for the Spike Activity of a Single Neuron. *Biophysical Journal*, 4(1):41–68.

Girardeau, G., Benchenane, K., Wiener, S. I., Buzsáki, G., and Zugaro, M. B. (2009). Selective suppression of hippocampal ripples impairs spatial memory. *Nature Neuroscience*, 12:1222–1223.

Greenberg, D. S., Houweling, A. R., and Kerr, J. N. (2008). Population imaging of ongoing neuronal activity in the visual cortex of awake rats. *Nature Neuroscience*, 11(7):749–751.

Grienberger, C. and Konnerth, A. (2012). Imaging Calcium in Neurons.

Gulledge, A. T., Dasari, S., Onoue, K., Stephens, E. K., Hasse, J. M., and Avesar, D. (2013). A sodium-pump-mediated afterhyperpolarization in pyramidal neurons. *The Journal of Neuroscience*, 33(32):13025–13041.

Hahn, P. J. and Durand, D. M. (2001). Bistability Dynamics in Simulations of Neural Activity in High-Extracellular-Potassium Conditions. *Journal of Computational Neuroscience*, 11:5–18.

Harris, K. D. and Thiele, A. (2011). Cortical state and attention.

Hesse, J., Schleimer, J.-H., and Schreiber, S. (2017). Qualitative changes in phase-response curve and synchronization at the saddle-node-loop bifurcation. *PHYSICAL REVIEW E*, 95.

Hodgkin, A. L. and Huxley, A. F. (1952). A quantitative description of membrane current and its application to conduction and excitation in nerve. *The Journal of Physiology*, 117(4):500–544.

Hounsgaard, J. and Nicholson, C. (1983). Potassium accumulation around individual purkinje cells in cerebellar slices from the guineapig. *The Journal of Physiology*, 340:359–388.

Hübel, N. and Dahlem, M. A. (2014). Dynamics from Seconds to Hours in Hodgkin-Huxley Model with Time-Dependent Ion Concentrations and Buffer Reservoirs. *PLoS Computational Biology*, 10(12):e1003941.

Huber, R., Ghilardi, M. F., Massimini, M., and Tononi, G. (2004). Local sleep and learning. *Nature*, 430:78–81.

Izhikevich, E. M. (2007). *Dynamical Systems in Neuroscience*. MIT Press.

Jung, H. Y., Mickus, T., and Spruston, N. (1997). Prolonged sodium channel inactivation contributes to dendritic action potential attenuation in hippocampal pyramidal neurons. *The Journal of neuroscience : the official journal of the Society for Neuroscience*, 17(17):6639–46.

Kager, H., Wadman, W. J., and Somjen, G. G. (2000). Simulated seizures and spreading depression in a neuron model incorporating interstitial space and ion concentrations. *Journal of Neurophysiology*, 84(1).

Kirst, C., Ammer, J., Felmy, F., Herz, A., and Stemmler, M. (2015). Fundamental Structure and Modulation of Neuronal Excitability: Synaptic Control of Coding, Resonance, and Network Synchronization. *bioRxiv*.

Kofuji, P. and Newman, E. A. (2004). Potassium buffering in the central nervous system. *Neuroscience*, 129(4):1045–1056.

Korytová, H. (1977). Arousal-induced increase of cortical [K+] in unrestrained rats. *Experientia*, 33(2):242–244.

Kramers, H. (1940). Brownian motion in a field of force and the diffusion model of chemical reactions. *Physica*, 7(4):284–304.

Krishnan, G. P., Filatov, G., Shilnikov, A., and Bazhenov, M. (2015). Electrogenic properties of the Na+/K+ ATPase control transitions between normal and pathological brain states. *Journal of Neurophysiology*, 113(9):3356–3374.

LeBeau, F. E. N., Towers, S. K., Traub, R. D., Whittington, M. A., and Buhl, E. H. (2002). Fast network oscillations induced by potassium transients in the rat hippocampus in vitro. *Journal of Physiology*, 542:167–179.

Lee, S. H. and Dan, Y. (2012). Neuromodulation of Brain States.

Lindner, B. (2004). Interspike interval statistics of neurons driven by colored noise. *Physical Review E*, 69(2):022901.

Litwin-Kumar, A. and Doiron, B. (2012). Slow dynamics and high variability in balanced cortical networks with clustered connections. *Nature Neuroscience*, 15:1498–1505.

Lux, H. D. and Neher, E. (1973). The equilibration time course of [K+]0 in cat cortex. *Experimental Brain Research*, 17(2):190–205.

Marder, E. (2011). Variability, compensation, and modulation in neurons and circuits. *Proceedings of the National Academy of Sciences*, 108(Supplement_3):15542–15548.

Marder, E. and Goaillard, J.-M. (2006). Variability, compensation and homeostasis in neuron and network function. *Nature Reviews Neuroscience*, 7(7):563–574.

Mitra, N. (1955). Quantitative analysis of cell types in mammalian neo-cortex. *Journal of anatomy*, 89(4):467–483.

Moseley, A. E., Lieske, S. P., Wetzel, R. K., James, P. F., He, S., Shelly, D. A., Paul, R. J., Boivin, G. P., Witte, D. P., Marino Ramirez, J., Sweadner, K. J., and Lingrel, J. B. (2002). The Na,K-ATPase 2 Isoform Is Expressed in Neurons, and Its Absence Disrupts Neuronal Activity in Newborn Mice. *The Journal of biological chemistry*, 278(7):5317–5324.

Neher, E. and Sakaba, T. (2008). Multiple Roles of Calcium Ions in the Regulation of Neurotransmitter Release.

Niell, C. M. and Stryker, M. P. (2010). Modulation of Visual Responses by Behavioral State in Mouse Visual Cortex. *Neuron*, 65(4):472–479.

O'Donnell, J., Zeppenfeld, D., McConnell, E., Pena, S., and Nedergaard, M. (2012). Norepinephrine: A neuromodulator that boosts the function of multiple cell types to optimize CNS performance.

Owen, J. A., Barreto, E., and Cressman, J. R. (2013). Controlling Seizure-Like Events by Perturbing Ion Concentration Dynamics with Periodic Stimulation. *PLoS ONE*, 8(9).

Panayiotopoulos, C. (2005). The Epilepsies: Seizures, Syndromes and Management. In *Oxfordshire (UK): Bladon Medical Publishing. Chapter 13, Reflex Seizures and Reflex Epilepsies.* Bladon Medical Publishing.

Pena, R. F., Vellmer, S., Bernardi, D., Roque, A. C., and Lindner, B. (2018). Self-consistent scheme for spike-train power spectra in heterogeneous sparse networks. *Frontiers in Computational Neuroscience*, 12:9.

Pilgrim, C., Reisert, I., and Grab, D. (1982). Volume densities and specific surfaces of neuronal and glial tissue elements in the rat supraoptic nucleus. *Journal of Comparative Neurology*, 211(4).

Pinsky, P. F. and Rinzel, J. (1994). Intrinsic and network rhythmogenesis in a reduced traub model for CA3 neurons. *Journal of Computational Neuroscience*, 1:39–60.

Purves, D. (2004). *Neuroscience*. Sinauer Associates, Publishers.

Rasmussen, R., Jensen, M. H., and Heltberg, M. L. (2017). Chaotic Dynamics Mediate Brain State Transitions, Driven by Changes in Extracellular Ion Concentrations. *Cell Systems*, 5(6):591–603.

Renart, A., De La Rocha, J., Bartho, P., Hollender, L., Parga, N., Reyes, A., and Harris, K. D. (2010). The asynchronous state in cortical circuits. *Science*, 327(5965):587–590.

Rimmele, T. S., Rocher, A.-B., Wellbourne-Wood, J., and Chatton, J.-Y. (2017). Control of Glutamate Transport by Extracellular Potassium: Basis for a Negative Feedback on Synaptic Transmission. *Cerebral Cortex*, 27(6):3272–3283.

Schleimer, J. H. (2013). *Spike statistics and coding properties of phase models*. PhD thesis, Humboldt-Universität zu Berlin, Mathematisch-Naturwissenschaftliche Fakultät I.

Schleimer, J.-H., Hesse, J., Contreras, S. A., and Schreiber, S. (2021). Firing statistics in the bistable regime of neurons with homoclinic spike generation. *Physical Review E*, 103(1):012407.

Schleimer, J.-H. and Schreiber, S. (2018). Phase-response curves of ion channel gating kinetics. *Mathematical Methods in the Applied Sciences*, 41(18):8844–8858.

Seigneur, J., Kroeger, D., Nita, D. A., and Amzica, F. (2006). Cholinergic action on cortical glial cells in vivo. *Cerebral Cortex*, 16(5):655–668.

Singer, W. and Lux, H. (1975). Extracellular potassium gradients and visual receptive fields in the cat striate cortex. *Brain Research*, 96(2):378–383.

Skinner, J. E. and Molnar, M. (1983). Event-related extracellular potassium ion activity changes in frontal cortex of the conscious cat. *Journal of Neurophysiology*, 49(1):204–215.

Softky, W. R. and Koch, C. (1993). The highly irregular firing of cortical cells is inconsistent with temporal integration of random EPSPs. *Journal of Neuroscience*, 13(1):334–350.

Somjen, G. G. (2004). *Ions in the brain : normal function, seizures, and stroke*. Oxford University Press.

Sompolinsky, H., Crisanti, A., and Sommers, H. J. (1988). Chaos in random neural networks. *Physical Review Letters*, 61(3):259–262.

Steriade, M. and McCarley, R. W. (2005). Synchronized Brain Oscillations Leading to Neuronal Plasticity during Waking and Sleep States. In *Brain Control of Wakefulness and Sleep*, pages 255–344. Springer US, Boston, MA.

Steriade, M., Nunez, A., and Amzica, F. (1993). A novel slow ($<$ 1 Hz) oscillation of neocortical neurons in vivo: Depolarizing and hyperpolarizing components. *Journal of Neuroscience*, 13(8):3252–3265.

Stimberg, M., Brette, R., and Goodman, D. F. (2019). Brian 2, an intuitive and efficient neural simulator. *eLife*, 8:e47314.

Tatsuki, F., Sunagawa, G. A., Shi, S., Susaki, E. A., Yukinaga, H., Perrin, D., Sumiyama, K., Ukai-Tadenuma, M., Fujishima, H., Ohno, R. i., Tone, D., Ode, K. L., Matsumoto, K., and Ueda, H. R. (2016). Involvement of Ca 2+ -Dependent Hyperpolarization in Sleep Duration in Mammals. *Neuron*, 90(1):70–85.

Traub, R. D. and Miles, R. (1991). *Neuronal networks of the hippocampus*. Cambridge University Press.

Traub, R. D. and Wong, R. K. (1982). Cellular mechanism of neuronal synchronization in epilepsy. *Science*, 216(4547):745–747.

Valderrama, M., Crépon, B., Botella-Soler, V., Martinerie, J., Hasboun, D., Alvarado-Rojas, C., Baulac, M., Adam, C., Navarro, V., and Le Van Quyen, M. (2012). Human gamma oscillations during slow wave sleep. *PLoS ONE*, 7(4):e33477.

van de Ven, G. M., Trouche, S., McNamara, C. G., Allen, K., and Dupret, D. (2016). Hippocampal Offline Reactivation Consolidates Recently Formed Cell Assembly Patterns during Sharp Wave-Ripples. *Neuron*, 92(5):968–974.

Van Vreeswijk, C. and Sompolinsky, H. (1998). Chaotic Balanced State in a Model of Cortical Circuits. *Neural Computation*, 10(6):1321–1371.

Warren, C. P., Hu, S., Stead, M., Brinkmann, B. H., Bower, M. R., and Worrell, G. A. (2010). Synchrony in normal and focal epileptic brain: the seizure onset zone is functionally disconnected. *Journal of neurophysiology*, 104(6):3530–3539.

Wei, Y., Ullah, G., Ingram, J., and Schiff, S. J. (2014). Oxygen and seizure dynamics: II. Computational modeling. *Journal of Neurophysiology*, 112(2):213–223.

Y. Kuramoto (1984). Chemical Oscillations, Waves, and Turbulence. *Springer-Verlag Berlin Heidelberg*.

Young, G. A., Steinfels, G. F., Khazan, N., and Glaser, E. M. (1978). Cortical EEG power spectra associated with sleep-awake behavior in the rat. *Pharmacology, Biochemistry and Behavior*, 8(1):89–91.

Zahler, R., Zhang, Z.-T., Manor, M., and Boron, W. F. (1997). Sodium Kinetics of Na,K-ATPase Isoforms in Intact Transfected HeLa Cells. *J. Gen. Physiol*, 110(2):201–213.

Zandt, B.-J., ten Haken, B., van Dijk, J. G., and van Putten, M. J. A. M. (2011). Neural Dynamics during Anoxia and the "Wave of Death". *PLoS ONE*, 6(7):e22127.

Zucker, R. S. (1999). Calcium- and activity-dependent synaptic plasticity. *Current Opinion in Neurobiology*, 9(3):305–313.

Acknowledgements

This thesis would not have been possible without so many people that made this path walkable. First, I would like to thank Susanne for welcoming me to her lab. I admired her clear sight regarding the relevance of observations on the scientific aspect and her constant interest in fairness in everyday life and for society in general. I appreciated the amazing effort Susanne invested in guaranteeing that all the lab members had a proper working environment and wellbeing.

I am very grateful to Jan-Hendrik, whose enthusiasm for science is contagious, and who encouraged me along this path with his support and his advice. I greatly appreciate all the knowledge he transferred to us, and all the ideas that emerged from the endless discussion time he invested. This work wouldn't have been possible without all the technical efforts that Jan-Hendrik and Janina put into automatizing the use of AUTO. I would also like to thank Farzada, for all the discussion time that also contributed to shaping a part of this thesis. I enjoyed our scientific/philosophical/encouraging coffee breaks. I also have to thank: Susanne, Jan-Hendrik, Farzada, Allan, Pia, Robert, Meng, Mahraz and Tiziano for proofreading parts of this thesis. And, I would also like to thank Allan Gulledge for the very fruitful collaboration.

The BCCN provided an incredibly connected community where I could meet amazing scientists. Furthermore, they financed not only my first years of the Ph.D. but also the attendance to multiple conferences that were enlightening.

The ITB felt like a home many times, but particularly during Christmas. I am very happy I could experience all the beautiful traditions.

The working environment during these years was encouraging. The joint lab meetings of the Schreiber and Kempter labs were very helpful not only to improve the way this work was exposed but also to develop a broader view of theoretical neuroscience. The lunch and coffee breaks were always full of interesting discussions ranging from neuroscientific facts, going through politics, and ending in speculations of crazy sci-fi futuristic scenarios. I had a lot of fun. This would not have been possible without the smart, friendly, open-minded, and enthusiastic colleagues; Pia, Meng, Tiziano, Roberta, Natalie, Paul, Rike, Katha, Fred, Nelson, Mahraz, Naomi, Thomas, Gaspar, Fabian, Robert, Philipp, Moritz, Erik, Paula.

Outside the lab, I can not thank enough for all the support I received from my friends. During the happy times, the bad times, the weird times, the fun times, the pandemic times. I am sure I wouldn't have been able to finish this journey without you; Juan David, Tiziano, Roberta, Caro, Christian, Colosin,

Pachangalas, Juanse, Dianis, Juli, Silvi, Vane, Meng, Natalie, Maria, Pits, Andrew.

Many other people were very important during this period. Being an inspiration not only scientifically but personally; in between them the Ceballos, Contreras, eurorazas, amigas-clermont.

I thank my family, encouraging me from the time the idea to start a PhD came to my mind and supporting me through every step that took me here. I am sure I wouldn't even have been able to start this journey without you; Catalina, Pedro, Luz, Juan David.

Juan David, thank you for making me happy along the way.

Statutory Declaration

I declare in lieu of oath that I have written this thesis independently, without illicit assistance from third parties and using solely the aids mentioned. The experimental data presented in the second chapter is the result of a collaboration with the lab of Allan T. Gulledge, Molecular and Systems Biology, Geisel School of Medicine at Dartmouth College. Allan T. Gulledge designed the experimental protocol and performed the recordings. The technique shown in chapter 3 was developed in collaboration with Jan-Hendrik Schleimer, Janina Hesse, and Susanne Schreiber.

Eidesstattliche Versicherung

Hiermit erkläre ich, dass ich die vorliegende Arbeit selbstständig und eigenhändig sowie ohne unerlaubte fremde Hilfe und ausschließlich unter Verwendung der aufgeführten Quellen und Hilfsmittel angefertigt habe. Die im zweiten Kapitel vorgestellten experimentellen Daten sind das Ergebnis einer Zusammenarbeit mit dem Labor von Allan T. Gulledge, Molekular- und Systembiologie, Geisel School of Medicine am Dartmouth College. Allan T. Gulledge entwarf das Versuchsprotokoll und führte die Aufzeichnungen durch. Die in Kapitel 3 gezeigte Technik wurde in Zusammenarbeit mit Jan-Hendrik Schleimer, Janina Hesse und Susanne Schreiber entwickelt.

Date: _____

Signature: _____